Hydrotreating of Light Gas Oil Using Carbon Nanotube Supported NiMoS Catalysts: Influence of Pore Diameters

A thesis submitted to the College of Graduate Studies & Research in partial fulfillment
of the requirements for the Master of Science Degree in the
Department of Chemical Engineering,

University of Saskatchewan

Saskatoon, SK

By Stefan Kasey Sigurdson

© Copyright Stefan Kasey Sigurdson, December 2009. All rights reserved.

COPYRIGHT

The author has consented that the libraries of the University of Saskatchewan may make this thesis freely available for inspection. Furthermore, the author agrees that permission for the copying of this thesis in any manner, either in whole or part, for scholarly purposes be granted primarily by the professor(s) who supervised this thesis or in their absence by the Department Head of Chemical Engineering or the Dean of the College of Graduate Studies. Duplication, publication, or any use of this thesis, in part or in whole, for financial gain without prior written approval by the University of Saskatchewan is prohibited. It is also understood that due recognition shall be given to the author of this thesis and to the University of Saskatchewan for any use of the material in this thesis.

Request for the permission to copy or make use of the material in this thesis in whole or in part should be addressed to:

The Department Head of Chemical Engineering
College of Engineering
University of Saskatchewan
57 Campus Drive
Saskatoon SK Canada
S7N 5A9

ABSTRACT

Multi-walled carbon nanotubes (MWCNTs) are a potential alternative to commonly used catalyst support structures in hydrotreating processes. Synthesis of MWCNTs with specific pore diameters can be achieved by chemical vapor deposition (CVD) of a carbon source onto an anodic aluminum oxide (AAO) template. AAO films consist of pore channels in a uniform hexagonal arrangement that run parallel to the surface of the film. These films are created by the passivation of an aluminum anode within an electrolysis cell consisting of certain weak acid electrolytes. Changing the concentration of the electrolyte (oxalic acid) and the electrical potential of the electrolysis cell altered the pore channel diameter of these AAO films. Controlling the pore diameter of these templates enabled the pore diameter of MWCNTs synthesized by CVD to be controlled as well. The produced MWCNTs were characterized by scanning electron microscopy (SEM), transmission electron microscopy (TEM), thermogravimetric analysis (TGA), Raman spectroscopy, and N_2 adsorption analysis. Anodizing conditions of 0.40 M oxalic acid concentration and 40.0 V maximum anodizing potential were found to produce AAO films that resulted in MWCNTs with optimum surface characteristics for a catalyst support application. CVD parameter values of 650°C reaction temperature and 8.00 mL/(min·g) C_2H_2-to-AAO ratio were found to produce the highest yield of MWCNT product.

The MWCNTs were synthesized for the purpose of supporting hydroprocessing catalysts, with several grades of NiMo/MWCNT sulfide catalysts

being prepared to determine the optimum pore size. These catalysts were characterized by techniques of TEM, CO chemisorption, N_2 adsorption, and H_2 temperature programmed reduction (TPR). A MWCNT grade with 67 nm inner diameters (found from TEM analysis) was found to offer the best hydrodesulfurization (HDS) and hydrodenitrogenation (HDN) activities for the treatment of coker light gas oil (CLGO). After determining the most suitable pore diameter, the optimum catalyst metal loadings were found to be 2.5 wt.% for Ni and 19.5 wt.% for Mo. The optimum catalyst was found to offer HDS conversions of 90.5%, 84.4%, and 73.5% with HDN conversions of 75.9%, 65.8%, and 55.3% for temperatures of 370°C, 350°C, and 330°C, respectively. An equal mass loading of commercial NiMo/γ-Al_2O_3 catalyst offered HDS conversions of 91.2%, 77.9%, and 58.5% with HDN conversions of 71.4%, 53.2%, and 31.3% for temperatures of 370°C, 350°C, and 330°C, respectively.

A kinetic study was performed on the optimum NiMo/MWCNT catalyst to help predict its HDS and HDN activities while varying the parameters of temperature, liquid hourly space velocity (LHSV), pressure, and gas-to-oil flow rate ratio. Rate expressions were then developed to predict the behavior of both the HDS and HDN reactions. Power law models were best fit with reaction orders of 2.6 and 1.2, and activation energies of 161 kJ/mol and 82.3 kJ/mol, for the HDS and HDN reactions, respectively. Generalized Langmuir-Hinshelwood models were found to have reaction orders of 3.0 and 1.5, and activation energies of 155 kJ/mol and 42.3 kJ/mol, for the HDS and HDN reactions, respectively.

ACKNOWLEDGEMENT

I would first like to thank my two supervisors, Dr. Ajay Dalai and Dr. John Adjaye, for their valued guidance and supervision throughout the planning, execution, and communication of my thesis work. I greatly appreciate the time taken by both to review and critique my written materials. I would also like to thank the other two members of my evaluation committee, Dr. Jafar Soltan and Dr. Catherine Niu, for their contributions to my graduate studies.

Secondly, I would also like to thank Dr. Sundaramurthy Vedachalam for his post-doctoral supervision, both through my first year of graduate work and as an undergraduate summer student. Thanks also go to Mr. Richard Blondin and Mr. Dragan Cekic for their assistance in the laboratory work that contributed to my project. My thanks also go to the Natural Science and Engineering Research Council of Canada for their much-appreciated financial assistance. I also greatly appreciate the work done by the University of New Brunswick and the Syncrude Canada Limited Research Department for their assistance in the electron microscopy contributions of this thesis.

Lastly, I would like to thank all the professors, post-doctorate fellows, graduate students, and undergraduates that have contributed to my six years at the University of Saskatchewan. Most of all, I would like to thank my mother, father, and brother for always supporting me and believing in me. They are the reason behind everything I do.

TABLE OF CONTENTS

LIST OF TABLES

LIST OF FIGURES

NOMENCLATURE

α	proportionality constant relating system pressure to H_2 partial pressure, dimensionless
β_{HDN}	isothermality ratio for the catalyst pellet in a hydrodenitrogenation reaction, dimensionless
β_{HDS}	isothermality ratio for the catalyst pellet in a hydrodenitrogenation reaction, dimensionless
γ_P	tortuosity of the catalyst pellets, dimensionless
$\Delta\rho_T$	temperature density correlation, lbs/ft^3
$\Delta\rho_P$	pressure density correlation, lbs/ft^3
$\Delta H_{R,HDN}$	heat of the hydrodenitrogenation reaction, kJ/mol
$\Delta H_{R,HDS}$	heat of the hydrodesulfurization reaction, kJ/mol
ε	catalyst bed porosity, dimensionless
ε_P	porosity of the catalyst pellets, dimensionless
$[\eta_O]_N$	effectiveness factor at the inlet of the hydrodenitrogenation reaction, dimensionless
$[\eta_O]_S$	effectiveness factor at the inlet of the hydrodesulfurization reaction, dimensionless
$[\eta_P]_N$	effectiveness factor at the outlet of the hydrodenitrogenation reaction, dimensionless
$[\eta_P]_S$	effectiveness factor at the outlet of the hydrodesulfurization reaction, dimensionless
$[\Phi_O]_N$	dimensionless Thiele modulus at the inlet of the hydrodenitrogenation reaction, dimensionless
$[\Phi_O]_S$	dimensionless Thiele modulus at the inlet of the hydrodesulfurization reaction, dimensionless

$[\Phi_P]_N$	dimensionless Thiele modulus at the outlet of the hydrodenitrogenation reaction, dimensionless
$[\Phi_P]_S$	dimensionless Thiele modulus at the inlet of the hydrodesulfurization reaction, dimensionless
λ_{H2}	hydrogen solubility in CLGO, mL/(kg·MPa)
λ_N	adsorption energy for all nitrogen heteroatoms within coker light gas oil, J/mol
λ_S	adsorption energy for all sulfur heteroatoms within coker light gas oil, J/mol
μ_L	viscosity of CLGO at the operating temperature, g/(s·cm)
$\rho_{15.6}$	density of CLGO at 15.6°C, g/mL
ρ_{20}	density of CLGO at 20°C, g/mL
ρ_L	density of CLGO at the operating conditions, g/mL
a_L	interfacial surface area over unit volume of a catalyst, cm^{-1}
a_S	liquid/solid interfacial surface area, cm^{-1}
$°API$	American Petroleum Institute gravity of petroleum liquids, dimensionless
A	surface area of catalysts and catalyst supports found from BET analysis, m^2/g
A_{HDN}	Arrhenius constant for the hydrodenitrogenation reaction rate, $s^{-1}\cdot(mol/L)^{(1-v)}$
A_{HDS}	Arrhenius constant for the hydrodesulfurization reaction rate, $s^{-1}\cdot(mol/L)^{(1-n)}$
$[C_S]_S$	catalyst surface concentration of sulfur species, mol/mL
$[C_N]_S$	catalyst surface concentration of nitrogen species, mol/mL
C_{AA}	concentration of aromatic amines, mol/L

C_{H2}	hydrogen concentration in the liquid phase at equilibrium, mol/mL
C_i	concentration of species ***i*** heteroatom, mol/L
C_O	feed concentration of species ***X*** heteroatom, mol/L
C_P	product concentration of species ***X*** heteroatom, mol/L
C_N	concentration of all nitrogen heteroatoms within coker light gas oil, mol/L
C_S	concentration of all sulfur heteroatoms within coker light gas oil, mol/L
C_{SA}	concentration of saturated quinoline, mol/L
C_X	concentration of species ***X***, mol/L
C_Y	concentration of ammonia, mol/L
d	average pore diameter of catalysts and catalyst supports, nm
d_P	average diameter of the catalyst particles, cm
$[D_N]_E$	effective diffusivity of organonitrogen compounds, cm^2/g
$[D_S]_E$	effective diffusivity of organosulfur compounds, cm^2/g
D_L	diffusivity of hydrogen in CLGO, cm^2/s
D_N	bulk diffusivity of organonitrogen compounds, cm^2/g
D_S	bulk diffusivity of organosulfur compounds, cm^2/g
E_{HDN}	activation energy for the hydrodenitrogenaton reaction, J/mol
E_{HDS}	activation energy for the hydrodesulfurization reaction, J/mol
G/L	ratio of volumetric flow rates between hydrogen gas and coker light gas oil, dimensionless (mL/mL)
H_{H2}	Henry's constant for hydrogen in CLGO, $MPa \cdot m^3/mol$
I_D	D-band intensity Raman spectroscopy of carbon nanotubes, dimensionless

I_G	G-band intensity Raman spectroscopy of carbon nanotubes, dimensionless
k_{AX}	apparent rate constant for the consumption of species X, $s^{-1} \cdot C_X^{(1-n)}$
k_B	rate constant of butene, mol/(L·s)
k_{HDN}	rate constant of hydrodenitrogenation, $s^{-1} \cdot (mol/L)^{(1-v)}$
k_{HDS}	rate constant of hydrodesulfurization, $s^{-1} \cdot (mol/L)^{(1-n)}$
k_L	H_2/CLGO mass transfer coefficient – gas/liquid side, cm/s
k_{OVR}	overall mass transfer coefficient for hydrogen, cm/s
k_S	H_2/CLGO mass transfer coefficient – liquid/solid side, cm/s
k_t	thermal conductivity of the NiMo/MWCNT catalyst pellet, J/(cm·K)
k_T	rate constant of thiophene, mol/(L·s)
k_X	rate constant for the consumption of species X, $s^{-1} \cdot C_X^{(1-n)} \cdot P_{H2}^{(1-m)}$
K_A	adsorption equilibrium constant for butane, Pa^{-1}
K_{AA}	adsorption equilibrium constant for aromatic amines, Pa^{-1}
K_B	adsorption equilibrium constant for butene, Pa^{-1}
K_{H2}	adsorption equilibrium constant for hydrogen gas, Pa^{-1}
K_{H2S}	adsorption equilibrium constant for hydrogen sulfide, Pa^{-1}
K_i	adsorption equilibrium constant for species i heteroatom, L/mol
K_N	adsorption equilibrium constant for nitrogen heteroatoms within coker light gas oil, L/mol
K_S	adsorption equilibrium constant for sulfur heteroatoms within coker light gas oil, L/mol
K_{SA}	adsorption equilibrium constant for saturated quinoline, Pa^{-1}
K_T	adsorption equilibrium constant for thiophene, Pa^{-1}

K_Y	adsorption equilibrium constant for ammonia, Pa^{-1}
L_A	liquid mass flow over cross-sectional area, $g/(s \cdot cm^2)$
$LHSV$	liquid hourly space velocity, h^{-1}
m	reaction order constant for the denominator of the HDS rate model, dimensionless
M_{AVE}	average molecular weight of CLGO, g/mol
n	reaction order constant for the numerator of the HDS rate model, dimensionless
N_λ	proportionality constant for the nitrogen adsorption equilibrium constant expression, L/mol
N_E	proportionality constant for the HDN reaction rate constant expression, $s^{-1} \cdot (mol/L)^{(1-v)} \cdot (Pa)^{(-p)}$
$N_{E\alpha}$	proportionality constant for the HDN reaction rate constant expression after system pressure substitution, $s^{-1} \cdot (mol/L)^{(1-v)} \cdot (Pa)^{(-p)}$
p	reaction order constant for H_2 partial pressure term, dimensionless
P	system pressure, Pa
P_A	partial pressure of butane, Pa
P_B	partial pressure of butene, Pa
P_{H2}	partial pressure of hydrogen gas, Pa
P_{H2S}	partial pressure of hydrogen sulfide, Pa
P_T	partial pressure of thiophene, Pa
r_B	reaction rate of butene, $mol/(L \cdot s)$
r_{HDN}	rate of the overall hydrodenitrogenation reaction, $mol/(L \cdot s)$
r_{HDS}	rate of the overall hydrodesulfurization reaction, $mol/(L \cdot s)$
r_{ij}	rate of change of species i heteroatom for reaction j, $mol/(L \cdot s)$

r_T	reaction rate of thiophene, mol/(L·s)
r_X	reaction rate of species ***X***, mol/(L·s)
R	universal gas constant, 8.314 J/(mol·K)
R_I	ratio of D-band and G-band intensities for Raman spectroscopy of carbon nanotubes, dimensionless
$(R^2)_{HDN}$	coefficient of regression for the hydrodenitrogenation reaction models, dimensionless
$(R^2)_{HDS}$	coefficient of regression for the hydrodesulfurization reaction models, dimensionless
$(R^2{}_A)_{HDN}$	adjusted coefficient of regression for the hydrodenitrogenation reaction models, dimensionless
$(R^2{}_A)_{HDS}$	adjusted coefficient of regression for the hydrodesulfurization reaction models, dimensionless
S_λ	proportionality constant for the sulfur adsorption equilibrium constant expression, L/mol
S_E	proportionality constant for the HDS reaction rate constant expression, $s^{-1}\cdot(mol/L)^{(1-n)}\cdot(Pa)^{(-p)}$
$S_{E\alpha}$	proportionality constant for the HDS reaction rate constant expression after system pressure substitution, $s^{-1}\cdot(mol/L)^{(1-n)}\cdot(Pa)^{(-p)}$
SG	specific gravity of CLGO at 15.6°C, dimensionless
T	reaction temperature, K
T_b	average boiling point of CLGO, K
T_S	pellet surface temperature, K
u	reaction order constant for the denominator of the HDN rate model, dimensionless
v	reaction order constant for the numerator of the HDN rate model, dimensionless

v_C	critical specific molar volume of CLGO, mL/mol
v_C^m	critical specific mass volume, mL/g
v_i	molar volume of sulfur/nitrogen molecules under standard conditions, mL/mol
v_L	molar volume of CLGO under standard conditions, mL/mol
v_N	hydrogen molar volume at standard conditions, L/mol
V	total pore volume found for catalysts and catalyst supports, cc/g
V_b	hydrogen molar volume at the normal boiling point, mL/mol
V_C	volume of loaded catalyst, mL
$WHSV$	weight hourly space velocity, h^{-1}
x_{HDN}	stoichiometric ratio of hydrogen consumption over nitrogen removal, dimensionless
x_{HDS}	stoichiometric ratio of hydrogen consumption over sulfur removal, dimensionless
X	association parameter, dimensionless

1 INTRODUCTION

As conventional crude oil reserves continually decline worldwide, much focus has been turned towards potential sources for producing synthetic crude oil. The most likely sources for meeting this demand are Alberta's oil sands; most specifically, the province's Athabasca bitumen deposits. Athabasca bitumen consists of hydrocarbons in their most complex form that are mined and extracted from the Athabasca oil sands. After undergoing a fluid coking process (i.e. thermal cracking), the bitumen feed is converted into naphtha, light gas oil (LGO), and heavy gas oil (HGO) liquid products, as well as into sour gas and coke byproducts. The liquid products can be further refined to produce varying grades of gasoline, diesel, and gas oil fuels. However, high concentrations of organic sulfur compounds within the synthetic crude feeds can make it difficult for the final fuel products to meet stringent emission specifications. An additional problem is the deactivation of noble metal catalysts within downstream refining processes due to high organonitrogen concentrations within the feedstock.

A problem that arises from the application of bitumen-derived gas oils as fuel, as well as with any petroleum feed source, is the harmful emission of impurities that would result from combustion engines. The regulation of fuel quality has become a worldwide effort in recent years in the face of growing health and environmental concerns. In Canada, a mandate was created that required the allowable sulfur content level for gasoline be lowered from 150 to 30 ppm nationwide as of June 1, 2005 (Department of Justice Canada, Sulfur in gasoline regulations, 1999). A similar

restriction was applied to Canadian diesel fuels which mandated that ultra-low sulfur diesel (ULSD) be produced or imported for all on-road vehicle use by September 1, 2007. This lowered the tolerable amount of sulfur content in diesel fuel to 15 ppm from the previous standard of 500 ppm. This same regulation for ULSD has been authorized for all types of off-road diesel consumption and will take effect June 1, 2012 (Department of Justice Canada, Sulfur in diesel fuel regulations, 2002).

For any type of hydroprocessing catalysis, nitrogen-containing compounds are the most common source of catalyst poisoning due to their strong adsorption on catalyst active sites. The basic nature of these compounds causes them to adsorb onto Lewis acid sites on the catalyst surface, inhibiting the availability of the sites. This poisoning may be reversible or irreversible, depending on the hydroprocessing conditions (Furimsky and Massoth, 1999). High concentrations of organic nitrogen compounds can cause significant deactivation for reforming, cracking, hydrotreating, or any other type of hydroprocessing catalysts.

The most common method of removing sulfur and nitrogen impurities from petroleum feedstock is by hydrotreating. Hydrotreating is a catalytic process where untreated petroleum products, such as bitumen-derived gas oils, are reacted with hydrogen gas under high temperature and pressure conditions to purify and/or convert the hydrocarbon molecules. In the case of synthetic crude oils resulting from Athabasca tar sands, the most important aspect of this process is the removal of sulfur and nitrogen from the feedstock. The impure organic compounds undergo

hydrodesulfurization (HDS) and hydrodenitrogenation (HDN) reactions, resulting in the impurities being removed in the form of H_2S and NH_3 gases, respectively. It is common industrial practice to use a heterogeneous catalyst system to perform such a process. A bimetallic catalyst is commonly used with a metal sulfide, often MoS_2 or WS_2, accompanied by a promoter, often Ni or Co. The metal particles are usually deposited on a γ–Al_2O_3 catalyst support by way of a co-impregnation method to increase the exposure of the catalyst active sites and to give mechanical strength to the catalyst pellets.

As the quality of Athabasca bitumen product streams become more demanding and the throughput of such products continues to increase, the role of the catalysts used in hydrotreating units become ever more important. Ways of improving on the performance of an existing catalyst process can include: finding a more effective active phase (carbide, nitride, phosphide, etc.), using a different catalyst preparation method (co-precipitation, chemical vapor deposition, etc.), testing different catalyst metals (Ru, Rh, etc.), or applying new types of catalyst supports (various metal oxides, mesoporous silicas, carbon nanotubes, etc.). Of all the new and innovative nanomaterial supports that have been applied to heterogeneous catalysis, carbon nanotubes (CNTs) have garnered much interest due to the high specific surface areas they can possess while still maintaining large pore diameters. Such large pore diameter (i.e. >50nm) CNTs can be synthesized by the application of an anodic aluminum oxide (AAO) template in a chemical vapor deposition (CVD) method.

In this thesis, the application of CNT catalyst supports with varying pore diameters is examined. These CNTs were used for the preparation of NiMo/CNT catalysts. The performance of these catalysts, along with a commercial NiMo/γ–Al_2O_3 catalyst under equivalent mass and volume loadings, were compared based on the HDS and HDN activities displayed during the hydrotreating of LGO derived from Athabasca bitumen.

1.1 Knowledge Gaps

From the literature review conducted in the succeeding section, it is shown that the limited number of studies applying NiMo/CNT catalyst for hydrotreating presents the opportunity to explore how the characteristics of such a catalyst would impact the performance of the process. The original concept of varying pore diameter when synthesizing CNTs from AAO templates, for the purpose of finding the best NiMo/CNT catalyst, would determine the optimum conditions for both AAO and CNT production. The use of CNTs created from AAO templates for hydrotreating catalyst purposes would be an entirely new endeavor in catalysis innovation. Finally, optimizing and modeling a NiMo/CNT catalyst for the HDS and HDN of gas oil derived from Athabasca bitumen, something rarely performed before, would better reflect the practical industrial application of such a catalyst.

1.2 Hypotheses

Several hypotheses were made as the basis and justification for this research:

- By varying the parameters for the synthesis of AAO templates, the pore diameters of the templates can be controlled. This will allow the diameter of the resulting CNTs to also be controlled. Based on this logic, the parameters of AAO electrolysis can be tuned in order to provide a CNT pore diameter that provides optimum HDS and HDN activities for a NiMo/CNT catalyst.

- The relatively large pore diameters of CNTs synthesized from AAO templates will lessen the effect of catalyst deactivation. Significant catalyst deactivation can be attributed to the constriction and/or blockage of pores due to coke deposits. The much larger CNT pore diameters compared to commercial NiMo/γ–Al_2O_3 catalysts will give such a NiMo/CNT catalyst less susceptibility to deactivation and better operating longevity.

- CNTs have inherently inert surfaces capable of hosting hydroxyl and carboxyl functional groups that are necessary for catalyst metal loading. Combined with the high specific surface areas exhibited by CNTs, it can be theorized that less sintering of metal particles would occur on the surface of a NiMo/CNT catalyst compared to a commercial NiMo/γ–Al_2O_3 catalyst. This would further limit the deactivation effects of a NiMo catalyst from the use of a CNT support.

1.3 Research Objectives

The objective of this research was to synthesize a NiMo/CNT catalyst that possessed optimum parameters of CNT pore diameter, Mo wt.% loading, and Ni wt.%

loading. These optimizations were based on the performances of the catalysts for HDS and HDN of bitumen-derived LGO. The work that was performed can be broken down into six essential parts:

- **Part 1: Variation of CNT pore diameter and resulting characterization**

The first part of the project was the tuning of the AAO synthesis procedure by varying the anodizing voltage and oxalic acid concentration. The objective was to examine how changes to the structure of the AAO templates affected the physical and structural characteristics of the resulting CNT product. Characterization methods used for this part of the project included scanning electron microscopy, transmission electron microscopy, thermogravimetric analysis, N_2 adsorption/desorption analysis, Raman spectroscopy and diffuse reflectance infrared Fourier transform spectroscopy.

- **Part 2: Effect of CNT pore diameter variation on catalyst performance**

Once differing grades of CNTs were produced from varying the AAO synthesis parameters, several grades of CNTs with incremented pore diameters were applied as catalyst supports for the HDS and HDN of LGO. Each grade of CNT support was loaded with equivalent amounts of Ni & Mo and studied under fixed hydrotreating reaction conditions. The amount of sulfur and nitrogen removal from feedstock was analyzed, along with a boiling point distribution of the gas oil products.

- **<u>Part 3</u>: Variation of CVD parameters and resulting characterization**

After determining the most suitable conditions for AAO film synthesis, a similar procedure was performed to determine the optimum conditions for the chemical vapor deposition of acetylene onto AAO templates. In addition to the CVD parameters that were applied for the first two parts of the project, eight other conditions were tested with the aim of performing the procedure at lower temperatures and C_2H_2-to-AAO ratios. The effectiveness from applying each of the nine synthesis conditions was determined based on the CNT yields obtained and on the quality of the CNTs as observed from TEM images of the products.

- **<u>Part 4</u>: Catalyst performance optimization and characterization**

Once the optimum CNT pore diameter for a hydrotreating catalyst support application was determined (i.e. the ideal conditions for AAO film synthesis), the optimum loadings of both Ni and Mo for a CNT support were determined as well. The metals were loaded on the support surface using an incipient wetness co-impregnation technique. The exact metal loadings were determined by inductively coupled plasma mass spectroscopy. N_2 adsorption/desorption and thermogravimetric analysis was performed on the catalysts before and after the hydrotreating experimental runs to determine the effects of coke formation on the surfaces of the catalysts. The changes to the characteristics and behavior of the catalysts due to metal

loading changes were further classified by Raman spectroscopy, N_2 adsorption/desorption, CO chemisorption, and H_2 temperature programmed reduction.

- **<u>Part 5</u>: Determination of rate equations for optimum NiMo/CNT catalyst**

After the optimum composition for a NiMo/CNT catalyst was determined, the best catalyst was tested against changes to the hydrotreating reaction conditions. The effects of changes to reaction temperature, pressure, LHSV and H_2-to-LGO ratio was determined for the HDS and HDN of bitumen-derived gas oil. The dependence of the catalyst's HDS and HDN activity on these parameters was modeled in the form of both power law and Langmuir-Hinshelwood kinetic rate equations. From this analysis, separate models were determined for both the HDS and HDN of LGO to predict the reaction kinetics of the NiMo/CNT catalyst.

- **<u>Part 6</u>: Stability study for optimum NiMo/CNT catalyst**

The final phase of the project consisted of a comparison between the optimum NiMo/CNT catalyst and a commercial NiMo/γ-Al_2O_3 catalyst under equivalent volumetric loadings. Each of the two catalysts was compared over an extended four week study span to better reflect the performance of the catalysts under industrial conditions. The purpose of this portion of the research was to determine the long term effects of deactivation for the two types of catalyst supports.

2 LITERATURE REVIEW – PETROLEUM HYDROTREATING

The first section of the literature review pertains to the background and concepts relating to the hydrotreating of petroleum. In regards to the hydroprocessing of bitumen-derived light gas oil, there are two facets of hydrotreating that are of particular importance: hydrodesulphurization and hydrodenitrogenation. These two essential reactions will be the focus of this section, as well as several other characteristics of hydrotreating. The different kinetic models used for describing the behavior of these reactions will be discussed in detail. The components and makeup of the heterogeneous catalysts used for hydrotreating processes are thoroughly reviewed in this section. Finally, the causes and effects of catalyst deactivation will be evaluated with the purpose of improving on the performance of conventional hydrotreating catalysts.

2.1 Characteristics of Hydrotreating

There are two main groupings used to categorize hydrotreating processes. The first such grouping falls under the category of hydropurification, where heteroatoms are removed from organic molecules by reacting with hydrogen gas. Elements that most often play the role of a heteroatom include sulfur, nitrogen, oxygen, vanadium, nickel, and arsenic. These specific hydropurification reactions are referred to as hydrodesulfurization (i.e. the removal of sulfur in the form of H_2S), hydrodenitrogenation (i.e. removing nitrogen in the form of NH_3),

hydrodeoxygenation (i.e. the removal of oxygen in the form of H_2O), and hydrodemetallization (i.e. the removal of nickel, vanadium, arsenic, etc.). The second grouping of hydrotreating processes is referred to as hydroconversion reactions. These reactions are classified as changes to the molecular weight of organic compounds, via the addition or removal of hydrogen atoms, or changes to the structure of organic compounds. Some specific hydroconversion reactions are termed as hydrogenation (i.e. increasing the hydrogen content of a molecule), hydrodearomatization (i.e. removal of aromatics by hydrogen saturation), isomerization (i.e. changing the structural formula of a compound while maintaining its molecular formula), and hydrocracking (i.e. reducing large organic molecules into smaller compounds via the addition of hydrogen atoms).

The common link between all hydrotreating processes is that they improve the quality of petroleum streams through a catalytic reaction with hydrogen gas. However, the motivation for applying any hydrotreating process can vary depending on the characteristics of the petroleum feed and the application of the resulting product stream. The most common reason for any hydrotreating application is for the purpose of preventing the emission of oxide pollutants (i.e. NO_X and SO_2) when the product is applied as a combustion engine fuel. There is also the case for hydrogen purification being applied to maintain the activity of downstream refining catalysts by removing any species that would otherwise strongly adsorb to the active sites of the catalyst. Adsorbed nitrogen and metal heteroatoms are most often the contaminants

responsible for downstream catalyst deactivation. A byproduct of hydrotreating for these two reasons is the improved quality of the treated stream in terms of smell and stability, as well as increasing the value of upgraded heavy crude feedstocks to be sold to other refining operations (Grange and Vanhaeren, 1997). For any gas oil derived from Athabasca bitumen, hydrotreating is imperative for the removal of contaminant sulfur and nitrogen organic compounds. The concern of sulfur emissions and refining catalyst deactivation from nitrogen make hydrodesulfurization and hydrodenitrogenation the two principle processes for hydrotreating bitumen-derived gas oils.

2.1.1 Hydrodesulfurization (HDS)

Hydrodesulfurization can be described as any reaction whereby sulfur is removed from an organic molecule through interacting with hydrogen on a solid catalyst surface. The overall HDS reaction can be expressed by the following simplified equation:

$$|R-S| \; + \; \tfrac{3}{2} H_2 \xrightarrow{CATALYST} |R-H| \; + \; H_2S \qquad [2.1]$$

The net reaction is the removal of a sulfur heteroatom from the organic molecule, *R*, in the form of H_2S gas. Figure 2.1 shows examples of various organosulfur molecules that are commonly found in petroleum fractions. While removing sulfur from alkyl compounds (i.e. mercaptans/thiols, sulfides, disulfides) can be achieved without much difficulty, aromatic sulfur compounds can prove to be

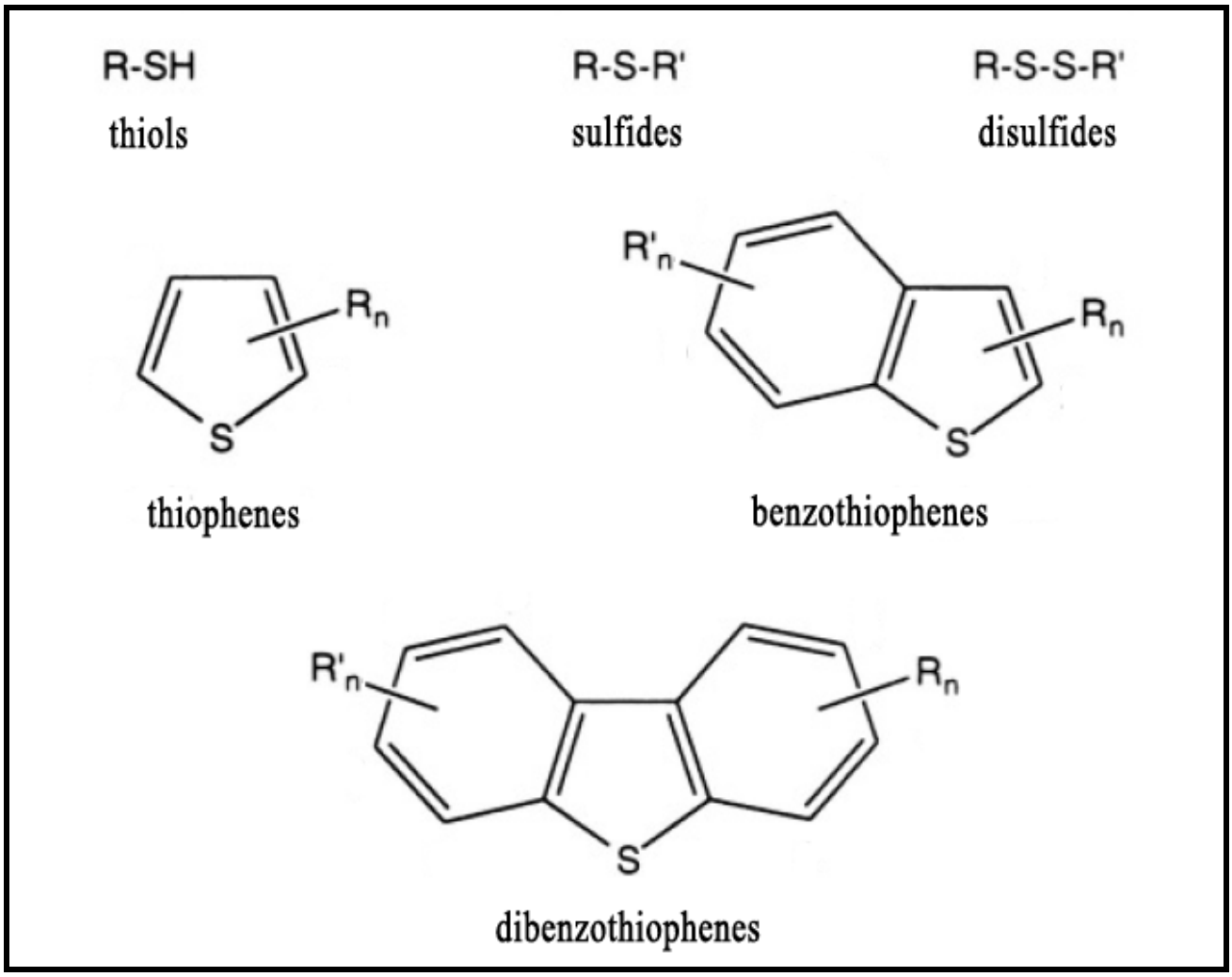

Figure 2.1: Common types of organosulfur constituents of petroleum crudes and distillates, R_n and R_n' representing short chain alkyl groups (Sanchez-Delgado, 2002).

difficult to purify. To compare the relative difficulties of desulfurization, if converting diethylsulfide were a difficulty level of 1, thiophene would be approximately a 5, benzothiophene would be a 15, and dibenzothiophene would be a 20 (Gruia, 2006).

The increase in the difficulty of conversion for these sulfur compounds is attributed to the delocalization of the lone-pair electrons belonging to the sulfur atoms. This lowers the exposure of the sulfur groups and decreases their adsorptivity onto catalyst active sites (Girgis and Gates, 1991). This steric hindrance results in a higher degree of difficulty for the ring opening that must happen for the removal of the sulfur heteroatom, often followed by saturation of the resulting intermediate olefin group. These reactions can also occur in reverse order, with the saturation of the aromatic ring preceding the removal of sulfur. These two separate reactions make up the desulfurization mechanism. An example of the dual reaction pathways for HDS of dibenzothiophene is shown in Figure 2.2, where hydrocarbon saturation and sulfur removal can happen interchangeably. The likelihood of one reaction pathway occurring more frequently than the other depends heavily on the composition of the feed, the characteristics of the catalyst used and the parameters of the reaction process. Higher partial pressures of H_2 (Houalla et al., 1978) and H_2S (Bhinde, 1979) have been found to increase the selectivity of hydrogenation to hydrogenolysis of sulfur. It is generally preferred to find the catalyst and reaction parameters that would

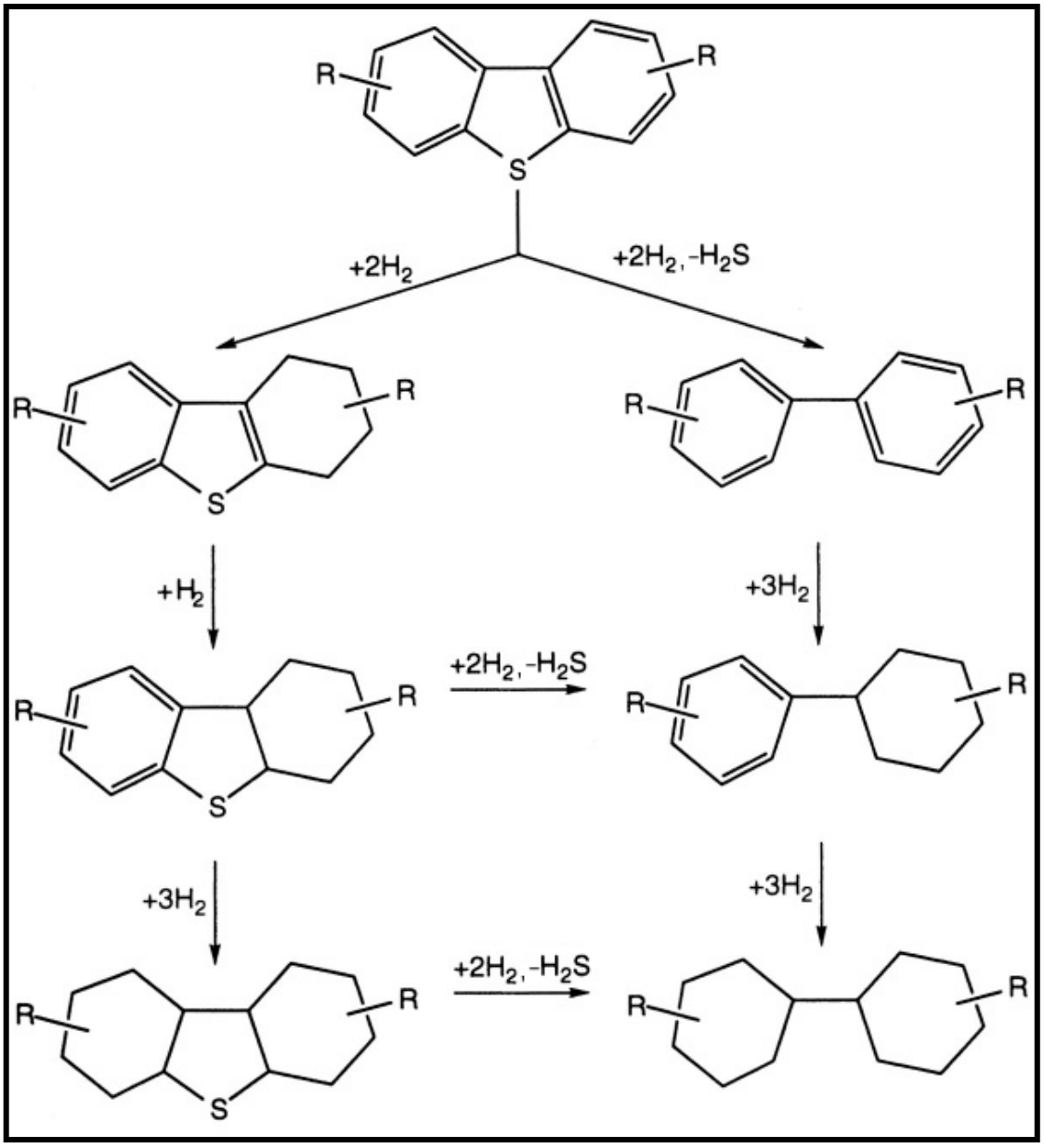

Figure 2.2: Potential reaction pathways for HDS of dibenzothiophenes to produce bicyclohexanes (Sanchez-Delgado, 2002).

favor the hydrogenolysis reaction over hydrogenation, resulting in higher octane ratings and less hydrogen gas being consumed.

2.1.2 Hydrodenitrogenation (HDN)

The overall reaction for an HDN process can be described as the removal of nitrogen content from organic compounds by reacting with hydrogen gas in the presence of a heterogeneous catalyst. The overall HDN reaction can best be described by the following equation:

$$\left|R-N\right| \; + \; 2H_2 \xrightarrow{CATALYST} \left|R-H\right| \; + \; NH_3 \qquad [2.2]$$

The net result is the removal of the nitrogen heteroatom from the organic *R* molecule in the form of ammonia gas. Shown in Figure 2.3 are some of the common types of organonitrogen molecules found in petroleum crudes and distillates. As shown in the figure, nitrogen is found almost exclusively in the form of heterocyclic compounds found in heavier petroleum fractions. The compounds can be separated into two classes: basic compounds and non-basic compounds. Basic compounds consist of a nitrogen heteroatom within a six-membered pyridinic ring structure bound by a single and double bond (ex. pyridine, quinoline, acridine). Non-basic compounds consist of a nitrogen heteroatom within a five-membered pyrollic ring structure bound by two single bonds (ex. pyrrole, indole, carbazole). When comparing basic and non-basic organonitrogen compounds, it is accepted that basic compounds are more reactive compared to non-basic compounds due to their stronger

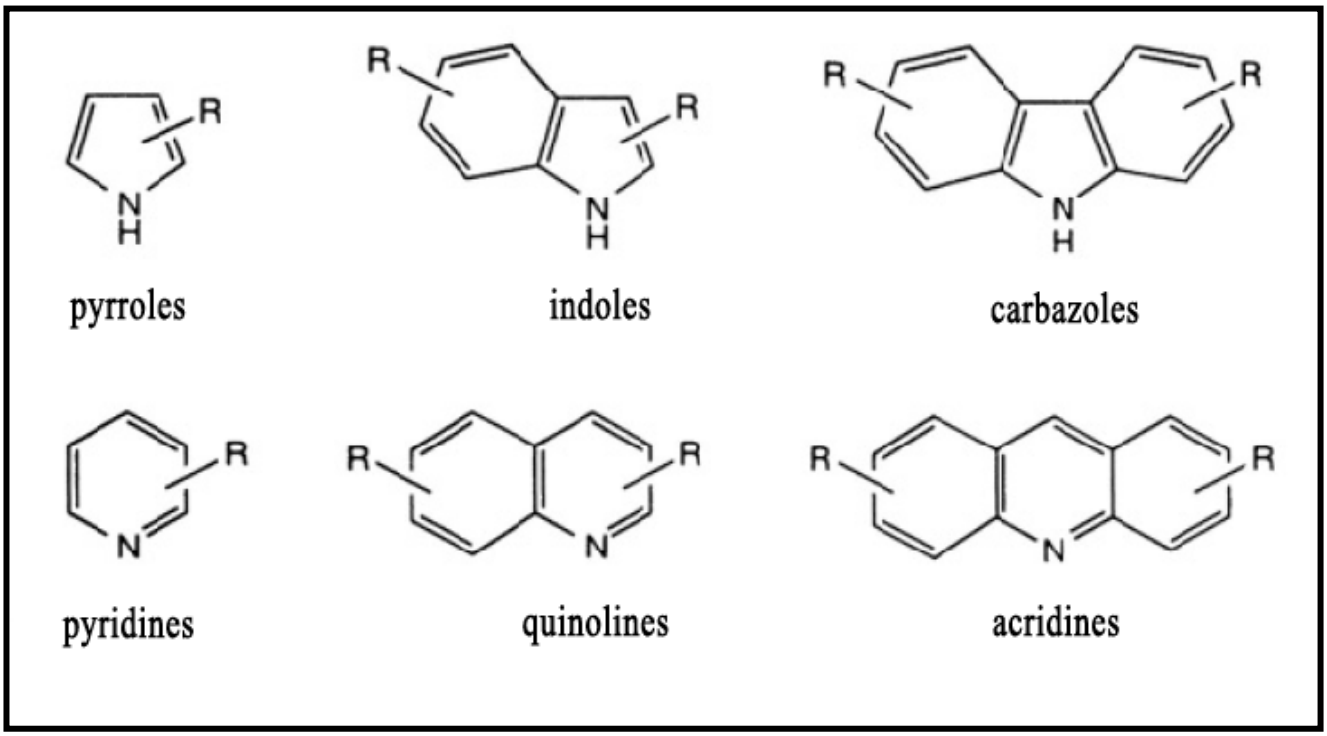

Figure 2.3: Common types of organonitrogen constituents of petroleum crudes and distillates, R representing short chain alkyl groups (Sanchez-Delgado, 2002).

adsorption properties on catalyst active sites (Zeuthen et al., 2001). This is the result of the lone pair electrons of the non-basic nitrogen heteroatom being delocalized within the aromatic ring and being inaccessible for donation as a Lewis base (Ho, 1988). The HDN conversion rates of organonitrogen compounds generally decrease as the molecular size of the aromatic compound increases, similar to the trend shown by organosulfur compounds for HDS. The reactivity of the basic nitrogen compounds would decrease in the order pyridine, quinoline, and acridine, while the reactivity of non-basic nitrogen compounds would decrease in the order of pyrrole, indole and carbazole (Topsoe et al., 1996).

It is commonly known that the overall HDN reaction is a more difficult process than the overall HDS reaction. The most significant factor contributing to this higher degree of difficulty is the C-N bond energy being higher than that of the C-S bond energy (Szymańska et al., 2003). The high energy of the C-N bond is thought to be the reason why complete hydrogenation of the N-containing aromatic ring is required before C-N bond cleavage can be achieved (Katzer et al., 1979). In other words, unlike the HDS overall reaction, hydrogenation of the pyridinic or pyrollic heterocycles must occur before the N-group can be removed from the organic molecule. This reaction mechanism is best illustrated in Figure 2.4, which shows the potential reaction pathways for the HDN of quinoline. As shown, the rate of nitrogen removal depends heavily on the equilibrium of the hydrogenation reactions. Hydrogenation of the nitrogen-associated aromatic ring structures is very dependent

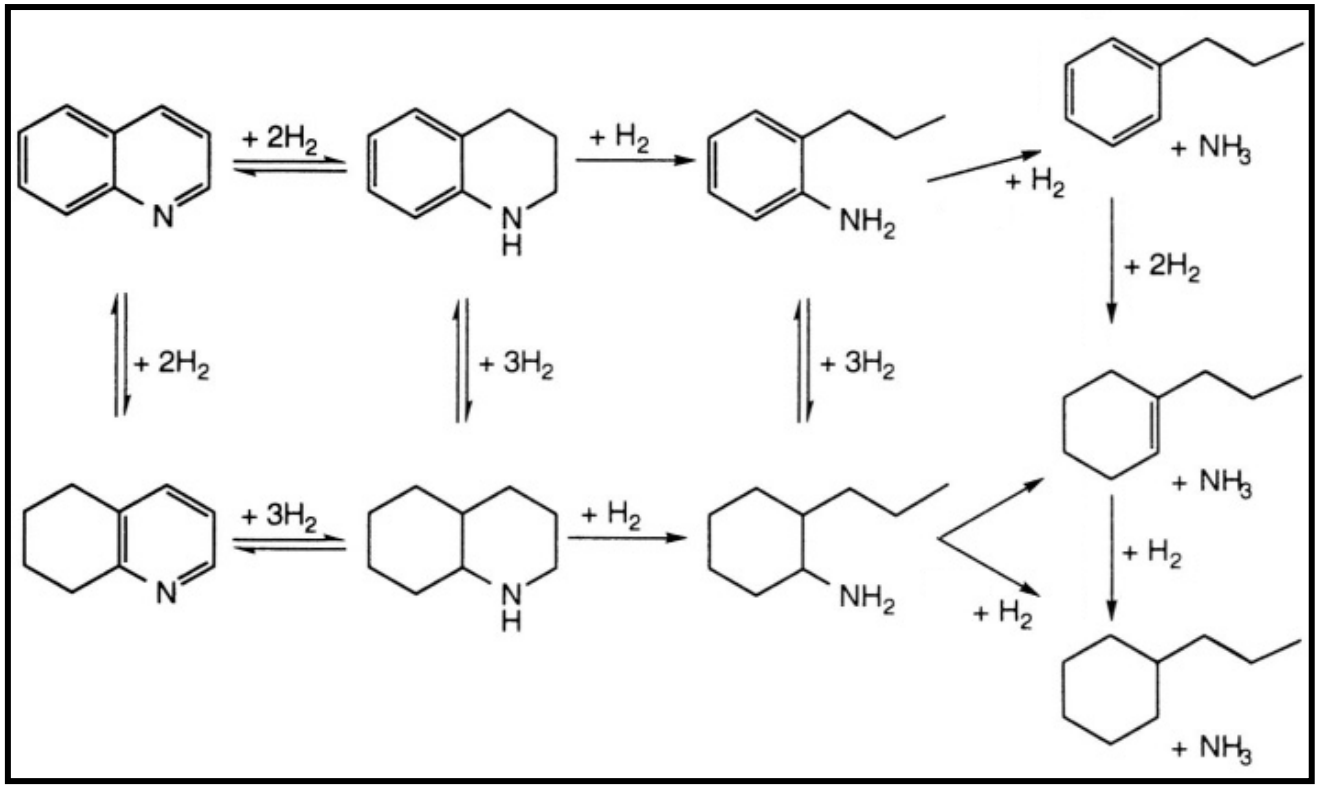

Figure 2.4: Potential reaction pathways for HDN of quinoline to produce propylcyclohexane (Sanchez-Delgado, 2002).

on the hydrogen partial pressure and is the rate limiting step of the overall HDN reaction. Unfortunately, reaction pathways that minimize hydrogen consumption and maximize the fuel applicability of the petroleum feeds are not thermodynamically favored at typical industrial operating conditions (Cocchetto and Satterfield, 1981). This means that selectively limiting the extent of hydrogenation to the heterocycle of the organonitrogen molecule is left for a specialized catalyst to perform.

As with HDS, high H_2S partial pressures have been found to increase the rate of overall HDN processes. This is attributed to the sulfide active phase of the metal sulfide catalyst being maintained, thereby sustaining the acidity of the catalyst (Satterfield and Yang, 1984). This desired presence of H_2S partial pressure naturally sustains the active phase of the hydrotreating catalyst due to the HDS and HDN processes being performed simultaneously in most industrial operations. A significantly high sulfur-to-nitrogen mass ratio often ensures the phase of the catalyst is maintained (2.2-1.6 wt% sulfur, 0.24-0.15 wt% nitrogen for Athabasca CLGO). However, basic nitrogen compounds, including hydrocarbons and ammonia, can act as significant inhibiting species to both HDS and HDN processes due to the strong adsorption properties of the molecules (Girgis and Gates, 1991). The interference and interdependence between the two overall reactions requires the application of a catalyst that can adequately remove the necessary amounts of each species. It also requires the kinetic studies of both the HDS and HDN reactions to often be performed

simultaneously, as the presence of each species has an underlying influence on the performance of the other reaction.

2.2 Kinetic Modeling of HDS and HDN

Two types of kinetic models are commonly applied to express the rate of hydrodesulfurization and hydrodenitrogenation in a hydrotreating process. These models are the power law model and the Langmuir-Hinshelwood model. The power law model is typically applied as a representation of the overall rate law for the various reactions taking place in the HDS and HDN processes. The Langmuir-Hinshelwood model is typically used to represent the inhibition in the reaction processes. Often, a hybrid of these two models is required to accurately predict the performance of a given hydrotreating system.

2.2.1 Power Law Models

A hydrotreating power law model often takes the following form:

$$\boxed{-r_X = k_X \cdot C_X^n \cdot P_{H_2}^p} \qquad [2.3]$$

where r_X is the rate of change in the heteroatom concentration, k_X is the rate constant, C_X is the concentration of the heteroatom X, P_{H2} is the partial pressure of hydrogen, and n & p are the respective reaction orders of X concentration and H_2 pressure (Botchwey *et al.*, 2004). For kinetic analysis at constant hydrogen pressure, the P_{H2}^m becomes incorporated into the rate constant term to create an apparent rate

constant, k_{AX}. The equation can then the integrated to derive an expression defining the rate constant in terms of the liquid hourly space velocity (LHSV), the reaction order with respect to concentration, and the heteroatom concentration before and after the reaction. For reaction orders not equal to 1, the rate constant becomes:

$$k_{AX} = LHSV\left(\frac{1}{n-1}\right)\left(\frac{1}{C_P^{\,n-1}} - \frac{1}{C_O^{\,n-1}}\right) \qquad [2.4]$$

where C_O and C_P are the heteroatom concentrations in the feed and product, respectively. For the unique case where the reaction order is equal to one, the rate constant becomes:

$$k_{AX} = LHSV \cdot \ln\left[\frac{C_O}{C_P}\right] \qquad [2.5]$$

For the application of this power law to gas oil hydrotreating, HDN generally follows reaction orders ranging from 0.5 to 1.5. While a particular HDN study performed on heavy gas oil found a reaction order of 1.5 for both basic and non-basic nitrogen compounds (Bej et al., 2001), along with a Maya crude study determining an HDN reaction order of 0.5 (Bej et al., 2001), a reaction order of 1.0 is most commonly found for the rate of nitrogen removal (Callejas and Martinez, 1999). HDS typically exhibits reaction orders ranging from 1.0 to 2.5 (Aoyagi et al., 2003). The reaction order for HDS has been shown to vary considerably with changes to the feedstock composition. Specifically, a trend of increasing molecular weights for organic sulfur

compounds corresponds to an increasing order for the overall HDS reaction (Ancheyta et al., 2002).

2.2.2 Langmuir-Hinshelwood Models

Because most real feeds for hydrotreating processes consist of many different compounds, it can be difficult to apply a single power law equation to represent the rates of the HDS and HDN reactions. Langmuir-Hinshelwood models express the rate of decomposition of specific molecules for hydrotreating. The model takes into account the percentage of catalyst active sites that are occupied by the adhered reactant at steady state, as well has the percentage of sites that are vacant or inhibited by other adhered compounds from the feed stream.

For a specific example, consider the following rate equations developed by Van Parijs and Froment (1986) for the hydrogenolysis of thiophene and the resulting hydrogenation of butene:

$$-r_T = \frac{k_T \cdot K_T \cdot K_{H2} \cdot P_T \cdot P_{H2}}{\left[1 + \left(K_{H2} P_{H2}\right)^{1/2} + \left(K_T P_T\right) + \left(K_{H2S}\, P_{H2S} / P_{H2}\right)\right]^3} \qquad [2.6]$$

$$-r_A = \frac{k_B \cdot K_B \cdot K_{H2} \cdot P_B \cdot P_{H2}}{\left[1 + \left(K_{H2} P_{H2}\right)^{1/2} + \left(K_A P_A\right) + \left(K_B P_B\right)\right]^2} \qquad [2.7]$$

In this case, the subscripts ***T***, ***A***, and ***B*** denote the compounds thiophene, butane, and butene, respectively. The parameters ***k***, ***K***, and ***P*** denote the rate constant,

adsorption equilibrium constant, and partial pressure, respectively. These equations assume hydrogenolysis and hydrogenation occur at separate sites, as well as the dissociation of adsorbed diatomic hydrogen.

As an example for HDN applications, Satterfield and Yang (1983) developed a generalized equation for the hydrotreatment of quinoline:

$$-r_{ij} = \frac{k_{ij} \cdot K_i \cdot C_i}{\left[K_{AA}C_{AA} + K_{SA}C_{SA} + K_Y C_Y\right]} \qquad [2.8]$$

The subscripts in this equation – Y, SA, and AA – denote the inhibiting ammonia, decahydroquinoline (saturated quinoline), and aromatic amines, respectively. The subscript ***i*** represents the reactant being consumed in the reaction, while ***j*** represents the specific reaction taking place, either hydrogenolysis or hydrogenation. Noteworthy in this equation is the independence of the reaction rates on hydrogen partial pressure, which is not always the case for HDN rate equations.

2.2.3 Generalized Langmuir-Hinshelwood Models

When dealing with real feeds containing a wide range of sulfur and nitrogen compounds, establishing rate equations for each type of compound would become tedious and quite complex. When this is the case, rate equations are often established resembling basic Langmuir-Hinshelwood models that represent the overall rate of HDS or HDN. Such equations attempt to achieve the simplicity of power law

functions while applying the theoretical ideals of Langmuir-Hinshelwood models. These equations often take on the following form:

$$r_{HDS} = \frac{k_{HDS} \cdot C_S{}^{n}}{\left[1 + K_S C_S\right]^{m}} \quad [2.9] \qquad r_{HDN} = \frac{k_{HDN} \cdot C_N{}^{v}}{\left[1 + K_N C_N\right]^{u}} \quad [2.10]$$

For these equations, ***k*** is the apparent reaction rate constant and ***K*** is the apparent adsorption equilibrium constant for each particular heteroatom. The exponent terms, ***n*** & ***v*** and ***m*** & ***u***, are experimentally determined constants taken to be independent of temperature. These four parameters are found by applying non-linear regression analysis to experimental kinetic data. The values of these parameters are taken to be specific to the given reaction system.

Equations 2.9 and 2.10 assume that the organosulfur and organonitrogen compounds do not inhibit the same active sites, and that the two reactions are not in competition with each other. In other words, the rates of the HDS and HDN reactions are independent of one another. It is more likely from a theoretical viewpoint that the two heteroatoms are competing for the same active sites, and that the concentration of one of these heteroatoms not only affects the rate of its own hydrogenolysis reaction, but of the competing hydrogenolysis reaction as well. Based on this assumption, the rate laws may be better represented by the following hybrid models:

$$r_{HDS} = \frac{k_{HDS} \cdot C_S{}^{n}}{\left[1 + K_S C_S + K_N C_N\right]^{m}} \quad [2.11] \qquad r_{HDN} = \frac{k_{HDN} \cdot C_N{}^{v}}{\left[1 + K_S C_S + K_N C_N\right]^{u}} \quad [2.12]$$

Similar to the equation 2.9 and 2.10 models, the unknown parameters are found by applying non-linear regression analysis to experimental data and the numerical solutions to each equation.

Within each of the rate constant and equilibrium constant parameters are unknown constants that can be determined through temperature and pressure variation.

$$k_{HDS} = P_{H_2}^{p} \cdot S_E \cdot \exp\left[\frac{-E_{HDS}}{RT}\right] \quad [2.13] \qquad K_S = S_\lambda \cdot \exp\left[\frac{\lambda_s}{RT}\right] \quad [2.14]$$

In both equations, ***R*** represents the universal gas constant, and ***T*** represents the operating temperature. The exponent terms E_{HDS} and λ_S represent the overall reaction activation energy and the heat of chemisorption, respectively, for the specified heteroatom. Both of these terms are taken to be independent of pressure and temperature. The terms S_E and S_λ represent the proportionality constants for both equations, independent of the effects of temperature and pressure. The hydrogen partial pressure term P_{H2} and the exponent term ***p*** take into account the exponential increase in reaction rate due to increases in hydrogen pressure. Under constant pressure conditions, the pressure term is commonly absorbed into the proportionality constant. If the hydrogen partial pressure is taken to be approximately constant and linearly proportional to the total system pressure, the P_{H2} variable can be replaced with the total pressure term ***P*** with the term S_E being adjusted accordingly:

$$\boxed{\left(P_{H_2}\right)^p \cdot S_E = \left(\alpha P\right)^p \cdot S_E = \left(P\right)^p \cdot \left[\alpha^p \cdot S_E\right] = \left(P\right)^p \cdot S_{E\alpha}} \quad [2.15]$$

In order for the hydrogen partial pressure to be considered relatively unchanged throughout the hydrotreating catalyst bed, the quantity of hydrogen gas flow must be considerably larger than the flow of the untreated petroleum. Additionally, the pressure drop over the catalyst bed must be negligible for this assumption to be valid.

2.3 Hydrotreating Catalyst

The purpose of any hydrotreating catalyst is to increase the rate by which the overall hydrotreating reactions of interest approach complete conversion. The commonality that exists between all types of hydrotreating catalysts is that they are high surface area pellets consisting of an active component and one or more promoters. These materials exist in the form of nanometer-sized particles that are dispersed on the surface of a catalyst support.

Molybdenum sulfide is the most commonly used active component for hydrotreating catalysts, as well as for numerous other hydroprocessing applications. The molybdenum is initially deposited onto the surface of a catalyst support by an incipient wetness impregnation method with an aqueous solution of ammonium heptamolybdate. After drying and calcination, the molybdenum particles take the form of MoO_3. Before the molybdenum can be applied as a catalyst, it must be

activated by being converted into the sulfide active phase. The transformation is performed by treating the loaded catalyst bed *in situ* by a mixture of diluted H_2S feed and H_2 or an alternate sulfur-containing feed and H_2 (Satterfield, 1991). This conversion to the active phase can be performed gradually by treating the petroleum feed itself, although it is more commonly done with a specialized sulfidation solution for better efficiency. If the oxide precursor exists in the MoO_2 phase before sulfidation, a considerable amount of the catalyst will not be converted to the sulfide phase and the catalyst will not achieve its maximum potential activity (Satterfield, 1991).

Less common compared to molybdenum is a tungsten active component (i.e. WS_2). The catalyst is prepared in an identical fashion to MoS_2 catalyst, only with an ammonium metatungstate salt precursor before impregnation. Tungsten sulfide is commonly accepted to provide less HDS and HDN activity than molybdenum sulfide, but can perform better aromatic and olefin hydrogenation (Furimsky, 1980). Because of this, tungsten and molybdenum are commonly used together within a single operation, either with a single dual phase catalyst or as a two-stage process with two distinct catalyst beds. Other Group VI and VIII catalyst metals that have been applied to hydrotreating operations include rhenium, ruthenium, and rhodium sulfides (Escalona et al., 2007).

It is common for industrial hydotreating catalysts to contain metal promoters doped within the crystal structure of the active component to increase the HDS and

HDN activity of the catalysts. Cobalt and nickel are the most common metals used to serve this purpose in conjunction with molybdenum or tungsten to give a bimetallic catalyst. It is a common rule of thumb that the maximum catalytic synergy is achieved when the molar ratio of the promoter to the total catalyst metals present (i.e. Co(Ni)/[Co(Ni) + Mo(W)] ≈ 0.3). This metal proportion holds relatively constant for all types of hydropurification and hydroconversion reactions (Gates et al., 1979).

Regardless of what catalyst metals are chosen for a hydrotreating application, the catalyst support that is most commonly applied in industry is γ–alumina. The support provides a high surface area and pore structure for the petroleum feed while still maintaining mechanical strength for the catalyst particles.

2.3.1 Active Components

As previously mentioned, molybdenum sulfide (MoS_2) is the most relied upon active component for industrial hydrotreating operations. For the coordination geometry of MoS_2, each Mo(IV) atom is surrounded by a trigonal prismatic coordination of sulfur atoms, with each sulfur atom adjacent to a pyramidal geometry of molybdenum atoms. The MoS_2 exists on the surface of a catalyst support in the form of a layered hexagonal crystal structure with weak interactions occurring between the sulfur atoms in the connecting layers (Satterfield, 1991). These hexagonal layers typically reach diameters of 300 nm with 5 to 10 sulfur slabs making up each hexagonal stack of the crystallite (Grange and Vanhaeren, 1997). The same

layered crystal structure is adopted by tungsten sulfide (WS_2) when applied as the catalyst active phase. Many theories have been proposed to explain the synergy that exists between the active phase metals and sulfur that make these crystal structures effective catalysts for hydrotreating reactions. The most common and simplistic model explaining the reactivity of these catalysts is the "rim-edge" model. Developed by Daage and Chianelli (1994), the model attempts to explain how the morphology of the MoS_2 or WS_2 crystal structure affects the reaction pathway selectivity (hydrogenation versus direct desulfurization) of the overall hydrodesulfurization reaction. Figure 2.5 shows a diagram illustrating this reactivity concept. The stack height of the metal sulfide slabs of a given diameter *d* influences the selectivity of the process by varying the ratio of rim sites to edge sites. The theory suggests the rim sites are active in hydrogenation and C-S bond breaking, while edge sites participate only in C-S bond breaking. The basal plane consists entirely of sulfur atoms and is considered dormant.

The rim and edge sites consist of molybdenum/tungsten atoms that are accessible to reactants due to sulfur anion vacancies in the metal sulfide crystal structure. These unsaturated sites, or active sites, are continually generated and degenerated by sulfur atoms reacting with the H_2 of the hydrotreating system to release H_2S in a reversible reaction. Sulfur or nitrogen heteroatoms from the feedstock molecules continuously bind to these active sites. These molecules potentially undergo some extent of hydrogenation (essential to HDN) if adsorbed at a

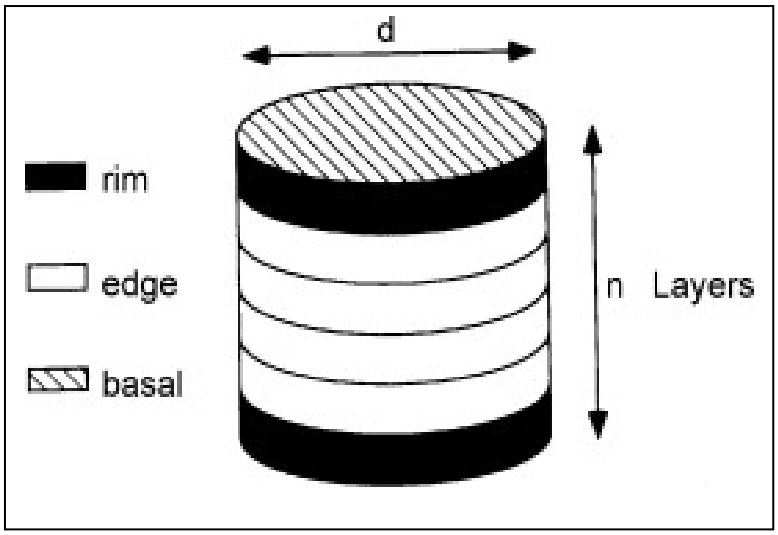

Figure 2.5: Illustration of the "rim-edge" model (Chianelli et al., 2009).

rim site before the molecule is released back into the hydrotreating system. The removed heteratom remains to saturate the active site, and the process repeats itself. In the case of nitrogen heteroatoms, the atom is strongly adsorbed and difficult to remove by NH_3 production. This is known as nitrogen poisoning and is further discussed in section 2.3.4. This model suggests that the extent of hydrogenation that occurs in a hydrotreating process can be predicted by the number of metal sulfide layers (*n*) that make up each hexagonal stack. From this theory, catalysts with predominantly single layer metal sulfide structures will have a greater selectivity for hydrogenated organic molecules, while increasing catalyst particle sizes will result in less extensive hydrogenation.

2.3.2 Promoters

The major shortcoming of the "rim-edge" model is that it fails to explain the influence that the doping of Co and Ni catalyst promoters has on the performance of MoS_2 and WS_2 hydrotreating catalysts. Many different proposals have been presented to explain the contribution of the catalyst promoters to the synergy exhibited by hydrotreating catalysts. There are two proposed theories that are widely discussed: the remote control or contact synergy theory, and the edge decoration or "CoMoS" theory (applicable to all types of promoters and active components).

The remote control model was theorized by Delmon and associates (Hagenbach et al., 1973) and proposed that interactions between separate MoS_2 and

Co_9S_8 sulfide phases on a CoMo catalyst surface were created from their close proximity. These interactions were described as their "contact synergy." Their remote control mechanism stated that organosulfur molecules would be adsorbed at MoS_2 active sites before reacting with dissociated hydrogen atoms arriving from the Co_9S_8 active sites. Although this theory is less accepted today compared to the edge decoration model, it does provide the concept of synergy/cooperation between two separate sulfide phases as opposed to a second metal simply promoting the activity of a metal sulfide (Chianelli et al., 2009).

The edge decoration model was proposed by Topsøe and associates (Wivel et al., 1981) and theorizes that the activity of the bimetallic catalysts originates from a separate phase created between the promoter, the active component, and the sulfur active phase. It is accepted that the highest catalyst activity is achieved when Co and Ni metals in their sulfide phase are doped along the outer surface area of the MoS_2 and WS_2 hexagonal slabs. The Co and Ni atoms substituted into the Mo and W positions within the crystal lattice exclusively along the exterior of the metal sulfide particles. These substituted metal promoters create a crystal phase between the active component and active phase (i.e. Mo/W and S), which was referred to as the "CoMoS" phase (Sørensen et al., 1985). Scanning tunneling microscopy studies have been performed to verify this theory, providing atomic-scale images of active MoS_2 nanoclusters promoted by both Co and Ni at the edge and rim sites (Lauritsen et al.,

2007). This theory has become the most widely accepted method of explaining the function of catalyst promoters in hydrotreating.

In industry, the most common promoter/active component combinations used for bimetallic hydrotreating catalysts used are NiMo, CoMo, NiW sulfide catalysts. Which catalyst offers the best performance depends heavily on the specifics of the application. This includes the reactor operating conditions, the feedstock impurities in relation to one another, and the priority of each hydrotreating reaction (i.e. hydrodesulfurization, hydrodenitrogenation, hydrodearomatization, etc.).

2.3.3 Deactivation

The activity of any bimetallic catalyst decreases at an appreciable rate over the operating time of any hydrotreating process. To compensate for the decline in the catalyst's activity, the temperature of an industrial hydrotreating reactor must be continually increased in an S-curve profile as a function of time on stream (Tamm et al., 1981). Considerable costs are the result of the increasing thermal energy demand employed by all packed bed hydrotreaters. The root of the deactivation problem lies in the coverage or loss of catalyst active sites. Furimsky and Massoth (1999) outline the four basic factors of catalyst deactivation:

1) Active site poisoning by a strong adsorption (i.e. nitrogen).

2) Active site coverage by deposition (i.e. coke, nickel, vanadium).

3) Pore mouth constriction and/or blockage from coking.

4) Sintering of the active phase.

Initially, rapid deactivation occurs due to coke formation that quickly reaches what is considered steady-state conditions for the operation. Continued deactivation over the course of the operation is due to pore constriction from coke formation and from feed contaminants, either through metal deposits or adsorbed nitrogen. Finally, catastrophic losses in feed conversion occur when ultimate pore blockage occurs for the catalyst support.

Poisoning of the metal sulfide catalysts occurs from the strong adsorption of compounds onto the coordinately unsaturated sites. Although organic sulfur and oxygen compounds have slight poisoning effects, nitrogen compounds are considered the main source of poisoning for hydrotreating catalysts. Their poisoning effects may be reversible or irreversible, depending on the characteristics of the feed and the operating conditions (Furimsky and Massoth, 1999). Irreversible poisoning is the result of polymer formation that occurs around the adsorbed nitrogen heteroatom. For the case of Athabasca bitumen-derived gas oils, considerable organonitrogen concentrations poison not only the HDN reactions, but the HDS reactions as well. For these gas oils, the nitrogen compounds appear to simply enhance the initial rapid deactivation from coke formation before reaching pseudo steady-state conditions.

Aside from initial coke formation, the deposition of metal impurities in the feedstock, most commonly nickel and vanadium, result in metal sulfide formations that block the active sites of the catalyst. The metals are removed from the feedstock by hydrodemetallization (HDM), with the metals remaining on the surface of the catalyst. Unlike nitrogen poisoning, the metal deposition does not reach a steady-state and continuously builds during the course of a hydrotreating run (Ledoux and Hantzer, 1990). In Maya crude oils, nickel and vanadium contaminants can be a significant problem, reaching concentrations up to 100 wppm for nickel and 500 wppm for vanadium (Maity et al., 2008). For Athabasca bitumen-derived gas oils, metal contaminants are not a significant problem for hydroprocessing.

The first two deactivation points suggested by Furimsky and Massoth are a function of the feed characteristics and cannot be controlled by conventional bimetallic sulfide catalysts. The deactivation pitfalls of pore constriction/blockage and active phase sintering, however, can be mitigated by choosing an effective catalyst support for the bimetallic catalyst. The constriction and blockage of pores by coke formation can be remedied by using a catalyst support with large pore diameters. The sintering of catalyst particles can be avoided by finding a support that provides a high surface area for catalyst dispersion with minimal interaction effects with the metal oxide precursors. The agglomeration of hexagonal catalyst slabs into larger crystallites can result from strong interactions with the catalyst support, reducing the number of edge active sites (Furimsky and Massoth, 1999). For these reasons,

support materials have become the focus of many hydrotreating researchers. There is a wealth of information on support effects can be found from catalyst support research efforts worldwide (Okamoto et al., 2003).

2.3.4 Support Materials

The majority of all metal sulfide hydrotreating catalysts are distributed as adsorbed particles over a catalyst support structure before being applied as pellets in a hydrotreating reactor. The purpose of the support is to increase the activity of the catalyst by increasing the exposure of the active sites to the reactants while still maintaining the mechanical strength of the material. As previously stated, γ-alumina is almost exclusively used as a hydrotreating catalyst support in industry. Significant efforts have been made in an attempt to improve upon the effectiveness of alumina. A review by Luck (1991) outlines five objectives for finding a superior catalyst support:

1) Improving the dispersion of the bimetallic sulfides.

2) Reducing the strong interaction between the active component and the support while the active component is in the initial oxide phase.

3) Decrease the spinell phase concentration of γ-alumina, increasing the usability of the catalyst promoters.

4) Improve the recovery potential for catalyst metals.

5) Reducing catalyst deactivation from coke formation.

The first objective addresses the possibility of applying a catalyst support with a higher accessible surface area compared to γ–alumina. Materials such as natural zeolites and synthetics such as SBA-15 have been known to have surface areas that far exceed those of commercial alumina supports. The key factor is if the hydrocarbon molecules being processed can access the measurable surface areas of these supports. The second objective addresses the strong surface interactions between the catalyst metal oxide precursors and aluminum oxide. These strong surface interactions make it difficult for the complete sulfidation and activation of the catalyst metal to occur due to the formation of metal aluminates (Breysse et al., 2008). The strong surface interactions also contribute to accelerated catalyst deactivation occurring due to sintering of the catalyst's active phase (Besenbacher et al., 2008). The third objective is closely related to the second as it deals with the formation of cobalt and nickel aluminates during catalyst preparation. The formation of these precursors renders Ni and Co metals unavailable as active phase promotes (Furimsky and Massoth, 1999). For the fourth objective, it would be beneficial to have a support that could be easily separated from the catalyst to provide recovery of the metals once the catalyst itself can no longer be effectively regenerated. When regenerating catalysts after extensive deactivation has occurred, it is impossible to achieve the initial activity of the fresh catalyst due to sintering effects (Guichard et al., 2009). However, recovering the catalyst metals from the alumina support is a difficult procedure. The final objective pertains to combating coke formation on catalyst

surfaces by improving the structure and dimensions of the support. Improving upon the pore diameters of a support has been shown to lessen effects of obstruction caused by coke formation (Netzel et al., 1996).

There have been many different support materials that have been applied as potential alternatives to γ–alumina for hydrotreating catalysts. Several of these alternative supports include: zeolites (Anderson et al., 1993), mesoporous silica materials such as SBA-15 and MCM-41 (Sampieri et al., 2005), zirconia (Duchet et al., 1991), titania (Ramirez et al., 1989), niobia (Faro Jr. and dos Santos, 2006), magnesium oxide (Zdražil, 2003), and activated carbon materials (Farag et al., 1999). Although each support material presents its own merits, none have succeeded in providing as a practical alternative to γ–alumina for the hydrotreatment of real world feedstocks. Carbon materials in particular have garnered significant interest as a support due to their minimal interactions with catalyst metals and lack of resistance against complete sulfidation of the catalyst metals. Many varieties of carbon structures are capable of possessing high surface areas for metal dispersion, controllable pore sizes to reduce coking effects and controllable surface functionalities (Breysse et al., 2003). One such variety of carbon materials that best exemplifies these traits are multi-walled carbon nanotubes (MWCNTs). The effectiveness of MWCNTs as a catalyst support will be further explored in hydrotreating application for bitumen-derived coker light gas oil.

3 LITERATURE REVIEW – CARBON NANOTUBE SYNTHESIS

The second portion of the literature review focuses on carbon nanotubes and their potential as a heterogeneous catalyst support for gas oil hydrotreatment. The definition and characterization of carbon nanotubes will be discussed for the purpose of understanding how they could be applied in a catalytic system. Several examples will be given of how carbon nanotubes loaded with catalyst metals can effectively be applied to catalyst bed applications. Several synthesis alternatives will be presented to determine which process can create carbon nanotubes both efficiently and effectively for the specific task of a support structure for hydrotreating catalysis.

3.1 Definition and Characterization of Carbon Nanotubes

Pure carbon can be found in many different types of allotropes. Figure 3.1 shows several of these carbon allotropes. The most commonly found allotrope of carbon is graphite. The graphite carbon allotrope is made up of one-atom thick sheets of carbon bound by a planar hexagon lattice. Each carbon atom is bonded to three other atoms by sp^2 covalent bonds, forming a trigonal planar bonding scheme for each atom. Another well-known allotrope of carbon is diamond. Diamond is defined by a crystal lattice of cubic closed-packed carbon atoms forming a zinc-blend type structure. Each carbon atom is bonded to four other atoms by sp^3 covalent bonds, forming a tetrahedral bonding scheme for each atom. A more rare form of carbon allotrope is fullerenes. Fullerenes are defined as a discrete, molecular species consisting of a number of carbon atoms, ranging from 20 to 84 atoms per sphere. The

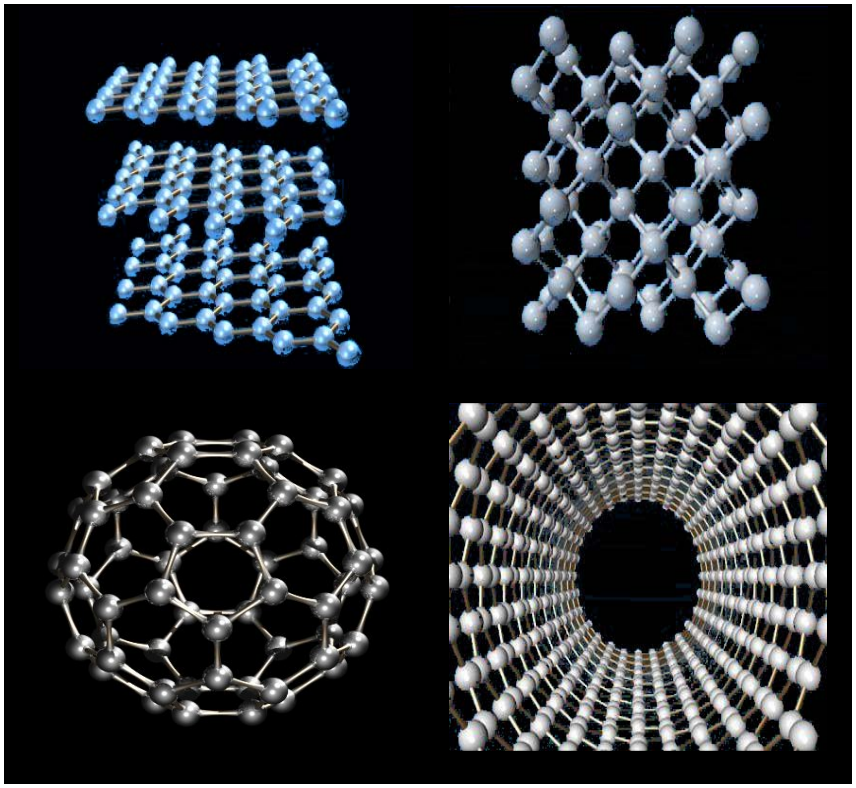

Figure 3.1: Diagrams of several carbon allotropes: Graphite (top left); Diamond (top right); Buckminsterfullerene (C_{60}, bottom left); Single-walled carbon nanotube (SWCNT, bottom right).

atoms are bonded by sp^2 covalent bonds in a slightly skewed trigonal planar bonding scheme. This allotrope is essentially a sheet of graphite rolled into a ball to form a spherical molecule.

The carbon nanotube allotrope can be defined in a very similar fashion to the fullerene allotrope. The carbon nanotube allotrope is defined as a sheet of graphite rolled into a cylinder to form an infinite cylindrical crystal lattice. Each cylinder formed by the carbon atoms for this allotrope is only a few nanometers in diameter. However, each synthesized tube can grow to be several millimeters in length. Because they are defined in a fashion very similar to fullerenes, carbon nanotubes are commonly referred to as a member of the fullerene family. Both allotropes consist of carbon atoms bonded by sp^2 covalent bonds in a slightly manipulated trigonal planar bonding scheme. Also contributing to the connection between these two allotropes is that carbon nanotubes were originally discovered as a by-product of a fullerene synthesis process by Sumio Iijima (1991). Since this discovery, carbon nanotubes (CNTs) have sparked unprecedented interest from a wide variety of scientific fields.

Carbon nanotubes can be classified by two main structural types: single-walled nanotubes and multi-walled nanotubes. Single-walled nanotubes (SWCNTs) are defined as a single atom-thick graphite layers rolled up into a hollow cylinder. The diameter of these tubes can range from 1.0 to 1.4 nanometers in span (Tanaka et al., 1999). Multi-walled carbon nanotubes (MWCNTs) are defined as a tube consisting of several concentrically arranged graphite cylinders. These tubes can range in outer

diameter from 10 to 250 nanometers and are comprised of 2 to 30 concentric graphite layers, giving the tubes considerable wall thickness (Tanaka et al., 1999). The concentric walls are regularly spaced 3.4Å apart, the same distance exhibited between crystal lattice sheets in graphite materials. Generally, MWCNTs are more common when compared to SWCNTs. This is due to the less complex methods that can be applied to produce MWCNTs.

MWCNTs have garnered interest as potential heterogeneous catalyst support structures due to the resistance they possess to acidic/basic conditions, the possibility of controlling their porosity & surface chemistry, and the potential for allowing great dispersion of doped catalysts due to their high specific surface areas (Auer et al., 1998). The pore diameter (i.e. the inner diameter) of the nanotubes can be controlled by variation of the synthesis conditions used to produce the CNTs. Increasing the size of the pore diameters often leads to a decrease in the specific surface area of the substance. This creates the need to find an adequate balance between these two properties in order to find the optimum catalyst activity for a given reactor application. Although MWCNTs resist decomposition under acidic or basic conditions, it is this inert behavior that they possess after initial synthesis that makes it difficult to deposit catalyst metals on their surface. This problem can be remedied by performing nitric acid treatments on the surface of the CNTs. These treatments can create oxygen functionalities, such as hydroxyl and carboxyl groups, on the outer and inner walls of the MWCNTs (Kyotani et al., 2001). Catalyst metals in the oxide

active phase become chemically adsorbed to these functional group sites on the CNT surface.

It is conceivable that transition metals often applied to hydrotreating catalysis, such as nickel, molybdenum, and tungsten, could be chemically deposited on the outer and inner walls of MWCNTs in their oxide phases. Due to the limited interaction between the catalyst metals and the graphitic surface of the MWCNTs, the conversion of the catalyst metals from the oxide phase to the sulfide phase would proceed far more extensively. In addition, MWCNTs with relatively large pore diameters could minimize the effects of coking on the catalyst surface while still providing a large area for the catalyst metals to disperse across the outer and inner walls of the nanotubes.

3.2 Synthesis Methods

The methods used to create CNTs can be divided into three essential categories: electric arc discharge, laser ablation, and chemical vapor deposition. Each method can be a suitable alternative for CNT synthesis, depending on the quality, efficiency, and production rate desired. A review was conducted to determine the most effective process for making hydrotreating catalyst supports.

3.2.1 Electric Arc Discharge

Carbon arc discharge is the simplest and most common way that carbon nanotubes are produced. This particular method is also commonly used to produce

60-atom fullerene molecules (Rao et al., 1996). Carbon nanotubes were initially discovered as a by-product of this method when the desired product was fullerenes. The process involves passing an electrical current of 50 to 100 amperes across two graphite carbon electrodes roughly 1mm apart (Xing et al., 2007). The electrodes are typically surrounded by an inert gas (such as helium, argon, or nitrogen) under low pressure conditions (5 to 70 kPa) (Reich et al., 2004). Operating at higher pressures typically results in fullerenes making up the majority of the product. The result of this electrical current is an electric potential of roughly 20 volts and a high temperature discharge between the electrodes (Reich et al., 2004). The arc discharge causes carbon to sublimate from the anode and form a rod-shaped deposit on the cathode. The anode is often rotated on a spindle to ensure a uniform electric discharge (Lee et al., 2002). The deposit consists of a hard outer shell of crystal graphite and an inner shell of soot consisting of nanotubes, fullerenes, and amorphous carbon. If the anode is doped with a metal catalyst (such as iron, nickel, or cobalt), the product is typically single-walled nanotubes. If not, then multi-walled nanotubes are typically the resulting product.

The most important parameter in this process is the pressure of the surrounding inert gas, which must be kept low enough to ensure nanotube production. The yield of this process can range from 30 to 90%, depending on the sustained temperature of the cathode and the speed of the anode rotation (Mildred et al., 2001). The main drawback in using this method is that the nanotubes usually have erratic

sizing and direction. As well, it is often quite difficult to purify the product of graphite, fullerene, and metal catalyst impurities. Expansion of the electric arc discharge process to large-scale synthesis is another potential drawback for its applicability as a catalyst support producer.

3.2.2 Laser Ablation

Laser ablation is a technique that was developed by Richard Smalley and company at Rice University in 1995 (Guo et al., 1995). The process consists of a laser, either pulsed or continuous, firing free electrons for the purpose of vaporizing a graphite target at a temperature of approximately 1200°C (Zeng et al., 2006). An inert gas such as helium or argon continuously flows into the reactor. This gas both maintains a low operating pressure of ~70 kPa and transports the vaporized carbon out of the reactor (Saito et al., 1998). The inert gas often flows past the graphite target perpendicular to the laser as it vaporizes the graphite. Usually located at the exit of the reactor is a water-cooled condenser. The vaporized carbon condenses at the condenser in the form of carbon nanotubes. From a pure graphite target, multi-walled carbon nanotubes are produced. If the target is doped with a metal catalyst (such as iron, nickel, cobalt, or yttrium), it typically results in single-walled carbon nanotubes being produced.

From this method, nanotubes can be produced at a rate of 45 grams per hour with yields ranging from 70 to 90% depending on the strength of the free electron

laser (Saito et al., 1998). Compared to all other methods of synthesis, this process produces the highest quality and most consistently sized nanotubes. The tubes often form on the condenser in long tube bundles containing a relatively low amount of impurities (Zeng et al., 2006). Although this method produces the highest quality carbon nanotubes, it requires a very high operating cost compared to other methods. This is due in large part to the high energy cost pertaining to running a high-powered free electron laser. Because this method is not very cost effective, it is unlikely that this process can be scaled up to produce nanotubes on an industrial level.

3.2.3 Chemical Vapor Deposition

The method of chemical vapor deposition is easily the most diverse of all the methods of carbon nanotube synthesis. The method consists of cracking a gaseous phase carbon source by exposing it to the heat produced from plasma or heated coil. Common to each type of chemical vapor deposition is a carbon-containing gas (alcohols, alkenes, metallocenes, carbon monoxide, etc.) and a carrier gas (nitrogen, hydrogen, argon, etc.) being bled into a reactor. The gaseous-phase carbon diffuses towards a heated substrate coated with a metal catalyst (such as iron, nickel, or cobalt). Because of thermal annealing, catalyst clusters form on the substrate and become the sites for carbon nanotube growth (Hafner et al., 1998). For nanotubes to be synthesized, a high operating temperature ranging from 500 to 1000°C (depending on the type of method used) is required (Dai, 2002). Some of the many types of chemical vapor deposition (CVD) include: plasma enhanced CVD, thermal CVD,

alcohol catalytic CVD, vapor phase growth, laser-assisted thermal CVD, cobalt-molybdenum catalyst (CoMoCat) process, and high pressure carbon monoxide disproportionation.

Because there are so many types of chemical vapor deposition, the yield from this method can range from 20% to nearly 100% (Ago et al., 2006). From this method, long nanotubes can be produced with diameters measured in excess of 200 nanometers (Wang et al., 2001). The types of chemical vapor deposition that do produce single-walled nanotubes (such as high pressure CO disproportionation) do so at a high purity and are capable of controlling the tube diameters (Chen et al., 2006). This method is the most practical method to be scaled up to meet industrial production needs. Most of the processes that could be scaled up produce multi-walled nanotubes containing many structural defects. These structural defects, however, are not a concern when the MWCNTs are to be applied as a support for metal catalyst.

3.3 Application as Catalyst Supports

There have been a limited number of studies applying MWCNTs as a support for hydrotreating catalyst. The effectiveness of a MWCNT-supported CoMo sulfide catalyst was tested in one study based on the HDS of thiophene and the HDN of pyrrole (Dong et al., 2006). The MWCNTs for this study were synthesized by CVD of CH_4 or CO in the presence of a NiMgO catalyst precursor (Chen et al., 1997). The inner diameters of these tubes ranged from 3 to 5 nm and were determined to have a

specific surface area of approximately 140 m^2/g. CoMo catalyst supported on these MWCNTs was found to have superior HDS & HDN activity when compared to an activated carbon support by using model feeds as a basis of comparison. A separate publication compared the HDS and HDA activity of MWCNT and γ–Al_2O_3 supported CoMo sulfide catalyst using a dibenzothiophene solution as a basis of comparison (Shang et al., 2007). The MWCNT-supported CoMo catalyst was found to be slightly less active than the γ–Al_2O_3 support. The MWCNTs used for this study had a reported specific surface area of 189 m^2/g and pore diameter of 8.9 nm. Only one study was found that applied a "real world" feedstock (in this case, light gas oil derived from Athabasca bitumen) (Eswaramoorthi et al., 2008). The MWCNTs used for this study were synthesized by a CVD method that used ferrocene as a metallic catalyst and toluene as a carbon source (Das et al., 2006). The CNTs produced from this method possessed inner diameters ranging from 10 to 15 nm and a 112 m^2/g specific surface area. The optimum metal loadings of Ni and Mo were found for this CNT support and its HDS and HDN activity was compared to a γ–Al_2O_3 support with similar loadings. The MWCNT-supported catalyst displayed slightly higher HDS and HDN activity than the γ–Al_2O_3-supported catalyst when compared on a weight basis. When compared on a volume basis, the γ–Al_2O_3 catalyst had slightly higher activity.

For each of the three applications discussed of MWCNT-supports being applied to hydrotreating, it should be noted that the inner diameters of the tubes were rather small, ranging from 3 to 14 nm. This would have made the pores possibly

susceptible pore clogging due to coke deposition. As well, the specific surface area of these tubes never exceeded 200 m^2/g, which is well short of the surface area typically exhibited by γ–Al_2O_3 (350-400 m^2/g). It is also worth noting that the SEM and TEM images of the MWCNTs from the hydrotreating studies showed considerably twisted morphologies, leading to considerable entanglement and decrease to the accessible surface area. These three noted problems would be expected to be rectified through the application of the aforementioned AAO template synthesis method.

4 LITERATURE REVIEW – ANODIC ALUMINA SYNTHESIS

The final section of the literature review pertains to creating anodic alumina film for the purpose of creating templates for carbon nanotube synthesis. The theory and behavior of aluminum anodization will be discussed with the intention of finding the most suitable materials and conditions to synthesize templates that could be applied within a chemical vapor deposition system. Additionally, a discussion of anodization parameter variation is conducted in order to explain the method of modifying the pore diameter of the anodic pore channels. Finally, numerous examples of anodic films being applied to synthesize carbon nanotubes are examined and conclusions are reached as to why this method is advantageous for making hydrotreating catalyst supports.

4.1 Growth Mechanism

When aluminum acts as an anode within an electrolysis cell, it is referred to as *aluminum anodization*. As the aluminum anodization occurs in the presence of certain weak acid electrolytes -- such as chromic acid, phosphoric acid, or oxalic acid -- a porous anodic aluminum oxide (AAO) film develops on the surface of the anode. These porous films develop due to electrolytes which dissolve the resulting oxide film at an appreciable rate. The pores develop in a remarkably uniform hexagonal array of pore channels, with each channel separated by an aluminum oxide barrier (Jagminas et al., 2003). These channel formations are made possible by the transport of aluminum and oxygen ions through an amorphous aluminum oxide barrier layer due

to electric field conditions (Thompson, 1997). The electrolyte anions adhere to the anode and increase O^{2-} ion production at the barrier layer surface. Trivalent or divalent ions, such as the four aforementioned electrolytes, adsorb more readily than monovalent ions to the positively charged alumina surface. As water molecules also adsorb to the anode surface, hydrogen bonding occurs between the hydrogen atoms of the water molecules and the oxygen atoms of the oxyanions. The weakening of the bonds that create the H_2O molecule result in the donation of O^{2-} ions from the water to the alumina barrier layer (O'Sullivan and Wood, 1970). Of the four previously mentioned weak acid electrolytes, oxalic acid results in the production of thicker, more manageable anodic films that don't readily dissolve into the electrolyte solution (Kape, 1961).

4.2 Synthesis Method

In the last decade, these AAO films have been implemented as templates for synthesizing many different types of functional nanostructured materials (Lee et al., 2006). The first such use of these films for this application was in 1995, when Masuda and Fukada (1995) produced porous platinum and gold porous films originating from an AAO template. This publication established a two-step anodization method for producing AAO film that is widely used today. An illustration of this method can be found in Figure 4.1 (Sung et al., 2006). The aluminum anode is first chemically polished in a strong acid to remove the naturally occurring oxide layer from its surface, as well as to create a smooth plate free of any

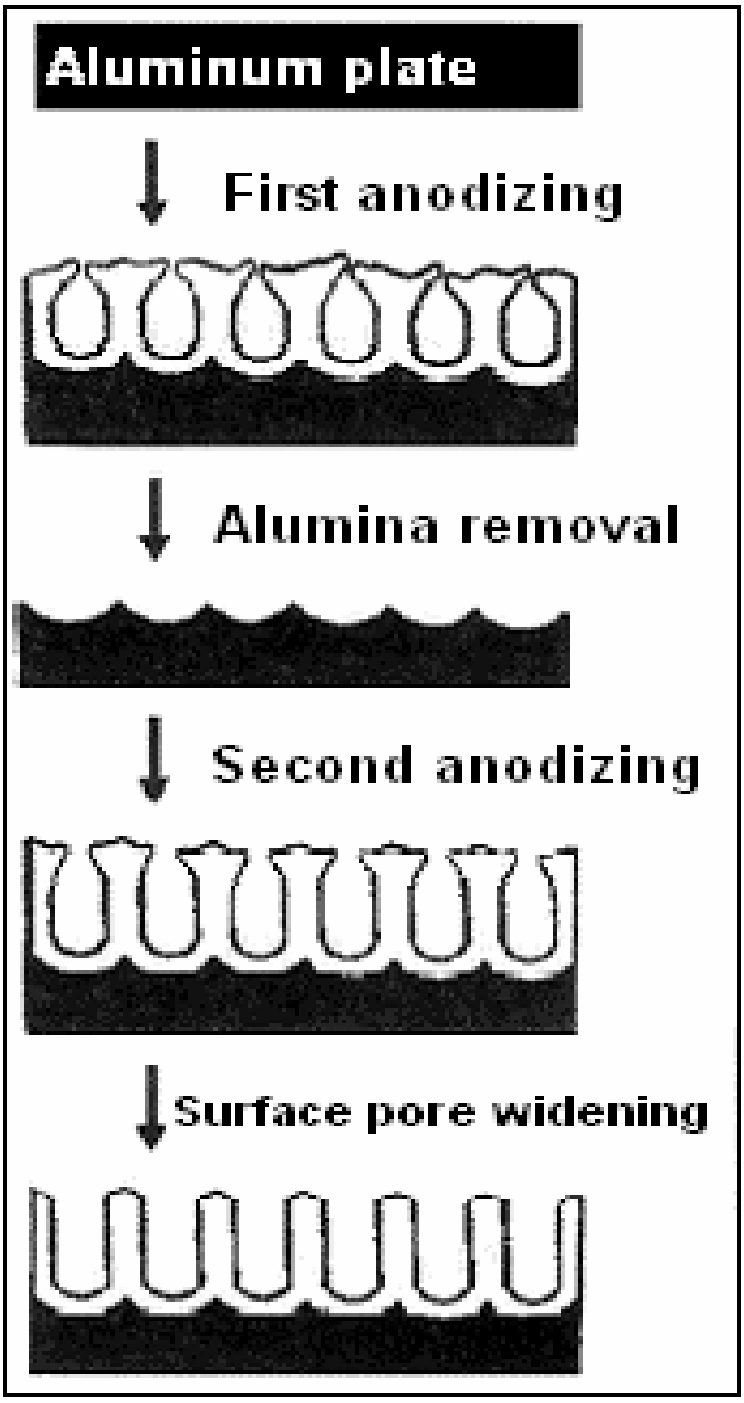

Figure 4.1: Illustration of the two-step anodization method (Sung et al., 2006).

physical imperfections. The plate is then introduced to the electrolysis cell and undergoes the first anodization procedure. This first anodization is typically 1 to 2 hours. The pores that are produced by this procedure are very narrow and are almost entirely closed along the outer surface of the film. To remove this inferior film, the plate is submersed in a heated deoxidizing solution, typically a chromic acid solution. The purified aluminum plate then undergoes a second anodization procedure that can last anywhere from 30 minutes to 66 hours. The result is a template with significantly wider pore diameters. However, the pores still narrow considerably at the exposed surface of the film. To give the pores their maximum potential size, the extracted film is etched by being immersed in a weak acid. Many different nanostructure synthesis processes can then be performed using the AAO template after its etching is completed.

4.3 Pore Diameter Control

For any given AAO template application, it would be highly useful if the diameter of the pore channels could be controlled in order to achieve a desired pore structure. Controlling the AAO structure can be done by changing the parameters of the electrolytic cell. A study performed by Zhao et al. (2007) examined the effects the anodizing conditions have on the anodic alumina structure. The publication examined the change in the pore diameter and wall thickness of the AAO film from varying the constant electrical potential of the cell, as well as from changes in the oxalic acid electrolyte concentration. The results of this study showed that the pore diameter of

the films increased linearly with increases in the oxalic acid concentration and the anodizing voltage. For the given system, reaction conditions of 0.3 mol/L oxalic acid concentration and 30 V electrical potential produced anodic pore diameters of 40 nm. For parameter specifications of 0.5 mol/L oxalic acid concentration and 50 V electrical potential, pore diameters of 80 nm were achieved. The thickness of the alumina walls dividing these pores was 40 nm for both reaction conditions.

It was found at low anodizing voltages (i.e. less than 30 V) that the AAO films began to demonstrate disordered pore arrangements. This essentially means pores developing in contradiction to the accepted hexagonal arrangement. Even more problematic pore development was found at anodization voltages reaching 60 V. At this relatively high voltage, the inner walls of the amorphous alumina structure began to exhibit cracking, a result of the dividing walls becoming too thin. This caused many pore channels to merge, which is considered as a failure of the template. Examples of these types of pore behavior can be seen in Figure 4.2 (Zhao et al., 2007). It can be concluded from reviewing this study that the anodizing voltage and electrolyte concentration of an anodization procedure can be tuned in order to produce a template for the synthesis of CNTs with desired pore diameters. The CNTs resulting from the tuned AAO template should have inner diameters and a specific surface area that would provide, as a catalyst support, the optimum HDS & HDN activity for a hydrotreating catalyst.

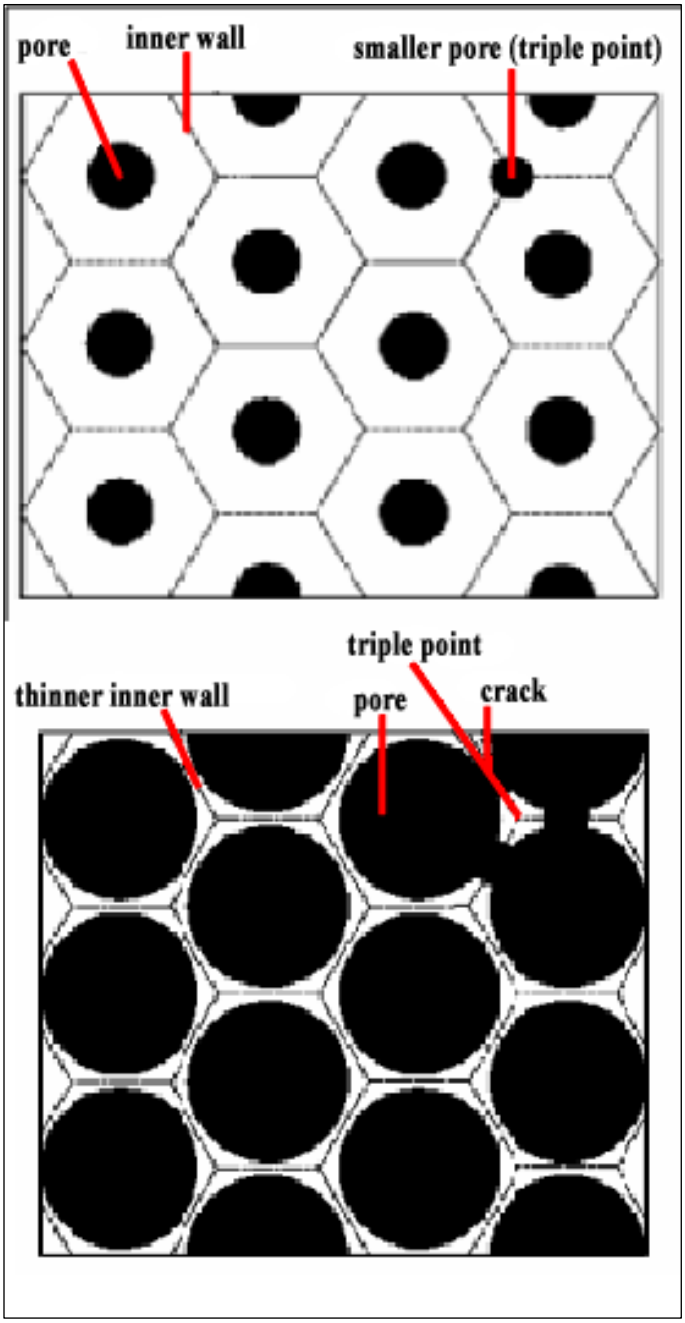

Figure 4.2: Defining the AAO film structure at low (above) and high (below) anodizing voltages (adapted from Zhao et al., 2007).

4.4 MWCNT Synthesis Via AAO Templates

There have been numerous studies performed based on the application of AAO films as templates for MWCNT synthesis (Kyotani et al., 1999; Sui et al., 2002; Kim et al., 2003; Yang et al., 2003; Jung et al., 2004; Im et al., 2004; Lee et al., 2005; Eswaramoorthi et al., 2006; Gras et al., 2006; Li K.Z. et al., 2007; Schneider et al., 2008). The common link between each of these studies is the use of AAO template in place of a more typical catalyst substrate in a chemical vapor deposition (CVD) process. For such a process, a carbon-based gas (i.e. acetylene, ethylene, propylene) decomposes in the presence of a carrier gas (i.e. nitrogen, argon, ammonia) with the carbon being deposited on the AAO template. The carbon that is deposited along the inner walls of the pore channels forms MWCNTs that may or may not grow beyond the surface of the AAO template. In addition, considerable amounts of amorphous carbon form on the surfaces of the AAO film. These reactions typically occur in a continuous gas flow quartz tube reactor at temperatures ranging from 550 to 800°C. The pore diameters within the AAO templates applied in these studies varied from 30 to 230 nm. An observed trend was that templates with pore diameters less than roughly 60 nm produced close-ended MWCNTs, while pore diameters more than roughly 60 nm produced open-ended nanotubes. This trend applied to processes that lacked any type of catalyst substrate (i.e. Si substrates). In the presence of any catalyst substrate, close-ended tubes were produced. It could be hypothesized for the mechanism of large diameter CNT growth that the hemispherical structures that

characterize close-ended nanotubes cannot be synthesized if the tube diameter is too large. For usage as a catalyst support, it would be beneficial for the MWCNTs to be open-ended to allow catalyst metals and reactant fluids to access the inner wall surface area of the tubes. For the study conducted by Eswaramoorthi et al. (2006), MWCNTs were produced with inner diameters ranging from 40 to 50 nm and a specific surface area of 310 m^2/g. This high surface area is uncharacteristic of such large diameter MWCNTs and could be hypothesized as being a result of the lack of entanglement of the nanotubes during synthesis. The lack of nanotube interaction is due to the parallel channels of the AAO template. Nanotube interaction and entanglement would otherwise lower the accessible surface area of the material. It can be concluded after reviewing various MWCNT synthesis studies from AAO templates that there are three distinct advantages of using this method for producing CNT catalyst supports. These advantages are: 1) The capacity to synthesize open-ended nanotubes; 2) The lack of nanotube entanglement when synthesized due to parallel AAO pore channels; and 3) The ability to directly control the diameter of the synthesized MWCNTs by varying the process parameters for AAO film production. In addition, the large diameter MWCNTs that can be produced by this method would make them ideal for application as a hydrotreating catalyst support to limit the initial catalyst deactivation attributed to coking.

5 EXPERIMENTAL METHOD

The experimental procedures that were performed during the course of this project can be divided into four subsections: 1) AAO synthesis via low-temperature electrolysis; 2) MWCNT synthesis via chemical vapor deposition; 3) MWCNT and NiMo/MWCNT catalyst characterization; and 4) Hydrotreating of gas oil. The section will discuss in detail the experimental procedures performed, as well as the scientific principles factoring into each portion of the research. Additionally, the experimental planning behind each executed step of the research will be both addressed and justified. The purpose of this section will be to provide a clear description of all the laboratory work that contributed to the conclusions reached in this thesis.

5.1 AAO Synthesis Via Low-Temperature Electrolysis

The AAO templates were synthesized using the two-step anodization procedure by Masuda & Fukuda (1995) with the exact details originating from a study performed by Eswaramoorthi et al. (2006). Shown in Figure 5.1 is a basic schematic for the electrolysis cell used to grow the anodic alumina film. The cell consisted of a graphite cathode and an aluminum electrode each having dimensions of 7.0 cm × 20.0 cm and spaced 1.0 cm apart. A DC power supply was applied to the cell and the electric potential across the electrodes was kept constant for the duration of each experimental run. The electrolysis vessel contains 1.3 L of oxalic acid electrolyte solution for each run at varying concentrations. Oxalic acid was used as an electrolyte

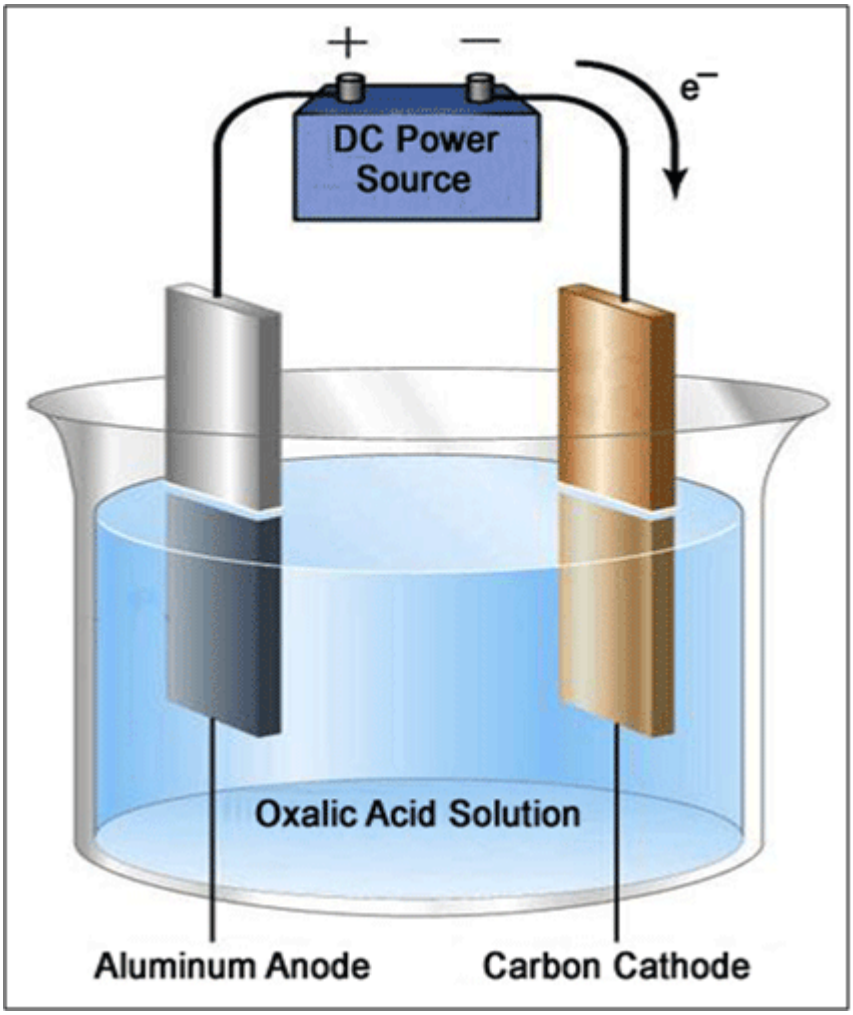

Figure 5.1: Illustration of the AAO electrolysis cell.

for anodization because of its capacity to allow for thick, manageable AAO films to synthesize. The vessel was equipped with a glycol cooling system that was maintained at a temperature of 1°C for all experimental runs performed.

Prior to the first anodization step, the aluminum anode was immersed in an 80°C polishing solution for 15 minutes to remove the naturally occurring oxide layer from its surface and to create a smooth plate free of any physical imperfections. The polishing solution was prepared with the following weight composition: 53.4% H_3PO_4, 41.7% H_2O, 4.7% HNO_3 and 0.2% $CuSO_4$. The first anodization was then performed with the polished anode at a constant potential of 40.0V for 1 hour. The anode was then removed and immersed for 40 minutes in a deoxidation solution heated to 70°C. The deoxidation solution consisted of the following weight composition: 92.1% H_2O, 7.0% H_3PO_4, and 0.9% CrO_3. The anode plate was then reintroduced to the electrolysis cell to undergo the second anodization procedure.

The run time for the second anodization was kept constant at 66 hours with one of three distinct energy potential profiles being used for each experimental run. An illustration of these three potential profiles can be seen in Figure 5.2. To achieve a 40.0 V cell potential for the second anodization, the voltage was simply set to 40.0 V and kept there for the duration of the 66 hour procedure. To reach a maximum potential of 50.0 V, the cell voltage was initially set at 40.0 V for an 18 hour period to avoid transpassive behavior being experienced by the aluminum anode. When an anode reaches transpassive behavior, the cell experiences a catastrophic flow of

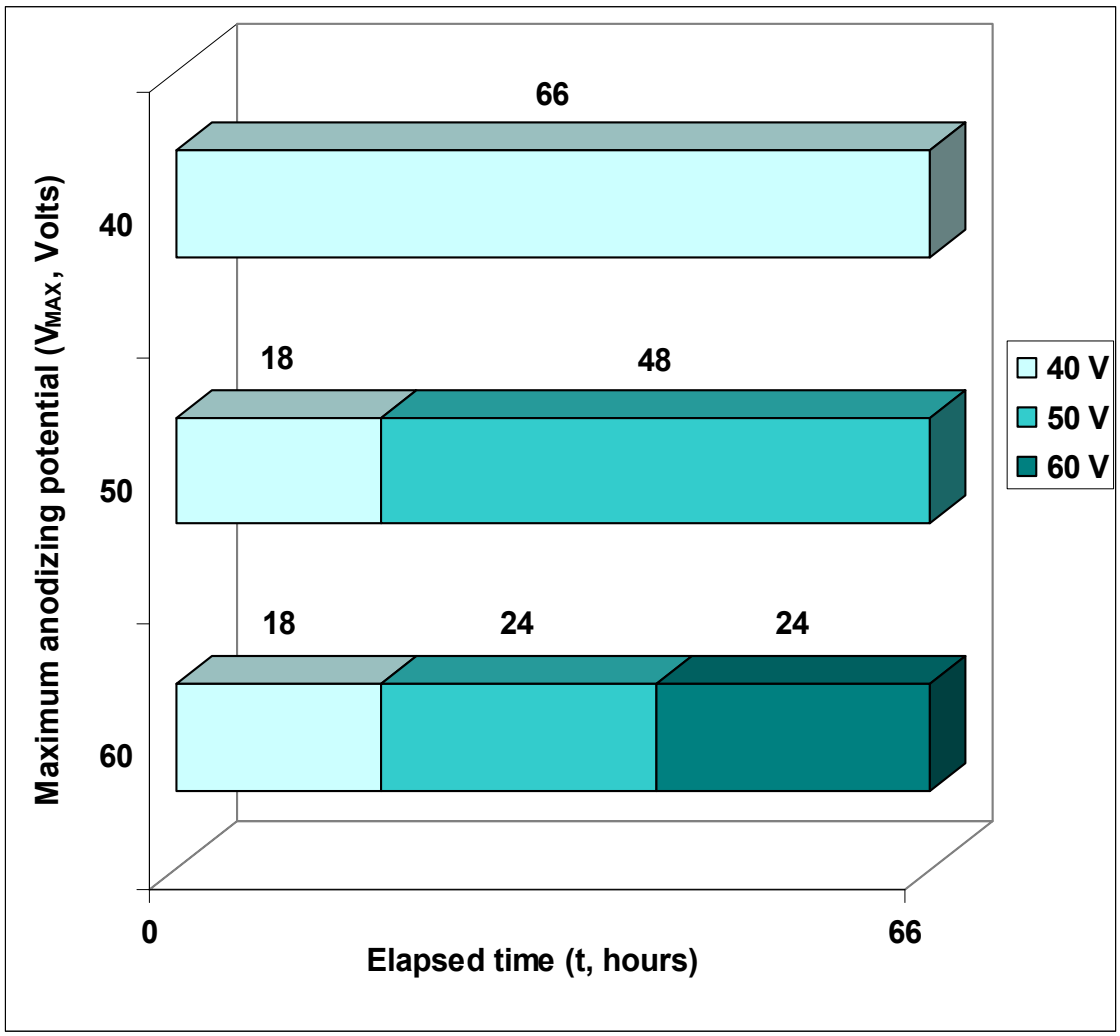

Figure 5.2: Energy potential intervals for maintaining passive behavior during the anodization procedure.

electrical current through the cell, causing a rapid increase in electrolyte temperature. The aluminum no longer exhibits passive film behavior, but rather direct corrosion into the electrolyte. Any AAO film originally synthesized disintegrates into the electrolyte, often referred to as "burning" of the passive layer (Lee et al., 2006). To avoid the type of cell failure, an initial passive layer is developed at a 40.0 V cell potential for 18 hours before advancing to a 50.0 V potential for 48 hours. This gives a mean cell potential of 47.3 V for this given anodization profile. To achieve a maximum cell potential of 60.0 V, the voltage of the DC power supply was set to 40.0V for 18 hours, followed by a 24-hour period at 50.0 V before reaching 60.0 V for a final 24-hour interval. This results in a mean cell potential of 50.9 V in order to reach a maximum potential of 60.0 V.

After the 66 hour second anodization is completed, the AAO film is removed from each side of the plate by exchanging the electrode terminals from the DC power source and passing a constant 1.50 A current across the cell. This means that, rather than hydrogen gas being produced at the graphite cathode, it is produced at the aluminum anode. Hydrogen ions pass through the AAO film so that hydrogen gas is produced between the film and the aluminum plate, causing the AAO to become separated from the electrode. Once extracted from the aluminum electrode, the AAO film undergoes an etching process in a 5 wt.% H_3PO_4 solution. This pore widening process is performed for 30 minutes and widens the entrance of the pore channels to their maximum achievable diameter.

5.1.1 Pore Channel Diameter Variation

In total, there are nine different anodizing conditions that were planned to be tested to determine the optimum settings for template synthesis. Each condition will consist of a unique combination of maximum anodizing voltage and oxalic acid concentration. Oxalic acid concentrations of 0.30 M, 0.40 M, and 0.50 M were tested with the maximum voltage profiles of 40.0 V, 50.0 V, and 60.0 V that were detailed earlier, giving the total of nine unique anodizing conditions. Two runs were to be performed for each condition to test the reproducibility of achieving the AAO pore structures. Each condition maintained a constant 66 hour runtime for each second anodization. The values of 0.30 M oxalic acid and 40.0 V were chosen as the minimum settings because they were the chosen set of parameters for the study performed by Eswaramoorthi et al. (2006). Because these settings produced 60 to 70 nm pore channels, and based on the belief that pore channels 60 nm or lower produced close-ended MWCNTs, it was decided to increase the values for each of these parameters beyond this setting. The oxalic acid concentration of 0.50 M was chosen as the maximum parameter setting because this is the approximate saturation point for oxalic acid under 1°C conditions. The maximum potential parameter setting of 60 V was chosen because of the observed difficulty in achieving anodizing voltages beyond this point in a 66-hour period without experiencing transpassivity. Table 5.1 on the following page outlines the planned structure of the experimental procedure.

Table 5.1
Procedure and naming scheme applied to the electrolysis operating conditions.

		Oxalic Acid Concentration (mol/L)		
		0.30	**0.40**	**0.50**
Maximum Anodizing Voltage (V)	**40**	**Condition 1**	**Condition 4**	**Condition 7**
	50	**Condition 2**	**Condition 5**	**Condition 8**
	60	**Condition 3**	**Condition 6**	**Condition 9**

5.2 MWCNT Synthesis Via Chemical Vapor Deposition

Shown in Figure 5.3 on the following page is a schematic diagram for the CVD process. The simplest definition of this type of CVD reaction is applying a gaseous carbon source in conjunction with AAO templates. For this project, acetylene was applied as the carbon source while argon was used as the carrier gas under atmospheric conditions. The flow rates of these gases were kept constant throughout the reaction process by the application of digital mass flow controllers. The AAO templates were set in the center of a 1 m long quartz tube reactor within a row of quartz boats. The quartz tube was surrounded by a heating furnace equipped with three distributed temperature controllers. These controllers were calibrated to provide a constant reactor temperature across the approximately 23 cm row of AAO templates in the lengthwise center of the quartz tube. The effluent gas mixture of argon, diatomic hydrogen, and acetylene passed through a water-based gas cooler before being vented to a fume hood. For the initial analysis studying the effect of AAO anodizing conditions on the CNT product, the parameters of the reaction were kept constant under conditions similar to those used by Eswaramoorthi et al. (2006). The temperature across the 23 cm row of AAO templates is set to a constant temperature of 650°C. With the AAO templates loaded, the reactor was heated to 650°C while argon was flowed through the reactor at a rate of 100 mL/min. Once the reaction temperature was reached, acetylene gas flow was introduced to the system along with the established argon flow over a span of 2 hours. Because the AAO mass

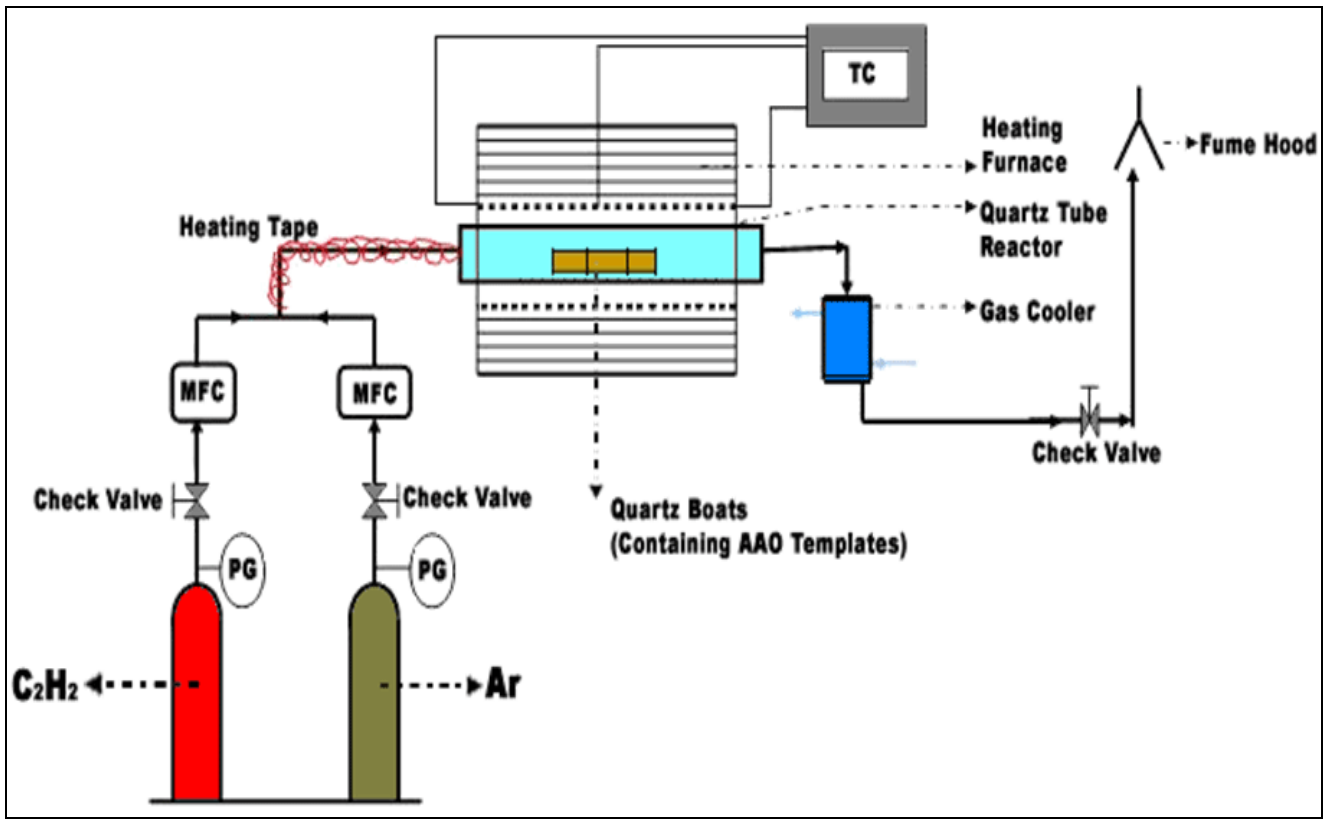

Figure 5.3: Illustration of CVD process applied for MWCNT synthesis.

would vary between each set of conditions in the anodization procedure, the ratio between the volumetric acetylene flow rate and the template mass was kept constant at 8.0 mL·C_2H_2/min : 1.0 g·AAO. For example, the use of a 5.0 g mass of AAO template would have resulted in an applied acetylene flow rate of 40 mL/min. For safety reasons, argon flow was continued during the reaction at a volumetric ratio of 2.5:1 relative to the acetylene flow. After 2 hours, the acetylene flow was ceased while argon flow was continued as the reactor cooled over a 6-hour period. After the optimum anodization parameter settings were found, based on the quality of the resulting MWCNTs and their effectiveness as a hydrotreating catalyst support, the parameters of the CVD process were optimized using the determined optimum AAO templates. Because the wall thickness and length of the produced MWCNTs are found to reach a limit over an extended reaction time (Kyotani et al., 2001), the reaction time of 2 hours was kept constant. Also to be kept constant was the argon/acetylene flow rate ratio along with the atmospheric pressure conditions. The decided parameters to be optimized were the reactor temperature and the C_2H_2-to-AAO ratio (mL/[min·g]).

5.2.1 HF Purification

Once the MWCNTs are synthesized, they must be separated from the AAO template that surrounds them along with the amorphous carbon layer generated on the surface of the templates during the CVD reaction. To accomplish this, the CVD product was immersed in a strong hydrofluoric acid solution (approximately 12 M) to

dissolve the amorphous alumina and carbon while leaving the MWCNTs unaffected. The products were continuously stirred in a 23 wt.% HF solution for 30 hours before the undissolved MWCNTs were filtered, washed in distilled water and dried. This method has been proven to have no detrimental effects to the MWCNTs while being capable of removing virtually all of the anodic alumina and carbonaceous byproducts.

5.2.2 HNO_3 Functionalization

In order for the MWCNTs to be used effectively as a catalyst support, functionalized groups must be created along both the outer and inner walls of the tubes. These hydroxyl and carboxyl groups make it possible for metal catalyst particles to become chemically adsorbed on the MWCNT surface. This limits the likelihood of the metal particles being lost during the hydrotreating process due to leaching into the petroleum feed. The conditions of the functionalization procedure vary from one publication to another. The procedure can have nitric acid concentrations varying from 15 to 70 wt.%, initial CNT concentrations varying from 0.1 to 10 mg/mL, and treatment durations varying from 1 to 48 hours (Rosca et al., 2005). For this project, the functional groups were created on the surface of the purified MWCNTs by immersing them in a 4.0 M HNO_3 solution (approximately 23 wt.% HNO_3) at a 4.0 mg/mL ratio under refluxing conditions for 5 hours (Liu H. et al., 2005). The functionalized MWCNTs were then filtered and washed before undergoing drying at 110°C for a 24-hour period. This method in particular has been

found to greatly increase the dispersion of CoMo hydrotreating catalyst particles on a MWCNT-support (Shang et al, 2004).

5.2.3 CVD Parameter Variation

Similar to the anodization optimization, there are nine different CVD operating conditions that were planned to be tested to determine the optimum settings for MWCNT synthesis. Each condition consisted of a unique combination of a reaction temperature and a C_2H_2-to-AAO ratio. Reaction temperatures of 450, 550, and 650°C were tested with C_2H_2-to-AAO ratios of 4.00, 6.00, and 8.00 mL/(min·g), giving a total of nine CVD operating conditions. The variation of these parameters was expected to have an effect on the wall thickness and length of the tubes as well as the overall morphology of the MWCNTs. A reaction time of 2 hours was maintained for all of the CVD operations. The initial conditions of a 650°C temperature and 8.00 mL/(min·g) gas/template ratio were taken from a publication by Eswaramoorthi et al. (2006). Based on the observed success of these conditions, it was decided to attempt to run the CVD operation more efficiently by experimenting with reaction temperatures less than 650°C and acetylene flow rates less than 8.00 mL/(min·g). Also contributing to this decision was the significant amount of polymer formation that would occur downstream of the quartz tube reactor, indicating that an excess of acetylene was being used. It was decided that a 0.250 g mass of AAO template would be the basis of comparison for each reaction condition. The HF purification step

Table 5.2
Procedure and naming scheme applied to the chemical vapor deposition operating conditions.

		C_2H_2 Flow Rate / AAO Mass Ratio (mL/min· g)		
		4.00	**6.00**	**8.00**
Reaction Temperature (°C)	**450**	**Condition 1**	**Condition 4**	**Condition 7**
	550	**Condition 2**	**Condition 5**	**Condition 8**
	650	**Condition 3**	**Condition 6**	**Condition 9**

would also remain constant for each condition with an acid concentration of 23 wt.% and a mixing time of 30 hours. Table 5.2 on the preceding page outlines the planned structure of the optimization procedure.

5.3 Characterization Techniques

Several characterization techniques were applied to the synthesized MWCNTs, both before and after the impregnation of transition metal catalysts. These methods were used to define the morphology and structure of the MWCNTs, as well as to explain the exhibited behavior of the catalyst.

Spectroscopy techniques were among the different methods used to examine the MWCNTs and NiMo/MWCNT catalysts. The quality, purity, and approximate outer diameters of the pure MWCNTs were determined by scanning electron microscopy (SEM). Using SEM on a sample produces high quality images on a nanometer scale. It creates these images by focusing a high-energy beam of electrons onto the sample and detecting interactions that occur at the sample surface. These images determine the surface characteristics of the MWCNTs such as their morphology, outer diameter, and purification from amorphous carbon and alumina contaminates. The best method of determining the inner diameter of the MWCNTs, as well as the wall thickness of the tubes, is via transmission electron microscopy (TEM). In this method, electrons are transmitted through an ultra-thin sample and interact with the sample as they pass through. As they pass out the other side, they

produce an image possessing a degree of transparency, allowing the inner pore diameter and wall thickness of the MWCNTs to be measured. In addition, after metal has been loaded on the MWCNT surface, the distribution and size of the metal particles can be observed both along the outer and inner surface of the tubes. The quality and morphology of the MWCNTs can also be determined analytically by Raman spectroscopy. This method studies the scattering of monochromatic light produced by a sample to determine the vibrational, rotational, and low frequency modes of the sample. The change in the scattering intensity due to changing the wavelength of the light determines the types of compounds present in the sample, particularly the metal oxide particles on the MWCNT surface. The distribution of the metal oxide particles between various types of MWCNTs can be compared based on the analyzed intensity of the light scattering. Another spectrometric technique that will be applied to the impregnated MWCNTs will be inductively coupled plasma mass spectrometry (ICP-MS). This analysis method works by applying ICP to produce ions from the sample and MS to separate and detect the ions. This technique can be used to determine the exact metal content of each catalyst sample, as there is usually a significant difference between the intended and actual percent metal content. The final spectroscopy technique, diffuse reflectance infrared Fourier transform (DRIFT) spectroscopy, collects spectra based on measuring the coherence of the infrared region of a radiative source. The specific purpose it served for this project

was to analyze the functional groups that were created on the surface of the MWCNTs treated with nitric acid.

In addition to the previously mentioned electron emission techniques, there are several adsorption/desorption techniques that can be applied to characterize the behavior of the MWCNTs and their resulting catalysts. BET analysis is based on the theory established by Brunauer, Emmett, and Teller for predicting the surface characteristics of a substance based on the size of the adsorption monolayer of an adsorbate (Gregg and Sing, 1967). Typically, it is nitrogen adsorption that is analyzed under liquid nitrogen conditions. Based on the amount of N_2 that is physically adsorbed by the MWCNTs, and on theoretical equations, the specific surface area (m^2/g), average pore diameter (nm), and pore volume (cm^3/g) of the nanotubes can be predicted. In contrast to applying physisorption of nitrogen to analyze the behavior of the catalyst, chemisorption of carbon monoxide can also be applied to the impregnated MWCNTs. Monitoring the amount of CO adsorbed by a sample can be used to show the degree that the metal catalyst particles are distributed on the MWCNT surface, and therefore that number of exposed active sites on the catalyst surface. Temperature programmed reduction (TPR) is another adsorption method that can be used for catalytic analysis. In this case, a sample is heated in the presence of hydrogen, reducing the oxidation state of the catalyst metals. The temperature at which the greatest rate of H_2 consumption occurs at reflects the optimum reduction temperature for the catalyst. This can reflect both the degree of dispersion of metals

on the support surface, as well as the strength of the surface interactions between the support and the catalyst metals.

The third and final category of characterization pertains to the pyrolysis of the MWCNT and NiMo/MWCNT catalyst samples. Thermogravimetric analysis (TGA) involves the controlled heating of a sample in the presence of air flow to determine the thermal stability of the sample.

5.3.1 Scanning Electron Microscopy

Scanning electron microscopy, located at the Syncrude Canada Ltd. Edmonton Research Centre, was used to analyze both the diameter of the AAO pore channels as well as the quality of the CNT product. The sample images were created and collected using a Hitachi S3400 SEM. Both substances were examined by mounting the samples onto aluminum slabs using carbon paint. A gold coating was then applied by vacuum sputtering to improve secondary electron signals and reduce charging.

5.3.2 Transmission Electron Microscopy

Transmission electron microscopy, located at the University of New Brunswick, allowed for the MWCNT dimensions of wall thickness and inner diameter to be measured, as well as for the number of open-ended nanotubes to be observed. The TEM images were retrieved using a 200 keV JEOL 2000FX STEM. Each sample began its preparation by undergoing sonification in ethanol for 10 minutes.

The sample solution was then placed on a 200 mesh Cu grid coated with a porous carbon film and allowed to dry overnight. The MWCNTs were viewed over the holes of the carbon film to better interpret the MWCNT structure. The sample images ranged from 20k to 500k times magnification.

5.3.3 Thermogravimetry

To determine the thermal stability of the synthesized MWCNTs, as well as the coking effects on spent NiMo/MWCNT catalysts, thermogravimetric (TGA) analysis was performed using 5 mg samples of each MWCNT grade produced. Using a Perkin-Elmer (Pyris Diamond) TGA instrument, data was collected at 0.5s intervals as the sample was heated to 850ºC at a rate of 10ºC/min under air flow at 100 mL/min.

5.3.4 N_2 Adsorption/Desorption

The Brunauer-Emmett-Teller (BET) surface area, pore volume, and pore diameter of the CNT samples were determined by analyzing the adsorption and desorption of N_2 at 77K with a Micromeritics 2000 ASAP analyzer. A 0.1 gram quantity of each sample was degassed for 2 hours under vacuum conditions and a temperature of 200ºC. The desired physical characteristics of each sample were determined using the procedure developed by BET (Gregg and Sing, 1967).

5.3.5 DRIFT Spectroscopy

Diffuse reflectance infrared Fourier transform (DRIFT) spectroscopy was performed with a Perkin-Elmer Spectrum GX instrument containing a DTGS detector and a KBr beam splitter. A 30 mg amount of each sample was placed inside a Spectrotech diffuse reflectance *in situ* cell having ZnSe windows and a mounted thermocouple capable of measuring the sample surface temperature. The average spectrum for each run was found after 64 scans with a nominal 4 cm^{-1} resolution.

5.3.6 CO Chemisorption

The carbon monoxide (CO) uptake of the NiMo/MWCNT catalysts was measured using the Micromeritics ASAP 2000 instrument. Before the chemisorption measurement, a 200 mg sample was dehydrated at 200 °C for 2 h and then evacuated until the static pressure remained less than 6.6×10^{-4} Pa. Pulses of CO were passed over the sample to measure the total gas uptake at 35°C.

5.3.7 Inductively Coupled Plasma Mass Spectroscopy

The elemental compositions of both the fresh and spent NiMo/MWCNT catalysts were analyzed with a PerkinElmer ELAN 5000 ICP-MS instrument. This analysis method works by applying inductively coupled plasma (ICP) to produce ions from the sample and mass spectroscopy (MS) to separate and detect the ions. The content of both the catalyst metals were determined both before and after they were screened in a CLGO hydrotreating application. The degree of metal leaching could

then be interpreted from these results and the overall effectiveness of the nitric acid functionalization procedure would be quantified. In addition to the Ni and Mo content of the samples, the aluminum content of the catalysts was also examined to quantify the effectiveness of the HF and HNO_3 acid treatment procedures.

5.3.8 Raman Spectroscopy

The vibration modes for the varying grades of MWCNTs were measured with wavelengths ranging from 100 to 3200 cm^{-1}. A Renishaw Raman microscope (Spectra-Physics 127 model), located at the Syncrude Canada Ltd. Edmonton Research Centre, was used possessing a He/Ne laser source. The prime intense bands that were targeted in this analysis were the D-band (located from 1330 to 1350 cm^{-1}), the G-band (located from 1580 to 1600 cm^{-1}), and the 2D-band (located from 2660 to 2700 cm^{-1}). These bands correspond to the fundamental vibrational modes of disordered graphite (Hardwick et al., 2006). It is from these bands that the quality and morphology of the MWCNTs can be interpreted.

5.3.9 H_2 Temperature Programmed Reduction

The reducibility of each prepared NiMo/MWCNT catalysts was analyzed by temperature programmed reduction (TPR) with H_2 using a ChemBET-3000 instrument. Approximately 200 mg of each catalyst was loaded into a quartz U-tube and heated to 200°C under argon flow for 2 h to remove water vapor and other volatile species from the catalyst surfaces. The TPR analysis was then performed

using a 3% volumetric H_2 gas mixture with the remainder consisting of N_2. The gas mixture was flowed through the system at a rate of 30 mL/min while the system was heated at a controlled rate of 10°C/min towards a final temperature of 850°C. The degree of H_2 consumption during each run was measured by a thermal conductivity detector.

5.4 Hydrotreating of CLGO

Once the MWCNTs were purified and functionalized, they were loaded with the catalyst metals by an incipient wetness co-impregnation method (Cruz et al., 2002; Eswaramoorthi et al., 2008). In this method, an aqueous solution was prepared containing the desired amounts of each catalyst metal intended to be loaded on the support surface. For the addition of molybdenum catalyst metal, the desired amount of ammonium heptamolybdate tetrahydrate ($[NH_4]_6Mo_7O_{24}\cdot 4H_2O$) was dissolved in the solution. For the loading of the nickel catalyst promoter, the appropriate amount of nickel nitrate hexahydrate ($Ni[NO_3]_2\cdot 6H_2O$) was applied to the solution composition. The amount of metal salt solution prepared was made approximately equal to the total pore volume of the dried MWCNT sample (~0.6 mL/g), ensuring the majority of the metal would be loaded along the interior walls of the tubes (Abbaslou et al., 2009). After the solution was well mixed with the MWCNTs and became fully adsorbed by the solid, the catalyst was dried at 120°C for 4 hours before undergoing calcination at 450°C for 5 hours under atmospheric conditions. The exact distribution of metal particles between the interior and exterior of the MWCNT walls depends

significantly on the curvature of the graphite walls, which affect the electron density of the electron-deficient interior and the electron-enriched exterior (Abbaslou et al., 2009; Menon et al., 2000). These π–electron distribution effects for the MWCNTs were not examined in this project.

After impregnation, the catalyst must be converted from its powder-based form into catalyst pellets so that it can be applied in a trickle bed reactor. The particles for such a process typically range in size from 20 to 25 mesh (0.85 to 0.71 mm) and can be achieved through the application of approximately 32 MPa of pressure in a pelletizer unit. It is not entirely necessary to add a binding agent to the catalyst before pelletization, as the sulfidation of the catalyst pellets provides sufficient hardening of the catalyst to avoid particle crumbling under high hydrotreating pressures. However, the addition of an often-used binding agent, such as coal tar, wood tar, or lignosulfonic acids, could be beneficial to the longevity of the catalyst pellets and their performance. The effect of these binding agents was determined to be beyond the scope of this project.

Shown in Figure 5.4 on the following page is the schematic diagram illustrating the process used to test the hydrotreating of CLGO using packed catalyst beds consisting of varying MWCNT-supports. The system consists of the following parts: liquid and gas feed sections, a high-pressure/high-temperature reactor simulating industrial hydrotreating conditions, a temperature-controlled furnace, a water scrubber capable of removing ammonium sulfide from the product stream, a

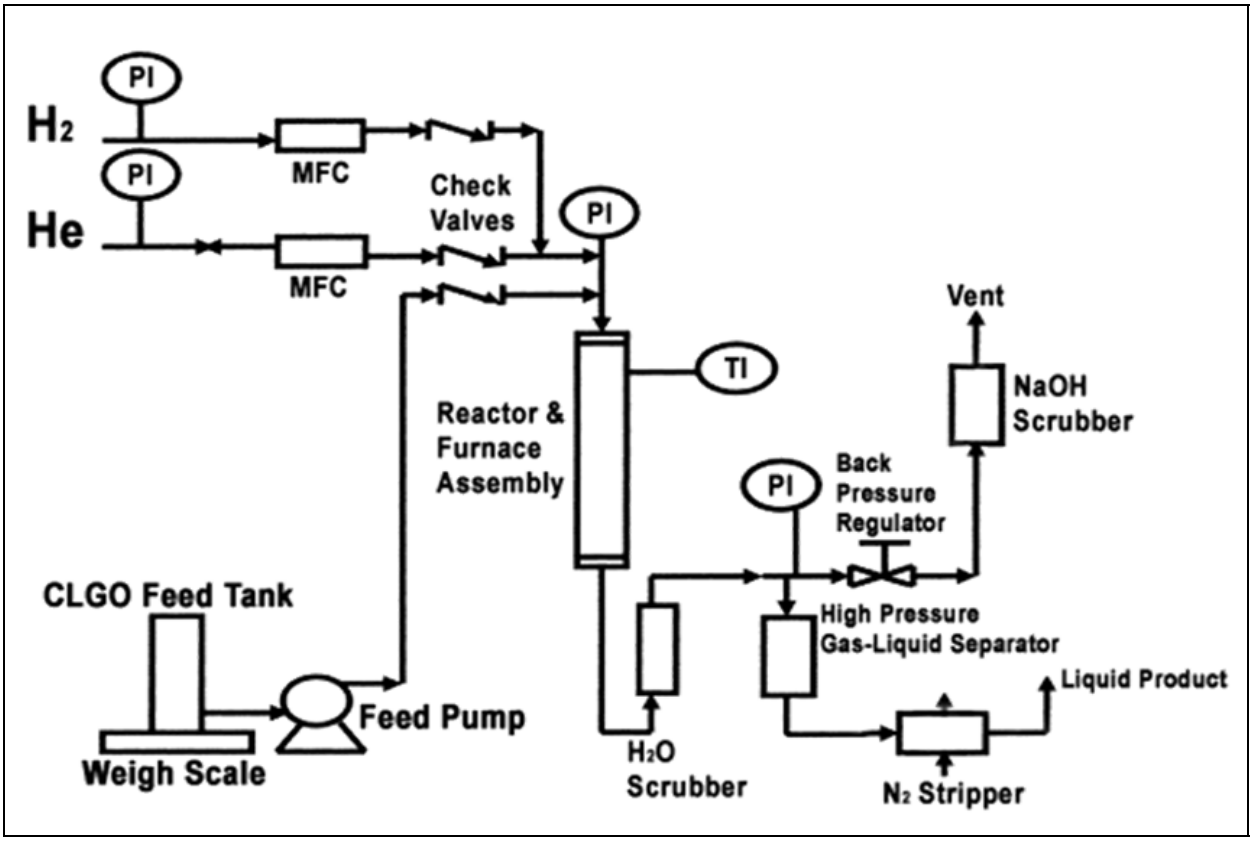

Figure 5.4: Illustration of the trickle bed reactor setup applied for hydrotreating of CLGO (Ferdous et al., 2004).

gas-liquid separator performing at high pressures, and a back pressure regulator for controlling the system pressure. For the initial experimentation, the parameters of the process were kept constant to examine the effects of the changing pore diameters and specific surface area of the MWCNT-support on the catalyst activity. Similar to this, the parameters remained constant for determining to optimum Ni and Mo loadings for the MWCNT support. The catalyst pellets (~5 mL) were first loaded into the reactor bed in a dilute mixture of 90 mesh silicon carbide. Placed above and below the bed were layers of 3mm diameters quartz beads and 16-60 mesh silicon carbide. Before commencing the reaction, the catalyst metals had to first be converted from the oxide phase to the sulfide phase, referred to as *sulfidation*. This was achieved by pumping a 2.8 vol.% butanethiol solution in an insulating oil solvent at 7 mL/h. Hydrogen gas was then flowed through the system at this time at a 600:1 volumetric ratio with the dilute sulfiding solution. The reactor was run under the conditions of 8.8 MPa pressure and 193°C temperature for 24 hours. After this time, the temperature was increased to 343°C and the reaction is continued for another 24 hours. After the sulfidation of the catalyst bed was completed, the sulfiding solution feed was replaced with a CLGO feed to begin the hydrotreating reaction. The CLGO feed was pumped through the reactor at a rate of 10 mL/h (9.0 g/h), giving a liquid hourly space velocity (LHSV) of 2.00 h^{-1} for volumetric comparisons and a weight hourly space velocity (WHSV) of 4.50 h^{-1} for weight-based comparisons. The reactor pressure and the volumetric ratio of hydrogen gas feed were kept at the same settings as they were for

the sulfidation procedure. At a reactor temperature of 370°C, the catalyst undergoes a precoking period of 3 to 5 days to allow the reactor setup to reach steady-state behavior as coke is deposited on the catalyst surface. During this period, the product samples are collected every 12 hours. After the precoking period, the hydrotreating process was carried out for 2 days for each of two reaction temperatures: 350°C and 330°C. As during the precoking phase, product samples were taken every 12 hours. Each collected product sample had its composition compared with that of the CLGO feed to determine the HDS and HDN activities exhibited by the catalyst for each specific sample. Before such analysis was performed, each collected sample underwent a 2 hour stripping process under continuous N_2 flow to remove any remaining dissolved NH_3 and H_2S within the liquid not previously removed by the water scrubber.

5.4.1 N and S Conversion

The concentrations of both of these elements were determined using an Antek 9000 NS analyzer, located within the Department of Chemical Engineering at the University of Saskatchewan. The nitrogen content of the liquid product was determined by the combustion-chemiluminence technique of the ASTM D4629 method. The sulfur content was measured using the combustion-fluorescence technique of the ASTM 5463 method. The instrumental error for both N and S analysis was found to be approximately ±3%, based on analyzing standard solutions of known composition.

5.4.2 MWCNT Pore Diameter Optimization

For determining the optimum pore diameter for a MWCNT catalyst support used for CLGO hydrotreating, it was decided to prepare four types of NiMo/MWCNT catalysts with varied pore diameters. From the AAO pore channel variation, MWCNTs with inner diameters ranging from 60 to 75 nm were synthesized. This led to the decision to prepare the four catalysts with approximate CNT inner diameters 60, 65, 70, and 75 nm and to name them *cat-60*, *cat-65*, *cat-70*, and *cat-75*, respectively. The intended Ni and Mo loadings for these catalysts was consistent with most commercial NiMo/γ-Al_2O_3 catalysts at 2.5 and 13.0 wt.%, respectively. The criterion for screening these catalysts were with 2.00 g loadings and with a 5 day precoking period. The remaining parameters were already addressed in section 5.4.

5.4.3 Boiling Point Distribution

To determine the boiling point distribution of the liquid feeds and products, a simulated distillation technique was used. The simulated distillation of the CLGO feed and product liquids was performed using a Varian Model CP 3800 Gas Chromatograph coupled with a Varian CP 8400 Autosampler. The results of the chromatography were interpreted through a Flame Ionization Detector (FID). In addition to the determined initial boiling point (IBP) and final boiling point (FBP) of each sample, the percentile boiling points were determined for each sample at 2% intervals, giving a total of 51 points. This analysis was performed for all grades of

CLGO feedstock that were used during the course of the project, as well as for all the product liquids from the MWCNT pore diameter optimization study.

5.4.4 Metal Loading Optimization

For finding the ideal metal loading of Ni and Mo for the optimum MWCNT catalyst support, the plan was to determine each loading in sequence. First, the optimum Mo loading would be found while keeping the Ni loading constant. The most suitable Ni loading would then be found in conjunction with the determined optimum Mo loading. Mo loadings of 13.0, 19.5, and 26.0 wt.% were tested with a Ni loading of 2.5 wt.% and labeled *cat-A*, c*at-B*, and *cat-C*, respectively. After the optimum Mo loading of 19.5 wt.% was found, Ni loadings of 5.0 and 7.5 wt.% were found in conjunction with it and labeled *cat-D* and *cat-E*, respectively. All pertinent characteristics of the MWCNT-supported catalysts screened in sections 5.4.2 and 5.4.4 can be found in Table 5.3. Loading weights of 2.00 g were used for screening these catalysts. From the results of the MWCNT pore optimization study (section 5.4.2), it was decided that lowering the precoking period to 3 days would be suffice compared to a 5 day period. Further details of the parameter settings were discussed in section 5.4.

5.4.5 HDS and HDN Kinetics Study

The details of the kinetic study plan that was implemented are shown in Table 5.4. The analysis plan was carried out for determined optimum NiMo/MWCNT

Table 5.3
Characteristics of the prepared NiMo/MWCNT catalysts for optimization of the MWCNT inner diameter and catalyst metal loadings.

Catalyst I.D.	Targeted TEM Inner Diameter (nm)	Targeted Ni Weight Loading (wt.%)	Targeted Mo Weight Loading (wt.%)
Cat-60	**60**	**2.5**	**13.0**
Cat-65	**65**	**2.5**	**13.0**
Cat-70	**70**	**2.5**	**13.0**
Cat-75	**75**	**2.5**	**13.0**
Cat-A	**65***	**2.5**	**13.0**
Cat-B	**65***	**2.5**	**19.5***
Cat-C	**65***	**2.5***	**26.0**
Cat-D	**65***	**5.0**	**19.5***
Cat-E	**65***	**7.5**	**19.5***

***Later found from CLGO screening to be the optimum conditions.**

Table 5.4
Kinetic study plan for determining the effect of temperature, LHSV, pressure, and H_2/CLGO ratio on the HDS and HDN activity of the optimum NiMo/MWCNT catalyst.

Elapsed Run Time (days)	Temperature (°C)	LHSV (h^{-1})	Pressure (MPa)	H_2/CLGO Ratio (mL/mL)
1-3	----------PRECOKING----------			
4-5	370	1.5	8.8	600
6-7	370	2.5	8.8	600
8-9	370	2.0	8.8	600
10-11	350	1.5	8.8	600
12-13	350	2.5	8.8	600
14-15	350	2.0	8.8	600
16-17	330	1.5	8.8	600
18-19	330	2.5	8.8	600
20-21	330	2.0	8.8	600
22-23	330	2.0	8.8	450
24-25	330	2.0	8.8	750
26-27	330	2.0	6.6	600
28-29	330	2.0	7.7	600
30-31	330	2.0	8.8	600
32-33	330	2.0	9.9	600
34-35	330	2.0	11.0	600

catalyst. The study was divided into three essential phases: 1) The principle kinetic modeling regarding the variation of the temperature and LHSV parameters; 2) A qualitative study of H_2/CLGO ratio (***G/L***) variation on the HDS and HDN reaction rates; and 3) Analyzing the relation of system pressure variation with the reaction rate proportionality constant ($\boldsymbol{k_A}$). After an initial 3 day precoking period, the kinetic data was collected by testing three different reaction temperatures (370, 350, and 330°C) along with three different space velocities (1.5, 2.0, and 2.5 h^{-1}) over an 18 day span. The H_2/CLGO volumetric ratio was then varied (450, 600, 750 mL/mL) over a period of 6 days to determine the qualitative effect this had on the HDS and HDN reaction rates. Finally, five system pressures ranging from 6.6 to 11.0 MPa were studied over a 10 day span to analyze the exponential relation between system pressure and $\boldsymbol{k_A}$. Three 12-hour samples were collected for each of the studied parameter conditions set for the hydrotreating reactor. The kinetic modeling was completed by applying 4th order Runge-Kutta numerical solutions in conjunction with a non-linear regression Microsoft Excel solver platform. The mathematical models used to interpret the results of this kinetic study were previously described in section 2.2. A statistical analysis was performed on each of the function parameters to test if they each contributed significantly to the accuracy of the models.

5.4.6 Catalyst Stability Study

In order to determine the true effectiveness of a NiMo/MWCNT catalyst compared to a commercial NiMoP/γ-Al_2O_3 catalyst, a long term study must be

performed under maintained reaction conditions. To monitor how catalyst deactivation from coking affected the HDS and HDN activities of the NiMo/MWCNT catalyst over the long term, a performance test was carried out over the span of a month. Product samples were collected at 24 hour intervals for 28 days at the following reaction conditions: 370°C reactor temperature, 8.8 MPa system pressure, 600 mL/mL H_2/CLGO ratio, 2.0 h^{-1} LHSV, and a 2.00 g (~5.0 mL) catalyst loading. The same test was performed for a NiMoP/γ-Al_2O_3 catalyst under identical conditions and with an equivalent 5.0 mL volumetric loading. Given that the commercial γ–alumina catalyst was twice as dense as the MWCNT catalyst, this corresponds to an approximate 4 g mass loading for the commercial catalyst study. While typical industrial scale studies of long-term catalyst performance are done over several months, the time constraints of this study only allowed for a small outlook of each catalyst's longevity.

6 RESULTS AND DISCUSSION

This chapter describes the results related to the research objectives of this project: 1) Variation of multi-walled carbon nanotube inner diameters; 2) The effect of MWCNT pore diameter variation on catalyst performance; 3) Variation of CVD parameters; 4) Metal loading optimization and characterization; 5) A kinetics study of HDS/HDN for the optimum NiMo/MWCNT catalyst; and 6) A stability study for the optimum NiMo/CNT catalyst. Detailed descriptions and interpretations have been included with the figures and tables of the numerical results. The ultimate objective is to explain how the optimum NiMo/MWCNT catalyst was found, what characteristics lead to it being determined as the optimum catalyst, and how to best predict the activity and longevity of the catalyst.

6.1 Variation of MWCNT Pore Diameter

The AAO templates were first viewed by SEM before being applied to MWCNT synthesis to determine how the anodizing conditions influenced their pore channel diameter. After viewing the quality of the produced carbon nanotubes via TEM analysis, the MWCNTs were characterized through several analytical techniques. These techniques were N_2 adsorption/desorption, Raman spectroscopy, thermogravimetric analysis, and DRIFT spectroscopy.

6.1.1 SEM Images of AAO Templates and Purified MWCNTs

Table 6.1 shows the changing pore structures observed from the SEM analysis as the oxalic acid concentration and energy potential were adjusted. Common across each AAO template was the irregular hexagonal arrangement of the pore channels. Although the channels were observed to not be ideally ordered, the amount of wall cracking and pore merging appeared to be minimal at the surface of the templates. As seen in Table 6.2, the diameter of the pores consistently increased as the electrolyte concentration and maximum cell potential were increased up until condition 9. With the exception of condition 9, the diameter of the pore channels and the inter-pore spacing remained relatively uniform within each run. Any deviation in the size of the pores was within ±5 nm. Comparisons between experimental runs performed under identical anodizing conditions confirmed the reproducibility of these results. For condition 9, irregularities and inconsistencies began to show in the wall thickness of the amorphous AAO. This caused the diameter of the pore channels to vary considerably from 100 nm to as low as 40 nm. The reason for these results obtained at 60.0 V and 0.50 M oxalic acid was due to the result of the anode's passivity being compromised by the application of more extreme anodizing conditions. Figure 6.1 shows an SEM image of the purified CNTs confirming the straight morphology of the nanotubes and the absence of any carbonaceous byproducts. Additional SEM images of the AAO templates can be found in Appendix A, showing both the reproducibility of the procedure and the results of alternative anodizing conditions.

Table 6.1
Images obtained from SEM analysis of AAO pore channels at different anodizing conditions.

		Oxalic Acid Concentration (mol/L)		
		0.30	**0.40**	**0.50**
Maximum Anodizing Voltage (V)	**40**	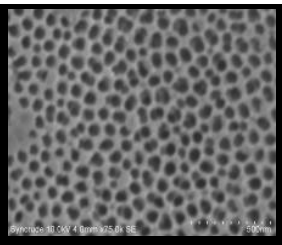	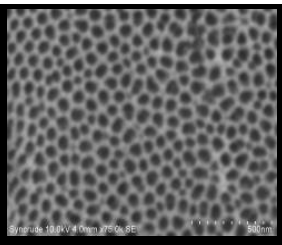	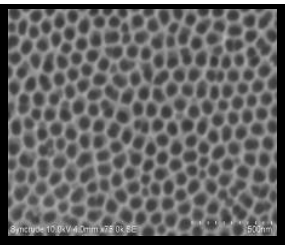
	50	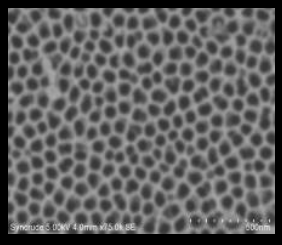	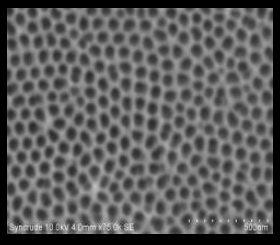	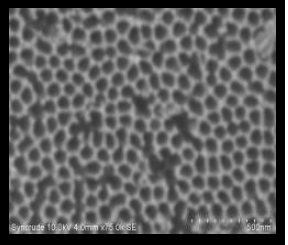
	60	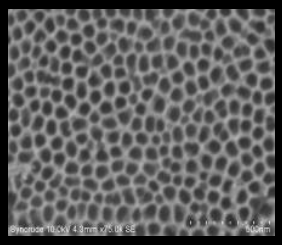	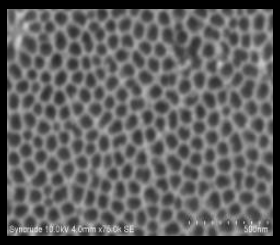	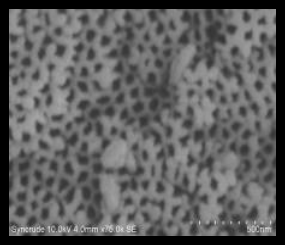

Table 6.2
AAO pore channel diameters observed from SEM analysis at different anodizing conditions.

		Oxalic Acid Concentration (mol/L)		
		0.30	**0.40**	**0.50**
Maximum Anodizing Voltage (V)	**40**	**65±5 nm**	**75±5 nm**	**85±5 nm**
	50	**75±5 nm**	**85±5 nm**	**85±5 nm**
	60	**85±5 nm**	**95±5 nm**	**70±30 nm**

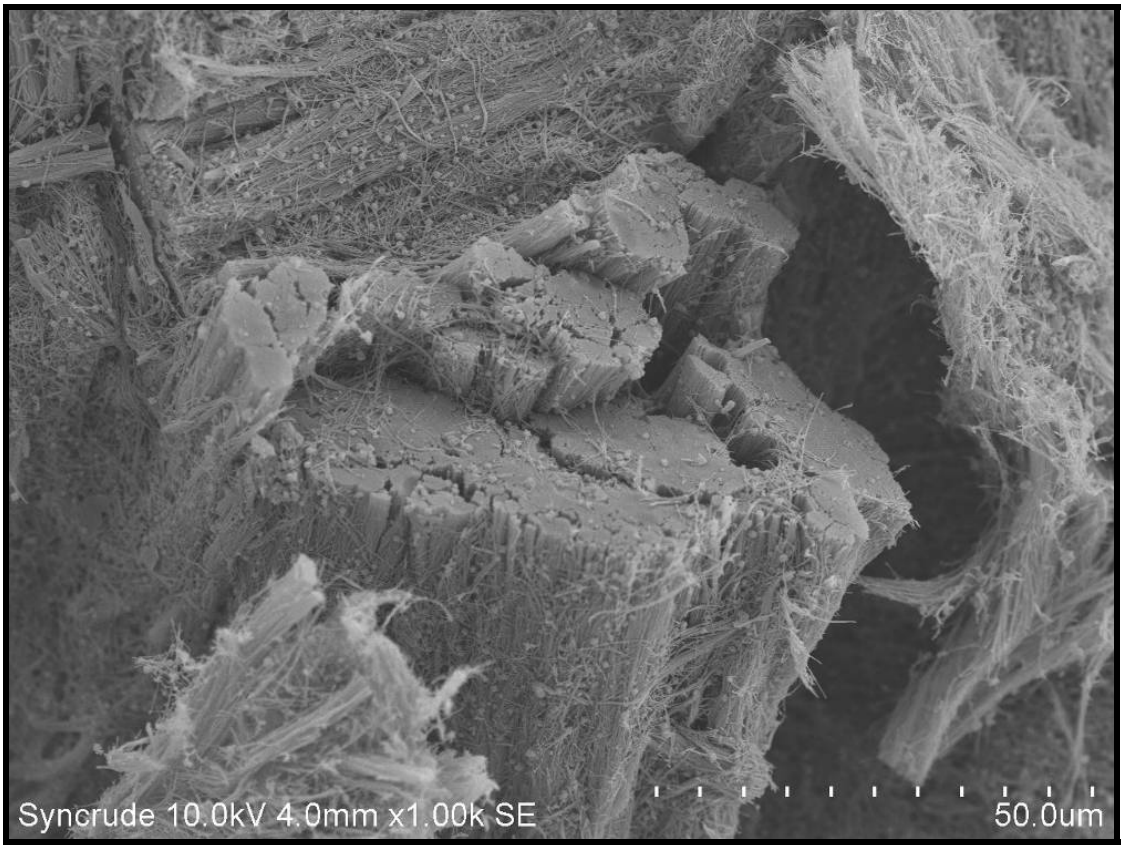

Figure 6.1: SEM image of purified MWCNTs synthesized using a condition 1 AAO template.

6.1.2 TEM Images of Functionalized MWCNTs

TEM was performed to analyze the microstructure of the CNT samples. Typical sample images can be seen in Figure 6.2. Digital micrograph software (version 3.6.5, Gatan Inc.) was used to measure the inner diameter and wall thickness for each set of CNTs. An average of ten measurements was used to determine the values for each of these two dimensions. The results of this analysis can be seen in Table 6.3. With the exception of condition 6, the average outer diameters of the CNTs corresponded with the range of AAO pore diameters that were found by SEM analysis. The typical length of the nanotubes extended to several micrometers in length. The thickness of the carbon walls of the CNTs remained at a relatively constant value of 10 nm. The significant thickness of the walls indicated that the synthesized CNTs had a multi-walled morphology. The exception to this trend occurred with condition 9, where walls as thick as only 8 nm were measured. It can only be assumed that these thinner walls are the result of the inconsistent AAO pore channels and pore intervals that were seen at the surface of the condition 9 templates. The majority of the CNTs were shown to be quite linear, with many of the nanotubes being close-ended. Although several images showed evidence of nanotubes with open ends (Figure 6.2c), they appeared to be in the minority. Figure 6.2d shows one of several examples of Y-branching that was evident in some of the TEM images. This is thought to occur as the CNTs grow beyond the surface of the AAO film. It

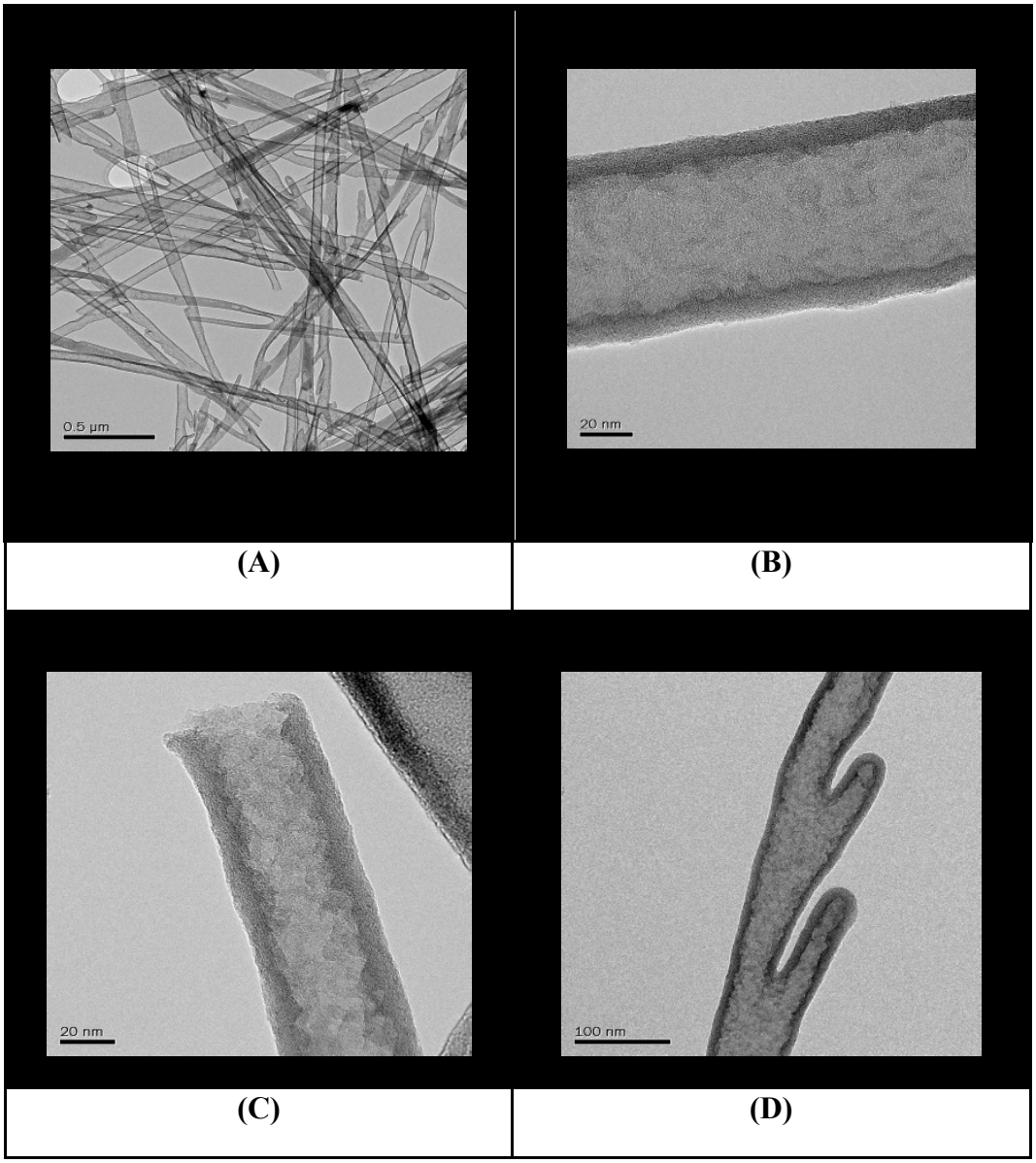

Figure 6.2: Sample TEM images of HNO_3 functionalized MWCNTs: (A) ×20k magnification, condition 2; (B) ×300k magnification, condition 2; (C) open-ended nanotube, ×300k magnification, condition 1; (D) Y-branched nanotube, ×100k magnification, condition 6.

Table 6.3
Dimensions from TEM analysis of CNTs from AAO at different anodizing conditions.

1) Inner diameter, nm 2) Wall thickness, nm 3) Outer diameter, nm		Oxalic Acid Concentration (mol/L)		
		0.30	0.40	0.50
Maximum Anodizing Voltage (V)	40	1) 58 2) 10 3) 68	1) 64 2) 10 3) 74	1) 68 2) 10 3) 78
	50	1) 63 2) 10 3) 73	1) 75 2) 10 3) 85	1) 74 2) 10 3) 84
	60	1) 69 2) 10 3) 79	1) 70 2) 10 3) 80	1) 79 2) 8 3) 87

was noted that the Y-branched nanotubes appeared to increase in number as the pore channel diameters increased within the AAO templates. This creates a challenge of finding the MWCNT diameter that balances the positive effect of pore size and the negative effect of Y-branching.

6.1.3 Surface Characterization by N_2 Adsorption/Desorption

Shown in Figure 6.3 is the isotherm that was exhibited by the condition 4 CNTs during the adsorption and desorption of N_2 at 77 K. The isotherm is consistent with that of a Type II isotherm as defined by Brunauer, Deming, Deming, & Teller classification. This isotherm classification is synonymous with marked increases in adsorption at high relative pressures between an adsorbate and macroporous materials (>50 nm). All other grades of synthesized CNTs exhibited similar adsorption profiles. Table 6.4 shows the results for surface area, total pore volume, and average pore diameter as determined for all nine anodization conditions. The surface area (***A***) was found by implementing the BET method, while the total pore volume (***V***) was determined by the single point method at a relative pressure of ~0.98 and for pore diameters less than ~110 nm. The average pore diameter (***d***) was then determined by assuming perfectly cylindrical pore spaces (i.e. $\boldsymbol{d} = 4\boldsymbol{V}/\boldsymbol{A}$), a reasonable assumption for the nanotubes produced. Each reported value represents the average taken between two experimental runs of each CNT synthesis condition. The reproducibility of the BET analysis between each run was reasonably high, with the error associated with each parameter being held within ±8 m^2/g, ±0.018 cc/g, and ±0.4 nm for the

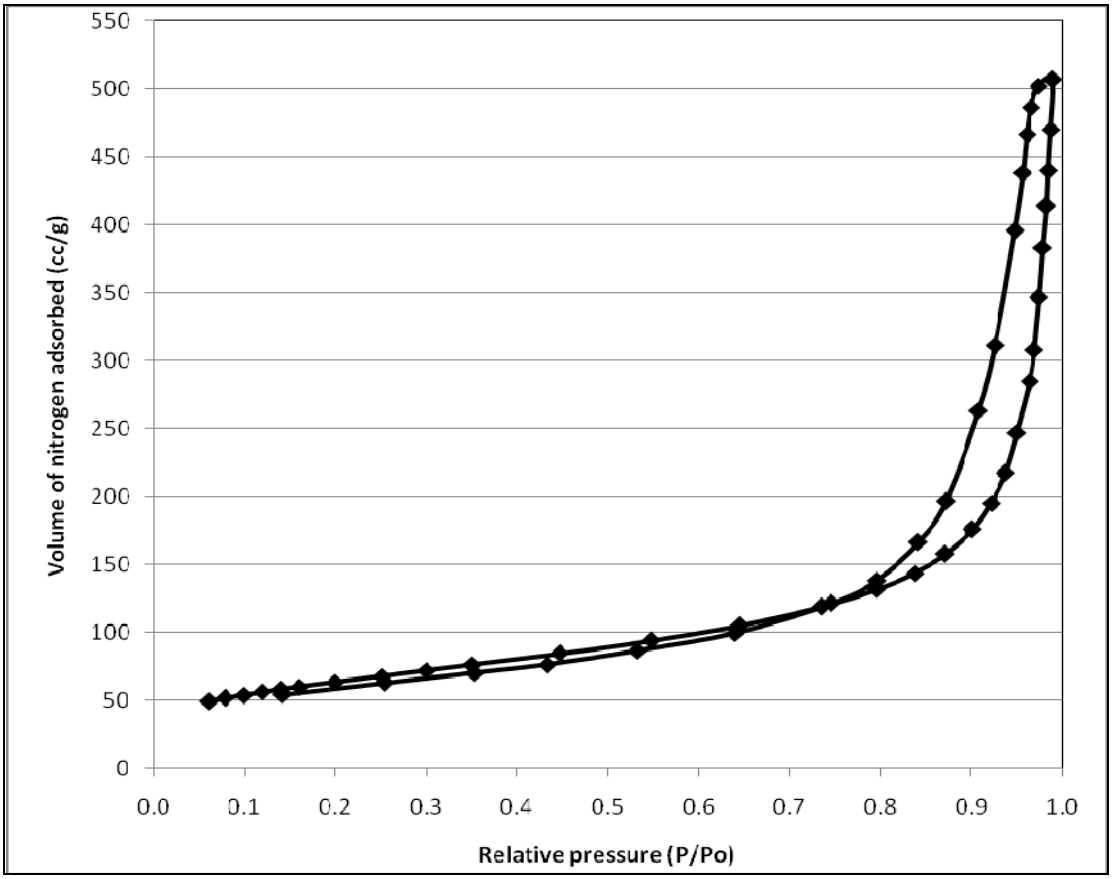

Figure 6.3: Nitrogen adsorption/desorption isotherm exhibited for condition 4 CNTs and similarly for all HNO_3 functionalized CNTs.

Table 6.4
BET parameters as determined by N_2 adsorption/desorption at 77 K.

1) BET surface area, m^2/g 2) Total pore volume, cc/g 3) Average pore diameter, nm		Oxalic Acid Concentration (mol/L)		
		0.30	0.40	0.50
Maximum Anodizing Voltage (V)	40	1) 192 2) 0.483 3) 10.1	1) 229 2) 0.658 3) 11.5	1) 215 2) 0.572 3) 10.7
	50	1) 206 2) 0.492 3) 9.6	1) 226 2) 0.614 3) 10.9	1) 214 2) 0.549 3) 10.3
	60	1) 206 2) 0.550 3) 10.7	1) 208 2) 0.570 3) 11.0	1) 218 2) 0.567 3) 10.4

reported BET surface area, total pore volume, and average pore diameter, respectively.

While no discernable trend could be found relating the anodizing conditions to the determined BET surface areas and pore volumes, it is worth noting that the pore diameter estimations from the N_2 adsorption/desorption procedure were far less than those observed from the TEM images. The most likely explanation for this discrepancy is that the majority of the CNTs remained close-ended after HNO_3 treatment, meaning the majority of the cylindrical pore spaces were left inaccessible. This would have a detrimental effect on the accessible surface area of the CNTs and, to a greater extent, their total pore volume. This would make the determined average pore diameters significantly smaller than observed.

The results from Table 6.4 show that the CNTs synthesized from condition 4 AAO templates produced the highest values for all three surface parameters. Possessing the highest values for each of these measurements would make the CNTs synthesized under these conditions the most ideal for application as a heterogeneous catalyst support. To explain why the CNTs produced from condition 4 AAO templates produced the best analytical surface parameters, it is hypothesized that there is a greater probability of Y-branching occurring as the diameter of the AAO pore channels increases. Because few open-ended Y-branched CNTs were observed, it can be seen that the Y-branching would significantly lower the total pore volume and average pore diameter of the CNTs. The branches of the Y-branched CNTs were

observed to be approximately half the diameter of their preceding nanotube. Based on the observed trend from CNT-AAO synthesis of large diameter CNTs being naturally open-ended (Kyotani et al., 1999; Sui et al., 2002) and small diameter CNTs being naturally close-ended (Kim et al, 2003; Yang et al., 2003), it is predicted that the Y-branches would naturally be close-ended. It is concluded that the parameters applied for condition 4 AAO templates gave pore channels that provided an optimum balance for the produced CNTs between the positive effect of large pore diameters and the negative effect of Y-branching. Smaller AAO pore channels would then result in smaller CNT pore diameters, while larger AAO pore channels would produce more detrimental Y-branched CNTs.

6.1.4 Raman Spectroscopy

The vibration characteristics for the numerous grades of synthesized MWCNTs were analyzed by Raman spectroscopy to determine their structure and quality. A sampling of these spectra can be found in Figure 6.4. It was found that two prime intense bands were common amongst each spectrum, as they corresponded to the fundamental vibrational modes of graphitic materials. The band that occurs between wavelengths of 1580 to 1600 cm^{-1} corresponds to the stretching mode of sp^2 graphite bonds and is commonly referred to as the G-band (Eklund et al., 1995; Lefrant, 2002; Dresselhaus et al., 2005; Delhaes et al., 2006). The band appearing at wavelengths between 1330 and 1350 cm^{-1} is referred to as the D-band and is interpreted as the extent of imperfections and disorder in the graphite sheets (Eklund

et al., 1995; Lefrant, 2002; Dresselhaus et al., 2005; Delhaes et al., 2006). The ratio of the intensity of these bands ($R_I = I_D/I_G$) is often used to represent the quality of the MWCNT morphology.

As shown in Figure 6.4, the MWCNTs synthesized from AAO templates were found to have relatively low R_I values (average value of 0.97) for each grade of MWCNTs. Comparatively, a commercial grade of MWCNTs having smaller pore diameters (approximately 10 nm) and twisted morphologies was found to have a much higher R_I value of 1.57. It can be concluded from these spectra that the large pore diameter MWCNTs have a high level of graphitization with less amorphous carbon than conventional MWCNTs. Varying the MWCNT pore diameters was not found to affect the structural integrity (i.e. R_I values) of the graphite layers.

6.1.5 Thermogravimetric Analysis

After performing TG experimentation on all nine grades of the functionalized CNTs, each one exhibited almost identical profiles for both percentage weight loss and rate of percentage weight loss versus system temperature. A sampling of these profiles can be seen in Figure 6.5. For each experimental run, the initial oxidizing or decomposition temperature of the CNTs from their exposure to air flow was found to be approximately 590°C. The highest rate of CNT oxidation in each case was found to occur at a system temperature of 630°C. The lack of multiple decomposition temperatures and multiple oxidation rate peaks are a reflection of the purity of the

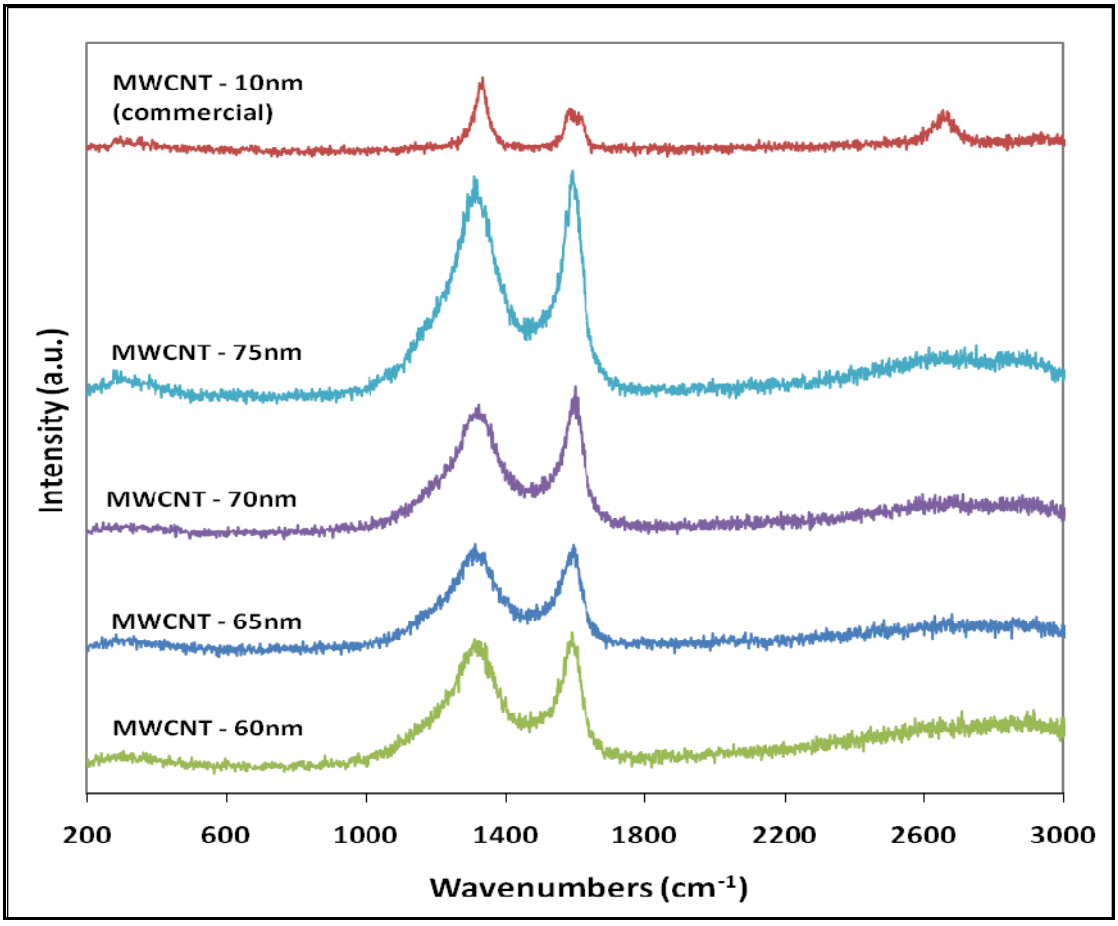

Figure 6.4: Raman spectra of MWCNTs functionalized by HNO_3, distinguished by their average pore diameters.

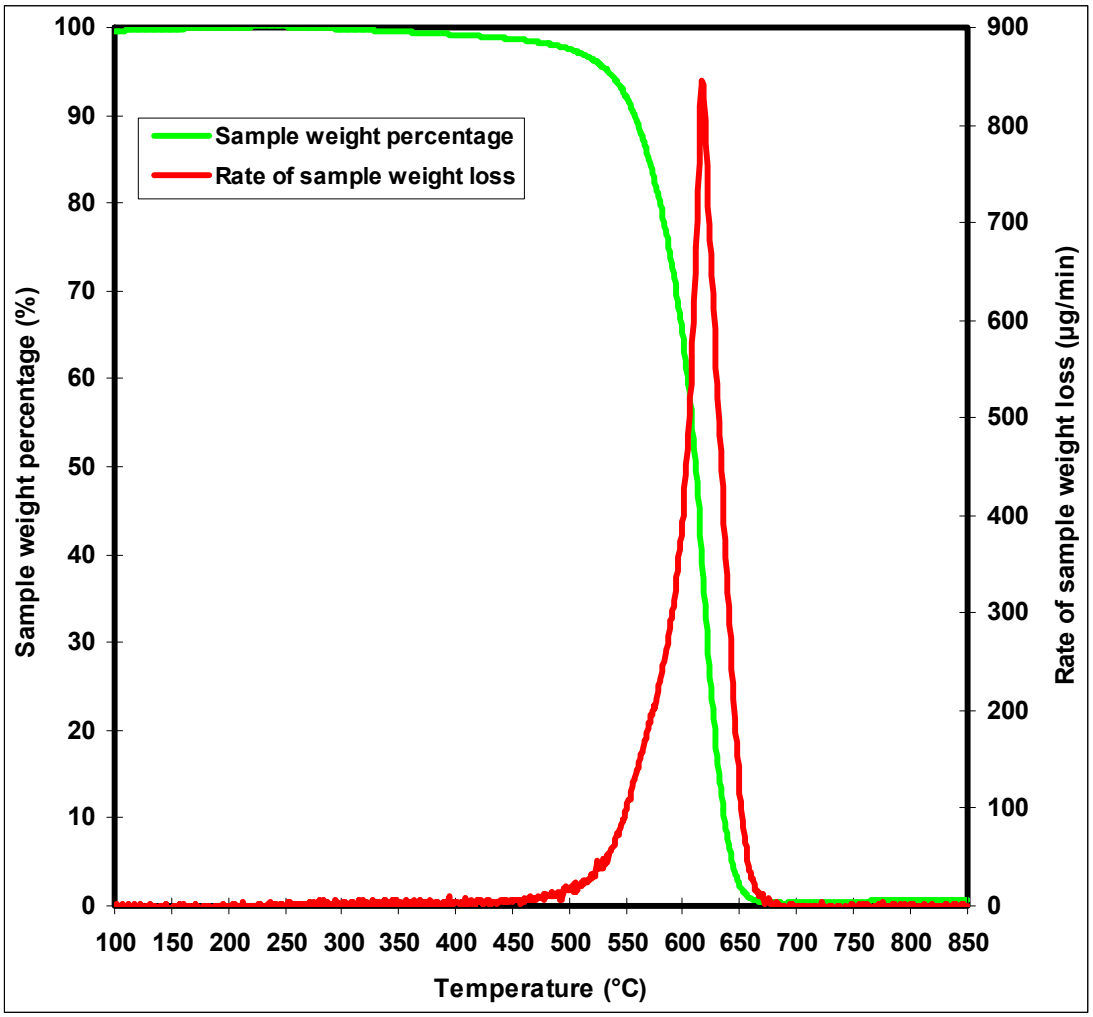

Figure 6.5: Sample TGA profile as exhibited by condition 9 MWCNTs.

CNT samples provided in each case. It can be concluded from the results of TGA that variation of the CNT pore diameter by the variation of the AAO synthesis parameters has no effect on the thermal stability of the CNTs.

6.1.6 DRIFT Spectroscopy

The functional groups created on the surface of the CNTs were characterized by DRIFT spectroscopy of adsorbed CO. To avoid OH contribution from ambient atmospheric moisture, the DRIFT spectroscopy study was carried by using an *in-situ* cell. The sample was heated at 150 °C for 1 hour under He flow (50 ml/min) and the spectrum was taken at 30°C. Figure 6.6 shows the typical DRIFT spectrum of the oxidized MWCNTs. The band appearing at 1734 cm^{-1} is assigned to the C=O vibration of either carboxyl or carbonyl groups in the nanotubes surface (Li J. et al., 2007) and 1596 cm^{-1} corresponds to the C=C stretching vibrations (Liu and Gao, 2005). As shown in the spectrum, the OH vibration (around 3500 cm^{-1}) from hydroxyl groups is barely noticeable in the oxidized MWCNTs. The peak at 1405 cm^{-1}, however, does indicate the presence of the O-H bending deformation from carboxylic groups (Kathi and Rhee, 2008). This showed that the C=O vibrations (strong band at 1734 cm^{-1}) resulted in the spectrum originated from carboxyl groups, with carbonyl groups possibly contributing as well. Overall, these observations indicate that the surface of the MWCNTs has been functionalized by HNO_3 oxidation and results in a greater number of carboxyl groups than hydroxyl groups on the surfaces of the MWCNTs.

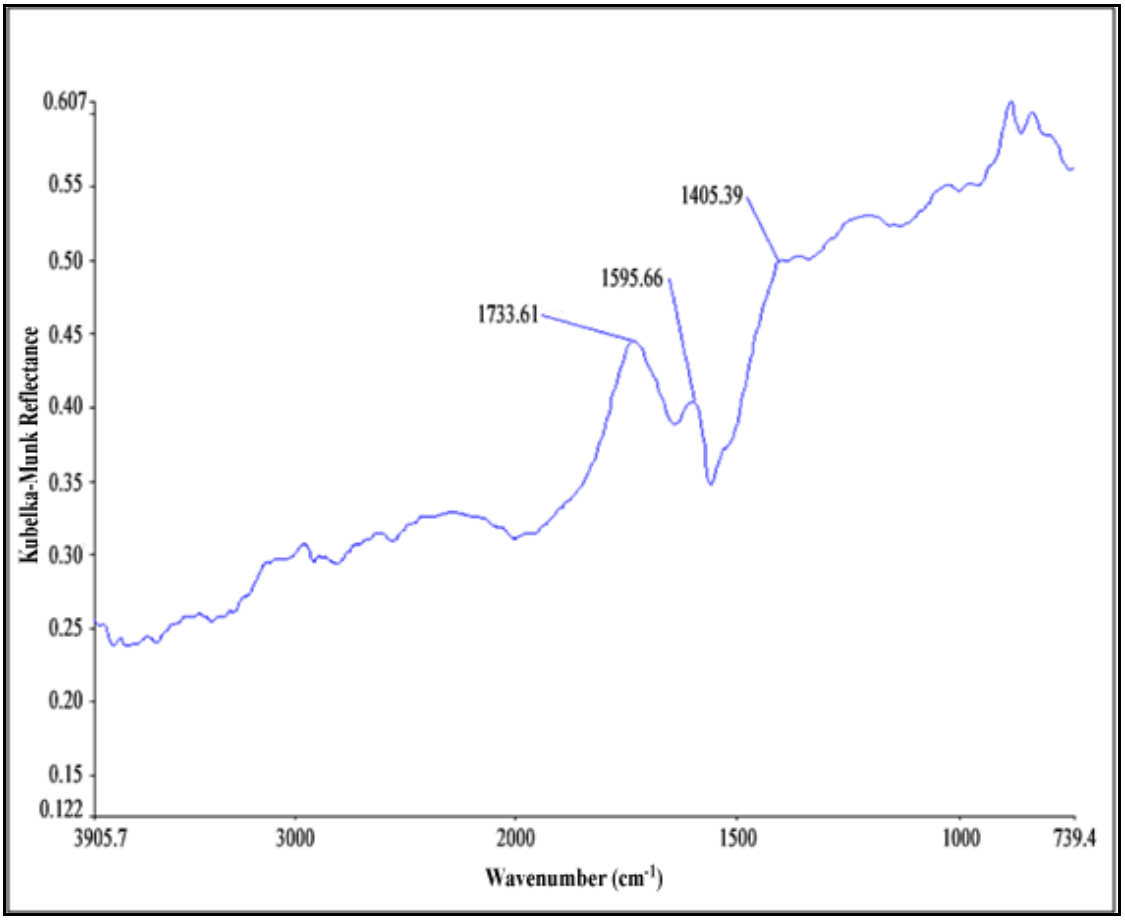

Figure 6.6: Typical *in-situ* DRIFT spectrum of HNO_3-functionalized MWCNTs.

6.2 Effect of MWCNT Pore Diameter on Catalyst Performance

Specific grades of functionalized MWCNTs were chosen for screening as catalyst supports for HDS and HDN of coker light gas oil derived from Athabasca bitumen. To serve this purpose, the nanotube supports were first loaded with Ni and Mo catalyst metals by the incipient wetness co-impregnation method, followed by dehydration and calcination procedures. Because MWCNTs with inner diameters ranging from 60 to 75 nm were achieved using the AAO-template synthesis method, four grades of NiMo/MWCNT catalysts were prepared with diameters at 5 nm increments. From the TEM analysis in section 6.1.2, AAO synthesis conditions of 1, 4, 5, and 8 were chosen to achieve approximate MWCNT inner diameters of 60, 65, 70, and 75 nm. The prepared catalysts were denoted according to their approximate inner diameters: cat-60, cat-65, cat-70, and cat-75. HAADF-STEM images were taken of the NiMo/MWCNT catalysts both before and after the hydrotreating application. The catalysts performance was characterized by N_2 adsorption/ desorption, CO chemisorption, and H_2 temperature programmed reduction. The boiling point distribution of the liquid gas oil products were determined and compared to that of the CLGO feed. The performance of each grade of MWCNT support was determined based on the removal of sulfur and nitrogen heteroatoms from the CLGO feed via the HDS and HDN reactions.

6.2.1 HAADF-STEM Images of Functionalized MWCNTs

High angle annular dark field scanning transmission electron microscopy (HAADF-STEM) was performed to observe the nanostructure of NiMo/MWCNT catalysts, both before and after hydrotreating a CLGO feed. Sample images of both the MWCNTs and NiMo/MWCNT samples observed by this technique can be found in Figure 6.6. By the same method used for TEM analysis in section 6.1.2, digital micrograph software (version 3.6.5, Gatan Inc.) was used to measure the inner diameter and wall thickness for each grade of MWCNTs. Within Figure 6.7, image 6.7a shows that consistent wall thicknesses of 10 nm were once again found for this batch of NiMo/MWCNT samples. Based on the assumed theoretical dimensions of 0.34 nm thick graphite layers and 0.14 nm spacing between the layers, the wall thicknesses correspond to 21-22 concentric graphite layers forming each nanotube. Image 6.7b shows the dispersion of NiMo particles in their oxide phases on the surfaces of the MWCNT supports. The catalyst particles were confirmed from these images to be chemisorbed to both the inner and outer walls of the MWCNTs. The particles were seen to varying in size approximately between 1 and 5 nm in diameter. Image 6.7c shows an example of spent NiMo/MWCNT, a catalyst sample examined after performing within a hydrotreating operation. Visible in the included sample image, as well as for all the spent catalyst images, are coke filaments shown branching off from the metal catalyst particles. These filaments are thought to contribute to the deactivation of the catalyst. The final image (6.7d) shows

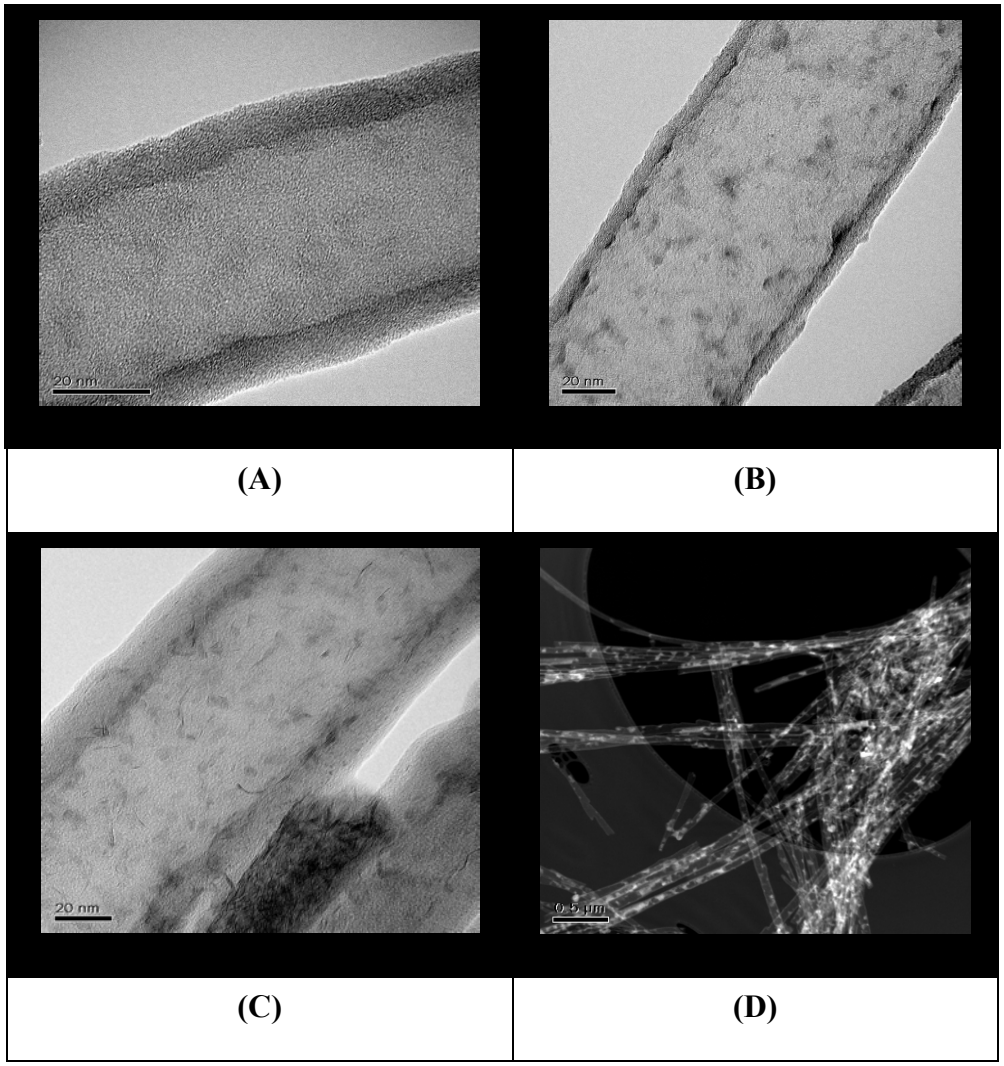

(A)	(B)
(C)	(D)

Figure 6.7: HAADF-STEM images of NiMo/MWCNT catalysts: (A) ×500k magnification image, functionalized condition 6 MWCNT; (B) ×300k magnification image, Cat-65 NiMo/MWCNT; (C) ×300k magnification image, coked Cat-65 NiMo/MWCNT; (D) ×20k magnification HAADF image, Cat-65 NiMo/MWCNT.

an HAADF interpretation of the NiMo/MWCNT catalysts, which illuminates material to an increasing degree as the atomic number of the material becomes greater. The amount of illuminated particles shown in the low magnification 6.6d image gives an example of how well dispersed the catalyst metals were from the incipient wetness loading technique.

6.2.2 Characterization by N_2 Adsorption/Desorption

Table 6.5 includes the results of N_2 adsorption/desorption analysis performed on the four pelletized catalysts. Also included in Table 6.5 are the actual inner diameters and wall thicknesses of the loaded NiMo/MWCNT catalysts as were determined from the averages of 10 HAADF-STEM images. As expected, the pelletizing and loading of metals on the MWCNTs caused their surface characteristics to decrease significantly, particularly for cat-60. This can be attributed to the blockage of pores caused by the loading of the metal particles and the compression of the catalyst supports, reducing the accessible surface area and total pore volume of the catalysts. It can be observed that these detrimental effects had more impact on cat-60 due to the catalyst having significantly lower inner diameters compared to the other catalysts. As was the case with the condition 4 MWCNTs, cat-65 was determined to have the most desirable surface characteristics as determined by N_2 adsorption/desorption analysis. Catalysts cat-75 and cat-70 were found to have the second and third most suitable surface characteristics, respectively, for a heterogeneous catalyst support application.

Table 6.5
Structural characteristics of the prepared NiMo/MWCNT catalysts (~2.5 wt.% Ni, ~13 wt.% Mo).

Sample	TEM Inner Diameter (nm)	TEM Wall Thickness (nm)	BET Surface Area (m^2/g)	Total Pore Volume (cc/g)	Average Pore Diameter (nm)
cat-60	57	10	106	0.165	6.2
cat-65	67	10	169	0.442	10.4
cat-70	71	10	141	0.320	9.1
cat-75	76	10	154	0.400	10.3

6.2.3 CO Chemisorption for Varied NiMo/CNT Pore Diameters

CO chemisorption was performed for the four NiMo/MWCNT catalysts with incremented pore diameters to determine if the exposure of the catalyst metals changed with changing support characteristics (see Table 6.6). It was found that cat-65 had the highest amount of CO uptake; 1.43 cc/g for a system pressure of 400 mmHg. This reflects the results from the screening of these catalysts via CLGO hydrotreatment, discussed later in section 6.2.6. The higher surface area and pore diameter of the 65 nm MWCNT resulted in a greater dispersion of the catalyst metals, leading to a greater amount of chemisorbed CO and superior catalyst performance. Based on the CO uptake at four different adsorption pressures (200, 266, 333, and 400 mmHg) and the estimated atomic cross-sectional areas of the metals (0.0649 nm^2/atom of Ni; 0.0730 nm^2/atom of Mo), the exposure percentage of the metals were estimated. These exposure estimates are also reported in Table 6.6. The relatively small results found for the exposure of the metals indicates that many of the metal atoms were left inaccessible within the catalyst particles. It is worth noting that an unreasonably large metal surface area would be achieved with perfect dispersion; approximately 490 m^2/g. Cat-65, as expected, achieved the highest degree of metal exposure at 3.10%, equivalent to 15.2 m^2/g of catalyst metal. The critical assumption of this analysis was that carbon monoxide chemisorption occurred exclusively on all the metal sites of the catalyst surfaces. Assuming this was the case, the catalyst metals would have provided only ~1.5% of the accessible surface area for each

Table 6.6
CO uptake of NiMo/MWCNT catalysts with varying pore diameters from chemisorption analysis.

Catalyst	CO Uptake @ 400 mmHg (cc/g)	Estimated Metal Exposure (%)
Cat-60 – 13.0 wt% Mo, 2.5 wt% Ni	**1.17**	**2.28**
Cat-65 – 13.0 wt% Mo, 2.5 wt% Ni	**1.43**	**3.10**
Cat-70 – 13.0 wt% Mo, 2.5 wt% Ni	**1.33**	**2.68**
Cat-75 – 13.0 wt% Mo, 2.5 wt% Ni	**1.22**	**2.41**

catalyst. Based on these results, it would appear that the metal dispersion was significantly underestimated.

6.2.4 Temperature Programmed Reduction with H_2

Temperature programmed reduction (TPR) of the catalysts using H_2 was performed under conditions of a 30 mL/min H_2 flow rate and a temperature ramping of 10°C/min. The reduction peaks for the catalysts with varied pore diameters can be found in Figure 6.8. The hydrogen consumption peaks, which occurred within a domain of 445-456°C for the MWCNT-supported catalysts and at 506°C for the commercial γ–alumina catalyst, are the result of Mo reduction from the amorphous Mo^{6+} (octahedral) oxide phase to the ordered Mo^{4+} (tetrahedral) oxide phase (Leyva et al., 2008; Qu et al., 2003; Yu et al., 2008). The lower reduction temperatures for the MWCNT catalysts indicate that there is less surface interaction with the catalyst metals compared to the commercial γ-alumina. This would theoretically make for an easier transition to the sulfide phase for the MWCNT catalysts in a hydrotreating application. Figure 6.8 shows a gradual decrease in the peak reduction temperature from approximately 456°C to 445°C as the accessible surface area of the catalysts allow for greater catalyst particle dispersion. The specific consumption peak temperatures for each catalyst were 456°C for cat-60, 453°C for cat-75, 450°C for cat-70, and 445°C for cat-65. Although cat-75 was found to have better surface characteristics found from N_2 adsorption/desorption study, cat-70 had an optimum reduction temperature slightly lower than that of cat-75. It could be concluded

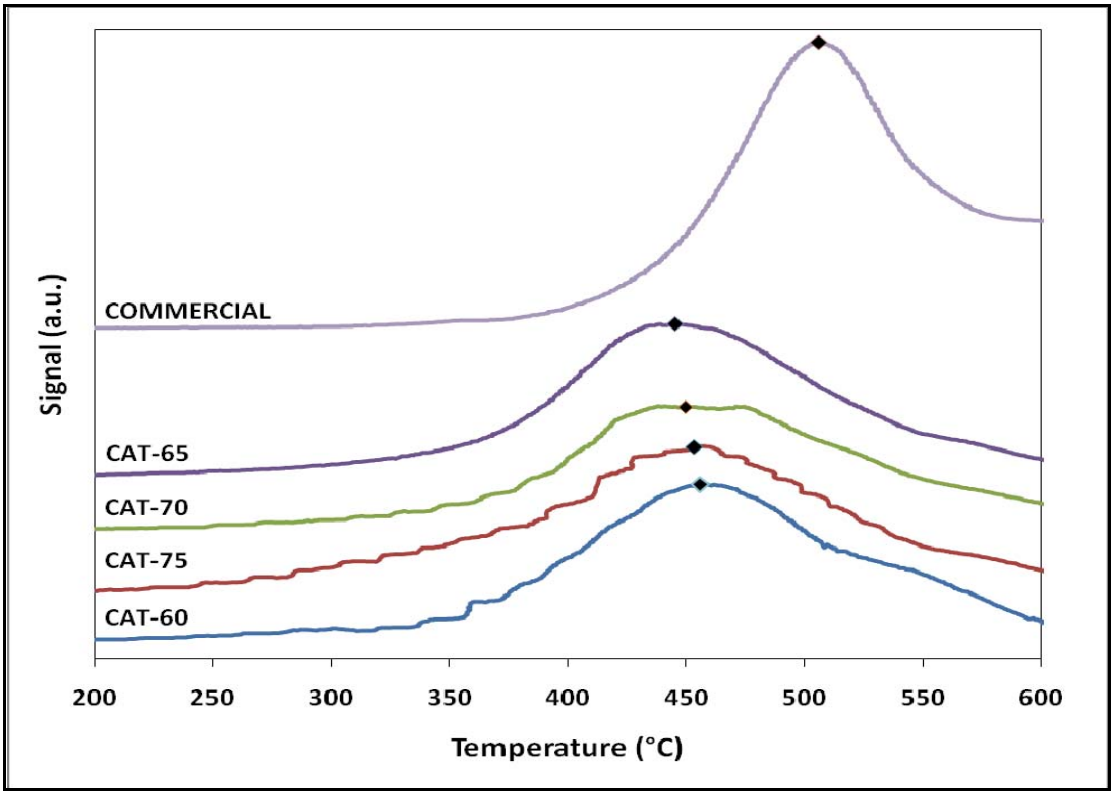

Figure 6.8: Temperature programmed reduction using H_2 of NiMo/MWCNT catalysts with varied pore diameters.

that the two supports were similar enough in surface features that the difference between their reduction temperatures was within the range of error for the instrument.

6.2.5 Boiling Point Distribution of CLGO Feed and Products

The initial simulated distillation procedure was to determine the boiling point range and resulting composition of the various CLGO feeds used throughout the project. These results can be found in Appendix C. The results from analyzing the product liquids from the pore optimization portion of the project were compared with the composition of the CLGO feed used for these runs as well as the product liquid from a weight-based comparison of commercial γ–alumina catalyst. Based on the boiling point range of a standard solution with molecular carbon numbers ranging from C5 to C60, the molecular compositions of the product liquids were divided into three sections: carbon numbers of 15 and under (≤C15), carbon numbers of 20 and over (≥C20), and carbon numbers ranging from 16 to 19 (C16-C19). Figure 6.9 shows the graphical interpretation of these results at a temperature of 370°C and a WHSV of 4.5 h^{-1}. By categorizing the molar composition of the product liquids in this method, a distinct relation was found between the carbon numbers and the pore diameter of the NiMo/MWCNT catalysts. As the average pore diameter lowered from 75 to 60 nm, the percentage of carbon numbers ≤C15 increased steadily from 25.4% to 28.4%. The inverse trend was found for carbon numbers ranging from C16 to C19, as the percentage of molecules within this range decreased steadily from 32.9% to 30.3% as the average pore diameter of the catalysts dropped from 75 to 60 nm. For

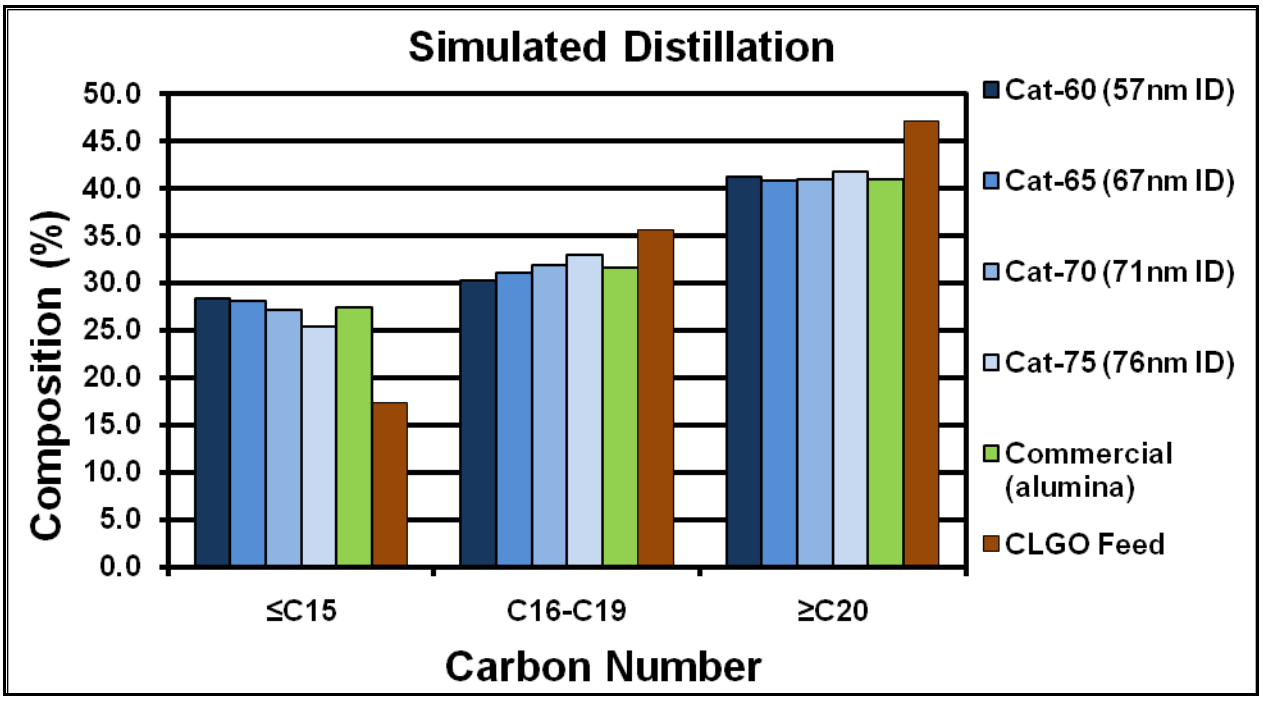

Figure 6.9: Carbon number composition of the steady-state coker light gas oil product from the hydrotreating application of NiMo/*MWCNT* catalysts. Temperature: 370°C. Pressure: 8.8 MPa. WHSV: 4.5 h^{-1}. H_2/CLGO volumetric flow ratio: 600/1. Catalyst loading: 2.00 g.

carbon numbers of ≥C20, the molar percentage of the products were relatively the same for all the catalysts ranging from 41.7% to 40.9%. The results show a trend of more extensive molecule refinement occurring as the pore diameter of the MWCNT supports become smaller. The reverse trend appears for carbon numbers ranging from C16 to C19, as a higher concentration of these molecules are found as the pore diameter of the catalyst support becomes larger. It could be concluded from these results that making the pores of the MWCNT supports more confined leads to more extensive cracking of the CLGO molecules during the hydrotreating process.

6.2.6 Catalyst Performance Based on N and S Conversion

The characteristics of the CLGO feed used for this section of the project can be found in Appendix C. HDS & HDN steady-state activities of each catalyst from the CLGO feed can be found numerically in Table 6.7 and graphically in Figures 6.10 and 6.11. Along with the four MWCNT-based catalysts, a commercial catalyst consisting of a γ–Al_2O_3 support was tested under an equivalent weight loading (WHSV = 4.5 h^{-1}) to evaluate the applicability of a NiMo/MWCNT sulfide catalyst. Except for the presence of phosphorus, the catalyst composition of the commercial catalyst was similar to the MWCNT-based catalysts. The composition of the commercial catalyst can be reported as approximately 3.0 wt.% Ni, 13 wt.% Mo, and 2.5 wt.% P. Each percentage of sulfur and nitrogen removal reported in Table 6.7 was determined by taking the mean of each sample conversion value once steady-state was reached. Figures 6.12 and 6.13 show the precoking periods of each experimental run

Table 6.7
HDS & HDN steady-state activities (wt.%) of NiMo/MWCNT catalysts with varying pore diameters determined by TEM and NiMoP/γ-Al_2O_3 commercial catalyst for the hydrotreatment of coker light gas oil. Pressure: 8.8 MPa. WHSV: 4.5 h^{-1}. Catalyst loading: 2.00 g. H_2/CLGO volumetric flow ratio: 600/1.

Catalyst	Inner Diameter (nm)	Sulfur/Nitrogen removal at each reaction temperature (wt.%)					
		370°C		350°C		330°C	
		Sulfur	Nitrogen	Sulfur	Nitrogen	Sulfur	Nitrogen
cat-60	57	74.3	34.2	57.0	22.8	44.5	16.5
cat-65	67	77.0	37.5	61.0	26.7	47.4	19.3
cat-70	71	68.3	31.1	53.5	21.8	44.0	17.3
cat-75	76	68.4	29.6	49.9	18.7	40.7	17.3
commercial	n/a	51.1	26.6	37.8	16.2	30.7	8.7

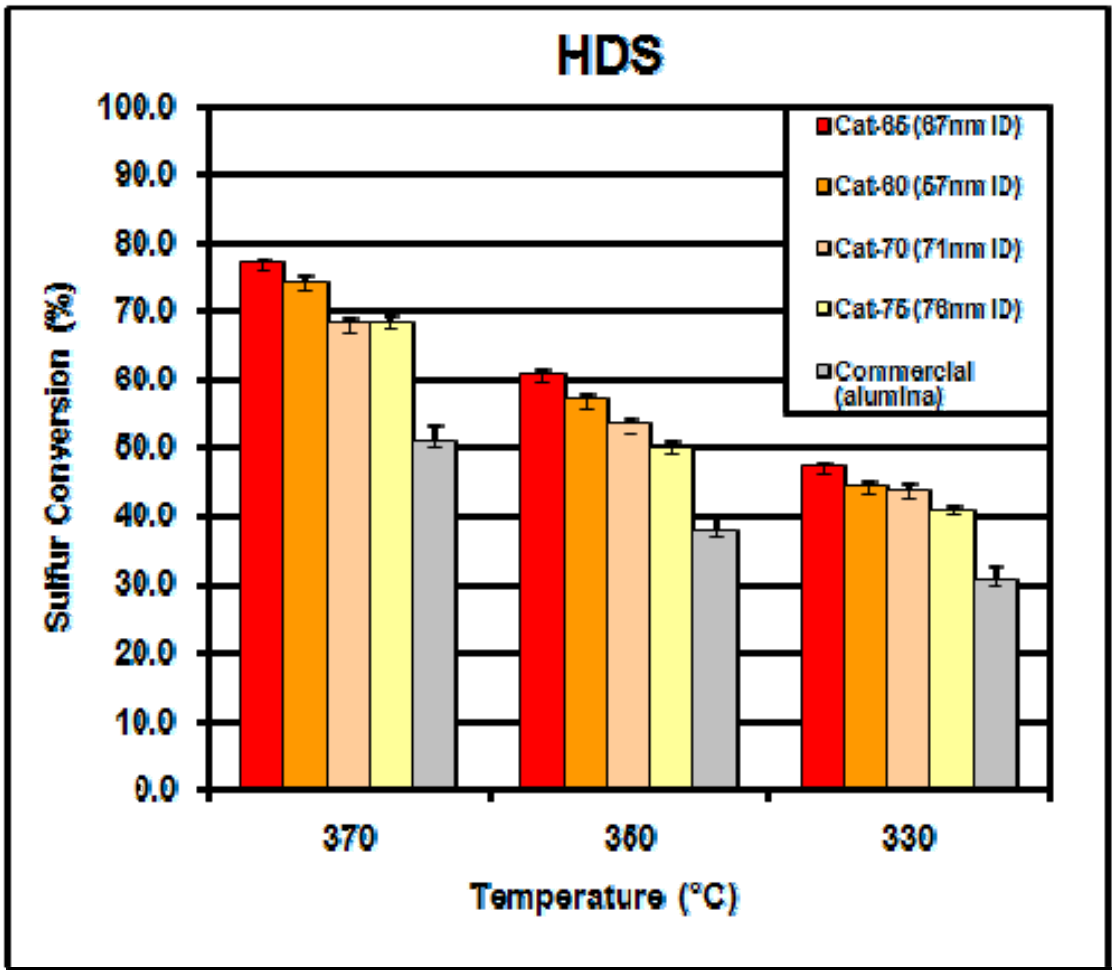

Figure 6.10: HDS steady-state activities (wt.%) of NiMo/MWCNT catalysts and NiMoP/γ-Al_2O_3 commercial catalyst for the hydrotreatment of coker light gas oil. Pressure: 8.8 MPa. WHSV: 4.5 h^{-1}. Catalyst loading: 2.00 g. H_2/CLGO volumetric flow ratio: 600/1.

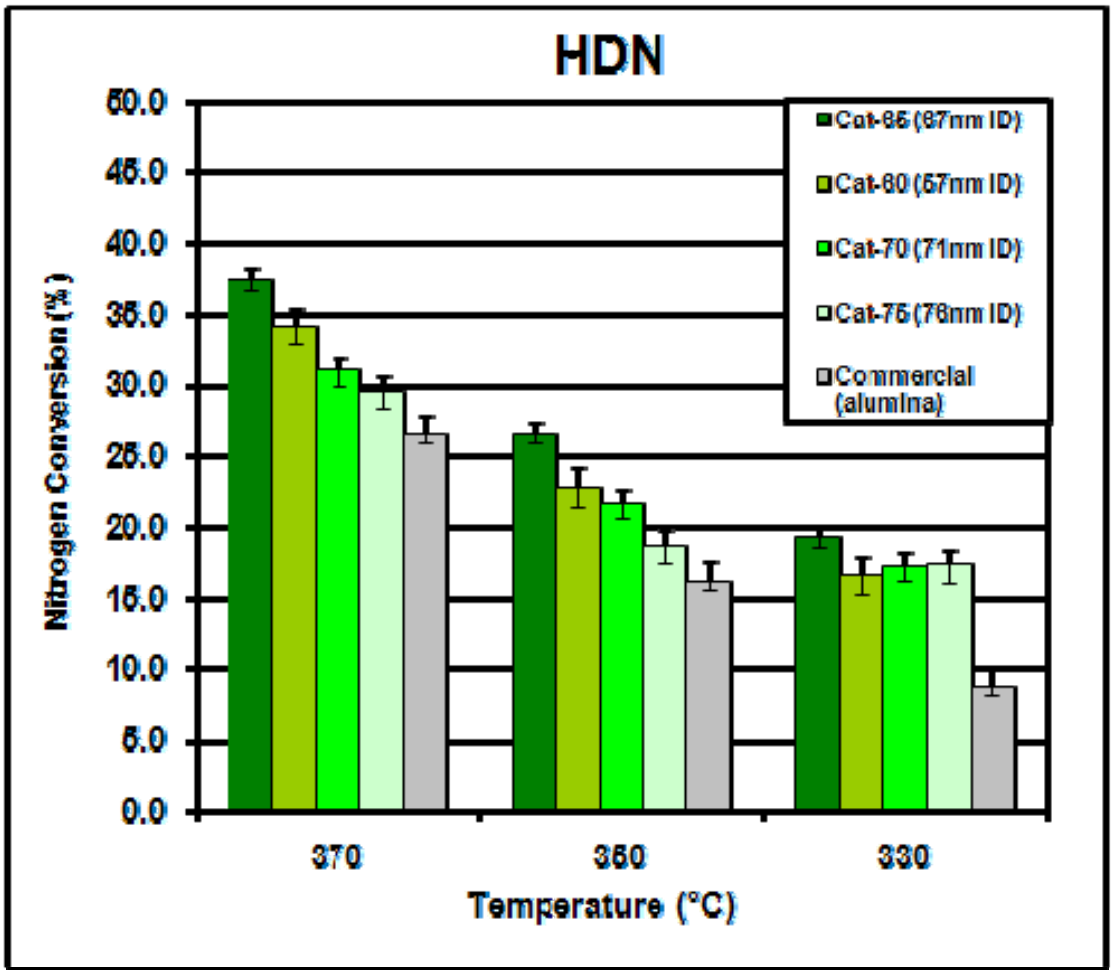

Figure 6.11: HDN steady-state activities (wt.%) of NiMo/MWCNT catalysts and NiMoP/γ-Al_2O_3 commercial catalyst for the hydrotreatment of coker light gas oil. Pressure: 8.8 MPa. WHSV: 4.5 h^{-1}. Catalyst loading: 2.00 g. H_2/CLGO volumetric flow ratio: 600/1.

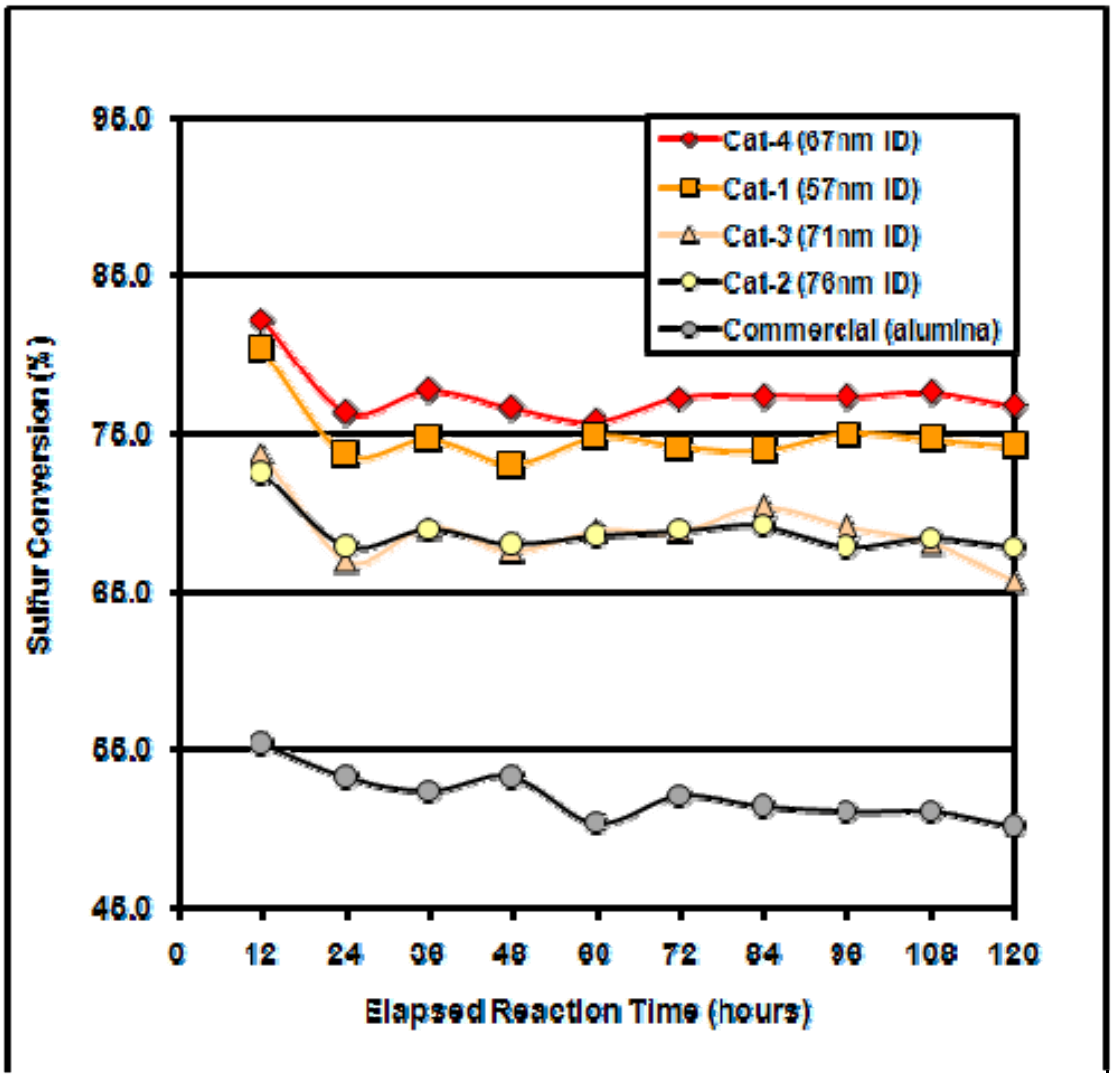

Figure 6.12: HDS activities (wt.%) during the precoking phase for NiMo/MWCNT catalysts and NiMoP/γ-Al_2O_3 commercial catalyst during the hydrotreatment of coker light gas oil. Temperature: 370ºC. Pressure: 8.8 MPa. WHSV: 4.5 h^{-1}. Catalyst loading: 2.00 g. H_2/CLGO volumetric flow ratio: 600/1.

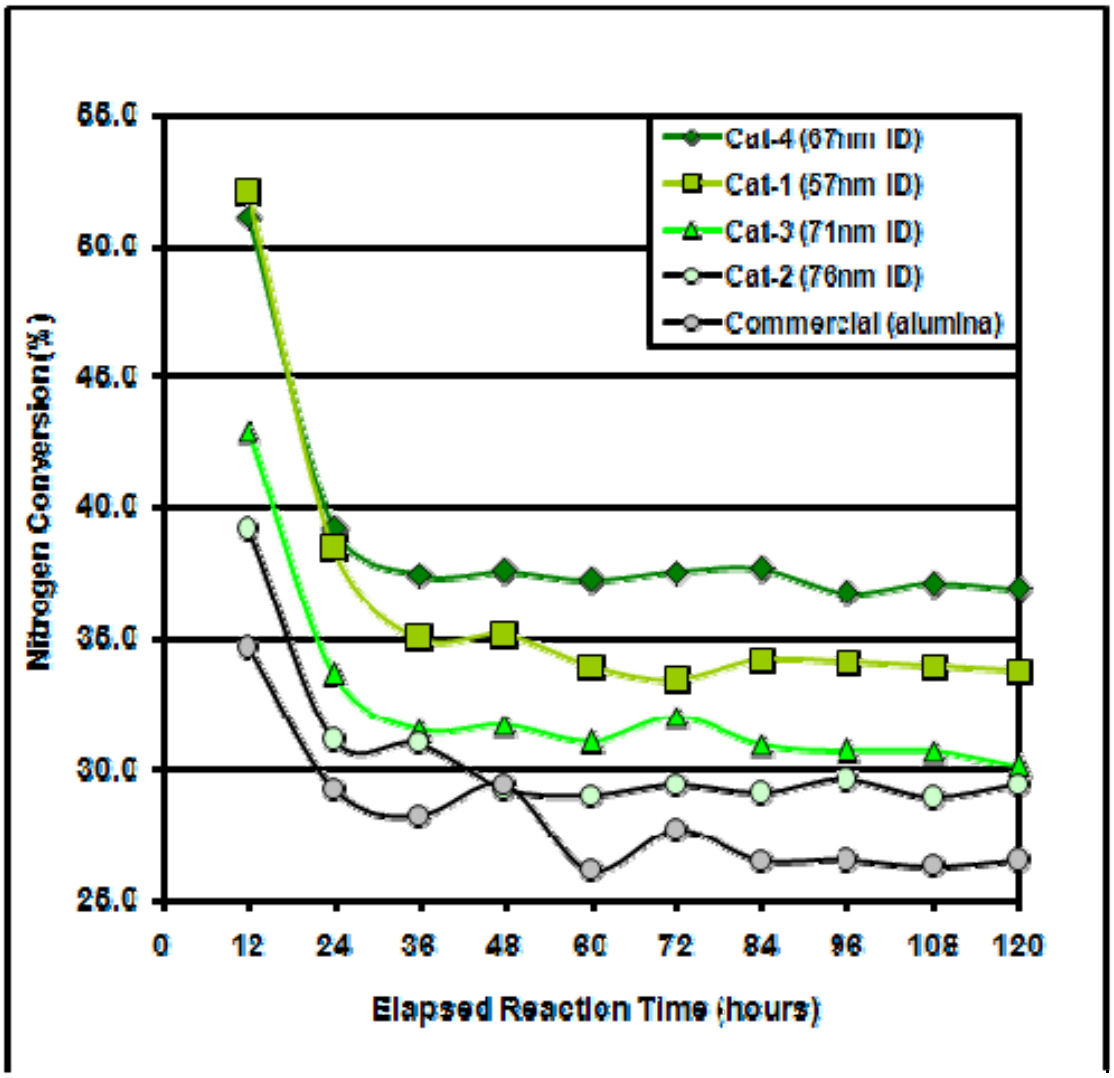

Figure 6.13: HDN activities (wt.%) during the precoking phase for NiMo/MWCNT catalysts and NiMoP/γ-Al_2O_3 commercial catalyst during the hydrotreatment of coker light gas oil. Temperature: 370ºC. Pressure: 8.8 MPa. WHSV: 4.5 h^{-1}. Catalyst loading: 2.00 g. H_2/CLGO volumetric flow ratio: 600/1.

and the approach to steady-state based on the HDS & HDN activities, respectively. For each catalyst, it was observed that both the HDS & HDN activity reached steady-state conditions in 24 hours. That being the case, the steady-state activity at 370°C for each catalyst was found by averaging the conversions found for the nine samples taken at steady-state. Similarly for reaction temperatures of 350°C and 330°C, the average conversion values were found from the three samples taken at steady-state.

As was shown in Table 6.7, cat-65 was found to have the highest HDS and HDN activities at each reaction temperature. The catalyst displayed sulfur conversions of 77.0%, 61.0%, and 47.4% at reaction temperatures of 370°C, 350°C, and 330°C, respectively. Similarly for nitrogen, steady-state conversions of 37.5%, 26.7%, and 19.3% were found at respective temperatures of 370°C, 350°C, and 330°C for cat-65. Under the same reaction conditions and at equal mass loading, the commercial γ–Al_2O_3 catalyst performed steady-state sulfur conversions of 51.1%, 37.8%, and 30.7%, along with nitrogen conversions of 26.6%, 16.2%, and 8.7%, for the three descending reaction temperatures. Cat-60 had the second highest activities for all cases with the exception of HDN at 330°C. A possible explanation for this would be the long term detrimental effects of precoking taking place for the smaller pores of cat-60. Longevity studies for this catalyst would be performed to confirm this. Cat-70 displayed the third highest activity for the majority of the cases studied, while cat-75 demonstrated the fourth highest activity for the majority of the conditions. It can be concluded from these results that the inner diameter of the

MWCNTs used for the cat-65 catalyst were responsible for sufficient mass transfer of reactant liquids and gases through the catalyst while still maintaining a high surface area necessary for metal sulfide dispersion. It can be concluded that the inner diameters of cat-60 were more susceptible to coking deactivation. The larger inner diameters of cat-70 & cat-75 either resulted in less dispersion of the catalyst metals or the direct transport of gas oil through the catalyst without undergoing any reaction.

6.3 Variation of CVD Parameters

For the pore diameter optimization phase of this study, the two main parameters of the chemical vapor deposition procedure where held constant. These parameters were a reactor temperature of 650°C and a C_2H_2/AAO ratio of 8.00 mL/min·g. Also held constant was a reaction time of two hours. In an effort to perform the CVD process more efficiently, MWCNT synthesis was performed at lower reaction temperatures and lower acetylene flow rates. In a similar fashion to the AAO pore optimization study, nine CVD operation conditions were studied with a 0.250 g AAO loading (condition 4 grade) and a 2-hour reaction period (see Table 6.8). The effectiveness of each condition was based on the mass of purified MWCNTs recovered, the percent yield of MWCNTs from the acetylene carbon source, and the MWCNT quality as viewed from TEM images. Both the determined mass recoveries and percent yields assumed 100% MWCNT purity after HF treatment.

Table 6.8
Naming scheme applied to the different chemical vapor deposition conditions for MWCNT synthesis on AAO templates.

		C_2H_2 Flow Rate / AAO Mass Ratio (mL/min· g)		
		4.00	**6.00**	**8.00**
Reaction Temperature (°C)	**450**	**Condition 1**	**Condition 4**	**Condition 7**
	550	**Condition 2**	**Condition 5**	**Condition 8**
	650	**Condition 3**	**Condition 6**	**Condition 9**

6.3.1 Yields for Each Operating Condition

Table 6.9 shows the results of the mass recovery and the MWCNT percent yield from the CVD optimization study. The conditions with a reaction temperature of 450°C produced low MWCNT yields of less than 14%. A reaction temperature of 550°C produced moderate yields falling between 30% and 45%. Significant yields were found at a reaction temperature of 650°C, where all the carbon percent yields exceeded 85%. The highest yield, 88.1%, and highest mass recovery, 0.298 g resulting from 0.250 g of template, were found at the original parameter settings of 650°C and 8.00 mL/min·g (condition 9).

6.3.2 TEM Images for Each Grade of MWCNTs

The TEM images of the MWCNT products are shown in Table 6.10. From the TEM images, no CNTs were produced for condition 1 and only aluminum-fluorine salt crystals were found. This reflects the low mass recovery that was found for condition 1 in section 6.3.1. Irregular CNTs accompanied by amorphous carbon were found for conditions 2, 4, and 5. Condition 3 and 7 showed the expected parallel MWCNTs with considerable pore diameters. However, the wall thickness of these MWCNTs appeared to oscillate from 1 to 10 nm, making their stability under hydrotreating operating conditions uncertain. Conditions 6, 8, and 9 produced the only MWCNTs that displayed consistent wall thicknesses and pore diameters. The

Table 6.9
Carbon mass and yields from C_2H_2 achieved for nine chemical vapor deposition conditions and 0.250 grams of AAO template per run.

1) Mass (g) / 2) Yield (%)		C_2H_2 Flow Rate / AAO Mass Ratio (mL/min· g)		
		4.00	6.00	8.00
Reaction Temperature (°C)	450	1) 0.005 2) 2.96	1) 0.025 2) 9.85	1) 0.045 2) 13.3
	550	1) 0.075 2) 44.3	1) 0.077 2) 30.4	1) 0.115 2) 34.0
	650	1) 0.170 2) 85.7	1) 0.218 2) 85.9	1) 0.298 2) 88.1

Table 6.10
TEM images of the MWCNTs from the nine chemical vapor deposition conditions.

		C_2H_2 Flow Rate / AAO Mass Ratio (mL/min· g)		
		4.00	**6.00**	**8.00**
Reaction Temperature (°C)	**450**	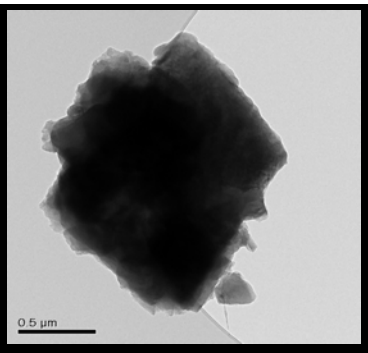	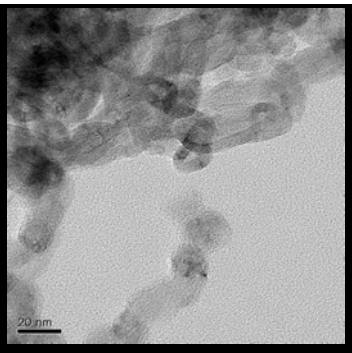	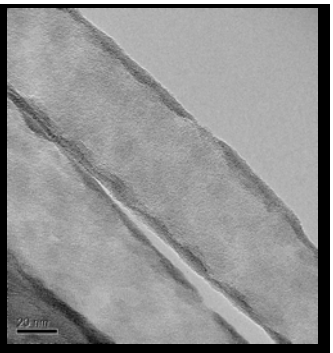
	550	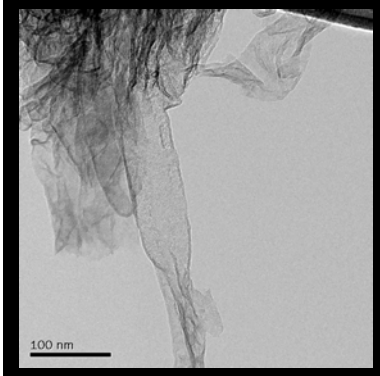		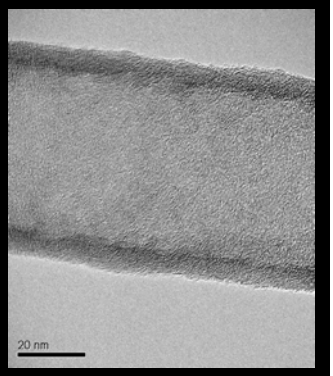
	650	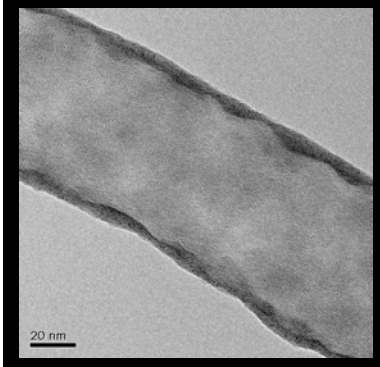	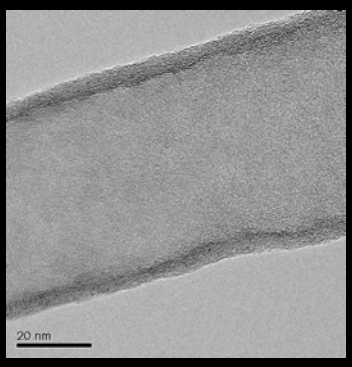	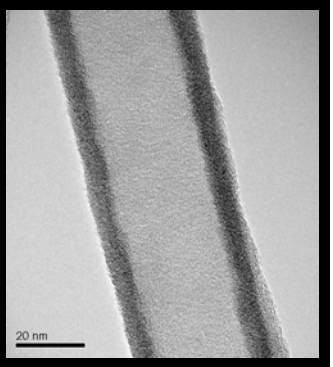

low yield achieved from condition 8 and the slightly inferior yield from condition 6 would make condition 9 most suitable for MWCNT synthesis.

6.4 Metal Loading Optimization and Characterization

After determining the most suitable pore diameter for the MWCNT catalyst support (~65 nm), the optimum loadings of the Ni and Mo catalyst metals were determined based on the HDS and HDN activities displayed for hydrotreating a CLGO feedstock. Molybdenum was the first metal to have its loading optimized. In total, three different Mo weight percentages were screened: 13.0, 19.5, and 26.0%. The Ni loading was kept constant at 2.5 wt.% for all three of these catalyst screenings. As well, the MWCNT catalyst support for each of these catalysts was retrieved from the same batch with an average pore diameter of 65 nm. After determining the superior Mo loading, catalyst with 2.5, 5.0, and 7.5 wt.% loadings were screened with the optimum Mo loading and MWCNT pore diameter remaining constant. The effects that varying the metal loadings had on the behavior of the catalysts were characterized by N_2 adsorption/desorption, CO chemisorption, and H_2 temperature programmed reduction. The end result of this section of the project was determining the optimum conditions for a NiMo/MWCNT catalyst for the purpose of performing kinetic modeling and stability studies on this catalyst. The performances of these NiMo/MWCNT catalysts were compared with a commercial NiMoP/γ-Al_2O_3 catalyst both on a mass basis (WHSV = 4.5 h^{-1}) and a volumetric basis (LHSV = 2.0 h^{-1}).

6.4.1 Characterization by N_2 Adsorption/Desorption

The determined BET surface characteristics for the NiMo/MWCNT catalysts with varied metal loadings can be found in Table 6.11. The results show a consistent decrease in the BET surface area, total pore volume, and average pore diameter as the amount of loaded metal was increased. Worth noting is the only slight decrease in the surface characteristics of the catalyst as the Mo loading was increased from 13.0 wt.% to 19.5 wt.%. The surface area only slightly decreased from 125 to 123 m^2/g, while the average pore diameter declined from 12.1 to 11.9 nm. Metal loadings beyond this amount resulted in significant decreases to the surface features of the catalyst. A commercial γ–alumina catalyst with similar Ni and Mo loadings was found to have a higher surface area and total pore volume compared to all the MWCNT-supported catalysts, but a lower average pore diameter compared to catalysts cat-A and cat-B. From the surface characteristics of the five MWCNT-supported catalysts, cat-B appeared to be the only catalyst were an increase in metal loading did not significantly decrease the desirable surface values for a heterogeneous catalyst.

6.4.2 CO Chemisorption for Varied Ni and Mo Loadings

Table 6.12 shows the results of the CO chemisorptions study for all five catalysts. Increasing the Mo loading on this catalyst support from 13.0 to 19.5 wt.% was found to only have a negligible effect on the amount of chemisorbed CO, declining slightly from 1.43 to 1.42 cc/g. A further increase in Mo loading was found

Table 6.11
Structural characteristics of the prepared NiMo/MWCNT catalysts (67 nm inner diameter) with varied metal loadings.

Catalyst	BET Surface Area (m^2/g)	Total Pore Volume (cc/g)	Average Pore Diameter (nm)
Cat-A: 13.0 wt% Mo, 2.5 wt% Ni	125	0.373	12.1
Cat-B: 19.5 wt% Mo, 2.5 wt% Ni	123	0.371	11.9
Cat-C: 26.0 wt% Mo, 2.5 wt% Ni	105	0.239	9.1
Cat-D: 19.5 wt% Mo, 5.0 wt% Ni	116	0.321	11.0
Cat-E: 19.5 wt% Mo, 7.5 wt% Ni	112	0.285	10.1
Commercial γ-alumina catalyst	182	0.492	10.8

Table 6.12
CO uptake of NiMo/MWCNT catalysts with varying metal loadings from chemisorption analysis.

Catalyst	CO Uptake @ 400 mmHg (cc/g)	Estimated Metal Exposure (%)
Cat-A: 13.0 wt% Mo, 2.5 wt% Ni	**1.43**	**3.10**
Cat-B: 19.5 wt% Mo, 2.5 wt% Ni	**1.42**	**2.15**
Cat-C: 26.0 wt% Mo, 2.5 wt% Ni	**0.85**	**1.02**
Cat-D: 19.5 wt% Mo, 5.0 wt% Ni	**1.48**	**1.93**
Cat-E: 19.5 wt% Mo, 7.5 wt% Ni	**1.73**	**2.19**

to drastically lower the exposure of the catalyst metals, while increasing the Ni loading had the expected promotion effect of increasing metal dispersion. As previously discussed in section 6.2.3, the CO chemisorption method used for this project appears to have underestimated the true exposure of the catalyst metals. The fraction of surface area contributed by the catalyst metals was found to be significantly low, ranging from 2.7% for cat-E to 1.3% for cat-C. Validation of this assumption can be found in a previous study, where roughly 5× as much CO uptake was found for a γ–alumina catalyst under similar loadings and conditions (Sigurdson et al., 2008). One trend reflected in both the N_2 physisorption study and the CO chemisorption study was that the increase in Mo loading from cat-A to cat-B did not compromise the surface characteristics of the catalyst.

6.4.3 Temperature Programmed Reduction with H_2

The hydrogen consumption peaks for catalysts with varied metal loadings can be found in Figure 6.14. The increase of Mo loading from cat-A to cat-B is shown to lower the reduction temperature, from 460°C to 453°C. A further increase to Mo loading resulted in a substantial increase in the maximum H_2 consumption temperature to 490°C. Increasing the Ni loading to 5.0 wt.% lead to a lower peak reduction temperature of 451°C, indicating that smaller molybdenum oxide particles resulted from the greater presence of Ni. Further increasing the Ni loading to 7.5 wt.% reduced the peak consumption temperature to 438°C. These results confirm the function of the Ni promoter to increase the dispersion of the catalyst particles. Each

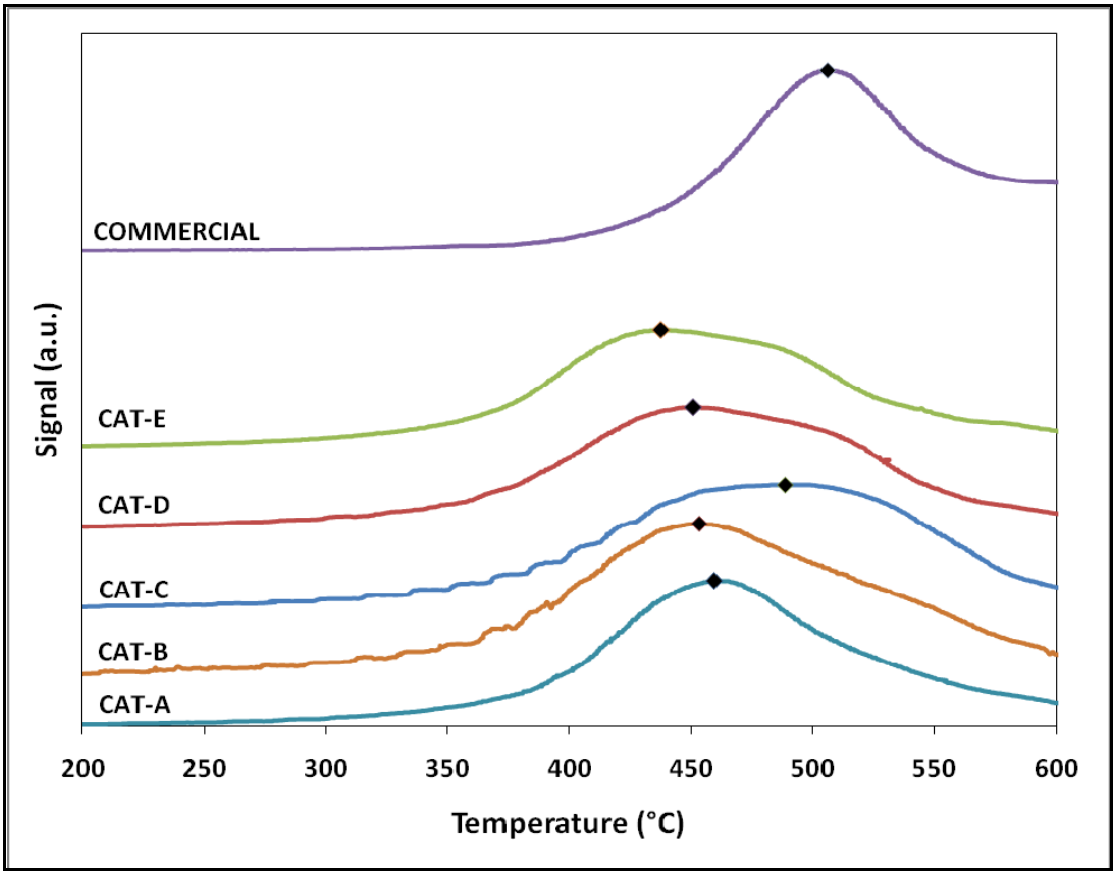

Figure 6.14: Temperature programmed reduction using H_2 of NiMo/MWCNT catalysts with varied metal loadings.

of the MWCNT-based catalysts had lower peak reduction temperatures than that of commercial alumina-based catalyst (506°C).

6.4.4 Optimization of Metal Loadings Based on N and S Conversion

The characteristics of the CLGO feedstock used during this project's metal loading optimization period can be found in Appendix C. The method of determining the ideal metal loading conditions was by first optimizing the molybdenum separately before optimizing the nickel loading. In total, three different Mo weight percentages were screened: 13.0, 19.5, and 26.0%. The Ni loading was kept constant at 2.5 wt.% for all three of these catalyst screenings. As well, the pore diameter of the carbon nanotube catalyst support was kept constant at approximately 67 nm. The graphical representations of the HDS and HDN activities for these catalysts can be found in Figures 6.15 and 6.16, respectively, while numerical results can be found in Table 6.13. From these results, it was concluded that a Mo loading of 19.5 wt.% was the optimum loading on the ideal MWCNT catalyst support.

Based on the results of the Mo loading test, the optimum Ni loading was found on the basis of a 19.5 wt.% Mo loading and a 65 nm MWCNT support. As with the Mo loadings, three weight percentages of Ni were screened in a CLGO hydrotreating application: 2.5, 5.0, and 7.5%. Figures 6.17 and 6.18 compare the steady-state HDS

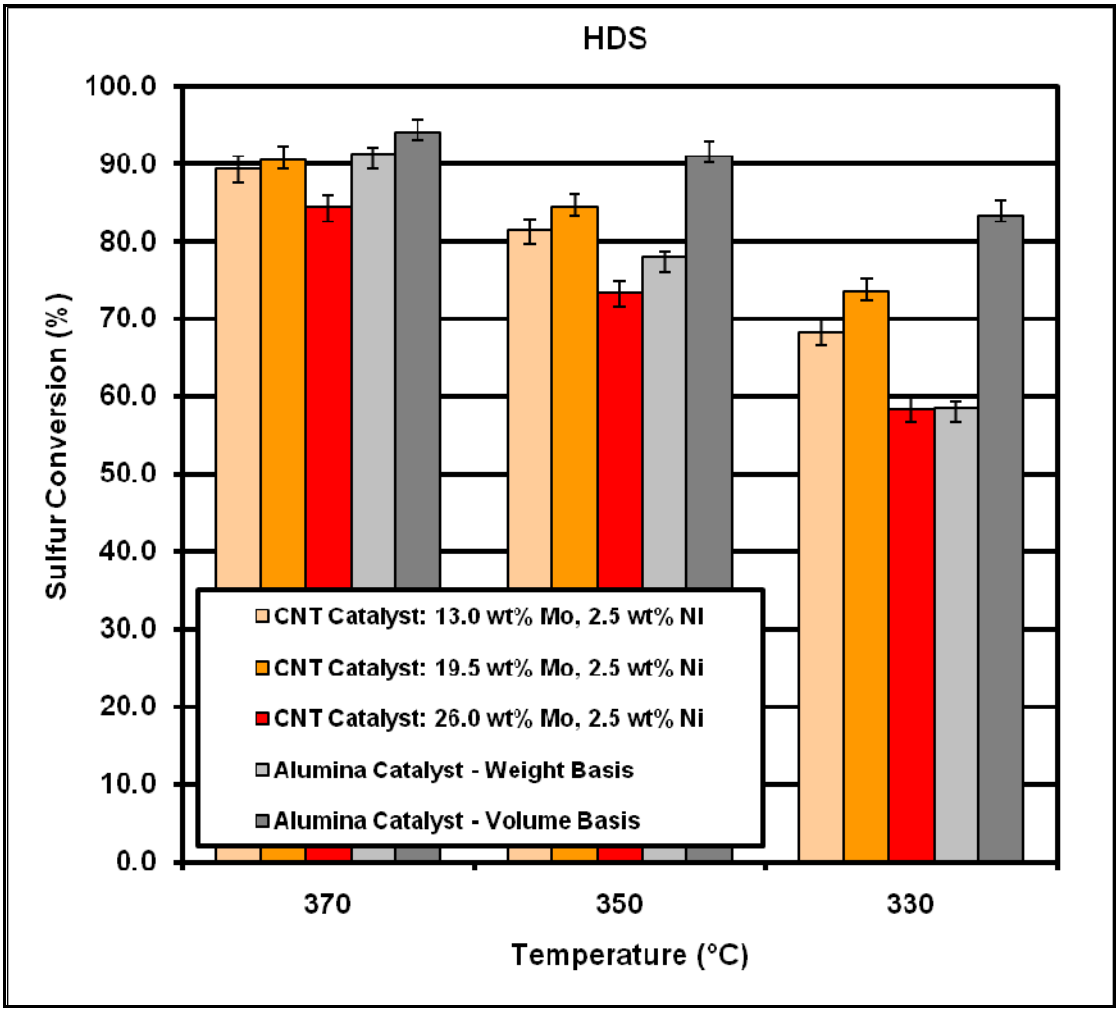

Figure 6.15: HDS steady-state activities (wt.%) for the Mo loading optimization of NiMo/*MWCNT* catalysts for hydrotreatment of coker light gas oil. Pressure: 8.8 MPa. Weight basis: WHSV = 4.5 h^{-1}. Volume basis: LHSV = 2.0 h^{-1}. Catalyst loading: 2.00 g. H_2/CLGO volumetric flow ratio: 600/1. Temperature: 370-330°C.

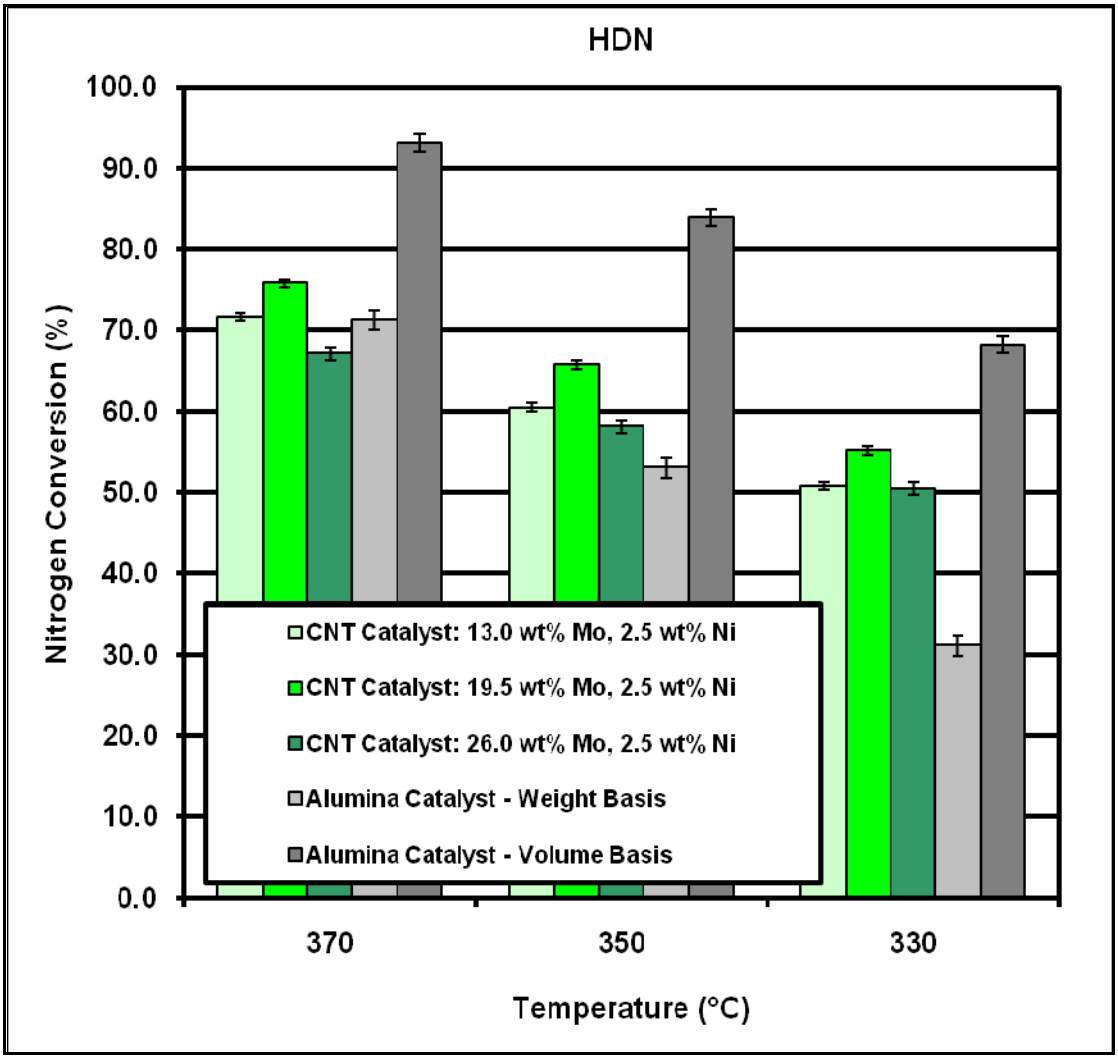

Figure 6.16: HDN steady-state activities (wt.%) for the Mo loading optimization of NiMo/*MWCNT* catalysts for hydrotreatment of coker light gas oil. Pressure: 8.8 MPa. Weight basis: WHSV = 4.5 h^{-1}. Volume basis: LHSV = 2.0 h^{-1}. Catalyst loading: 2.00 g. H_2/CLGO volumetric flow ratio: 600/1. Temperature: 370-330°C.

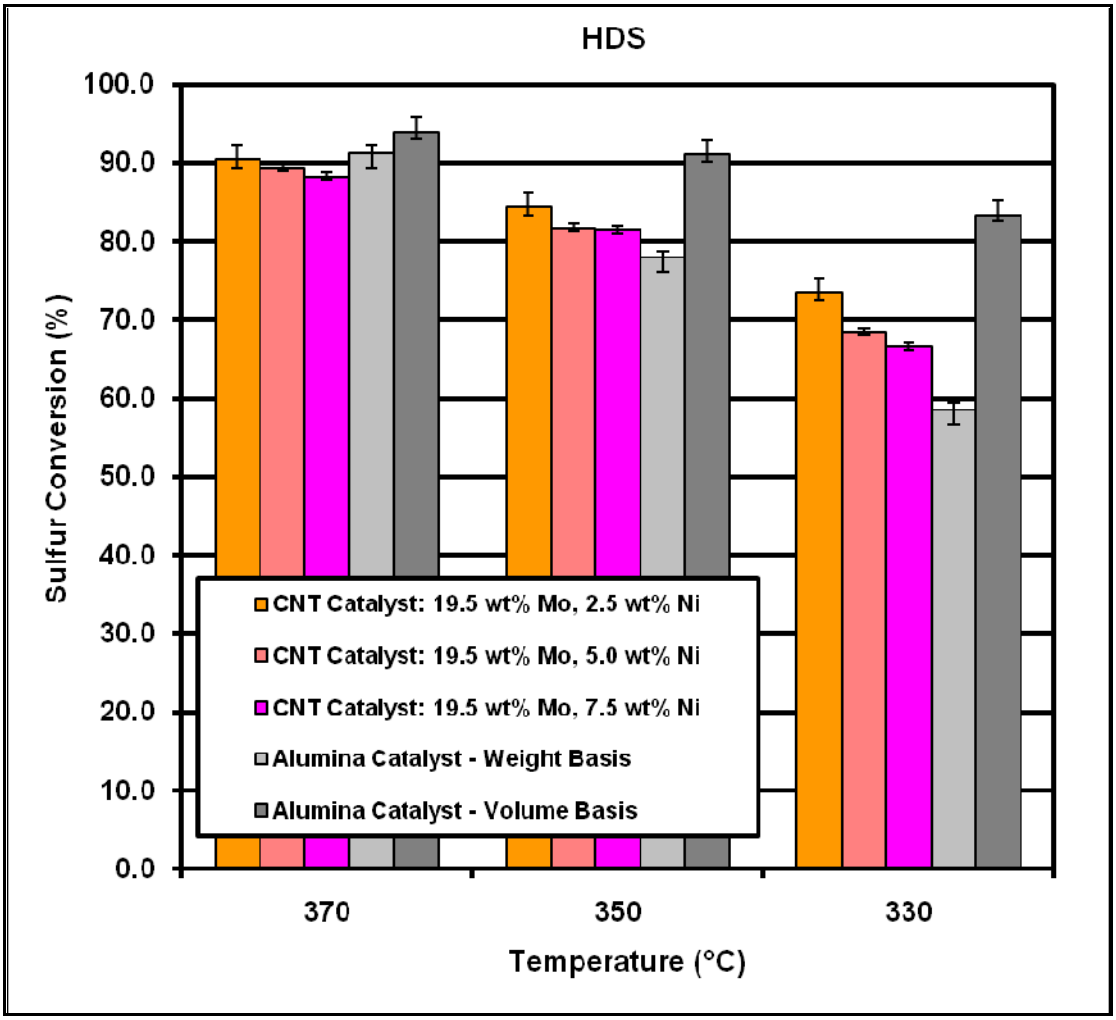

Figure 6.17: HDS steady-state activities (wt.%) for the Ni loading optimization of NiMo/*MWCNT* catalysts for hydrotreatment of coker light gas oil. Pressure: 8.8 MPa. Weight basis: WHSV = 4.5 h^{-1}. Volume basis: LHSV = 2.0 h^{-1}. Catalyst loading: 2.00 g. H_2/CLGO volumetric flow ratio: 600/1. Temperature: 370-330°C.

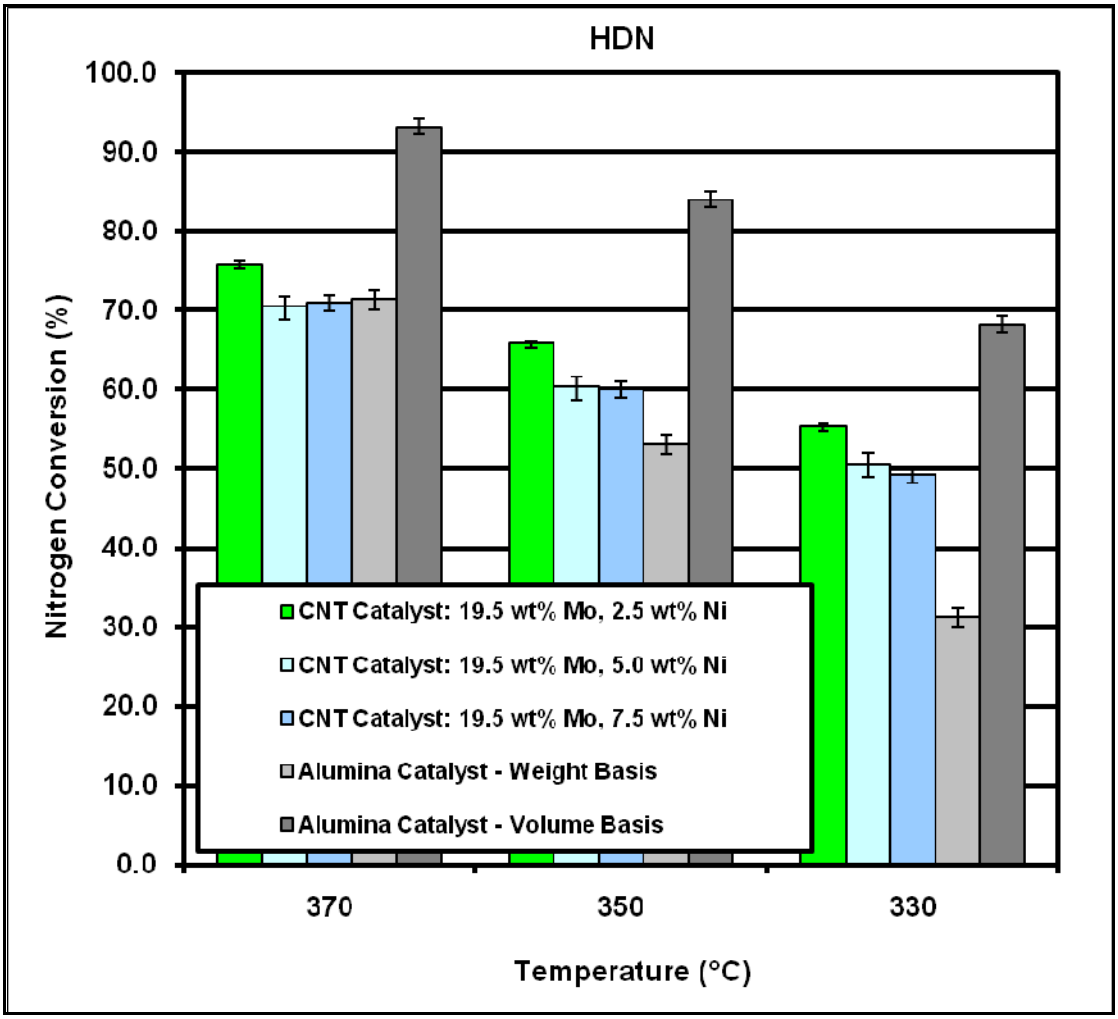

Figure 6.18: HDN steady-state activities (wt.%) for the Ni loading optimization of NiMo/*MWCNT* catalysts for hydrotreatment of coker light gas oil. Pressure: 8.8 MPa. Weight basis: WHSV = 4.5 h^{-1}. Volume basis: LHSV = 2.0 h^{-1}. Catalyst loading: 2.00 g. H_2/CLGO volumetric flow ratio: 600/1. Temperature: 370-330°C.

and HDN activities, respectively, for each of the three catalysts. Tabulated results can also be found in Table 6.13. It was found from varying the Ni loading that the HDS and HDN activities of the MWCNT-based catalyst decreased as the nickel weight percentage was increased beyond 2.5%. It was concluded that metal loadings of 2.5 wt.% Ni and 19.5 wt.% Mo were the optimum loadings for the cat-65 MWCNT support. For descending reaction temperatures of 370, 350, and 330°C, this optimum catalyst produced sulfur conversions of 90.5, 84.4, and 73.5%, respectively, and nitrogen conversions of 75.9, 65.8, and 55.3%, respectively.

Each MWCNT catalyst prepared and screened during metal loading optimization study was compared to a commercial γ–alumina catalyst based on equivalent weight and volumetric amounts. All five MWCNT-supported catalysts displayed lower HDS and HDN activities than the commercial catalyst on a volumetric basis. The commercial catalyst showed slightly higher sulfur conversions of 93.9, 91.0, and 83.4%, along with much higher nitrogen conversions of 93.2, 84.0, and 68.2%, as the reaction temperatures decreased. A definitive conclusion can't be reached on the effectiveness of each catalyst based on this comparison alone. This is due to the commercial catalyst containing approximately 1.5× as much Ni and 2× as much Mo when the catalysts are compared on a volumetric basis. Optimizing the conditions of the MWCNT functionalizing via HNO_3 could allow higher metal loadings to be better dispersed on the MWCNT supports. It was determined that stability studies comparing the γ–alumina and MWCNT supports in a CLGO

Table 6.13
HDS & HDN steady-state activities (wt.%) of NiMo/MWCNT catalysts compared to $NiMoP/\gamma\text{-}Al_2O_3$ commercial catalyst for the optimization of metal loadings in coker light gas oil hydrotreatment. Pressure: 8.8 MPa. Weight basis: WHSV = 4.5 h^{-1}. Volume basis: LHSV = 2.0 h^{-1}. Catalyst loading: 2.00 g. H_2/CLGO volumetric flow ratio: 600/1.

Catalyst	Sulfur and nitrogen removal at each reaction temperature (wt.%)					
	370°C		350°C		330°C	
	Sulfur	Nitrogen	Sulfur	Nitrogen	Sulfur	Nitrogen
CNT – 13.0 wt.% Mo, 2.5 wt.% Ni	89.4	71.7	81.4	60.6	68.3	50.8
CNT – 19.5 wt.% Mo, 2.5 wt.% Ni	90.5	75.9	84.4	65.8	73.5	55.3
CNT – 26.0 wt.% Mo, 2.5 wt.% Ni	84.4	67.2	73.4	58.3	58.4	50.6
CNT – 19.5 wt.% Mo, 5.0 wt.% Ni	89.4	70.5	81.6	60.3	68.4	50.6
CNT – 19.5 wt.% Mo, 7.5 wt.% Ni	88.3	71.0	81.4	60.0	66.5	49.3
Commercial – Weight Basis	91.2	71.4	77.9	53.2	58.5	31.3
Commercial – Volume Basis	93.9	93.2	91.0	84.0	83.4	68.2

hydrotreating application would have to be performed to determine how long-term deactivation affects the sulfur and nitrogen conversions for each catalyst. These studies were performed over a 28-day study period for each catalyst and are further discussed in section 6.6 of this report.

6.5 Kinetics Study of HDS/HDN for the Optimum NiMo/CNT Catalyst

The properties of the CLGO feedstock used for this portion of the research can be found in Appendix C. The methods of calculating the molar concentrations of N and S and the HDN and HDS reaction rates are presented in Appendix D. The reaction parameters at each sampling time and the N and S conversion data of the product liquid are reported in Appendix E. The purpose of this section of the project was to determine the effect of reaction parameters on the HDS and HDN activities of a NiMo/MWCNT catalyst within a hydrotreating trickle bed reactor. Based on this data, kinetic models were established using a non-linear regression solver platform to predict the hydrotreating activities of the NiMo/MWCNT catalyst during operation. The effect of H_2S and NH_3 concentration on both the mass transfer resistances and hydrotreating activities were assumed negligible (Korsten and Hoffman, 1996).

6.5.1 Mass Transfer Resistances for the HDS/HDN Reactions

An evaluation of the mass transfer resistances was performed for the NiMo/MWCNT hydrotreating process to determine their effect on the results on the kinetic analysis. This evaluation was divided into two parts: external mass transfer,

consisting of the diffusion of H_2 (gas phase) into the CLGO (liquid phase) exterior to the catalyst particles; and internal mass transfer, consisting of the diffusion of the organic sulfur and nitrogen compounds within the interior pores of the catalyst particles to reach the active sites. The details of the external and internal mass transfer analysis can be found in Appendix F and Appendix G, respectively.

The external mass transfer resistance analysis was performed using a criterion developed by Charles N. Satterfield (1969). The criterion determines whether the rate of hydrogen conversion in the HDN and HDS reactions or the rate of hydrogen mass transfer through the CLGO liquid phase to the catalyst surface is the rate determining step for the overall hydrotreating reactions. Table F.1 of Appendix F reports the most pertinent results of the analysis, as well as the range of possible values for the parameters as the reaction conditions were changed. For each reaction condition, the left side of Satterfield's criterion for both reactions ($\boldsymbol{S_{HDS}}$ and $\boldsymbol{S_{HDN}}$) was of the same magnitude (10^{-4}) as the overall mass transfer coefficient for hydrogen gas. The values of $\boldsymbol{S_{HDS}}$ validated Satterfield's criterion for all reaction conditions, while all values of $\boldsymbol{S_{HDN}}$ did not. It can be concluded from these results that mass transfer from the gas phase to the catalyst surface can be ignored for the overall hydrodenitrogenation reaction, but not for the overall hydrodesulfurization reaction. This reflects the higher consumption of H_2 for the HDS reaction. Under the primary conditions shown in Table F.1 (T = 350°C; P = 88 bar; LHSV = 2.0 h^{-1}), hydrogen is consumed for HDS at 6.5 times the rate for HDN. Because of these findings, the bulk mass transfer

limitations cannot be ignored for the overall HDS process. This reflects the high demand of hydrogen that exists due to the high concentration of sulfur in the petroleum feedstock. The result of this determination means that the apparent reaction rates that are found over the course of the kinetic study will be more sensitive to the reaction conditions than the intrinsic rates of the reactions.

The first step when examining the internal mass transfer limitations for the NiMo/MWCNT hydrotreating process was to find if isothermal conditions could be assumed throughout the cross-section of the catalyst pellet. The isothermality of the catalyst pellet was confirmed by two ways: finding the highest potential temperature rise between the core and surface of the pellet (Fogler, 2006), and by the confirmation of Anderson's criterion (1963). Table G.1 of Appendix G presents the important results and range of parameter values for these particular examinations. From analyzing the highest temperature difference between the center and surface of the catalyst pellets, it was found that the value of ΔT_{MAX} would never exceed 0.05 K. This appeared to make isothermality a reasonable assumption. Further contributing to this assumption was the verification of Anderson's criterion. The right side of the criterion was found to be far greater than the left side for both reactions; $\times 10^4$ greater in magnitude for HDS and $\times 10^5$ greater in magnitude for HDN. Confirmation of this inequality makes the assumption of isothermal behavior of the NiMo/MWCNT catalyst theoretically acceptable.

The effectiveness factor, a ratio of the actual overall reaction rate with respect to the maximum potential reaction rate (i.e. if the internal catalyst surfaces were exposed to the conditions of the external catalyst surfaces), is typically determined by first determining the dimensionless Thiele modulus. However, determining the Thiele modulus requires information regarding the intrinsic reaction rates. It is often difficult to determine these intrinsic reaction rates, especially with the external mass transfer resistances that were found for the given reaction system. To overcome this obstacle, an alternative dimensionless modulus (Satterfield, 1970) defined by the overall reaction rate was determined as a means of estimating the effectiveness factor for each of the examined operating conditions. The bulk diffusivities of sulfur and nitrogen compounds were assumed to be the same as all compounds in the CLGO feedstock. Because the CLGO diffusivities were found to be $\times 10^{-1}$ lower in magnitude compared to H_2 diffusion in CLGO, only organosulfur and organonitrogen diffusion was considered for internal mass transfer resistances.

The modulus ($\boldsymbol{\Phi}$) and effectiveness factor ($\boldsymbol{\eta}$) were determined at both the inlet and outlet of the trickle bed reactor. The results are tabulated in Table G.2 for the HDS reaction and Table G.3 for the HDN reaction. The inlet and outlet value ranges of $\boldsymbol{\Phi}$ for HDS were 0.755-0.441 and 6.375-1.049, respectively. These modulus values corresponded to average effectiveness factors for the HDS reaction of 0.963 at the inlet and 0.837 at the outlet. For the HDN reaction, inlet and outlet modulus ranges of 0.476-0.178 and 1.184-0.223, respectively, were found. The average

effectiveness factors found from these HDN modulus values were 0.980 and 0.961 for the reactor inlet and outlet, respectively. The high effectiveness factor values found are an indication that the HDS/HDN reactions are beyond first-order rate laws and that these results should be interpreted with caution. The observed trends were expected as the inlet factor values were controlled by the LHSV and the outlet factor values were controlled by the reaction temperature. Lower space velocities resulted in higher η inlet values, while lower reaction temperatures resulted in higher η outlet values. The lower values at the outlet of the reactor reflect the fact that the diffusion limitations in the catalyst pellets are more noticeable at lower impurity concentrations. The internal mass transfer resistances appeared to have a greater impact on the HDS reaction than on the HDN reaction, as the factor values for sulfur removal dropped significantly from the inlet to the outlet. It can be concluded that the rate of the HDS reaction is governed by the rate of diffusion much more significantly than the HDN reaction.

6.5.2 Power Law Models

Power law models were the first rate equations fitted with the kinetic study data. The results of the determined parameters for both the HDS and HDN rate laws are reported in Table 6.14. As was previously discussed in section 2.2.1, power law models for hydrotreating light gas oils can have HDS reaction orders ranging from 1.o to 2.5, while HDN reaction orders often range from 0.5 to 1.5. The reaction orders found from modeling the NiMo/MWCNT application appear to be in agreement with

Table 6.14
Power law parameter values fitted for the HDS and HDN reactions of CLGO. Pressure: 8.8 MPa. Catalyst loading: 2.00 g. H_2/CLGO volumetric flow ratio: 600/1.

$-r_{HDS} = k_{HDS} \cdot C_S^n$ **(6.1)**		$-r_{HDN} = k_{HDN} \cdot C_N^v$ **(6.2)**	
E_{HDS}	161 **kJ/mol**	E_{HDN}	82.3 **kJ/mol**
A_{HDS}	4.68×10^{11} $\mathbf{M^{-1.6}\cdot s^{-1}}$	A_{HDN}	4.10×10^{3} $\mathbf{M^{-0.2}\cdot s^{-1}}$
n	2.6	v	1.2
$(R^2)_{HDS}$	0.9887	$(R^2)_{HDN}$	0.9080
$(R^2{}_A)_{HDS}$	0.9872	$(R^2{}_A)_{HDN}$	0.8960

these reported values (2.6 for HDS, 1.2 for HDN). The determined activation energies for the HDS (161 kJ/mol) and HDN (82.3 kJ/mol) reactions from the power law models are more comparable to previous literature values on an HDN basis, and less so on an HDS basis. Trytten et al. (1990) found apparent and intrinsic activation energies of 109 kJ/mol and 165 kJ/mol, respectively, for the HDS of light gas oil using NiMo/γ-alumina catalyst. For HDN, apparent and intrinsic activation energies of 78 kJ/mol and 103 kJ/mol were found. These results, however, were both from first-order power law functions. Similar first-order power law studies for heavy gas oils (Diaz-Real et al., 1993; Gusta et al., 2006) yielded HDS energies ranging from 87 kJ/mol to 88 kJ/mol and HDN energies from 83 kJ/mol to 105 kJ/mol. The most likely reason for the HDS activation energy being less comparable to the HDN value is because of the H_2 mass transfer limitations found from the external resistance study. Hydrogen gas transfer to the catalyst exterior was impacted more significantly by temperature changes and, as the rate limiting step in the reaction, would cause the rate law to depend more heavily on the reaction temperature.

The relatively high values for the coefficients of regressions, both standard (R^2) and adjusted (R^2_A), reflect the accuracy of the power law HDS and HDN models for the collected kinetic data. This, along with the simplicity of these equations, make the power law models most practical for predicting the NiMo/MWCNT catalyst performance for CLGO hydrotreating.

6.5.3 Independent Langmuir-Hinshelwood Models

The first generalized Langmuir-Hinshelwood models and their fitted parameters are shown in Table 6.15. The two reactions were modeled independently assuming the reactions occurred on separate active sites. This means that each reaction is only inhibited by its own species. Most noteworthy from this study was the only slight decrease in the HDS activation energy from the power law model (161 kJ/mol to 155 kJ/mol) compared to the significant decrease in the HDN activation energy (82.3 kJ/mol to 42.3 kJ/mol). This greater decline in the activation energy magnitude is the result of a greater order of inhibition being found for the HDN reaction ($\boldsymbol{u}$ = 3.0 compared to $\boldsymbol{m}$ = 1.2). Taking into account the inhibition of active sites leads to the expected result of increased reaction orders; 3.0 for HDS and 1.5 for HDN. The heats of adsorption ($\boldsymbol{\lambda_S}$ = 71.9 kJ/mol, $\boldsymbol{\lambda_N}$ = 79.3 kJ/mol) found for both adsorption equilibrium constants were considerably higher than those found in a previous study; 3.4 to 11.6 kJ/mol for $\boldsymbol{\lambda_S}$ (Vishwakarma et al., 2007). However, this same study also found activation energies that were lower by a magnitude of 10^1. The many adsorption equilibrium constants reported by Girgis and Gates (1991) for sulfur and nitrogen compounds ranged in magnitude from 10^1 to 10^3 L/mol, while the K values calculated in this study ranged from 10^4 to 10^6 in magnitude. It can be concluded that these higher-than-expected adsorption constants are the result of the reaction orders in this study being significantly higher than the first-order rate laws collected by Girgis and Gates.

Table 6.15
Independent Langmuir-Hinshelwood parameter values fitted for the HDS and HDN reactions of CLGO. Pressure: 8.8 MPa. Catalyst loading: 2.00 g. H_2/CLGO volumetric flow ratio: 600/1.

$r_{HDS} = \frac{k_{HDS} \cdot C_S^{\ n}}{\left[1 + K_S C_S\right]^m}$ **(6.3)**		$r_{HDN} = \frac{k_{HDN} \cdot C_N^{\ v}}{\left[1 + K_N C_N\right]^u}$ **(6.4)**	
E_{HDS}	155 **kJ/mol**	E_{HDN}	42.3 **kJ/mol**
A_{HDS}	4.68×10^{11} $\mathbf{M^{-2.0}\cdot s^{-1}}$	A_{HDN}	6.96 $\mathbf{M^{-0.5}\cdot s^{-1}}$
n	3.0	v	1.5
S_λ	1.86×10^{-6} $\mathbf{M^{-1}}$	N_λ	5.59×10^{-7} $\mathbf{M^{-1}}$
λ_S	71.9 **kJ/mol**	λ_N	79.3 **kJ/mol**
m	1.2	u	3.0
$(R^2)_{HDS}$	0.9905	$(R^2)_{HDN}$	0.9146
$(R^2{}_A)_{HDS}$	0.9876	$(R^2{}_A)_{HDN}$	0.8890

The addition of a second species concentration term leads to an expected increase in the coefficient of regression values and makes these the most accurate rate laws of those that were modeled. However, their accuracy is only a slight improvement over the power law models and sacrifices simplicity in doing so. Their usage would be beneficial if a high degree of accuracy were to be desired.

6.5.4 Co-dependent Langmuir-Hinshelwood Models

The second Langmuir-Hinshelwood hybrid models were co-dependent and were therefore solved simultaneously. The underlining principle behind these models is that both reactions occurred on the same active sites. This means that the adsorption equilibrium constants for each species (S and N) were considered the same for both equations. The fitted parameters for these simultaneous equations were determined and tabulated in Table 6.16. The models were fitted by finding the highest sum of the two coefficients of regression. Negligible change occurred in the values of the activation energies and the heats of adsorption, meaning that the effect of temperature on the values of the rate and adsorption constants remained unchanged. The order of HDN inhibition significantly decreased from 3.0 to 1.7, while the inhibition order for the HDS process increased slightly from 1.2 to 1.3. Making the adsorption equilibrium constants shared across each rate expressions led to slight decreases the coefficient of regression values. However, considering the direct influence that sulfur concentration has on the rate of nitrogen conversion, and vice

Table 6.16
Co-dependent Langmuir-Hinshelwood parameter values fitted for the HDS and HDN reactions of CLGO. Pressure: 8.8 MPa. Catalyst loading: 2.00 g. H_2/CLGO volumetric flow ratio: 600/1.

$r_{HDS} = \frac{k_{HDS} \cdot C_S^{\ n}}{\left[1 + K_S C_S + K_N C_N\right]^m}$ **(6.5)**		$r_{HDN} = \frac{k_{HDN} \cdot C_N^{\ v}}{\left[1 + K_S C_S + K_N C_N\right]^u}$ **(6.6)**	
E_{HDS}	155 **kJ/mol**	E_{HDN}	42.3 **kJ/mol**
A_{HDS}	4.68×10^{11} $\mathbf{M^{-2.0}\cdot s^{-1}}$	A_{HDN}	6.46 $\mathbf{M^{-0.5}\cdot s^{-1}}$
n	3.0	v	1.5
m	1.3	u	1.7
S_λ	9.13×10^{-7} $\mathbf{M^{-1}}$	S_λ	9.13×10^{-7} $\mathbf{M^{-1}}$
λ_S	71.9 **kJ/mol**	λ_S	71.9 **kJ/mol**
N_λ	4.35×10^{-7} $\mathbf{M^{-1}}$	N_λ	4.35×10^{-7} $\mathbf{M^{-1}}$
λ_N	79.3 **kJ/mol**	λ_N	79.3 **kJ/mol**
$(R^2)_{HDS}$	0.9899	$(R^2)_{HDN}$	0.9140
$(R^2_A)_{HDS}$	0.9862	$(R^2_A)_{HDN}$	0.8823

versa, makes the co-dependent generalized models the most accurate from a theoretical viewpoint.

6.5.5 System Pressure Variation

The system pressure of the NiMo/MWCNT hydrotreating process was varied between 6.6 and 11.0 MPa at 1.1 MPa increments. The purpose of this study was to determine how pressure variation affected the apparent proportionality constants of the HDS and HDN reaction models (i.e. defining A_{HDS} and A_{HDN} as a function of system pressure). Two gas oil product samples were collected at each system pressure. Figure 6.19 shows the results of the measured sulfur and nitrogen concentrations in the product samples. A consistent increase, as expected, was found in the conversion rates for both the HDS and HDN reactions as the pressure in the trickle bed reactor was increased. The pressure increase had a more profound effect on nitrogen conversion over sulfur conversion. Increasing the pressure from 6.6 MPa to 11.0 MPA led to a nitrogen conversion increase from 21.0% to 30.2%. An increase from 62.4% to 65.4% was found for sulfur conversion as a result of increasing the system pressure from 6.6 MPa to 11.0 MPa.

Power law expressions were developed for the apparent proportionality constants (i.e. apparent Arrhenius constants) of each type of HDS and HDN reaction model: the power law models, the independent generalized Langmuir-Hinshelwood models, and the co-dependent generalized Langmuir-Hinshelwood models. Plots of

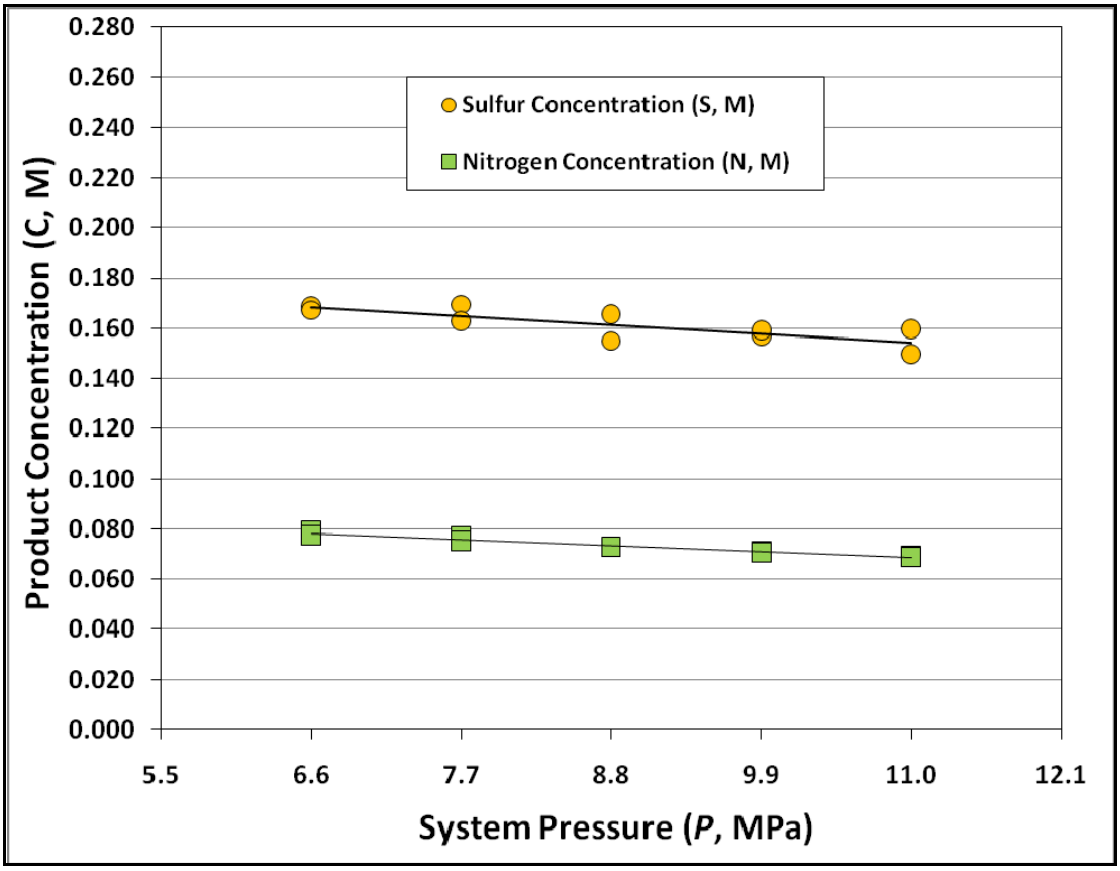

Figure 6.19: HDS and HDN steady-state activities for the system pressure variation during the hydrotreatment of coker light gas oil. Weight basis: WHSV = 4.5 h^{-1}. Volume basis: LHSV = 2.0 h^{-1}. NiMo/MWCNT catalyst loading: 2.00 g. H_2/CLGO volumetric flow ratio: 600/1. Temperature: 330°C.

these established expressions can be found in Figures 6.20, 6.21, and 6.22 on the following pages. The constants that were determined from each plot were the true proportionality/Arrhenius constants ($S_{E\alpha}$ and $N_{E\alpha}$) and the pressure term exponents (p_S and p_N). The determined values for each of these constants, as well as the coefficient of regression (R^2) for each plotted trend line, are included in each graph. For each of the three HDS reaction models, a pressure term exponent of 0.33 was determined from the collected experimental data. The conclusion that was reached from Figure 6.19 was confirmed from the plotted power relations, as the effect of system pressure variation was found to have a greater influence on the HDN activity of the NiMo/MWCNT catalyst than the HDS activity. The pressure term exponents for the HDN reaction models were found to be 0.87 for the power law model, 0.81 for the independent GLH model, and 0.82 for the co-dependent GLH model. A possible explanation for the greater dependence on pressure for nitrogen removal is the lower reaction order of hydrodenitrogenation and nitrogen conversion being its rate limiting step. By contrast, the mass transfer of sulfur compounds was concluded to be the rate limiting step for the overall hydrodesulfurization reaction. Increasing the system pressure would significantly increase the conversion steps of both the HDS and HDN reaction by increasing H_2 partial pressure. However, this pressure increase would have less effect on the mass transfer of heteroatom compounds to catalyst active sites, thereby having a greater effect on the HDN reaction than the HDS reaction.

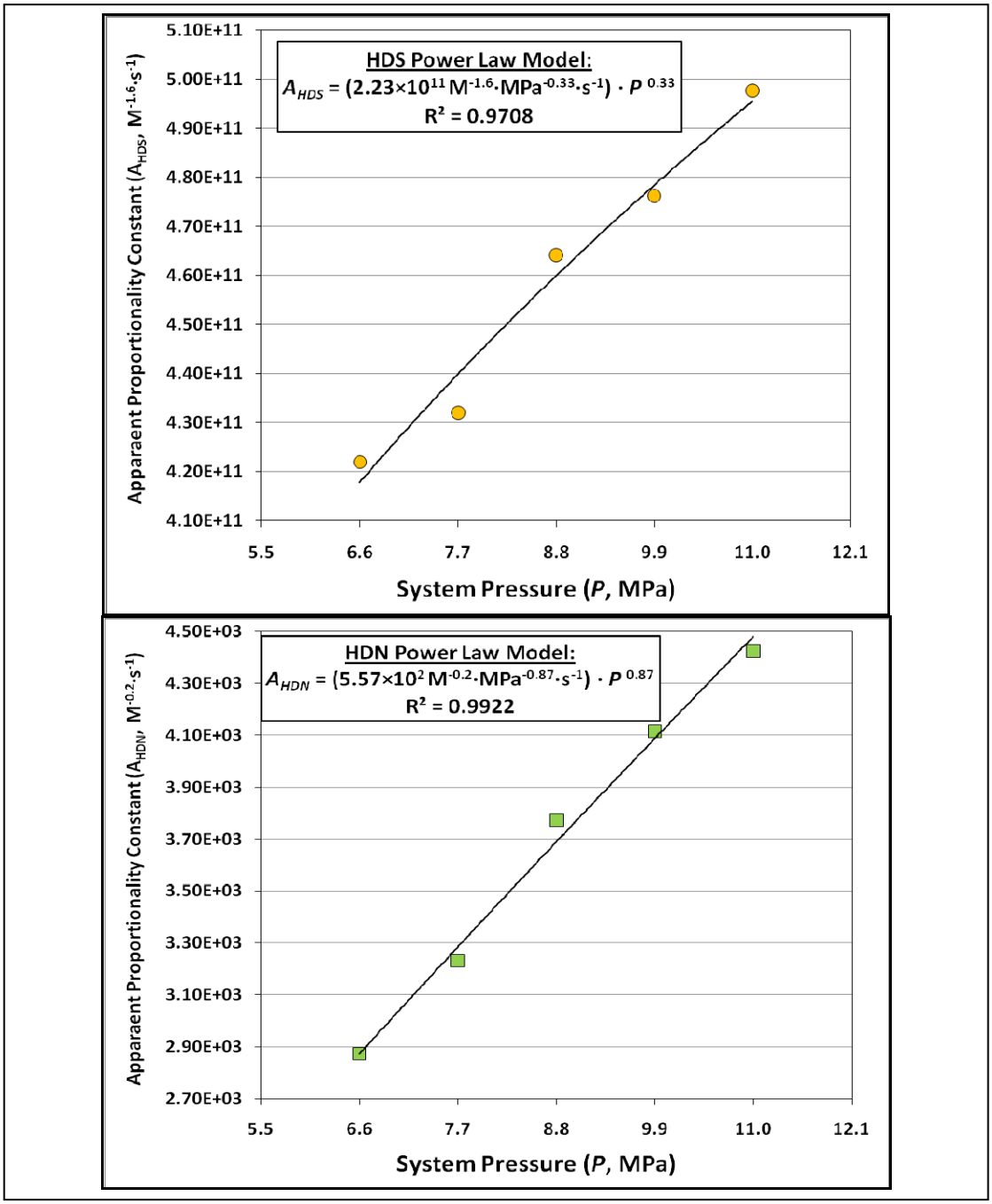

Figure 6.20: Apparent proportionality constants as functions of system pressure for both the HDS and HDN power law models. Weight basis: WHSV = 4.5 h^{-1}. Volume basis: LHSV = 2.0 h^{-1}. NiMo/MWCNT catalyst loading: 2.00 g. H_2/CLGO volumetric flow ratio: 600/1. Temperature: 330°C.

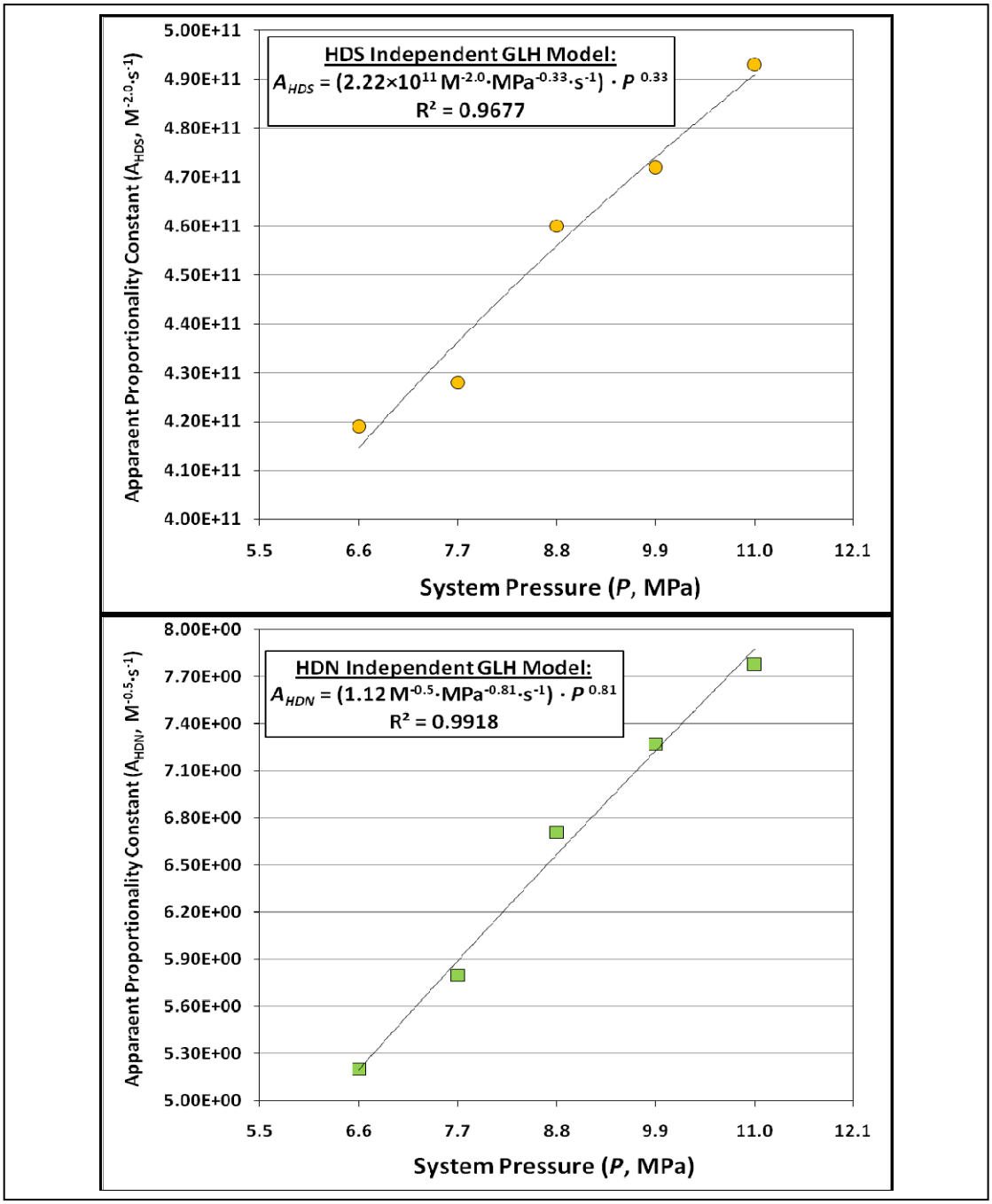

Figure 6.21: Apparent proportionality constants as functions of system pressure for both the HDS and HDN independent generalized Langmuir-Hinshelwood models. Weight basis: WHSV = 4.5 h^{-1}. Volume basis: LHSV = 2.0 h^{-1}. NiMo/MWCNT catalyst loading: 2.00 g. H_2/CLGO volumetric flow ratio: 600/1. Temperature: 330°C.

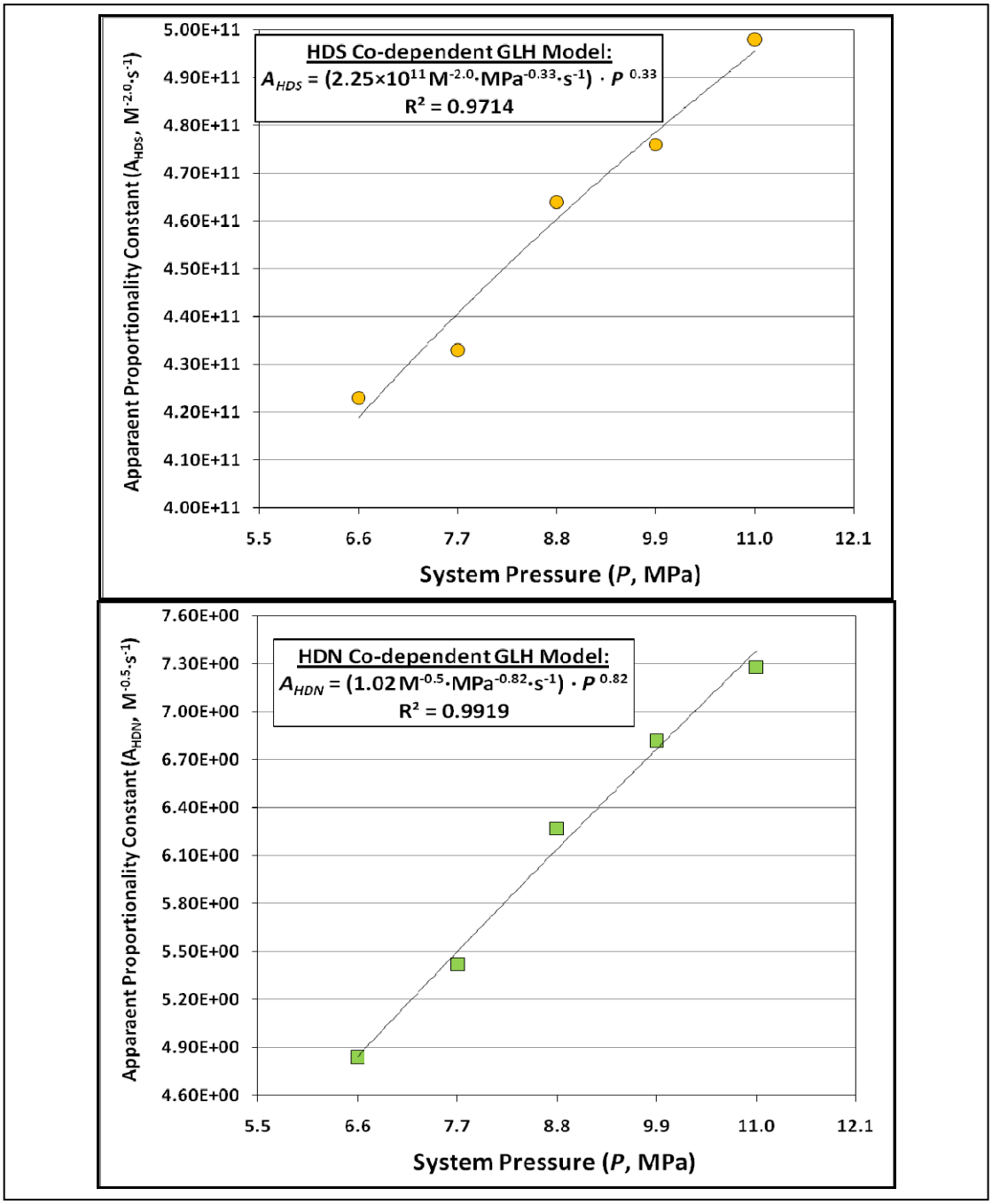

Figure 6.22: Apparent proportionality constants as functions of system pressure for both the HDS and HDN co-dependent generalized Langmuir-Hinshelwood models. Weight basis: WHSV = 4.5 h^{-1}. Volume basis: LHSV = 2.0 h^{-1}. NiMo/MWCNT catalyst loading: 2.00 g. H_2/CLGO volumetric flow ratio: 600/1. Temperature: 330°C.

6.5.6 Gas/Liquid Flow Ratio Variation

The final system parameter that was varied for the NiMo/MWCNT hydrotreating process was the ratio between the volumetric flow rates of H_2 and CLGO (***G/L***). Three gas oil product samples were taken at three distinct ***G/L*** flow ratios. The ***G/L*** parameter values were maintained by maintaining a CLGO volumetric flow rate 10 mL/h and varying the H_2 flow rate from 75, 100, and 125 mL/min. The results from the analysis of this specific parameter can be found in Figure 6.23. Increasing the flow rate of H_2 relative to the flow rate of CLGO was shown to significantly improve the conversion of sulfur compounds for the operation. Using volumetric flow ratios of 450, 600, and 750 mL/mL resulted in average sulfur conversions of 59.0, 64.1, and 67.5%, respectively. The same trend was not found for nitrogen removal from the coker light gas oil, as the nitrogen concentration in the product samples remained relatively constant during the changes to the quantity of H_2 in the system. An average nitrogen removal of 28.5% was obtained across all of the tested volumetric flow ratios. It can be concluded from the results of Figure 6.23 that, because mass transfer was determined to be the rate limiting step in the overall HDS reaction, increasing the flow of H_2 in the system would improve the mass transfer of reactants to the active sites of the catalyst. From this same viewpoint, increasing H_2 flow would not have a significant effect on the overall HDN reaction, as nitrogen

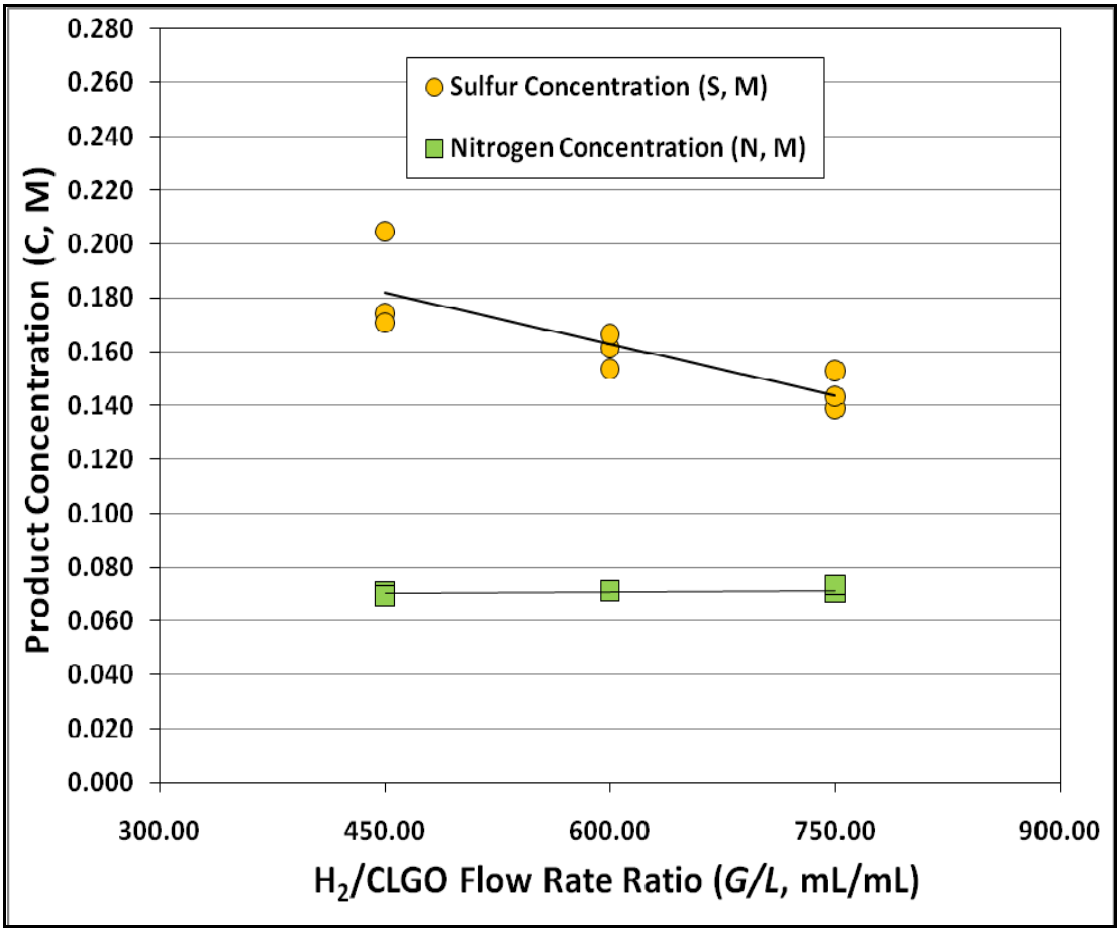

Figure 6.23: HDS and HDN steady-state activities for H_2/CLGO flow rate ratio variation during the hydrotreatment of coker light gas oil. Weight basis: WHSV = 4.5 h^{-1}. Volume basis: LHSV = 2.0 h^{-1}. NiMo/MWCNT catalyst loading: 2.00 g. Pressure: 8.8 MPa. Temperature: 330°C.

conversion was determined from section 6.5.1 to be the rate limiting step for nitrogen removal. It can be concluded for the range of ***G/L*** values tested that HDS performance for the NiMo/MWCNT catalyst reactor is dependent upon the H_2/CLGO volumetric flow ratio, while HDN performance in independent from the H_2/CLGO volumetric flow ratio.

6.6 Stability Study for the Optimum NiMo/CNT Catalyst

The sixth and final phase of the project was to perform a stability study with the optimum NiMo/MWCNT catalyst and compare it under equivalent volumetric conditions with a γ-alumina commercial catalyst. Samples were collected and analyzed every 24 hours over a 28 day span. The average steady-state conversions of sulfur and nitrogen were determined after allowing a three day pre-coking phase for each catalyst before reaching steady-state conditions. The results can be found in Figures 6.24 and 6.25 on the following page. The optimum NiMo/MWCNT catalyst displayed steady-state conversions of 87.7% for sulfur compounds 58.9% for nitrogen compounds. An equal volume loading of commercial catalyst had steady-state activities of 94.7% sulfur removal and 89.6% nitrogen removal. Because this was a volume-based comparison, the commercial catalyst contained significantly higher metal masses (~390 mg Mo, ~50 mg Ni for the MWCNT catalyst; ~520mg Mo, ~120 mg Ni for the γ-alumina catalyst). Also contributing to the potential inequality of the catalyst comparison was the presence of phosphorus on the surface of the commercial catalyst. Experimenting with phosphorus loading on the surface of the MWCNT

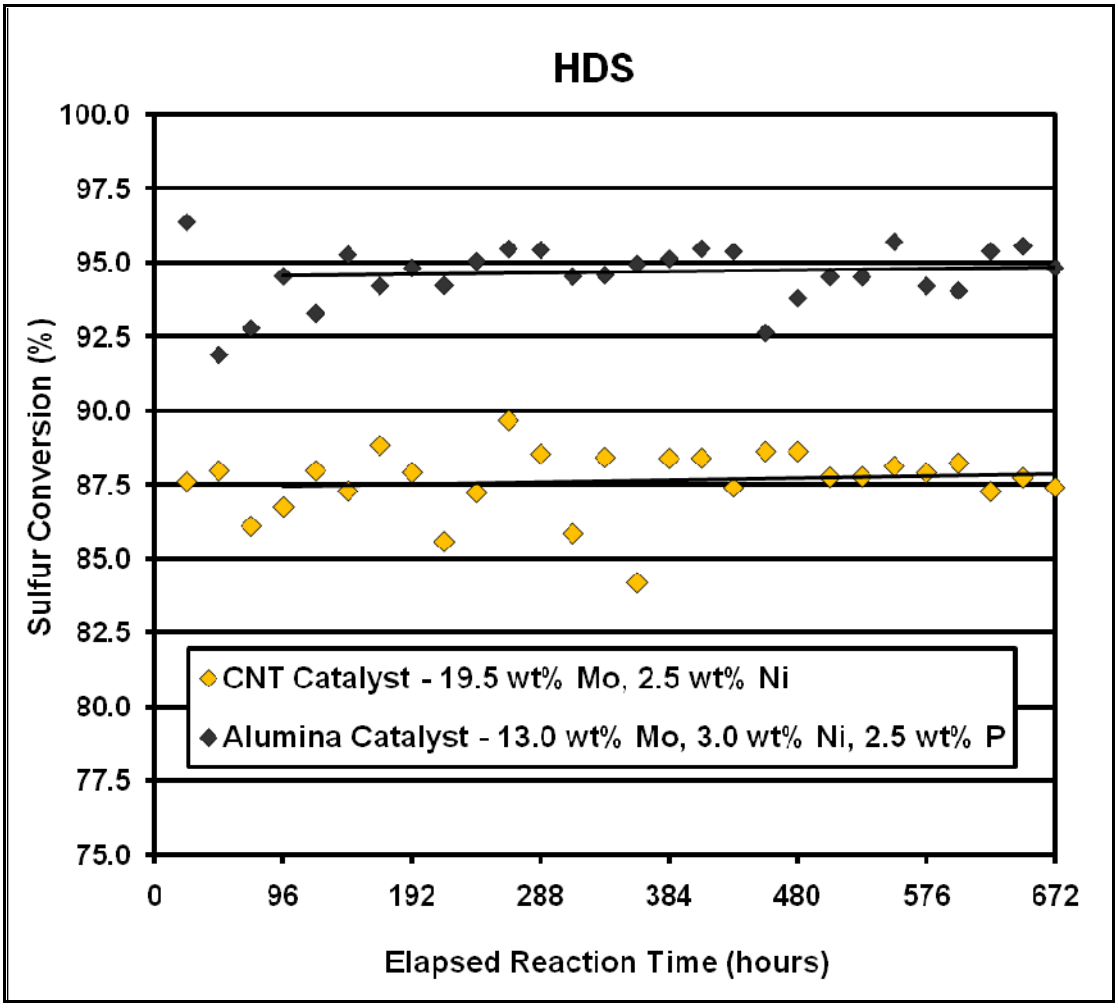

Figure 6.24: HDS steady-state activities over a 28-day stability study for the hydrotreatment of coker light gas oil. Volume basis: LHSV = 2.0 h^{-1}. NiMo/MWCNT catalyst loading: 2.00 g. Pressure: 8.8 MPa. Temperature: 370°C. H_2/CLGO volumetric flow ratio: 600/1.

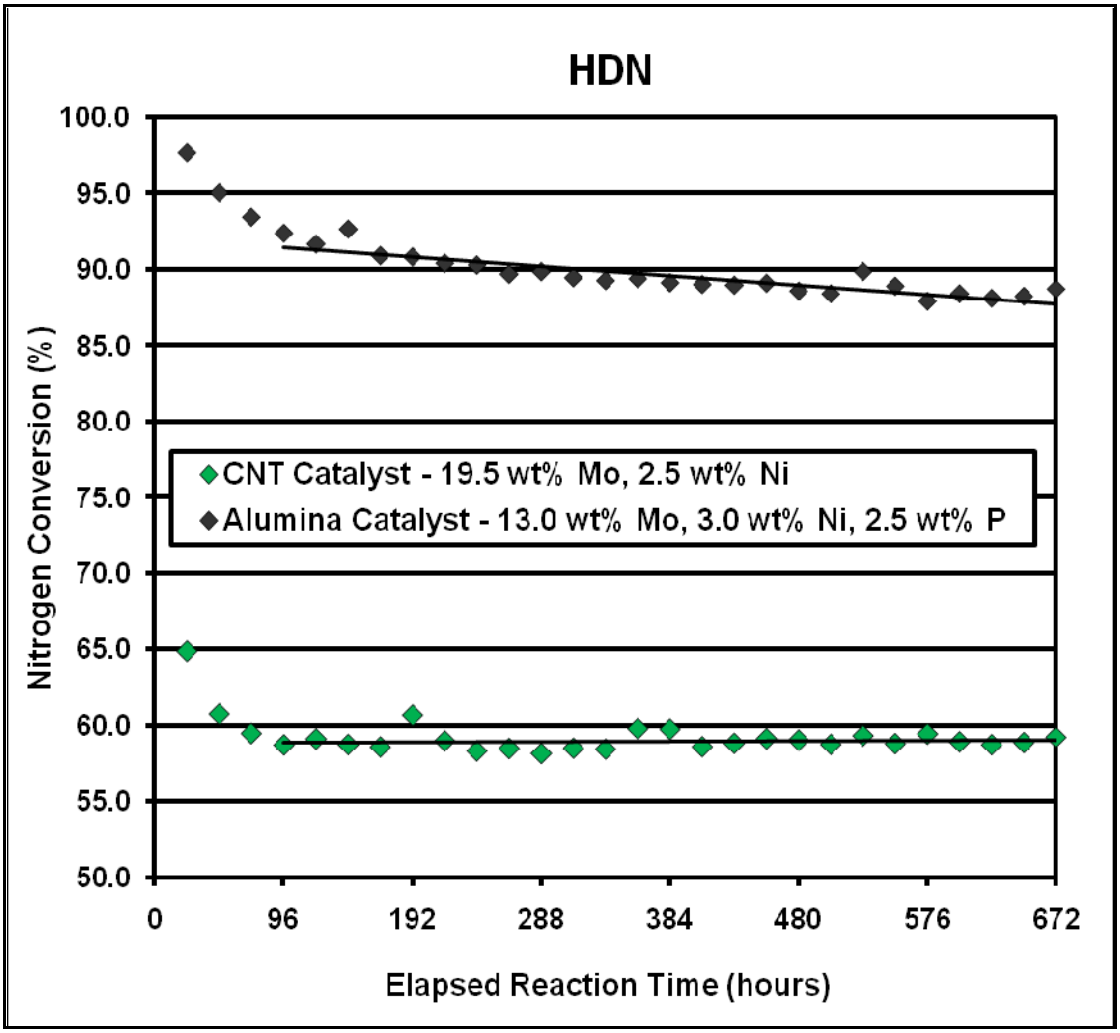

Figure 6.25: HDN steady-state activities over a 28-day stability study for the hydrotreatment of coker light gas oil. Weight basis: WHSV = 4.5 h^{-1}. Volume basis: LHSV = 2.0 h^{-1}. NiMo/MWCNT catalyst loading: 2.00 g. Pressure: 8.8 MPa. Temperature: 370°C. H_2/CLGO volumetric flow ratio: 600/1.

support would be required to determine if it would benefit the HDS and HDN activities of the catalyst. Attempting longer and more extreme nitric acid refluxing conditions during the functionalization of the MWCNTs could allow for increased hydrotreating activities from higher metal loadings.

7 CONCLUSIONS AND RECOMMENDATIONS

7.1 Conclusions

The essential result of this study was determining the applicability and potential of multi-walled carbon nanotubes derived from anodic alumina templates as a catalyst support for gas oil hydrotreating. Through each phase of the project, several key conclusions were reached:

- **Part 1: Variation of CNT pore diameter and resulting characterization**

AAO films with varying pore channel diameters were successfully grown by changing the parameters of energy potential and oxalic acid concentration in an anodization process, resulting in MWCNTs with varying inner diameters from approximately 60 to 80 nm. The templates grown at a 40.0 V maximum potential and a 0.40 M oxalic acid concentration were found to result in CNTs with the most desirable structural characteristics. Specifically, CNTs with a 229 m^2/g BET surface area, a 0.658 cc/g single-point pore volume, and an 11.5 nm average pore diameter were achieved from AAO templates grown under these conditions.

- **Part 2: Effect of CNT pore diameter variation on catalyst performance**

MWCNTs with approximate inner diameters of 67 nm were found to provide the optimum HDS and HDN activities for a Ni (2.5 wt.%) Mo (13.0 wt.%) catalyst. The catalyst displayed sulfur conversions of 77.0%, 61.0%, and 47.4% and nitrogen

conversions of 37.5%, 26.7%, and 19.3% at reaction temperatures of 370°C, 350°C, and 330°C, respectively.

- **Part 3: Variation of CVD parameters and resulting characterization**

After testing nine different operating conditions for the chemical vapor deposition process, it was concluded that parameters of 650°C reaction temperature and 8.00 mL/(min·g) C_2H_2/AAO ratio produced the highest carbon yield (88.1%) of MWCNT product.

- **Part 4: Catalyst performance optimization and characterization**

The optimum loadings for the cat-65 support were found to be 2.5 and 19.5 weight percent for Ni and Mo, respectively. This catalyst was screened with CLGO and was found to give sulfur conversions of 90.5%, 84.4%, and 73.5% with nitrogen conversions of 75.9%, 65.8%, and 55.3% for temperatures of 370°C, 350°C, and 330°C, respectively. An equal mass loading of commercial NiMo/γ-Al_2O_3 catalyst offered HDS conversions of 91.2%, 77.9%, and 58.5% with HDN conversions of 71.4%, 53.2%, and 31.3% for temperatures of 370°C, 350°C, and 330°C, respectively.

- **Part 5: Determination of rate equations for optimum NiMo/CNT catalyst**

From a kinetic study, power law models were fitted for the HDS and HDN reactions, with reaction orders of 2.6 and 1.2, respectively, and activation energies of 161 kJ/mol and 82.3 kJ/mol, respectively. Generalized Langmuir-Hinshelwood

models were also fitted for the HDS and HDN reactions, with respective reaction orders of 3.0 and 1.5, and activation energies of 155 kJ/mol and 42.3 kJ/mol.

- **Part 6: Stability study for optimum NiMo/CNT catalyst**

For a 28-day stability study, the optimum NiMo/MWCNT catalyst displayed steady-state conversions of 87.7% for sulfur 58.9% for nitrogen. An equal volume loading of commercial γ–alumina catalyst had steady-state activities of 94.7% sulfur removal and 89.6% nitrogen removal.

7.2 Recommendations

Having completed the scope of the given MWCNT catalyst support project, the following recommendations are made for future work in the field of study:

- Optimizing the nitric acid refluxing conditions for functionalizing MWCNT supports should be performed to find the maximum loading of catalyst metals. Parameters to be considered would be HNO_3 concentration and refluxing time.

- The applicability of different bimetallic sulfide hydrotreating catalysts for the AAO-derived MWCNT supports, such as CoMo and NiW, should be tested to determine if their performance is comparable to or better than NiMo sulfide catalyst.

- The effects of adding promoters to the surface of the AAO-derived MWCNT supports, such as phosphorus and boron, should be attempted to determine if their promotion effects could be improved on a carbon nanotube support.

8 LIST OF REFERENCES

Abbaslou R.M.M., Tavassoli A., Soltan J., Dalai A.K., "Iron catalysts supported on carbon nanotubes for Fischer-Tropsch synthesis: Effect of catalytic site position", Applied Catalysis A: General, 47-52, 367, 2009

Ago H., Uehara N., Yoshihara N., Tsuji M., Yumura M., Tomonaga N., Setoguchi T., "Gas analysis of the CVD process for high yield growth of carbon nanotubes over metal-supported catalysts", Carbon, 2912-2918, 44, 2006

Ahmed T., Hydrocarbon Phase Behavior, Houston: Gulf Publishing, 1989

Ancheyta J., Angeles M.J., Macias M.J., Marroquin G., Morales R., "Changes in apparent reaction order and activation energy in the hydrodesulfurization of real feedstocks", Energy and Fuels, 189-193, 16, 2002

Ancheyta J., Speight J.G., Hydroprocessing of Heavy Oils and Residua, Boca Raton, FL: CRC Press, 2007

Anderson J.A., Pawelec B., Fierro J.L.G., "Mo-USY zeolites for hydrodesulfurization. I. Structure and distribution of molybdenum oxide phase", Applied Catalysis A: General, 37-54, 99, 1993

Anderson J. B., "Criterion for isothermal behavior of a catalyst pellet", Chemical Engineering Science, 147-148, 18, 1963

Aoyagi K., McCaffrey W.C., Gray M.R., "Kinetics of hydrocracking and hydrotreating of coker and oilsands gas oils", Petroleum Science and Technology, 997-1015, 21, 2003

Auer E., Freund A., Pietsch J., Tacke T., "Carbons as supports for industrial precious metal catalysts", Applied Catalysis A: General, 259-271, 173, 1998

Bej S.K., Dalai A.K., Adjaye J., "Comparison of hydrodenitrogenation of basic and nonbasic nitrogen compounds present in oil sands derived heavy gas oil", Energy & Fuels 377-383, 15, 2001

Besenbacher F., Brorson M., Clausen B.S., Helveg S., Hinnemann B., Kibsgaard J., Lauritsen J.V., Moses P.G., Nørshov J.K., Topsøe H., "Recent STM, DFT, and HAADF-STEM studies of sulphide-based hydrotreating catalysts: Insight into mechanistic, structural and particle size effects", Catalysis Today, 86-96, 130, 2008

Bhinde, M.V., "Quinoline hydrodenitrogenation kinetics and reaction inhibition", Ph.D. Dissertation, University of Delaware, Newark, 1979

Botchwey C., Dalai A.K., Adjaye J., "Two-stage hydrotreating of Athabasca heavy gas oil with interstage hydrogen sulfide removal: Effect of process conditions and kinetic analyses", Industrial and Engineering Chemistry Research 5854-5861, 43, 2004

Breysse M., Geauntet C., Afanasiev P., Blanchard J., Vrinat M., "Recent studies on the preparation, activation and design of active phases and supports of hydrotreating catalysts", Catalysis Today, 3-13, 130, 2008

Callejas M.A., Martinez M.T., "Hydroprocessing of maya residue: Intrinsic kinetics of sulfur, nitrogen, and vanadium removal reactions", Energy and Fuels, 629-636, 13, 1999

Chen P., Zhang H.B., Lin G.D., Hong Q., Tsai K.R., "Growth of carbon nanotubes by catalytic decomposition of CH_4 or CO on a catalyst", Carbon, 1495-1501, 35, 1997

Chen Y., Ciuparu D., Lim S., Haller G., Pfefferle L.D., "The effect of the cobalt loading on the growth of single wall carbon nanotubes by CO disproportionation on Co-MCM-41 catalysts", Carbon, 67-78, 44, 2006

Chianelli R.R., Berhault G., Torres B., "Unsupported transition metal sulphide catalysts: 100 years of science and application", Catalysis Today, 275-286, 147, 2009

Cocchetto J.F., Satterfield C.N., "Chemical Equilibria among quinoline and its reaction products in hydrodenitrogenation", Industrial and Engineering Chemistry Process Design and Development, 49-53, 20, 1981

Cruz J., Avalos-Borja M., López-Cordero R., Banares M.A., Fierro J.L.G., Palacios J.M., López-Agudo, "Influence of pH of the impregnation solution on the phosphorus promotion in W/Al_2O_3 hydrotreating catalysts", Applied Catalysis A: General, 97-110, 224, 2002

Daage M., Chianelli R.R., "Structure-function relations in molybdenum sulphide catalysts: The 'rim-edge' model", Journal of Catalysis, 414-427, 149, 1994

Dai H., "Carbon nanotubes: opportunities and challenges", Surface Science, 218-241, 500, 2002

Das N., Dalai A.K., Mohammadzadeh J.S.S., Adjaye J., "The effect of feedstock and process conditions on the synthesis of high purity CNTs from aromatic hydrocarbons", Carbon, 2236-2245, 44, 2006

Delhaes P., Couzi M., Trinquecoste M., Dentzer J., Hamidou H., Vix-Guterl C., "A comparison between Raman spectroscopy and surface characterizations of multiwall carbon nanotubes", Carbon, 3005-3013, 44, 2006

Department of Justice Canada, "Sulfur in gasoline regulations, 1999", Canadian Environmental Protection Act, 1999

Department of Justice Canada, "Sulfur in diesel fuel regulations, 2002", Canadian Environmental Protection Act, 1999

Diaz-Real R.A., Mann R.S., Sambi I.S., "Hydrotreatment of Athabasca bitumen derived gas oil over Ni-Mo, Ni-W, and Co-Mo catalysts", Industrial and Engineering Chemistry Research, 1354-1358, 32, 1993

Dong K., Ma X., Zhang H., Lin G., "Novel MWCNT-support for Co-Mo sulfide catalyst in HDS of thiophene and HDN of pyrrole", Journal of Natural Gas Chemistry, 28-37, 15, 2006

Dresselhaus M.S., Dresselhaus G., Saito R., Jorio A., "Raman spectroscopy of carbon nanotubes", Physics Reports, 47-99, 409, 2005

Duchet J.C., Tilliete M.J., Cornet D., Vivier L., Perot G., Bekakra L., Moreau C., Szabo G., "Catalytic properties of nickel molybdenum sulphide supported on zirconia", Catalysis Today, 579-592, 10, 1991

Eklund P.C., Holden J.M., Jishi R.A., “Vibrational modes of carbon nanotubes; Spectroscopy and theory”, Carbon, 959-972, 33, 1995

Escalona N., Vrinat M., Laurenti D., Gil Llambias F.J., "Rhenium sulfide in hydotreating”, Applied Catalysis A: General, 113-120, 322, 2007

Eswaramoorthi I., Sundaramurthy V., Dalai A.K., “Partial oxidation of methanol for hydrogen production over carbon nanotubes supported Cu-Zn catalysts”, Applied Catalysis A: General, 22-34, 313, 2006

Eswaramoorthi I., Sundaramurthy V., Das N., Dalai A.K., Adjaye J., “Application of multi-walled carbon nanotubes as efficient support to NiMo hydrotreating catalyst”, Applied Catalysis A: General, 187-195, 339, 2008

Farag H., Whitehurst D.D., Sakanishi K., Mochida I., “Carbon versus alumina as a support for Co-Mo catalysts reactivity towards HDS of dibenzothiophenes and diesel fuel”, Catalysis Today, 9-17, 50, 1999

Faro Jr. A.C., dos Santos A.C.B., “Cumene hydrocracking and thiophene HDS on niobia-supported Ni, Mo, and Ni-Mo catalysts”, Catalysis Today, 402-409, 118, 2006

Ferdous D., Dalai A.K., Adjaye J., “A series of $NiMo/Al_2O_3$ catalysts containing boron and phosphorous: Part II. Hydrodenitrogenation and hydrodesulfurization using heavy gas oil derived from Athabasca bitumen”, Applied Catalysis A: General, 153-162, 8, 2004

Fogler H.S., Elements of Chemical Reaction Engineering, Upper Saddle River, NJ: Prentice Hall PTR, 2006

Froment G.F., Bischoff K.B., Chemical Reactor Analysis and Design, New York: Wiley, 1990

Furimsky E., “Role of MoS_2 and WS_2 in hydrodesulfurization”, Catalysis Reviews - Science and Engineering, 371-400, 22, 1980

Furimsky E., Massoth F.E., “Deactivation of hydroprocessing catalysts”, Catalysis Today, 381-495, 52, 1999

Gates B.C., Katzer J.R., Schuit G.C.A., Chemistry of Catalytic Processes, New York: McGraw-Hill, 1979

Girgis M.J., Gates B.C., "Reactivities, reaction networks, and kinetics in high-pressure catalytic hydroprocessing", Industrial and Engineering Chemistry Process Design and Development, 2021-2058, 30, 1991

Goto S., Smith J.M., "Trickle-bed reactor performance: I. Holdup and mass transfer effects", American Institute of Chemical Engineers Journal, 706-713, 21, 1975

Grange P., Vanhaeren X., "Hydrotreating catalysts, an old story with new challenges", Catalysis Today, 375-391, 36, 1997

Gras R., Duvail J.L., Minea T., Dubosc M., Tessier P.Y., Cagnon L., Coronel P., Torres J., "Template synthesis of carbon nanotubes from porous alumina matrix on silicon", Microelectronic Engineering, 2432-2436, 83, 2006

Gregg S.J., Sing K.S.W., Adsorption, Surface Area and Porosity, London; New York: Academic Press, 1967

Gruia A., "Chapter 8: Hydrotreating", Handbook of Petroleum Processing, 321-354, Dordrecht: Springer, 2006

Guichard B., Roy-Auberger M., Devers E., Pichon C., Legens C., "Characterization of aged hydrotreating catalysts. Part II: The evolution of the mixed phase. Effects of deactivation, activation and/or regeneration", Applied Catalysis A: General, 9-22, 367, 2009

Guo T., Nikolaev P., Rinzler A.G., Tománek D., Colbert D.T., Smalley R.E., "Self-assembly of tubular fullerenes", Journal of Physical Chemistry, 10694-10697, 99, 1995

Gusta E., Sundaramurthy V., Dalai A.K., Adjaye J., "Hydrotreating of heavy gas oil derived from Athabasca bitumen over Co-Mo/γ-Al_2O_3 catalyst prepared by sonochemical method", Topics in Catalysis, 147-153, 37, 2006

Hafner J.H., Bronikowski M.J., Azamian B.R., Niko-Laevl P., Rinzler A.G., Colbert D.T., Smith K.A., Smalley R.E., "Catalytic growth of single-wall carbon nanotubes from metal particles", Chemical Physics Letters, 195-202, 296, 1998

Hagenbach G., Courty P., Delmon B., “Physicochemical investigations and catalytic activity measurements on crystallized molybdenum sulfide-cobalt sulfide mixed catalysts”, Journal of Catalysis, 264-273, 31, 1973

Hardwick L.J., Buqa H., Novák P., “Graphite surface disorder detection using in situ Raman microscopy”, Solid State Ionics, 2801-2806, 177, 2006

Ho T.C., “Hydrodenitrogenation catalysis”, Catalysis Reviews, Science and Engineering, 117-160, 30, 1988

Houalla M., Nag N.K., Sapre A.V., Broderick D.H., Gates B.C., “Hydrodesulfurization of dibenzothiophene catalyzed by sulfided CoO-MoO_3/-Al_2O_3: The reaction network”, American Institute of Chemical Engineers Journal, 1015-1021, 24, 1978

Iijima S., “Helical microtubules of graphitic carbon”, Nature, 56-58, 354, 1991

Im W.S., Cho Y.S., Choi G.S., Yu F.C., Kim D.J., “Stepped carbon nanotubes synthesized in anodic aluminum oxide templates”, Diamond and Related Materials, 1214-1217, 13, 2004

Jagminas A., Lichusina S., Kurtinaitiene M., Selskis A., “Concentration effect of the solutions for alumina template ac filling by metal arrays”, Applied Surface Science, 194-202, 211, 2003

Jiménez F., Kafarov V., Nunez M., “Modeling of industrial reactor for hydrotreating of vacuum gas oils: Simultaneous hydrodesulfurization, hydrodenitrogenation, and hydrodearomatization reactions”, Chemical Engineering Journal, 200-208, 134, 2007

Jung M., Kim H.G., Lee J.K., Joo O.S., Mho S., “EDLC characteristics of CNTs grown on nanoporous alumina templates”, Electrochimica Acta, 857-862, 50, 2004

Kape J.M., “Control in aluminum anodizing”, Metal Finishing, 54-60, 59, 1961

Kathi J., Rhee K.Y., “Surface modification of multi-walled carbon nanotubes using 3-aminopropyltriethoxysilane”, Journal of Materials Science, 33-37, 43, 2008

Kim M.J., Choi J.H., Park J.B., Kim S.K., Yoo J.B., Park C.Y., "Growth characteristics of carbon nanotubes via aluminum nanopore template on Si substrate using PECVD", Thin Solid Films, 312-317, 435, 2003

Korsten H., Hoffman U., "Three-phase reactor model of hydrotreating in pilot trickle-bed reactors", American Institute of Chemical Engineers Journal, 1350-1360, 42, 1996

Kyotani T., Nakazaki S., Xu W.H., Tomita A., "Chemical modification of the inner walls of carbon nanotubes by HNO_3 oxidation", Carbon, 782-785, 39, 2001

Kyotani T., Pradhan B.K., Tomita A., "Synthesis of carbon nanotube composites in nanochannels of an anodic aluminum oxide film", Bulletin of the Chemical Society of Japan, 1957-1970, 72, 1999

Lauritsen J.V., Kibsgaard J., Olesen G.H., Moses P.G., Hinnemann B., Helveg S., Nørskov J.K., Clausen B.S., Topsøe H., Lægsgaard E., Besenbacher F., "Location and coordination of promoter atoms in Co- and Ni-promoted MoS_2-based hydrotreating catalysts", Journal of Catalysis, 220-233, 249, 2007

Ledoux M.J., Hantzer S., "Hydrotreatment catalyst poisoning by vanadium and nickel porphyrin. ESR and NMR", Catalysis Today, 479-496, 7, 1990

Lee O.J., Hwang S.K., Jeong S.H., Lee P.S., Lee K.H., "Synthesis of carbon nanotubes with identical dimensions using an anodic aluminum oxide template on a silicon wafer", Synthetic Metals, 263-266, 148, 2005

Lee S.J., Baik H.K., Yoo J.E., Han J.H., "Large scale synthesis of carbon nanotubes by plasma rotating arc discharge technique", Diamond and Related Materials, 914-917, 11, 2002

Lee W., Ji R., Gosele U., Nielsch K., **"**Fast fabrication of long-range ordered porous alumina membranes by hard anodization", Nature Materials, 741-747, 5, 2006

Lefrant S., "Raman and SERS studies of carbon nanotube systems", Current Applied Physics, 479-482, 2, 2002

Leyva C., Rana M.S., Ancheyta J., "Surface characterization of Al_2O_3-SiO_2 supported NiMo catalysts: An effect of support composition", Catalysis Today, 345-353, 130, 2008

Li J., Tang T., Zhang X., Li S., Li M., "Dissolution, characterization and photofunctionalization of carbon nanotubes", Materials Letters, 4351-4353, 61, 2007

Li K.Z., Wei J., Li H.J., Zhang Y.L., Wang C., Hou D.S., "Preparation of well-aligned carbon nanotubes by pyrolysis of phenolic resin in anodic alumina pores", Applied Surface Science, 7365-7368, 253, 2007

Liu H., Cheng G., Zheng R., Zhao Y., Liang C., "Influence of acid treatments of carbon nanotube precursors on Ni/CNT in the synthesis of carbon nanotubes", Journal of Molecular Catalysis, 17-22, 230, 2005

Liu Y., Gao L., "A study of the electrical properties of carbon nanotube-$NiFe_2O_4$ composites: Effect of the surface treatment of the carbon nanotubes", Carbon, 47-52, 43, 2005

Luck F., "A review of support effects on the activity and selectivity of hydrotreating catalysts", Bulletin des Sociétés Chimiques Belges, 781-800, 100, 1991

Maity S.K., Ancheyta J., Alonso F., Vazquez J.A., "Study of accelerated deactivation of hydrotreating catalysts by vanadium impregnation method", Catalysis Today, 405-410, 130, 2008

Masuda H., Fukuda K.**,** **"**Ordered metal nanohole arrays made by a two-step replication of honeycomb structures of anodic alumina", Science, 1466-1468, 268, 1995

Menon M., Andriotis A.N., Froudakis G.E., "Curvature dependence of the metal catalyst atom interaction with carbon nanotube walls", Chemical Physics Letters, 425-434, 320, 2000

Mildred S., Dresselhaus M.S., Dresselhaus G., Avouris P., Carbon Nanotubes: Synthesis, Structure, Properties, and Applications, Berlin; New York: Springer, 2001

Netzel D.A., Miknis F.P., Mitzel J.M., Zhang T., Jacobs P.D., Haynes Jr. H.W., "Carbon-13 solid-state NMR investigation of coke deposits on spent catalysts used in coal liquefaction", Fuel, 1397-1405, 75, 1996

Okamoto Y., Breysse M., Dhar G.M., Song C., "Effect of support of hydrotreating catalysis for ultra clean fuels", Catalysis Today, 1-3, 86, 2003

O'Sullivan J.P., Wood G.C., "The morphology and mechanism of formation of porous anodic films on aluminium", Proceedings of the Royal Irish Academy Section A: Mathematical and Physical Sciences, 511-543, 317, 1970

Probst K., Wohlfahrt K., "Empirical estimate of effective diffusion coefficients in porous systems", Chemie Ingenieur Technik, 737-738, 51, 1979

Qu L., Zhang W., Kooyman P.J., Prins R., "MAS NMR, TPR, and TEM studies of the interaction of NiMo with alumina and silica-alumina supports", Journal of Catalysis, 7-13, 215, 2003

Ramirez J., Vrinat M., Breysse M., Lacroix M., Diaz G., Fuentes S., "Hydrodesulphurization activity of characterization of sulphided molybdenum and cobalt-molybdenum catalysts: comparison of alumina-, silica-alumina-, and titania-supported catalysts", Applied Catalysis, 211-224, 52, 1989

Rao C.N.R., Sen R., Govindaraj A., "Fullerenes and carbon nanotubes", Current Opinion in Solid State and Materials Science, 279-284, 1, 1996

Reid R.C., Prausnitz J.M., Poling B.E., The Properties of Gases and Liquids, New York: McGraw-Hill, 1987

Rosca I.D., Watari F., Uo M., Akasaka T., "Oxidation of multiwalled carbon nanotubes by nitric acid", Carbon, 3124-3131, 43, 2005

Saito R., Dresselhaus G., Dresselhaus M.S., Physical Properties of Carbon Nanotubes, London: Imperial College Press, 1998

Sampieri A., Pronier S., Blanchard J., Breysse M., Brunet S., Fajerwerg K., Louis C., Pérot G., "Hydrodesulfurization of dibenzothiophene on MoS_2/MCM-41 and MoS_2/SBA-15 catalysts prepared by thermal spreading of MoO_3", Catalysis Today, 537-544, 107, 2005

Sanchez-Delgado R.A., "Chapter 1: Hydrodesulfurization and hydrodenitrogenation", Organometallic Modeling of the Hydrodesulfurization and Hydrodenitrogenation Reactions, 1-34, Dordrecht; Boston: Kluwer Academic Publishers, 2002

Satterfield C.N., "Chapter 3: Diffusion and reaction in porous catalysts", Mass Transfer in Heterogeneous Catalysis, 129-163, Cambridge, MA; London: Massachusetts Institute of Technology Press, 1970

Satterfield C.N., “Chapter 9: Processing of petroleum and hydrocarbons”, Heterogeneous Catalysis in Industrial Practice, 339-417, New York: McGraw-Hill, 1991

Satterfield C.N., Cocchetto J.F., “Reaction network and kinetics of the vapor-phase catalytic hydrodenitrogenation of quinoline”, Industrial and Engineering Chemistry Process Design and Development, 53-62, 20, 1981

Satterfield C.N., Pelossof A.A., Sherwood T.K., “Mass transfer limitations in trickle bed reactor”, American Institute of Chemical Engineers Journal, 224-226, 15, 1969

Satterfield C.N., Yang S.H., “Simultaneous hydrodenitrogenation and hydrodeoxygenation of model compounds in trickle bed reactor”, Journal of Catalysis, 335-346, 81, 1983

Satterfield C.N., Yang S.H., “Catalytic hydrodenitrogenation of quinoline in a trickle-bed reactor. Comparison with vapor phase reaction”, Industrial and Engineering Chemistry Process Design and Development, 11-19, 23, 1984

Schneider J.J., Maksimova N.I., Engstler J., Joshi R., Schierholz R., Feile R., “Catalyst free growth of a carbon nanotube-alumina composite structure”, Inorganica Chimica Acta, 1770-1778, 361, 2008

Shang H., Liu C., Xu Y., Qiu J., Wei F., “States of carbon nanotube supported Mo-based HDS catalysts”, Fuel Processing Technology, 117-123, 88, 2007

Shang H., Liu C., Xu Y., Zhao H., Song H., “Effect of the surface modification of multi-walled carbon nanotubes (MWCNTs) on hydrodesulfurization activity of Co-Mo/MWCNTs catalysts”, New Carbon Materials, 129-136, 19, 2004

Sim W.J., Daubert T.E., “Prediction of vapour-liquid equilibria of undefined mixtures”, Industrial and Engineering Chemistry Process Design and Development, 386-393, 19, 1980

Sigurdson S., Sundaramurthy V., Dalai A.K., Adjaye J., “Phosphorus promoted trimetallic NiMoW/γ-Al_2O_3 sulfide catalysts in gas oil hydrotreating”, Journal of Molecular Catalysis A: Chemical, 30-37, 291, 2008

Sigurdson S., Sundaramurthy V., Dalai A.K., Adjaye J., "Effect of anodic alumina pore diameter variation on template-initiated synthesis of carbon nanotube catalyst supports", Journal of Molecular Catalysis A: Chemical, 23-32, 306, 2009

Sørensen O., Clausen B., Candia R., Topsøe H., "HREM and AEM studies of HDS catalysts: Direct evidence for the edge location of cobalt in Co-Mo-S", Applied Catalysis, 363-372, 13, 1985

Sui Y.C., Cui B.Z., Guardian R., Acosta D.R., Martinez L., Perez R., "Growth of carbon nanotubes and nanofibres in porous anodic alumina film", Carbon 1011-1016, 40, 2002

Sung D.D., Choo M.S., Noh J.S., Chin W.B., Yang W.S., "A new fabrication method of aluminum nanotube using anodic porous alumina film as a template", Bulletin of the Korean Chemical Society, 1159-1163, 27, 2006

Tamm P.W., Harnsberger H.F., Bridge A.G., "Effects of feed metals on catalyst aging in hydroprocessing residuum", Industrial and Engineering Chemistry Process Design and Development, 262-273, 20, 1981

Tanaka K., Yamabe T., Fukui K., The Science and Technology of Carbon Nanotubes, Amsterdam; Oxford: Elsevier, 1999

Thompson G.E., "Porous anodic alumina: fabrication, characterization and applications", Thin Solid Films, 192-201, 297, 1997

Topsoe H., Clausen B.S., Massoth F.E., Hydrotreating Catalysis - Science and Technology, New York: Springer-Verlag, 1996

Trytten L.C., Gray M.R., Emerson C.S., "Hydroprocessing of narrow-boiling gas oil fractions: dependence of reaction kinetics on molecular weight", Industrial and Engineering Chemistry Research, 725-730, 29, 1990

Van Parijs I.A., Froment G.F., "Kinetic modeling of catalytic reactions with a varying concentration of active sites: An analysis of the remote control model for HDS-catalysts", Applied Catalysis, 273-285, 21, 1986

Vishwakarma S.K., Sundaramurthy V., Dalai A.K., "Performances of Co-W/γ-Al_2O_3 catalysts on hydrotreatment of light gas oil derived from Athabasca bitumen", Industrial and Engineering Chemistry Research, 4778-4786, 46, 2007

Wang X.W., Liu Y., Zhu D., "Controlled growth of well-aligned carbon nanotubes with large diameters", Chemical Physics Letters, 419-424, 340, 2001

Wijngaarden R.J., Kronberg A., Westerterp K.R., Industrial Catalysis: Optimizing Catalysts and Processes, Weinheim; Chichester: Wiley-VCH, 1998

Wilke C.R., Chang P., "Correlation of diffusion coefficients in dilute solutions", Chemical Engineering Progress, 264-270, 1, 1955

Wivel C., Candia R., Clausen B.S., Mørup S., Topsøe H., "On the catalytic significance of a Co-Mo-S phase in Co-Mo/Al_2O_3 hydrodesulfurization catalysts: Combined *in situ* Mössbauer emission spectroscopy and activity studies", Journal of Catalysis, 453-463, 68, 1981

Xing G., Jia S.L., Shi Z.Q., "The production of carbon nano-materials by arc discharge under water or liquid nitrogen", New Carbon Materials, 337-341, 22, 2007

Yang D.J., Zhang Q., Chen G., Yoon S.F., Ahn J., Wang S.G., Zhou Q., Wang Q., Li J.Q., "Thermal conductivity of multiwalled carbon nanotubes", Physical Review B, 165440 [6 pages], 66, 2002

Yang Y., Hu Z., Wu Q., Lu Y.N., Wang X.Z., Chen Y., "Template-confined growth and structural characterization of amorphous carbon nanotubes", Chemical Physics Letters, 580-585, 373, 2003

Yu Z., Fareid L.E., Moljord K., Blekkan E.A., Walmsley J.C., Chen D., "Hydrodesulfurization of thiophene on carbon nanofiber supported Co/Ni/Mo catalysts", Applied Catalysis B: Environmental, 482-489, 84, 2008

Zdražil M., "MgO-supported Mo, CoMo and NiMo sulphide hydrotreating catalysts", Catalysis Today, 151-171, 86, 2003

Zeng Q., Li Z., Zhou Y., "Synthesis and application of carbon nanotubes", Journal of Natural Gas Chemistry, 235-246, 15, 2006

Zeuthen P., Knudsen K.G., Whitehurst D.D., "Organic nitrogen compounds in gas oil blends, their hydrotreated products and the importance to hydrotreatment", Catalysis Today, 307-314, 65, 2001

APPENDICES

APPENDIX A:
Further Examples for SEM Images of AAO Templates

Alternative Anodizing Conditions:

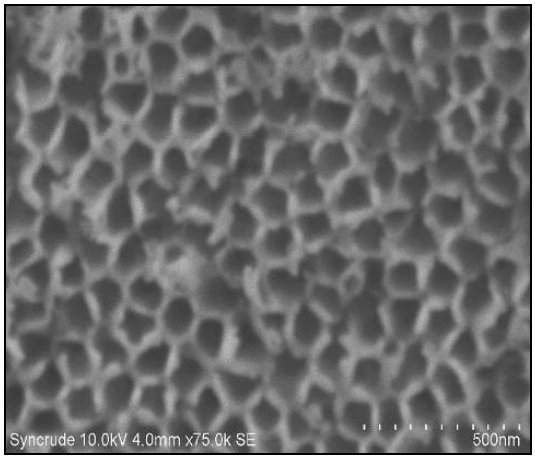

Figure A.1: SEM image of AAO template after anodization burning.

- The above image shows an AAO template created by directly applying a 50.0 V potential to the anodization cell (and 0.30 M oxalic acid electrolyte) without first applying a 40.0 V potential for an 18 hour period. The result is transpassive behavior, or anodization burning, of the AAO template. The pore diameters were irregular and varied from 100 to 150 nm. The templates resulted in low MWCNT yields.

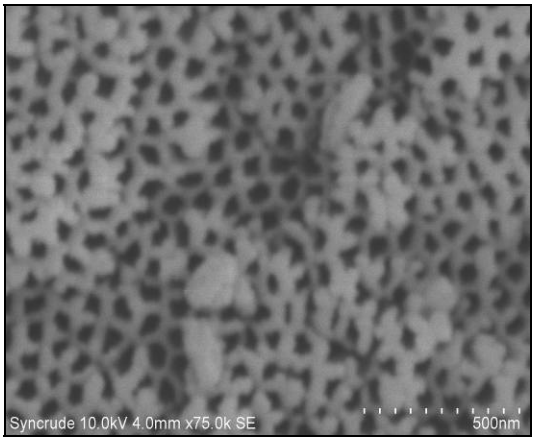

Figure A.2: SEM image of condition 9 AAO template.

- The above image shows an AAO template created by applying a 60.0 V maximum potential and a 0.50 M oxalic acid electrolyte to the anodization cell under the conditions discussed in section 5.1. The result is irregular and obstructed pore channels for the AAO template, varying from 40 to 100 nm. The templates resulted in low MWCNT yields.

Alternative Anodizing Conditions (continued):

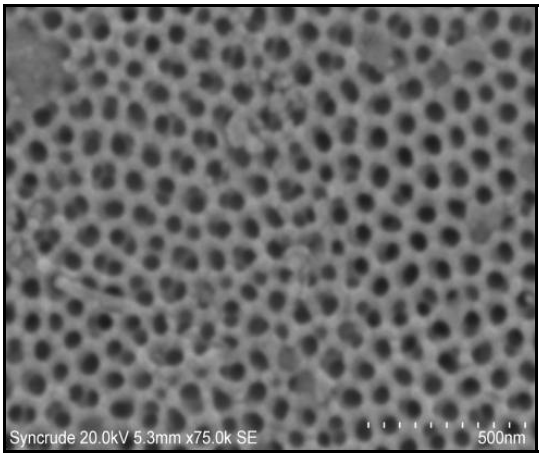

Figure A.3: SEM image of AAO template from a 99.0 wt.% Al anode.

- The above image shows an AAO template created by using a lower grade aluminum anode for the electrolysis process; 99.0 wt.% as opposed to 99.9 wt.% (40.0 V maximum potential, 0.40 M oxalic acid electrolyte). The result is lower pore diameters - 50 nm as opposed to the expected 70 nm from a more pure Al anode – and ultimately lower MWCNT yields.

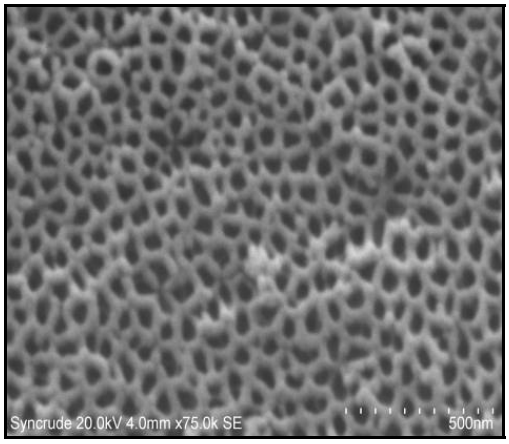

Figure A.4: SEM image of AAO template from milder anodizing conditions.

- The above image shows an AAO template created by applying a 30.0 V maximum potential and a 0.20 M oxalic acid electrolyte to the anodization cell in an attempted to ultimately produce small MWCNT diameters. The result is smaller, slightly irregular pore channels for the AAO template with expected diameters of 40 nm. As with the three previous templates, the end result was low MWCNT yields.

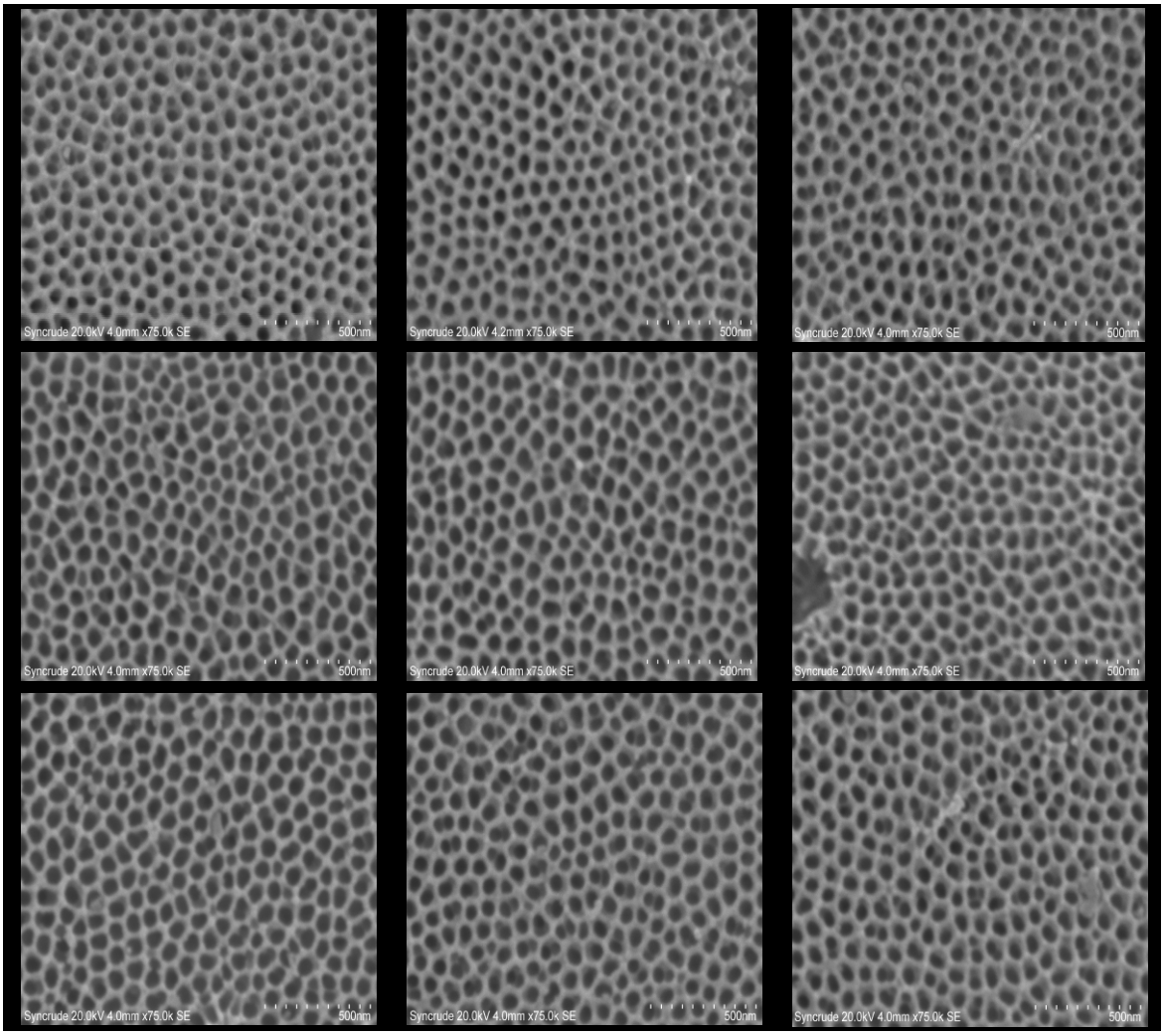

Figure A.5: SEM images showing the consistency of condition 4 grade AAO templates used in sections 6.3 through 6.6 of this report.

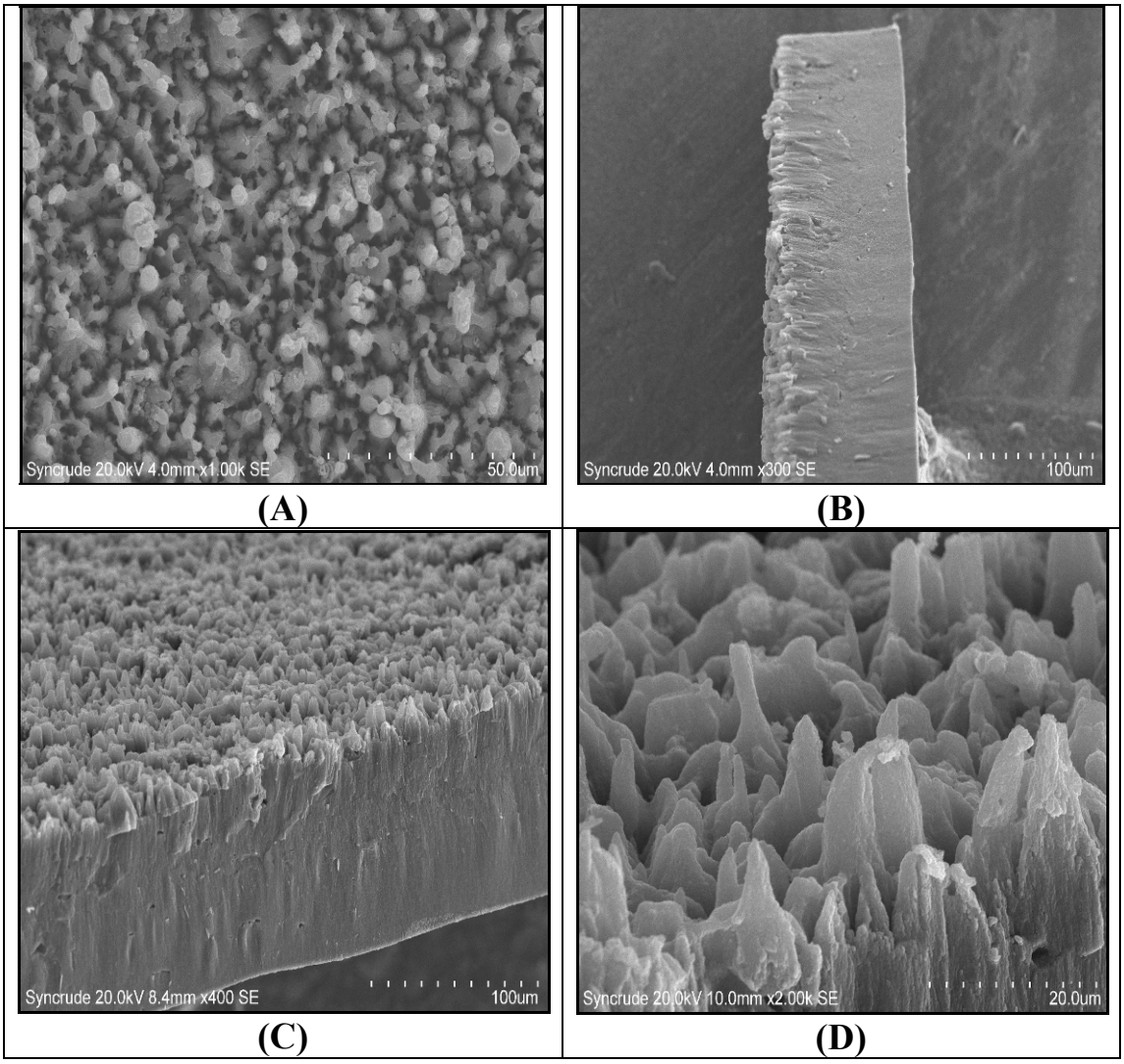

Figure A.6: SEM images of AAO/MWCNT aggregates after the chemical vapor deposition process: (A) ×700 magnification image, bird's-eye view of close-ended MWCNTs above the AAO template; (B) ×200 magnification image, ~100 µm thick AAO template with amorphous carbon and MWCNTs; (C) ×300 magnification image, side and pore channel surface of the AAO/MWCNT aggregate; (D) ×1500 magnification image, close-ended nanotubes and amorphous carbon.

APPENDIX B:
Further Examples for TEM and HAADF-STEM Images of MWCNTs and NiMo/CNT Catalysts

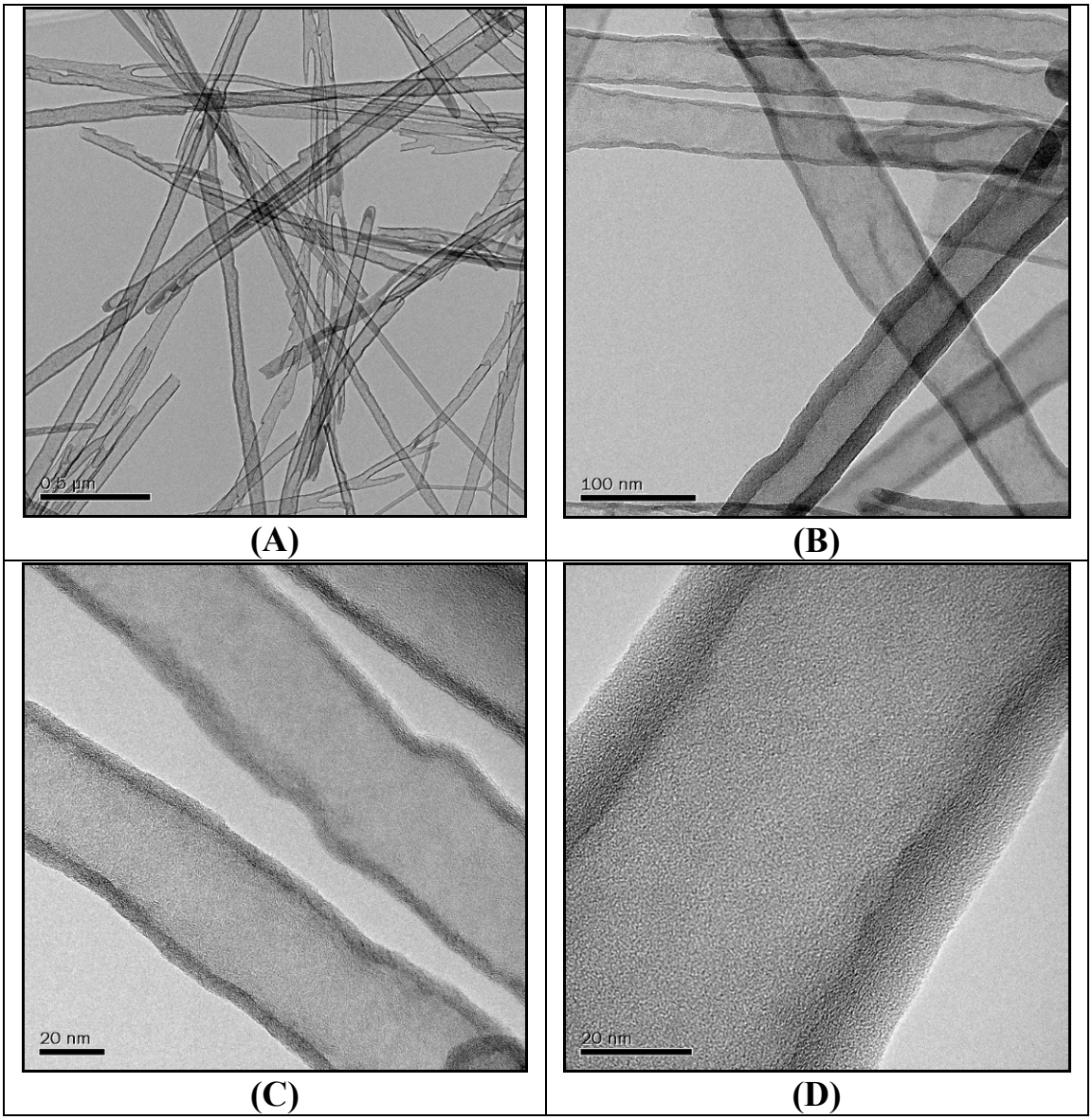

Figure B.1: TEM images of the optimum cat-65 grade MWCNTs after purification and functionalization: (A) ×20k magnification image; B) ×100k magnification image; (C) ×300k magnification image; (D) ×500k magnification image.

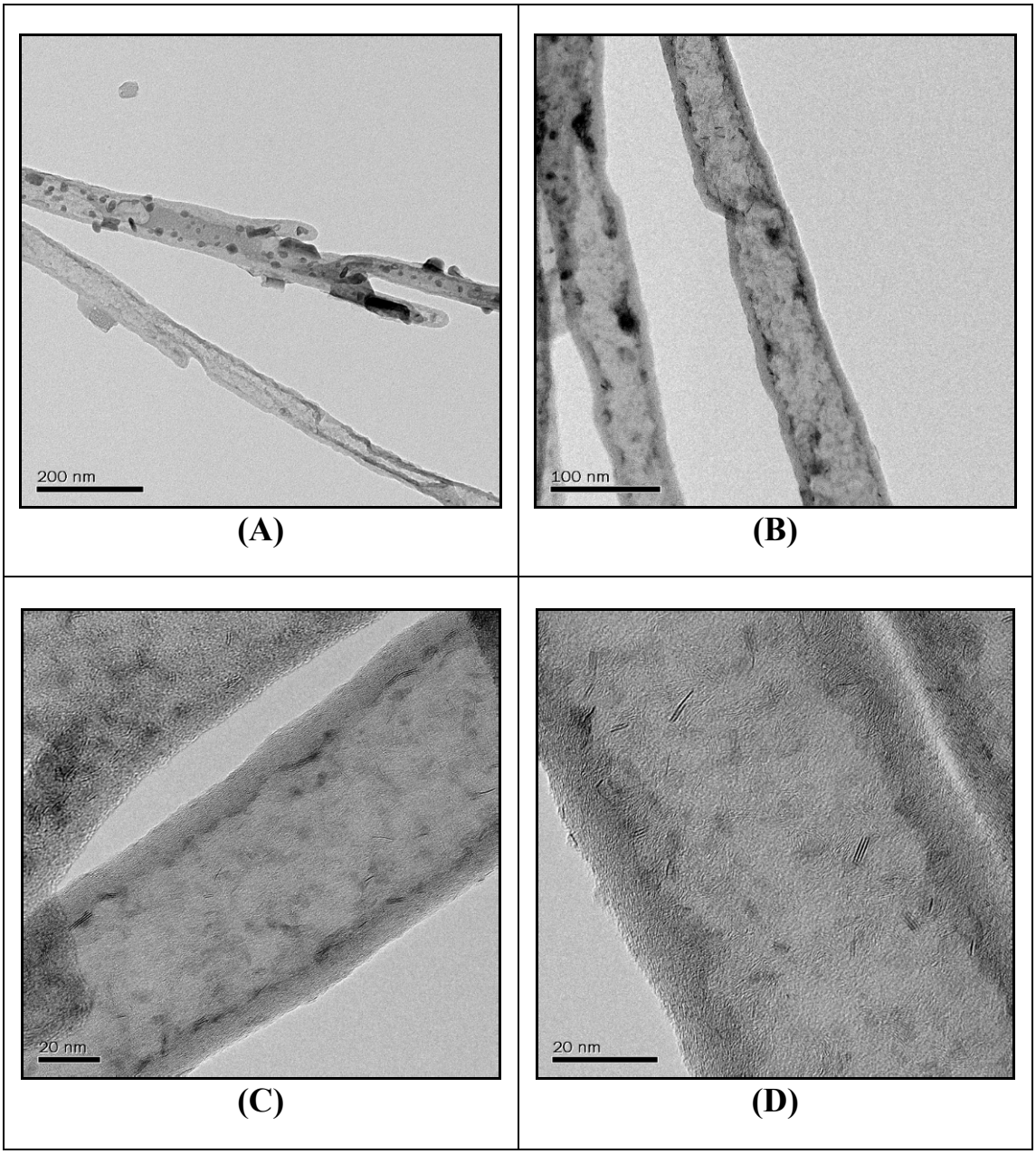

Figure B.2: TEM images of NiMo/MWCNT catalysts both prior to and after hydroprocessing: (A) ×50k magnification image, fresh *cat-60* NiMo/MWCNT; (B) ×100k magnification image, spent *cat-60* NiMo/MWCNT; (C) ×300k magnification image, spent *cat-75* NiMo/MWCNT; (D) ×500k magnification image, spent *cat-70* NiMo/MWCNT (note the distinct carbon filaments).

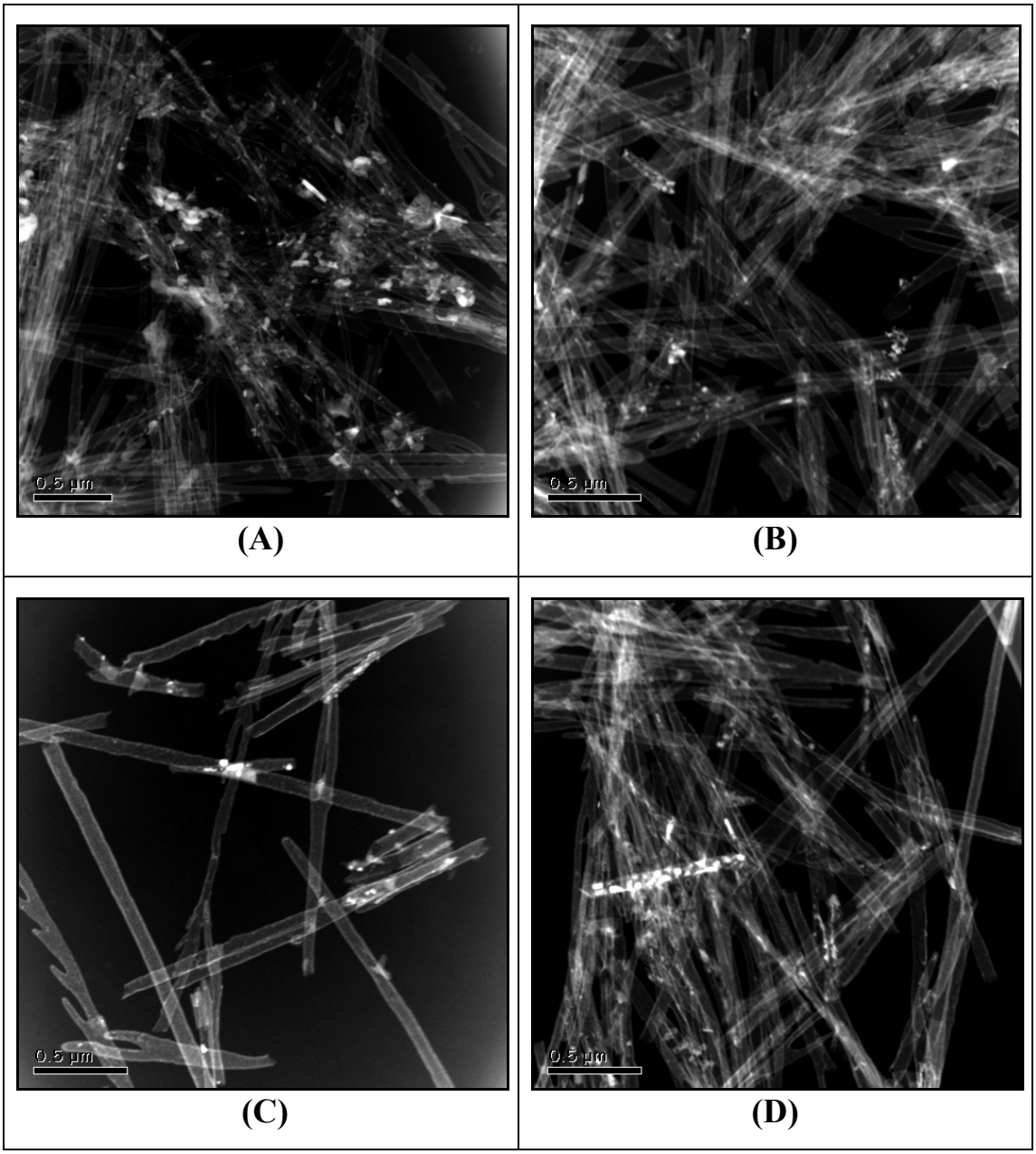

Figure B.3: HAADF-STEM images of NiMo/MWCNT catalysts both prior to and after hydroprocessing: (A) ×20k magnification image, spent *cat-60* NiMo/MWCNT, metal particles not well-distributed; (B) ×20k magnification image, fresh *cat-75* NiMo/MWCNT, well distributed metal particles; (C) ×20k magnification image, fresh *cat-70* NiMo/MWCNT, well distributed metal particles (note the well distributed metal on the Y-branched MWCNT on the bottom left); (D) ×20k magnification image, spent *cat-65* NiMo/MWCNT (note the heavy loading of metal particles on the MWCNT left of center).

APPENDIX C:
Characteristics of the Coker Light Gas Oil (CLGO) Derived from Athabasca Bitumen Used for Hydrotreating Experimentation

	Values	
Characteristic	**Pore Diameter Optimization (section 6.2)**	**Metal Loading Optimization, Kinetic Studies, Longevity Study (sections 6.4, 6.5, 6.6)**
nitrogen content (wt.%)	**0.237**	**0.162**
sulfur content (wt.%)	**2.185**	**1.636**
density (reported, g/mL)	**0.90**	**0.90**
simulated distillation		
Initial Boiling Point (°C)	**210**	**157**
Final Boiling Point (°C)	**548**	**481**
hydrocarbon content (wt.%)		
IBP-250°C	**4.4**	**21.0**
250-300°C	**24.4**	**29.6**
300-350°C	**30.8**	**27.7**
350-400°C	**22.0**	**14.8**
400-450°C	**10.3**	**5.2**
450-500°C	**5.1**	**1.7**
500-550°C	**3.0**	**--**

APPENDIX D:
Calculating Molar Product Concentrations of N/S and Reaction Rates of HDN/HDS

The sulfur and nitrogen concentrations in the feed and product gas oil liquids are found via the following equations:

$$C_S = \frac{(ppm_{wt}) \cdot \rho_L}{(10^6) \cdot M_S} = \frac{(ppm_{wt}) \cdot \left(0.90 \times 10^3 \frac{g}{L}\right)}{(10^6) \cdot \left(32.0640 \frac{g}{mol}\right)} \quad [D.1]$$

$$C_N = \frac{(ppm_{wt}) \cdot \rho_L}{(10^6) \cdot M_N} = \frac{(ppm_{wt}) \cdot \left(0.90 \times 10^3 \frac{g}{L}\right)}{(10^6) \cdot \left(14.0067 \frac{g}{mol}\right)} \quad [D.2]$$

$\boldsymbol{\rho_L}$ = Density of CLGO feedstock and product (assumed equal) = 0.90 g/mL

$\boldsymbol{C_{S/N}}$ = Sulfur/nitrogen heteroatom concentration, mol/L (M)

$\boldsymbol{M_{S/N}}$ = Sulfur/nitrogen molecular weight, g/mol

The global rates of both the hydrodesulfurization and hydrodenitrogenation reactions were found from the following equations:

$$\{R_{HDS}\} = \frac{\left([C_O]_S - [C_P]_S\right) \cdot LHSV}{\left(3600 \frac{s}{h}\right) \cdot \rho_{CAT}} \quad [D.3]$$

$$\{R_{HDN}\} = \frac{\left([C_O]_N - [C_P]_N\right) \cdot LHSV}{\left(3600 \frac{s}{h}\right) \cdot \rho_{CAT}} \quad [D.4]$$

$\boldsymbol{\{R_{HDS/HDN}\}}$ = Global rate of the HDS/HDN reaction, mol/(s·kg-cat)

$\boldsymbol{[C_{O/P}]_{S/N}}$ = Feedstock/product concentration of sulfur/nitrogen, mol/L

$\boldsymbol{LHSV}$ = Liquid hourly space velocity, h^{-1}

$\boldsymbol{\rho_{CAT}}$ = Catalyst pellet density = 0.38 g/mL (NiMo/MWCNT catalyst)

APPENDIX E:
Product Concentrations and Conversions of N/S from the Kinetics Study of HDS/HDN for the Optimum NiMo/MWCNT Catalyst

Run Time (days)	T (°C)	LHSV (h^{-1})	P (MPa)	G/L (mL/mL)	$[C_P]_S$ (mol/L)	$[C_O-C_P]_S/[C_O]_S$ (no units)	$[C_P]_N$ (mol/L)	$[C_O-C_P]_N/[C_O]_N$ (no units)
0.5	370	1.5	8.8	600	0.0490	0.890	0.0339	0.658
1.0	370	1.5	8.8	600	0.0546	0.878	0.0373	0.623
1.5	370	1.5	8.8	600	0.0537	0.880	0.0373	0.624
2.0	370	1.5	8.8	600	0.0529	0.882	0.0378	0.619
2.5	370	1.5	8.8	600	0.0571	0.872	0.0378	0.619
3.0	370	1.5	8.8	600	0.0516	0.884	0.0379	0.618
4.0	370	1.5	8.8	600	0.0489	0.890	0.0307	0.690
4.5	370	1.5	8.8	600	0.0458	0.897	0.0297	0.701
5.0	370	1.5	8.8	600	0.0481	0.892	0.0300	0.698
6.0	370	2.5	8.8	600	0.0522	0.883	0.0432	0.565
6.5	370	2.5	8.8	600	0.0583	0.870	0.0447	0.549
7.0	370	2.5	8.8	600	0.0583	0.869	0.0443	0.553
8.0	370	2.0	8.8	600	0.0559	0.875	0.0458	0.538
8.5	370	2.0	8.8	600	0.0657	0.853	0.0388	0.608
9.0	370	2.0	8.8	600	0.0618	0.862	0.0344	0.653

Run Time (days)	T (°C)	LHSV (h^{-1})	P (MPa)	G/L (mL/mL)	$[C_P]_S$ (mol/L)	$[C_O\text{-}C_P]_S/[C_O]_S$ (no units)	$[C_P]_N$ (mol/L)	$[C_O\text{-}C_P]_N/[C_O]_N$ (no units)
10.0	350	1.5	8.8	600	0.0671	0.850	0.0474	0.522
10.5	350	1.5	8.8	600	0.0667	0.851	0.0474	0.522
11.0	350	1.5	8.8	600	0.0845	0.811	0.0463	0.533
12.0	350	2.5	8.8	600	0.0986	0.779	0.0607	0.388
12.5	350	2.5	8.8	600	0.1059	0.763	0.0602	0.393
13.0	350	2.5	8.8	600	0.0966	0.784	0.0599	0.396
14.0	350	2.0	8.8	600	0.0859	0.808	0.0548	0.447
14.5	350	2.0	8.8	600	0.0903	0.798	0.0555	0.440
15.0	350	2.0	8.8	600	0.0913	0.796	0.0552	0.443
16.0	330	1.5	8.8	600	0.1306	0.708	0.0637	0.357
16.5	330	1.5	8.8	600	0.1310	0.707	0.0646	0.349
17.0	330	1.5	8.8	600	0.1338	0.700	0.0643	0.352
18.0	330	2.5	8.8	600	0.1770	0.604	0.0743	0.251
18.5	330	2.5	8.8	600	0.1748	0.609	0.0740	0.254
19.0	330	2.5	8.8	600	0.1813	0.594	0.0746	0.248
20.0	330	2.0	8.8	600	0.1616	0.638	0.0712	0.282

Run Time (days)	T (°C)	LHSV (h^{-1})	P (MPa)	G/L (mL/mL)	$[C_P]_S$ (mol/L)	$[C_O\text{-}C_P]_S/[C_O]_S$ (no units)	$[C_P]_N$ (mol/L)	$[C_O\text{-}C_P]_N/[C_O]_N$ (no units)
20.5	330	2.0	8.8	600	0.1536	0.656	0.0709	0.285
21.0	330	2.0	8.8	600	0.1665	0.627	0.0712	0.282
22.0	330	2.0	8.8	450	0.1741	0.610	0.0709	0.285
22.5	330	2.0	8.8	450	0.1708	0.618	0.0706	0.288
23.0	330	2.0	8.8	450	0.2046	0.542	0.0693	0.301
24.0	330	2.0	8.8	750	0.1530	0.658	0.0704	0.290
24.5	330	2.0	8.8	750	0.1389	0.689	0.0706	0.288
25.0	330	2.0	8.8	750	0.1435	0.679	0.0733	0.261
26.0	330	2.0	6.6	600	0.1688	0.622	0.0792	0.202
26.5	330	2.0	6.6	600	0.1672	0.626	0.0775	0.219
27.5	330	2.0	7.7	600	0.1851	0.586	0.0758	0.235
28.0	330	2.0	7.7	600	0.1627	0.636	0.0752	0.241
29.0	330	2.0	8.8	600	0.1549	0.653	0.0727	0.267
29.5	330	2.0	8.8	600	0.1655	0.630	0.0731	0.263
30.5	330	2.0	9.9	600	0.1570	0.649	0.0711	0.283
31.0	330	2.0	9.9	600	0.1593	0.643	0.0708	0.286

Run Time (days)	T (°C)	LHSV (h^{-1})	P (MPa)	G/L (mL/mL)	$[C_P]_S$ (mol/L)	$[C_O-C_P]_S/[C_O]_S$ (no units)	$[C_P]_N$ (mol/L)	$[C_O-C_P]_N/[C_O]_N$ (no units)
32.0	330	2.0	11.0	600	0.1655	0.629	0.0693	0.301
32.5	330	2.0	11.0	600	0.1497	0.665	0.0689	0.306

APPENDIX F:
Evaluating the External Mass Transfer Resistances for the HDS and HDN Reactions

A criterion developed by Charles N. Satterfield (1969) was used for determining if the rate of hydrogen diffusion within petroleum distillates as part of HDS and HDN reactions was the rate determining step. The criterion is defined as:

$$\left(\frac{10 d_P}{3 C_{H2}}\right) \cdot \left(\frac{-1}{V_C} \cdot \frac{dn}{dt}\right) > k_{OVR} \qquad [F.1]$$

The variables are defined as:

k_{OVR} = Overall mass transfer coefficient for hydrogen, cm/s

C_{H2} = Hydrogen concentration in the liquid phase at equilibrium, mol/mL

$\left(\frac{-1}{V_C} \cdot \frac{dn}{dt}\right)$ = Rate of hydrogen conversion in the reaction, mol/(s·mL)

V_C = Volume of loaded catalyst = 5.26 mL

d_P = Average diameter of the catalyst particles = 0.17 cm*

*Average particle diameter is between 10 and 14 mesh (US) in size.

The validation of the Satterfield criterion would indicate that hydrogen conversion was dominant over hydrogen mass transfer in the overall reaction.

Estimation of the overall mass transfer coefficient (k_{OVR}):

The overall mass transfer coefficient was found by the following equation:

$$\frac{1}{k_{OVR}} = \frac{1}{k_L} + \frac{1}{k_S} \qquad [F.2]$$

The variables are defined as:

k_L = H_2/CLGO mass transfer coefficient – gas/liquid side, cm/s

k_S = H_2/CLGO mass transfer coefficient – liquid/solid side, cm/s

Calculation of the gas/liquid mass transfer coefficient (k_L):

The gas/liquid mass transfer coefficient was estimated using a correlation by Goto and Smith (1975):

$$\frac{k_L \cdot a_L}{D_L} = \alpha_1 \cdot \left(\frac{L_A}{\mu_L} \right)^{\alpha_2} \cdot \sqrt{\frac{\mu_L}{\rho_L \cdot D_L}} \qquad [F.3]$$

The variables are defined as:

a_L = Interfacial surface area over unit volume $\approx \left(\frac{6(1-\varepsilon)}{d_P} \right)^{*}$ = 24.7 cm^{-1}

*This assumes the interfacial surface area is equal to the catalyst pellet surface area.

ε = Bed porosity = 0.3 (Wijngaarden et al., 1998)

L_A = Liquid mass flow over cross-sectional area, g/(s·cm^2)

μ_L = Viscosity of CLGO at the operating temperature, g/(s·cm)

D_L = Diffusivity of hydrogen in CLGO, cm^2/s

ρ_L = Density of CLGO at the operating conditions, g/mL

α_1 = Constant based on the catalyst particle properties* = 7

α_2 = Constant based on the catalyst particle properties* = 0.4

* α_1 and α_2 values found by Korsten and Hoffman (1996) for d_P = 0.17 cm.

Calculation of CLGO viscosity (μ_L):

A correlation developed by Glasso (Ahmed, 1989) was used for estimating the viscosity of CLGO at the operating temperatures:

$$\mu_L = 3.141\times10^{10}\cdot(T-460)^{-3.444}\left(\log^{\circ} API\right)^{a} \qquad [F.4]$$

$$a = 10.313\cdot\log(T-460)-36.447 \qquad [F.5]$$

The variables are defined as:

T = Operating temperature, °R

$$\text{°}\boldsymbol{API} = \frac{141.5}{SG} - 131.5$$

SG = Specific gravity of CLGO at 15.6°C = 0.901

°API ≈ 25.6

a = -7.61 to -7.12 (for temperatures ranging from 330°C to 370°C)

$\boldsymbol{\mu_L}$ = 0.544 cP to 0.442 cP (for temperatures ranging from 330°C to 370°C)

Calculation of CLGO average molecular weight (M_{AVE}):

A correlation developed by Winn (Sim and Daubert, 1980) was used for calculating the average molecular weight of gas oil:

$$M_{AVE} = m_1\cdot T_b^{\,m_2}\cdot\rho_{15.6}^{\,\beta} \qquad [F.6]$$

The variables are defined as:

$\boldsymbol{M_{AVE}}$ = Average molecular weight of CLGO, g/mol

$\boldsymbol{T_b}$ = Average boiling point of CLGO = 299°C = 570°F

$\rho_{15.6}$ = Density of CLGO at 15.6°C = 0.90 g/mL

m_1 = Empirical constant* = 2.41×10^{-6}

m_2 = Empirical constant* = 2.847

β = Empirical constant* = -2.13

*Modified Winn values for gas oil fractions provided by Trytten et al. (1990).

M_{AVE} = 212 g/mol

Calculation of diffusivity of hydrogen in gas oil (D_L):

A correlation by Wilke and Chang (1955) was used for calculating the effective diffusivity of hydrogen:

$$\frac{D_L \cdot \mu_L}{T} = \left(7.4\times10^{-8}\right)\cdot \frac{\sqrt{X \cdot M_{AVE}}}{V_b^{0.6}} \qquad [F.7]$$

The variables are defined as:

X = Association parameter = 1 for hydrocarbon mixtures

V_b = Hydrogen molar volume at the normal boiling point

V_b = 14.3 mL/mol (Wiljngaarden et al., 1998)

D_L = 2.42×10^{-4} cm^2/s to 3.18×10^{-4} cm^2/s
(for temperatures ranging from 330°C to 370°C)

Calculation of CLGO density at reaction temperatures and pressures:

A correlation by Standing and Katz (Jiménez et al., 2007) was found for determining the density of gas oils at reactor operating conditions:

$$\rho_L = \rho_{15.6} - \Delta\rho_T + \Delta\rho_P \qquad [F.8]$$

$\Delta\rho_T$ = Temperature density correlation, lbs/ft^3

$\Delta\rho_P$ = Pressure density correlation, lbs/ft^3

$$\Delta\rho_P = \left[0.167 + \left(16.181\times10^{-0.0425\rho_{15.6}}\right)\right]\cdot\left[\tfrac{P}{1000}\right] - 0.01\cdot\left[0.299 + \left(263\times10^{-0.603\rho_{15.6}}\right)\right]\cdot\left[\tfrac{P}{1000}\right]^2 \qquad \text{[F.9]}$$

$$\Delta\rho_T = \left[0.0133 + \left(152.4\cdot(\rho_{15.6}+\Delta\rho_P)^{-2.45}\right)\right]\cdot[T-520] - \left[8.10\times10^{-6} - \left(0.0622\times10^{-0.764(\rho_{15.6}+\Delta\rho_P)}\right)\right]\cdot[T-520]^2 \qquad \text{[F.10]}$$

The values applied to these equations were:

P = 960 psia to 1600 psia

T = 1086°R to 1158°R (330°C to 370°C)

From these pressure and temperature values:

$\Delta\rho_P$ = 0.221 lbs/ft^3 to 0.365 lbs/ft^3

$\Delta\rho_T$ = 9.33 lbs/ft^3 to 10.2 lbs/ft^3

ρ_L = 46.2 lb/ft^3 to 47.2 lb/ft^3 = 740 kg/m^3 to 756 kg/m^3

Finally, from the previously calculated values:

k_L = 2.05×10^{-4} cm/s to 2.86×10^{-4} cm/s

Calculation of the liquid/solid mass transfer coefficient (k_S):

The liquid/solid mass transfer coefficient was estimated using a correlation by Van Krevelen and Krekels (Froment and Bishoff, 1990):

$$\frac{k_S}{D_L\cdot a_S} = 1.8\cdot\sqrt{\frac{L_A}{a_S\cdot\mu_L}}\cdot\left(\frac{\mu_L}{\rho_L\cdot D_L}\right)^{1/3} \qquad \text{[F.11]}$$

The variables are defined as:

a_S = Liquid/solid interfacial surface area = a_L = 24.7 cm^{-1}

Using the previously determined terms:

k_S = 3.17×10^{-3} cm/s to 5.12×10^{-3} cm/s

Calculation of the equilibrium concentration of hydrogen in gas oil (C_{H2}):

The equilibrium concentration of hydrogen in gas oil was calculated by applying Henry's constant with the assumption of limited solubility:

$$C_{H2} = \frac{P}{H_{H2}} \qquad [F.12]$$

The variables are defined as:

H_{H2} = Henry's constant for hydrogen in CLGO, MPa·m^3/mol

P = Operating pressure = 6.6 MPa to 11.0 MPa

Henry's constant can be calculated using the equation below:

$$H_{H2} = \frac{v_N}{\lambda_{H2} \cdot \rho_L} \qquad [F.13]$$

The variables are defined as:

v_N = Hydrogen molar volume at standard conditions = 22.4 L/mol

ρ_L = Density of CLGO at the operating conditions = 740 kg/m^3 to 756 kg/m^3

λ_{H2} = Hydrogen solubility in CLGO, mL/(kg·MPa)

A correlation established by Korsten and Hoffmann (1996) was applied to estimate the solubility of hydrogen in gas oil fractions:

$$\lambda_{H2} = z_0 + z_1 \cdot T + z_2 \cdot \frac{T}{\rho_{20}} + z_3 \cdot T^2 + z_4 \cdot \frac{1}{(\rho_{20})^2} \qquad \text{[F.14]}$$

The parameters are defined as:

z_0 = -0.55973

z_1 = -0.42947×10^{-3}

z_2 = 3.07539×10^{-3}

z_3 = 1.94593×10^{-6}

z_4 = 0.83578

T = Operating temperature = 330°C to 370°C

ρ_{20} = Density of CLGO at 20°C = 0.897 g/mL

For the operating conditions, the following value ranges were found:

λ_{H2} = 1.68×10^{3} mL/(kg·MPa) to 1.85×10^{3} mL/(kg·MPa)

H_{H2} = 0.0176 MPa·m^3/mol to 0.0163 MPa·m^3/mol

C_{H2} = 6.24×10^{-4} mol/mL to 4.04×10^{-4} mol/mL

Calculating the hydrogen conversion rate for HDS and HDN:

The following simplified stoichiometric equations were used for finding the rate of hydrogen conversion for both hydrodesulfurization and hydrodenitrogenation:

$$|R-S| + \underline{x_{HDS}} H_2 \xrightarrow{CATALYST} |R-H|_{[2x_{HDS}-2]} + H_2S \qquad \text{[F.15]}$$

$$|R-N| + \underline{x_{HDN}} H_2 \xrightarrow{CATALYST} |R-H|_{[2x_{HDN}-3]} + NH_3 \qquad \text{[F.16]}$$

The rates of nitrogen and sulfur removal for varying operating conditions applied to the hydrotreating process were determined from section 6.5 and Appendix E of the report. Equations F.15 and F.16 allow for the following substitutions:

HDS:

$$\left(\frac{-1}{V_C}\cdot\frac{dn}{dt}\right)=\frac{x_{HDS}\cdot r_{HDS}}{V_C} \qquad [F.17]$$

HDN:

$$\left(\frac{-1}{V_C}\cdot\frac{dn}{dt}\right)=\frac{x_{HDN}\cdot r_{HDN}}{V_C} \qquad [F.18]$$

Where r_{HDS} is the molar rate of sulfur removal and r_{HDN} is the molar rate of nitrogen removal achieved from the hydrotreating catalyst (mol/s). Assuming the hydrogenation of a 5-membered thiophenic ring for sulfur removal and a 6-membered basic pyridinic ring for nitrogen removal, the following stoichiometric values were assumed for the HDS and HDN reactions of coker light gas oil:

$x_{HDS} = 4.0$; $x_{HDN} = 5.0$

Given these assumed values for each reaction, the following value ranges were found for each side of the Satterfield inequality:

Hydrodesulfurization Reaction:

Left hand side of Satterfield's criterion = 8.51×10^{-4} cm/s to 1.16×10^{-3} cm/s

Right hand side of Satterfield's criterion = 1.93×10^{-4} cm/s to 2.71×10^{-4} cm/s

Hydrodenitrogenation Reaction:

Left hand side of Satterfield's criterion = 9.83×10^{-5} cm/s to 2.51×10^{-4} cm/s

Right hand side of Satterfield's criterion = 1.93×10^{-4} cm/s to 2.71×10^{-4} cm/s

A summary of all the operating conditions and estimated parameters contributing to these results can be found in Table E.1 on the following page.

Table F.1
Summary of the external mass transfer resistances study performed for a trickle bed hydrotreating reactor loaded with NiMo/MWCNT catalyst.

Parameter	Symbol	Value	Units	Value Range
Pressure	**P**	88	bar	66 to 110
Temperature	**T**	350	°C	330 to 370
Average boiling point temperature of CLGO	$\mathbf{T_b}$	570	°F	-
Liquid hourly space velocity	**LHSV**	2.0	h^{-1}	1.5 to 2.5
Feed flow rate	**L**	9.0	g/h	6.75 to 11.25
Particle size	$\mathbf{d_P}$	0.17	cm	-
Bed porosity (Wijngaarden et al., 1998)	**ε**	0.3	-	-
Interfacial surface area per unit volume	$\mathbf{\alpha_L}$	24.7	cm^{-1}	-
Liquid mass flow per unit area	$\mathbf{L_A}$	1.62	$\times 10^{-3}$ g/(cm^2·s)	1.22 to 2.02
CLGO density under operating conditions	$\mathbf{\rho_L}$	748	kg/m^3	740 to 756
CLGO density at 15.6°C	$\mathbf{\rho_{15.6}}$	900	kg/m^3	-
CLGO density at 20°C	$\mathbf{\rho_{20}}$	897	kg/m^3	-
Pressure density correlation	$\mathbf{\Delta\rho_P}$	0.293	lbs/ft^3	0.221 to 0.365
Temperature density correlation	$\mathbf{\Delta\rho_T}$	9.76	lbs/ft^3	9.33 to 10.2
CLGO specific gravity at 60°F	**SG**	0.901	-	-
API density rating	**°API**	25.6	-	-
Constant in viscosity correlation (Ahmed, 1989)	**α**	-7.36	-	-7.61 to -7.12
CLGO average molecular weight	$\mathbf{M_{AVE}}$	212	kg/mol	-
CLGO viscosity at operating temperature	$\mathbf{\mu_L}$	0.489	cP	0.544 to 0.442
Henry's constant	$\mathbf{H_{H2}}$	0.0170	MPa-m^3/gmol	0.0176 to 0.0163
Hydrogen molecular volume, standard conditions	$\mathbf{v_N}$	22400	cc/mol	-
Concentration of H_2 in CLGO	$\mathbf{C_{H2}}$	5.19	$\times 10^{-4}$ mol/cc	6.24 to 4.04
Solubility of H_2 in CLGO (Hoffman et al., 1996)	$\mathbf{\lambda_{H2}}$	1.77	$\times 10^{3}$ cc/kg	1.68 to 1.85
Bulk diffusivity of hydrogen	$\mathbf{D_L}$	2.78	$\times 10^{-4}$ cm^2/s	2.42 to 3.18
Particle properties constant (Goto & Smith, 1975)	$\mathbf{á_1}$	7.0	-	-
Particle properties constant (Goto & Smith, 1975)	$\mathbf{á_2}$	0.4	-	-
Liquid side: H_2/CLGO mass transfer coefficient	$\mathbf{k_L}$	2.46	$\times 10^{-4}$ cm/s	2.05 to 2.86
Solid side: H_2/CLGO mass transfer coefficient	$\mathbf{k_S}$	4.11	$\times 10^{-3}$ cm/s	3.17 to 5.12
Overall mass transfer coefficient	$\mathbf{k_{OVR}}$	2.32	$\times 10^{-4}$ cm/s	1.93 to 2.71
Rate of H_2 consumption for the HDS reaction	$\mathbf{(x_{HDS}\cdot r_{HDS})/V_C}$	9.93	$\times 10^{-7}$ mol·H_2/(s·cc)	7.47 to 11.09
Rate of H_2 consumption for the HDN reaction	$\mathbf{(x_{HDN}\cdot r_{HDN})/V_C}$	1.53	$\times 10^{-7}$ mol·H_2/(s·cc)	0.86 to 2.40
Satterfield's criterion for HDS, left-side value	$\mathbf{S_{HDS}}$	10.8	$\times 10^{-4}$	8.51 to 11.6
Satterfield's criterion for HDN, left-side value	$\mathbf{S_{HDN}}$	1.67	$\times 10^{-4}$	0.98 to 2.51

APPENDIX G:
Evaluating the Internal Mass Transfer Resistances for the HDS and HDN Reactions

The preliminary calculations performed as part of this evaluation was to see if isothermality could be assumed within the catalyst pellets. The determination of each pellet's degree of isothermality was performed in two ways: by finding both the highest potential temperature rise between the core and the surface of the pellet (Fogler, 2006), as well as by confirming Anderson's criterion (1963).

Maximum temperature rise (ΔT_{MAX}):

$$\beta = \frac{\Delta T_{MAX}}{T_S} = \frac{\Delta H_{R,i} \cdot D_i \cdot [C_i]_S}{k_t \cdot T_S} \qquad [G.1]$$

The variables are defined as:

$\Delta H_{R,i}$ = Heat of HDS/HDN reaction, kJ/mol

$[C_i]_S$ = Catalyst surface concentration of sulfur/nitrogen species, mol/mL

k_t = Thermal conductivity of the NiMo/MWCNT catalyst pellet.

k_t = 0.155 W/(cm·K) (assuming a pure CNT pellet, Yang et al., 2002)

T_S = Pellet surface temperature = 603 K to 643 K (reaction temperatures)

Calculation of the HDS/HDN heats of reaction:

The hydrodesulfurization heat of reaction for coker light gas oil from Athabasca bitumen was approximated by using the heat of reaction range for most thiophene molecules; 63 to 66 kJ/mol of hydrogen consumed (Ancheyta and Speight, 2007). The hydrodenitrogenation heat of reaction for CLGO from Athabasca bitumen

was approximated by using the heat of reaction range for most quinoline molecules; 65 to 68 kJ/mol of hydrogen consumed (Satterfield and Cocchetto, 1981). These values were converted to units of kJ/mol of sulfur/nitrogen removed by using the stoichiometric coefficients (x_{HDS} and x_{HDN}) discussed in Appendix F.

$\Delta H_{R,HDS}$ = 63 to 66 kJ/mol of H_2 consumed

$\Delta H_{R,HDS}$ = 252 to 264 kJ/mol of sulfur

$\Delta H_{R,HDN}$ = 65 to 68 kJ/mol of H_2 consumed

$\Delta H_{R,HDN}$ = 260 to 272 kJ/mol of nitrogen

Calculating the effective diffusivities of organosulfur and organonitrogen compounds in CLGO ($/D_S/_E/D_N/_E$):

The effective diffusivity of sulfur compounds was estimated by the following equation:

$$\left[D_i\right]_E = \frac{\varepsilon_P \cdot D_i}{\gamma_P} \qquad [G.2]$$

The variables are defined as:

ε_P = Porosity of the catalyst pellets

γ_P = Tortuosity of the catalyst pellets

D_i = Bulk diffusivity of organosulfur compounds, cm^2/g

A correlation by Probst and Wohlfahrt (1979) was used to find the ratio of porosity and tortuosity of pelletized catalysts:

$$\frac{\varepsilon_P}{\gamma_P} = \left[\frac{{\varepsilon_P}^m}{\left(2-\varepsilon_P\right)^{m+1}}\right] \qquad [G.3]$$

Values of ***m*** were found to range from 0.70 to 1.65 for porous compressed catalysts (group D). It was recommended to use an ***m*** value of 1.05 when not otherwise determined (Wijngaarden et al., 1998). Porosity values were found to range from 0.05 to 0.65 (average value was used, 0.35). Based on these conditions, the porosity/tortuosity values were found:

$$\frac{\varepsilon_P}{\gamma_P} = 0.1190 \quad (0.0012 \text{ to } 0.4441)$$

Calculating the bulk diffusivities of organosulfur and organonitrogen compounds in CLGO (D_S/D_N):

The assumption was made that the organosulfur and organonitrogen compounds held the same density, average boiling point, average molecular weight and average molar volume as the coker light gas oil feedstock. The bulk diffusivities of each species were found using the Tyn-Calus correlation (Reid et al., 1987):

$$D_i = \left(8.93 \times 10^{-8}\right) \cdot \left(\frac{v_L^{\,0.267}}{v_i^{\,0.433}}\right) \cdot \left(\frac{T}{\mu_L}\right) = \left(8.93 \times 10^{-8}\right) \cdot \left(\frac{T}{\mu_L \cdot v_i^{\,0.166}}\right) \quad [G.4]$$

The variables are defined as:

T = Operating temperature = 603 K to 643 K

μ_L = CLGO viscosity at operating conditions = 0.544 cP to 0.442 cP (see Appendix F)

v_i = Molar volume of sulfur/nitrogen molecules under standard conditions, mL/mol

v_L = Molar volume of CLGO under standard conditions, mL/mol

The molar volume of the gas oil was found by the following:

$$\boxed{v_i = (0.285) \cdot v_C^{\,1.048}} \qquad [G.5]$$

$\boldsymbol{v_C}$ = Critical specific molar volume of CLGO, mL/mol

The critical specific molar volume is given by:

$$\boxed{v_C = v_C^m \cdot M_{AVE}} \qquad [G.6]$$

$\boldsymbol{M_{AVE}}$ = 212 g/mol (determined in Appendix F)

$\boldsymbol{v_C^m}$ = Critical specific mass volume, mL/g

The critical specific mass volume of liquid was calculated using a correlation by Raizi and Daubert (Ahmed, 1989):

$$\boxed{v_C^m = \left(7.5214 \times 10^{-3}\right) \cdot T_b^{\,0.2896} \cdot SG^{-0.7666}} \qquad [G.7]$$

The variables are defined as:

$\boldsymbol{v_C^m}$ = Critical specific mass volume, ft^3/lb

$\boldsymbol{T_b}$ = Average boiling point temperature = 299°C = 1030°R

$\boldsymbol{SG_{15.6}}$ = Specific gravity at 15.6°C = 0.901

These values lead to the following results:

$\boldsymbol{v_C^m}$ = 3.79 mL/g

$\boldsymbol{v_C}$ = 802 mL/mol

$\boldsymbol{v_i}$ = 315 mL/mol

$\boldsymbol{D_i} = \boldsymbol{D_S} = \boldsymbol{D_N} = 3.81\times10^{-5}$ cm^2/g to 5.00×10^{-5} cm^2/g

$\boldsymbol{[D_S]_E} = \boldsymbol{[D_N]_E} = 4.53\times10^{-6}$ cm^2/g to 5.95×10^{-6} cm^2/g

The effective diffusivity values lead to isothermality ratios of:

$\boldsymbol{\beta_{HDS}} = 4.69\times10^{-5}$ to 5.78×10^{-5}

$\boldsymbol{\beta_{HDN}} = 1.07\times10^{-5}$ to 1.32×10^{-5}

Because the HDS and HDN reactions are occurring simultaneously, the sum of the beta values would give the overall maximum temperature change with respect to the catalyst surface temperature. This gives a highest possible $\boldsymbol{\Delta T_{MAX}}$ value of 0.046 K, which can be considered negligible.

Anderson's Criterion:

$$\frac{\left|\Delta H_{R,i}\right| \cdot \{R_i\} \cdot d_P^{\,2}}{k_t \cdot T_S} < \frac{3 \cdot T_S \cdot R}{E_i} \qquad \text{[G.8]}$$

The variables are defined as:

$\boldsymbol{\{R_i\}}$ = Global reaction rate: HDS/HDN, mol/(s·mL)

$\boldsymbol{k_t}$ = Catalyst thermal conductivity = 0.155 W/(cm·K)

$\boldsymbol{R}$ = Universal gas constant = 8.314 J/(mol·K)

$\boldsymbol{E_i}$ = Energy of activation: HDS/HDN, J/mol

The range of operating conditions tested, the values for the left and right hand side of Anderson's criterion were as follows:

Left hand side of Anderson's criterion (HDS) = 3.64×10^{-6} to **5.30×10^{-6}**

Right hand side of Anderson's criterion (HDS) = 0.0241 to **0.0251**

Left hand side of Anderson's criterion (HDN) = 3.48×10^{-7} to **9.44×10^{-7}**

Right hand side of Anderson's criterion (HDN) = 0.0472 to **0.0919**

The results confirm that isothermal behavior can be assumed when examining the internal mass transfer resistances of the hydrotreating process. Table G.1 at the end of this appendix provides a summary of the pertinent parameters and results of the catalyst pellet isothermality study.

Calculation of Φ:

A dimensionless modulus (Φ), analogous to the Thiele modulus found without knowledge of the intrinsic reaction rate, was found for each collected sample in the kinetic study. The dimensionless modulus was used to represent an estimation of the pore diffusion resistance (Satterfield, 1970):

$$\Phi = \frac{{d_P}^2}{4 \cdot [D_i]_E} \cdot \frac{\{R_i\}}{[C_i]_S} \qquad [G.9]$$

The variables are defined as:

d_P = Average diameter of the catalyst particles = 0.17 cm

$\{R_i\}$ = Global reaction rate: HDS/HDN, mol/(s·mL)

$[D_i]_E$ = Effective diffusivity of sulfur/nitrogen compounds, cm^2/g

$[C_i]_S$ = Catalyst surface concentration of sulfur/nitrogen species, mol/mL

The change in the global reaction rate and the change in surface concentration of sulfur and nitrogen heteroatoms allow the dimensionless modulus to be calculated at both the inlet and outlet of the reactor. In finding the dimensionless modulus, a rough approximation of the effectiveness factor (η) could be determined by applying the following equations in unison (Satterfield, 1970):

$$\boxed{\Phi = (\phi)^2 \cdot \eta} \qquad [G.10]$$

$$\boxed{\eta = \frac{3}{\phi}\left[\frac{1}{\tanh(\phi)} - \frac{1}{\phi}\right]} \qquad [G.11]$$

Solving for the effectiveness factor using equations [G.10] and [G.11] will only provide a rough estimate of both $\boldsymbol{\eta}$ and $\boldsymbol{\varphi}$, the true Thiele modulus. This is because equation G.10 only applies to integer-power rate equations for spherical catalyst pellets. Additionally, equation G.11 only applies to isothermal first-order reactions for spherical catalysts. Nonetheless, these equations to provide a measure of comparison between the effectiveness factors for each collected sample.

Table G.2 provides a summary of all the dimensionless modulus values for the inlet and outlet ($[\Phi_O]_S$ and $[\Phi_P]_S$), as well as all the determined effectiveness factors ($[\eta_O]_S$ and $[\eta_P]_S$), for the hydrodesulfurization kinetic study.

Table G.3 provides a summary of all the dimensionless modulus values for the inlet and outlet ($[\Phi_O]_N$ and $[\Phi_P]_N$), as well as all the determined effectiveness factors ($[\eta_O]_N$ and $[\eta_P]_N$), for the hydrodenitrogenation kinetic study.

Table G.1
Summary of the isothermality study performed for NiMo/MWCNT catalyst pellets loaded in a trickle bed hydrotreating reactor.

Parameter	Symbol	Value	Units	Range
Pressure	P	88	bar	66 to 110
Temperature	T	350	°C	330 to 370
Average boiling point temperature of CLGO	T_b	570	°F	-
Liquid hourly space velocity	LHSV	2.0	h^{-1}	1.5 to 2.5
Feed flow rate	L	9.0	g/h	6.75 to 11.25
Particle size	d_P	0.17	cm	-
CLGO viscosity at operating temperature	μ_L	0.489	cP	0.544 to 0.442
Critical molar volume of CLGO molecules	v_L	802	cc/mol	-
Heat of HDS reaction	ΔH_{HDS}	258	kJ/mol	252 to 264
Heat of HDN reaction	ΔH_{HDN}	266	kJ/mol	260 to 272
Effective diffusivity of sulphur	$(D_E)_S$	5.21	$\times 10^{-6} cm^2/s$	4.53 to 5.95
Effective diffusivity of nitrogen	$(D_E)_N$	5.21	$\times 10^{-6} cm^2/s$	4.53 to 5.95
Porosity of catalyst pellet	ε_P	0.35	-	0.05 to 0.65
Parameter m (Probst and Wohlfahrt, 1979)	m	1.05	-	0.70 to 1.65
Porosity/tortuosity ratio	ε_P/γ_P	0.119	-	0.444 to 1.20×10^{-3}
Diffusivity of sulfur compounds	D_S	4.38	$\times 10^{-5} cm^2/s$	3.81 to 5.00
Diffusivity of nitrogen compounds	D_N	4.38	$\times 10^{-5} cm^2/s$	3.81 to 5.00
Surface concentration in CLGO	$C_{S,S}$	4.47	$\times 10^{-4}$ mol/cc	4.47 to 0.45
Surface concentration in CLGO	$C_{N,S}$	0.99	$\times 10^{-4}$ mol/cc	0.99 to 0.33
Thermal conductivity of MWCNT catalyst pellet	k_T	0.155	J/(cm·K)	0.14 to 0.17
Activation energy of HDS	E_{HDS}	155	kJ/mol	155 to 161
Activation energy of HDN	E_{HDN}	42.3	kJ/mol	42.3 to 82.3
β value for HDS	β_{HDS}	5.22	$\times 10^{-5}$	4.69 to 5.78
β value for HDN	β_{HDN}	1.20	$\times 10^{-5}$	1.07 to 1.32
Global rate of HDS reaction	$\{R_{HDS}\}$	2.48	mol/(s·cc)	1.87 to 2.77
Global rate of HDN reaction	$\{R_{HDN}\}$	3.05	mol/(s·cc)	1.73 to 4.79
Anderson's criterion, left-side value (HDS)	$(A_{HDS})_{LEFT}$	4.79	$\times 10^{-6}$	3.64 to 5.30
Anderson's criterion, right-side value (HDS)	$(A_{HDS})_{RIGHT}$	0.0251	-	0.0241 to 0.0251
Anderson's criterion, left-side value (HDN)	$(A_{HDN})_{LEFT}$	6.08	$\times 10^{-7}$	3.48 to 9.44
Anderson's criterion, right-side value (HDN)	$(A_{HDN})_{RIGHT}$	0.0919	-	0.0472 to 0.0919

Table G.2
Summary of the dimensionless modulus values and effectiveness factors for the internal mass transfer resistances study of CLGO hydrodesulfurization.

Run Time (days)	T (°C)	LHSV (h^{-1})	P (MPa)	G/L (mL/mL)	$[\Phi_O]_S$ (no units)	$[\Phi_P]_S$ (no units)	$[\eta_O]_S$ (no units)	$[\eta_P]_S$ (no units)
0.5	370	1.5	8.8	600	0.451	4.108	0.970	0.760
1.0	370	1.5	8.8	600	0.444	3.635	0.971	0.782
1.5	370	1.5	8.8	600	0.445	3.704	0.971	0.778
2.0	370	1.5	8.8	600	0.446	3.768	0.971	0.775
2.5	370	1.5	8.8	600	0.441	3.453	0.971	0.791
3.0	370	1.5	8.8	600	0.448	3.876	0.971	0.770
4.0	370	1.5	8.8	600	0.451	4.117	0.970	0.758
4.5	370	1.5	8.8	600	0.454	4.430	0.970	0.744
5.0	370	1.5	8.8	600	0.452	4.194	0.970	0.755
6.0	370	2.5	8.8	600	0.745	6.375	0.951	0.667
6.5	370	2.5	8.8	600	0.733	5.620	0.952	0.695
7.0	370	2.5	8.8	600	0.733	5.620	0.952	0.695
8.0	370	2.0	8.8	600	0.590	4.718	0.961	0.731
8.5	370	2.0	8.8	600	0.576	3.914	0.962	0.768
9.0	370	2.0	8.8	600	0.581	4.203	0.962	0.754

Run Time (days)	T (°C)	LHSV (h^{-1})	P (MPa)	G/L (mL/mL)	$[\Phi_O]_S$ (no units)	$[\Phi_P]_S$ (no units)	$[\eta_O]_S$ (no units)	$[\eta_P]_S$ (no units)
10.0	350	1.5	8.8	600	0.491	3.270	0.968	0.800
10.5	350	1.5	8.8	600	0.492	3.293	0.968	0.799
11.0	350	1.5	8.8	600	0.469	2.478	0.969	0.844
12.0	350	2.5	8.8	600	0.751	3.401	0.951	0.793
12.5	350	2.5	8.8	600	0.735	3.100	0.952	0.809
13.0	350	2.5	8.8	600	0.755	3.492	0.951	0.789
14.0	350	2.0	8.8	600	0.622	3.237	0.959	0.802
14.5	350	2.0	8.8	600	0.615	3.042	0.960	0.813
15.0	350	2.0	8.8	600	0.613	3.000	0.960	0.815
16.0	330	1.5	8.8	600	0.470	1.609	0.969	0.898
16.5	330	1.5	8.8	600	0.470	1.602	0.969	0.899
17.0	330	1.5	8.8	600	0.465	1.554	0.969	0.902
18.0	330	2.5	8.8	600	0.669	1.688	0.956	0.893
18.5	330	2.5	8.8	600	0.674	1.723	0.956	0.891
19.0	330	2.5	8.8	600	0.658	1.622	0.957	0.897
20.0	330	2.0	8.8	600	0.566	1.563	0.963	0.901

Run Time (days)	T (°C)	LHSV (h^{-1})	P (MPa)	G/L (mL/mL)	$[\Phi_O]_S$ (no units)	$[\Phi_P]_S$ (no units)	$[\eta_O]_S$ (no units)	$[\eta_P]_S$ (no units)
20.5	330	2.0	8.8	600	0.581	1.691	0.962	0.893
21.0	330	2.0	8.8	600	0.556	1.491	0.964	0.906
22.0	330	2.0	8.8	450	0.541	1.388	0.964	0.913
22.5	330	2.0	8.8	450	0.547	1.431	0.964	0.910
23.0	330	2.0	8.8	450	0.480	1.049	0.968	0.935
24.0	330	2.0	8.8	750	0.583	1.701	0.962	0.892
24.5	330	2.0	8.8	750	0.611	1.964	0.960	0.876
25.0	330	2.0	8.8	750	0.601	1.872	0.961	0.881
26.0	330	2.0	6.6	600	0.551	1.459	0.964	0.908
26.5	330	2.0	6.6	600	0.554	1.481	0.964	0.906
27.5	330	2.0	7.7	600	0.519	1.252	0.966	0.921
28.0	330	2.0	7.7	600	0.563	1.547	0.963	0.902
29.0	330	2.0	8.8	600	0.579	1.669	0.962	0.894
29.5	330	2.0	8.8	600	0.558	1.506	0.963	0.905
30.5	330	2.0	9.9	600	0.575	1.635	0.962	0.896
31.0	330	2.0	9.9	600	0.570	1.599	0.963	0.899

Run Time (days)	T (°C)	LHSV (h^{-1})	P (MPa)	G/L (mL/mL)	$[\Phi_O]_S$ (no units)	$[\Phi_P]_S$ (no units)	$[\eta_O]_S$ (no units)	$[\eta_P]_S$ (no units)
32.0	330	2.0	11.0	600	0.558	1.506	0.963	0.905
32.5	330	2.0	11.0	600	0.589	1.758	0.961	0.888

Table G.3
Summary of the dimensionless modulus values and effectiveness factors for the internal mass transfer resistances study of CLGO hydrodenitrogenation.

Run Time (days)	T (°C)	LHSV (h^{-1})	P (MPa)	G/L (mL/mL)	$[\Phi_O]_N$ (no units)	$[\Phi_P]_N$ (no units)	$[\eta_O]_N$ (no units)	$[\eta_P]_N$ (no units)
0.5	370	1.5	8.8	600	0.333	0.974	0.978	0.937
1.0	370	1.5	8.8	600	0.316	0.839	0.979	0.945
1.5	370	1.5	8.8	600	0.316	0.839	0.979	0.945
2.0	370	1.5	8.8	600	0.313	0.822	0.979	0.946
2.5	370	1.5	8.8	600	0.313	0.822	0.979	0.946
3.0	370	1.5	8.8	600	0.313	0.818	0.979	0.947
4.0	370	1.5	8.8	600	0.349	1.129	0.977	0.928
4.5	370	1.5	8.8	600	0.355	1.184	0.977	0.924
5.0	370	1.5	8.8	600	0.353	1.167	0.977	0.925
6.0	370	2.5	8.8	600	0.476	1.093	0.969	0.930
6.5	370	2.5	8.8	600	0.463	1.028	0.970	0.934
7.0	370	2.5	8.8	600	0.467	1.045	0.969	0.933
8.0	370	2.0	8.8	600	0.363	0.786	0.976	0.949
8.5	370	2.0	8.8	600	0.411	1.050	0.973	0.932
9.0	370	2.0	8.8	600	0.441	1.271	0.971	0.919

Run Time (days)	T (°C)	LHSV (h^{-1})	P (MPa)	G/L (mL/mL)	$[\Phi_O]_N$ (no units)	$[\Phi_P]_N$ (no units)	$[\eta_O]_N$ (no units)	$[\eta_P]_N$ (no units)
10.0	350	1.5	8.8	600	0.302	0.631	0.980	0.959
10.5	350	1.5	8.8	600	0.302	0.631	0.980	0.959
11.0	350	1.5	8.8	600	0.308	0.660	0.980	0.957
12.0	350	2.5	8.8	600	0.374	0.611	0.975	0.960
12.5	350	2.5	8.8	600	0.379	0.624	0.975	0.959
13.0	350	2.5	8.8	600	0.381	0.632	0.975	0.958
14.0	350	2.0	8.8	600	0.345	0.624	0.977	0.959
14.5	350	2.0	8.8	600	0.339	0.606	0.978	0.960
15.0	350	2.0	8.8	600	0.342	0.614	0.977	0.960
16.0	330	1.5	8.8	600	0.238	0.370	0.984	0.976
16.5	330	1.5	8.8	600	0.232	0.356	0.985	0.977
17.0	330	1.5	8.8	600	0.234	0.360	0.985	0.976
18.0	330	2.5	8.8	600	0.278	0.371	0.982	0.976
18.5	330	2.5	8.8	600	0.281	0.377	0.981	0.975
19.0	330	2.5	8.8	600	0.274	0.365	0.982	0.976
20.0	330	2.0	8.8	600	0.250	0.348	0.983	0.977

Run Time (days)	T (°C)	LHSV (h^{-1})	P (MPa)	G/L (mL/mL)	$[\Phi_O]_N$ (no units)	$[\Phi_P]_N$ (no units)	$[\eta_O]_N$ (no units)	$[\eta_P]_N$ (no units)
20.5	330	2.0	8.8	600	0.253	0.353	0.983	0.977
21.0	330	2.0	8.8	600	0.250	0.348	0.983	0.977
22.0	330	2.0	8.8	450	0.253	0.353	0.983	0.977
22.5	330	2.0	8.8	450	0.255	0.359	0.983	0.976
23.0	330	2.0	8.8	450	0.267	0.382	0.982	0.975
24.0	330	2.0	8.8	750	0.257	0.362	0.983	0.976
24.5	330	2.0	8.8	750	0.255	0.359	0.983	0.976
25.0	330	2.0	8.8	750	0.231	0.313	0.985	0.979
26.0	330	2.0	6.6	600	0.178	0.223	0.988	0.985
26.5	330	2.0	6.6	600	0.194	0.248	0.987	0.984
27.5	330	2.0	7.7	600	0.209	0.273	0.986	0.982
28.0	330	2.0	7.7	600	0.214	0.282	0.986	0.981
29.0	330	2.0	8.8	600	0.236	0.323	0.984	0.979
29.5	330	2.0	8.8	600	0.233	0.316	0.985	0.979
30.5	330	2.0	9.9	600	0.251	0.350	0.983	0.977
31.0	330	2.0	9.9	600	0.253	0.355	0.983	0.977

Run Time (days)	T (°C)	LHSV (h^{-1})	P (MPa)	G/L (mL/mL)	$[\Phi_O]_N$ (no units)	$[\Phi_P]_N$ (no units)	$[\eta_O]_N$ (no units)	$[\eta_P]_N$ (no units)
32.0	330	2.0	11.0	600	0.267	0.382	0.982	0.975
32.5	330	2.0	11.0	600	0.270	0.389	0.982	0.974

APPENDIX H:
Power Law Models of HDS/HDN Fitted for the Optimum NiMo/CNT Catalyst

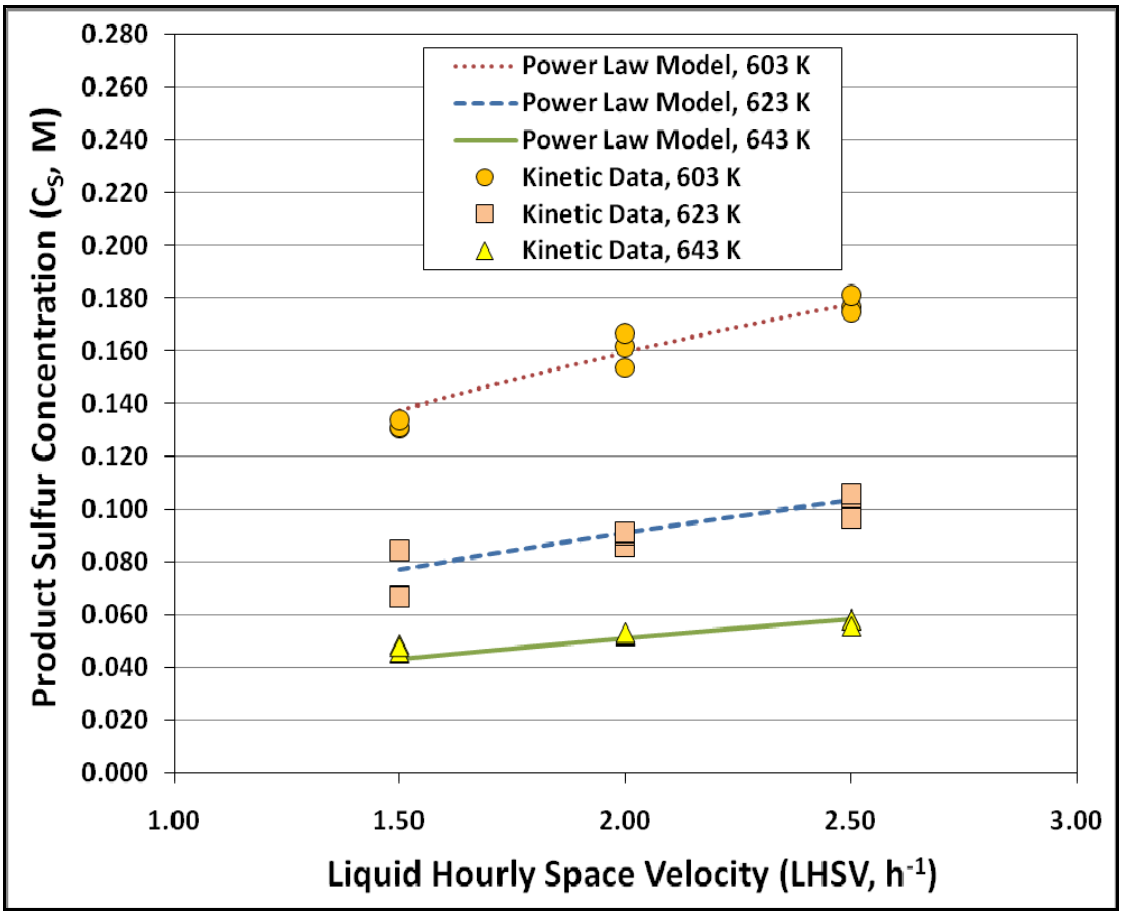

$$-r_{HDS} = k_{HDS} \cdot C_S^n$$

E_{HDS}	161 **kJ/mol**
A_{HDS}	4.68×10^{11} $\mathbf{M^{-1.6}\cdot s^{-1}}$
n	2.6
$(R^2)_{HDS}$	0.9887
$(R^2{}_A)_{HDS}$	0.9872

Figure H.1: Power law model for the hydrodesulfurization of coker light gas oil.

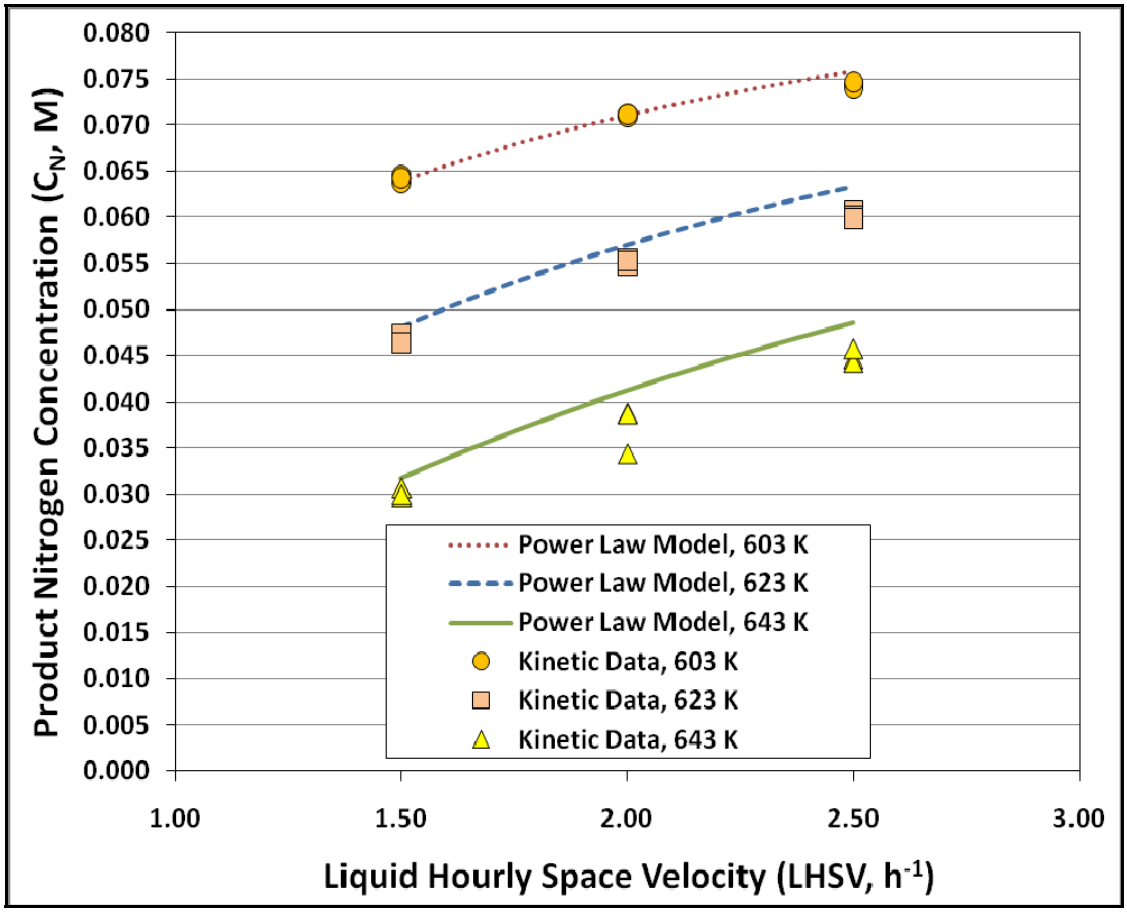

$$-r_{HDN} = k_{HDN} \cdot C_N^{v}$$

E_{HDN}	82.3 **kJ/mol**
A_{HDN}	4.10×10^{3} $\mathbf{M^{-0.2}\cdot s^{-1}}$
v	1.2
$(R^2)_{HDN}$	0.9080
$(R^2{}_A)_{HDN}$	0.8960

Figure H.2: Power law model for the hydrodenitrogenation of coker light gas oil.

APPENDIX I:
Independent Hybrid Models of HDS/HDN Fitted for the Optimum NiMo/CNT Catalyst

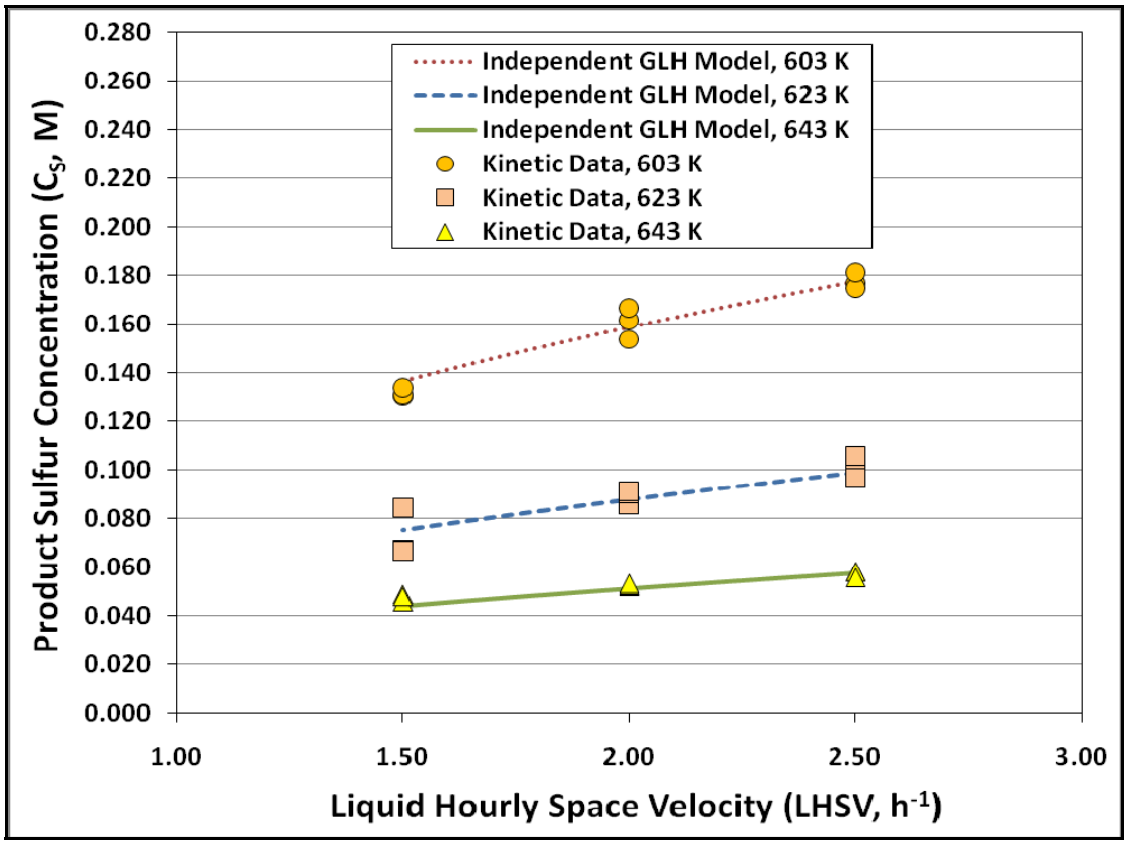

$$r_{HDS} = \frac{k_{HDS} \cdot C_S^{\,n}}{\left[1 + K_S C_S\right]^m}$$

E_{HDS}	155 **kJ/mol**	λ_S	71.9 **kJ/mol**
A_{HDS}	4.68×10^{11} $\mathbf{M^{-2.0}\cdot s^{-1}}$	m	1.2
n	3.0	$(R^2)_{HDS}$	0.9905
S_λ	1.86×10^{-6} $\mathbf{M^{-1}}$	$(R^2_A)_{HDS}$	0.9876

Figure I.1: Independent generalized Langmuir-Hinshelwood model for the hydrodesulfurization of coker light gas oil.

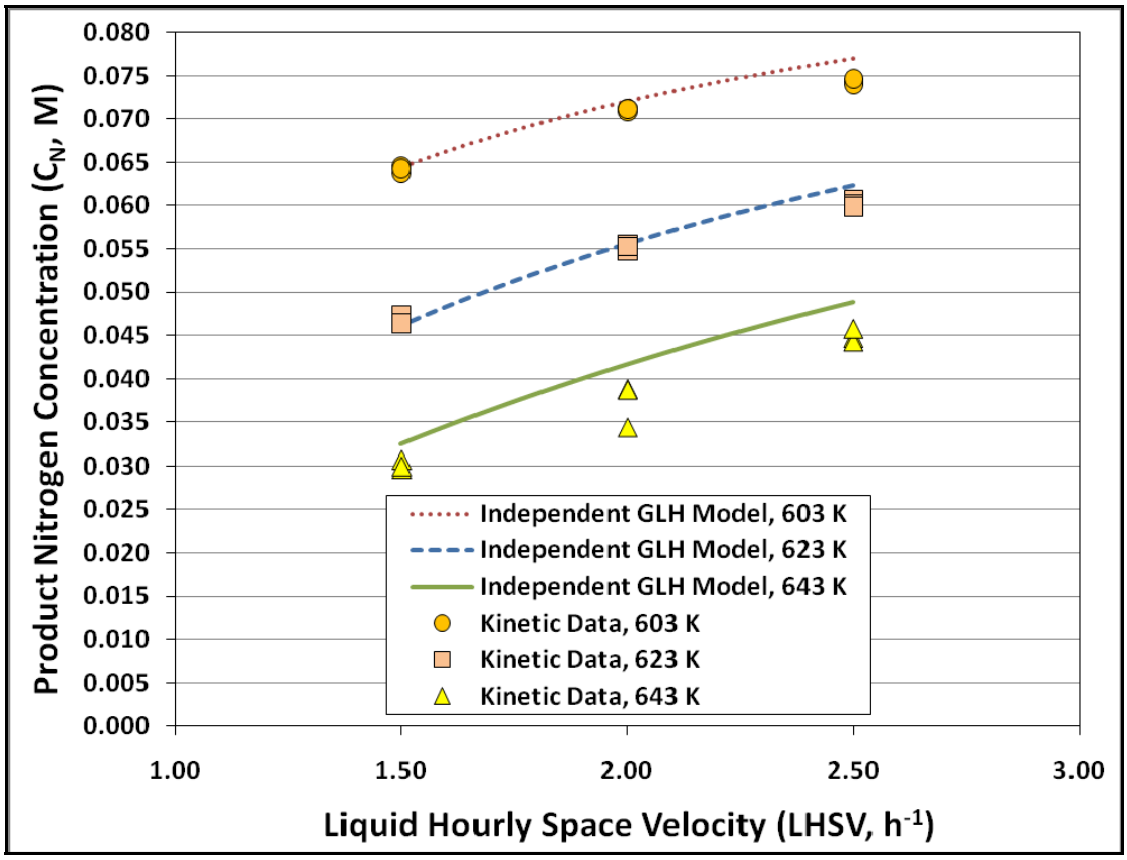

$$r_{HDN} = \frac{k_{HDN} \cdot C_N{}^{v}}{\left[1 + K_N C_N\right]^{u}}$$

E_{HDN}	42.3 **kJ/mol**	λ_N	79.3 **kJ/mol**
A_{HDN}	6.96 $\mathbf{M^{-0.5} \cdot s^{-1}}$	u	3.0
v	1.5	$(R^2)_{HDN}$	0.9146
N_λ	5.59×10^{-7} $\mathbf{M^{-1}}$	$(R^2{}_A)_{HDN}$	0.8890

Figure I.2: Independent generalized Langmuir-Hinshelwood model for the hydrodenitrogenation of coker light gas oil.

APPENDIX J:
Co-dependent Hybrid Models of HDS/HDN Fitted for the Optimum NiMo/CNT Catalyst

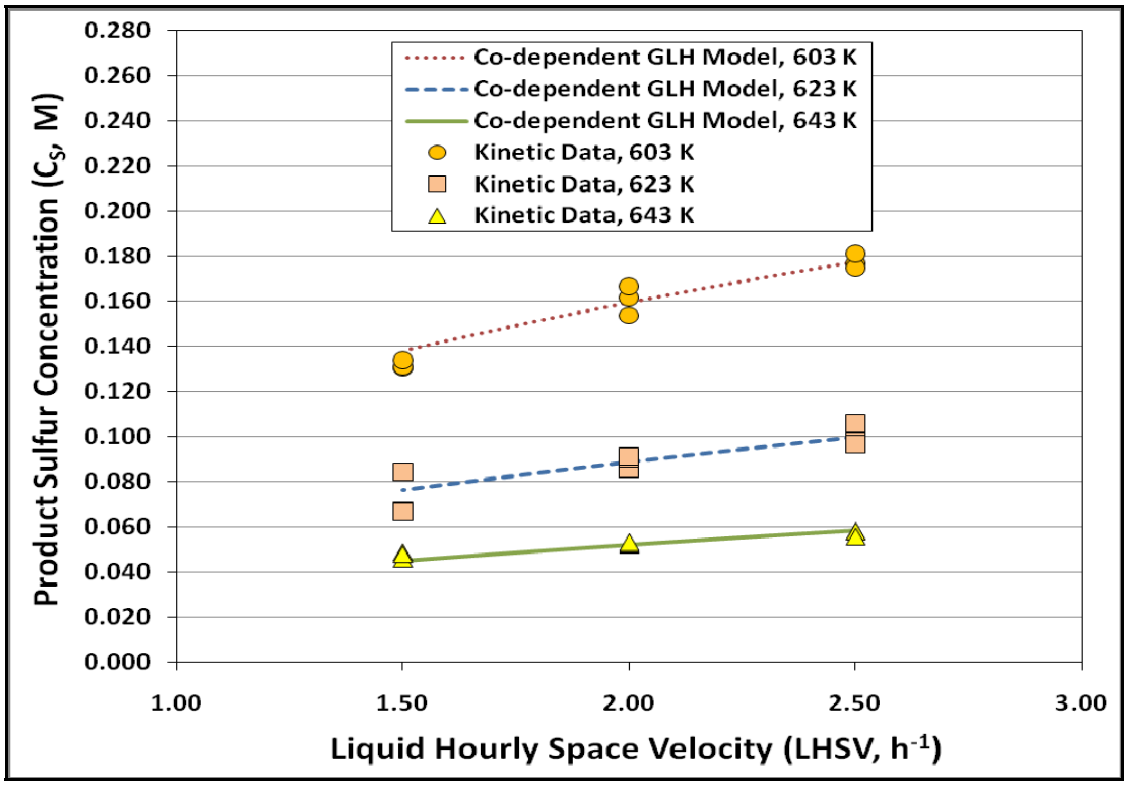

$$r_{HDS} = \frac{k_{HDS} \cdot C_S^{\,n}}{\left[1 + K_S C_S + K_N C_N\right]^m}$$

E_{HDS}	155 **kJ/mol**	λ_S	71.9 **kJ/mol**
A_{HDS}	4.68×10^{11} $\mathbf{M^{-2.0}\cdot s^{-1}}$	N_λ	4.35×10^{-7} $\mathbf{M^{-1}}$
n	3.0	λ_N	79.3 **kJ/mol**
m	1.3	$(R^2)_{HDS}$	0.9899
S_λ	9.13×10^{-7} $\mathbf{M^{-1}}$	$(R^2{}_A)_{HDS}$	0.9862

Figure J.1: Co-dependent generalized Langmuir-Hinshelwood model for the hydrodesulfurization of coker light gas oil.

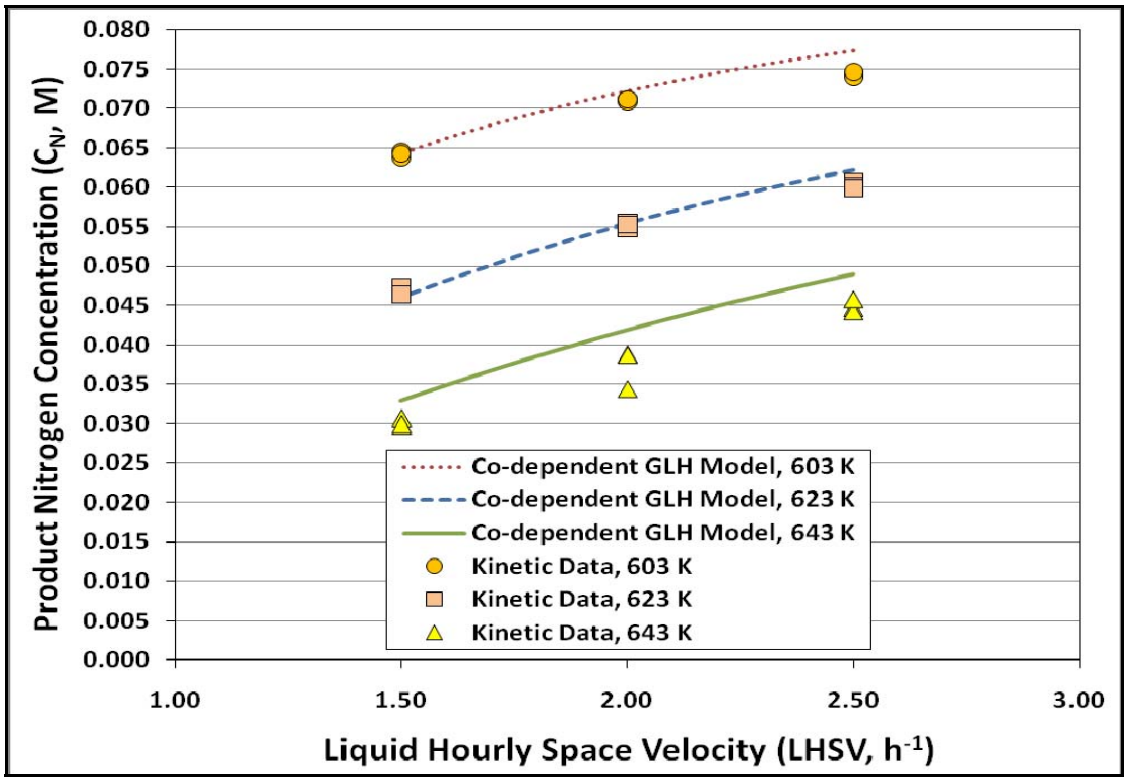

$$r_{HDN} = \frac{k_{HDN} \cdot C_S^{\ v}}{\left[1 + K_S C_S + K_N C_N\right]^u}$$

E_{HDN}	42.3 **kJ/mol**	λ_S	71.9 **kJ/mol**
A_{HDN}	6.46 $\mathbf{M^{-0.5} \cdot s^{-1}}$	N_λ	4.35×10^{-7} $\mathbf{M^{-1}}$
v	1.5	λ_N	79.3 **kJ/mol**
u	1.7	$(R^2)_{HDN}$	0.9140
S_λ	9.13×10^{-7} $\mathbf{M^{-1}}$	$(R^2_A)_{HDN}$	0.8823

Figure J.2: Co-dependent generalized Langmuir-Hinshelwood model for the hydrodenitrogenation of coker light gas oil.